Geomechanical characterization of geothermal reservoirs in the Bavarian Molasse Basin

Zur Erlangung des akademischen Grades eines
DOKTORS DER NATURWISSENSCHAFTEN

von der KIT-Fakultät für
Bauingenieur-, Geo- und Umweltwissenschaften
des Karlsruher Instituts für Technologie (KIT)
genehmigte

DISSERTATION

von

M.Sc. Robin Jonas Seithel
aus Karlsruhe

Tag der mündlichen Prüfung:

24. 07. 2019

Referent: Prof. Dr. Thomas Kohl
Korreferent: Prof. Dr. Kurosch Thuro

Karlsruhe 2019

To my grandparents

ABSTRACT

The ICCP report shows that a reduction in CO_2 emissions is necessary to stabilize global warming at 1.5 °C by 2030 (IPCC, 2018). Regarding this trend, Stadtwerke Munich has decided to replace the fossil energy with CO_2 neutral renewable energy sources. In the heating sector, geothermal energy offers a reliable, competitive source without greenhouse gas emissions. With the further expansion of the heating network, this energy source is becoming increasingly important in the Greater Munich Area. In recent years, microseismic events have been observed at a few existing power plants, leading to a public and scientific interest in a better characterization of the geomechanical reservoir behavior. However, to maintain high level acceptance, it is necessary to understand the mechanisms of induced seismicity in order to prevent such events in the future. This means that stress field in combination with the highly coupled poro-thermo-mechanical processes at the injection or production well must be evaluated more precisely.

The scientific understanding of the stress field before the present study is based on oil exploration in the 1950 and 1960, which largely covered only the Cenozoic strata. These data provide a good characterization of the orientation of the maximum horizontal stress (S_H) within the molasse sediments in the entire Bavarian Molasse Basin. However, the stress regime could not be determined and a depth limitation does not allow conclusions to be drawn about the stress field within the currently used Upper Jurassic Mesozoic reservoir. The borehole database recorded since the beginning of the geothermal development in 2003 allows to investigate additional stress field components and to improve the understanding of the geomechanical reservoir behavior. This present thesis consists of five studies focusing on the S_h-magnitude, the S_H-component and the stress rotation within the Upper Jurassic reservoir as wells as the seismic reactivation potential of fault structures.

I perform a detailed analysis of formation integrity tests (FIT), leak-off tests (LOT), cementation pressures and stimulation pressures from geothermal wells to interpret the S_h-magnitude. In a lithology dependent analysis of the S_h-magnitude I can determine a control factor of the sedimentological composition for the S_h-magnitude. Tests within the clay-rich Cenozoic strata indicate a minimum S_h of 16.5 MPa km^{-1}, within the limestone to marlstone of Purbeck a minimum S_{hgrad} of 15.5 MPa km^{-1} and within the Upper Jurassic carbonates a minimum S_{hgrad} of 14 MPa km^{-1}. Furthermore, the analysis of the LOT shows for the first time a normal-faulting stress regime in the central Molasse basin. Regarding the stress magnitudes, I was able to demonstrate that the horizontal differential stress magnitude ($S_H - S_h$) increases vertically from the Cenozoic sediments to the Upper Jurassic reservoir.

The interpretation of image logs provides detailed information about the stress regime and S_H-orientation for the Upper Jurassic reservoir. In total, good quality stress indicators have been identified at the borehole wall for 10 out of 17 wells, allowing a high quality mis-fit gridding for the S_H-orientation study. Results show an N-S S_H-orientation in

five wells, a counterclockwise rotation of 15° in three wells and a rotation of 30° and 60° counterclockwise each in one well. In addition, the interpretation of the borehole failure mechanism results in a strike-slip stress regime of $1.1 < S_H/S_v < 1.56$.

Subsequently, the stress field rotation observed in the Upper Jurassic reservoir is investigated in depth by numerical simulation. The numerical studies show that the counterclockwise rotation of the stress field can be caused by clockwise rotating fault structures of N000°E. A stiffness reduction within the deformation zone significantly changes the local stress orientation at N015°E to N045°E oriented fault structures, whereas at N060°E to N090°E fault structures the stiffness reduction has a minor influence on the stress field rotation. The observed N-S S_H-orientation (no local stress rotation) at the N045°E oriented fault zone in Unterhaching indicates that there must be a high differential stress in the Upper Jurassic reservoir that prevents stress rotation. To observe an counterclockwise stress rotation of 30° detected in Sauerlach, this study shows that such rotation is possible if there is a N010°E - N020°E oriented fault with reduced stiffness. The combination of numerical modeling results and stress observations can not only help to explain the stress reorientation at some of the sites, but also provide further information about the tectonic stress regime.

In the reactivation potential study, I was able to improve the understanding of the geomechanical behavior of fault structures in which induced microseismicity is detected in the Greater Munich Area. I was able to identify S_H, S_h, S_H-orientation and μ as the most sensitive parameters for the seismic hazard of fault structures. In this context, changes of the stress field components and alterations of the fault structure are the most dominant processes. Under critical fault conditions, e.g. at Unterhaching site, microseismicity in the area of fault structures, which is triggered by direct poro-thermo-elastic effects, enters a phase of aseismic deformation. At the Poing site, the five-year delay of the first microseismic detection in a fault structure with non-critical conditions shows long-term injection-related consequences. I interpreted that local injection induced poro-thermo-mechanical effects trigger a stress rearrangement or geochemical solution alter the fault resistance, which can lead to seismic deformations.

In this thesis I could provide a revised model for the stress field at the Cenozoic strata with indications of normal-faulting or transpressional faulting regime and gain new insights into the stress magnitude and the heterogeneous character of the S_H-orientation in the Upper Jurassic reservoir. Finally, I was able to integrate the developed stress field information from the Upper Jurassic into a reactivation potential study to investigate microseismicity of fault structures near the injection well. This understanding helps to identify poro-thermo-mechanical and geochemical effects to be considered in further geothermal development strategies for the Upper Jurassic reservoir in the Greater Munich Area.

Zusammenfassung

Der Bericht des ICCP verdeutlicht, dass eine Reduzierung der CO_2-Emissionen notwendig ist, um die globale Erwärmung bis 2030 auf 1.5 °C zu stabilisieren (IPCC, 2018). Vor diesem Hintergrund haben sich die Stadtwerke München entschlossen, fossile Energieträger durch CO_2-neutrale erneuerbare Energien zu ersetzen. Im Wärmesektor bietet die Geothermie eine zuverlässige, wettbewerbsfähige Alternative ohne Treibhausgasemissionen. Mit dem weiteren Ausbau des Wärmenetzes gewinnt die tiefe Geothermie im Großraum München zunehmend an Bedeutung. In den letzten Jahren wurden an einzelnen bestehenden Kraftwerken mikroseismische Ereignisse beobachtet, was zu einer öffentlichen und wissenschaftlichen Diskussion über eine verbesserte Charakterisierung des geomechanischen Reservoirverhaltens führte. Zur Aufrechterhaltung der hohen Akzeptanz der Bevölkerung ist es jedoch notwendig, die Ursachen dieser induzierten Seismizität zu verstehen, um derartige Vorfälle in Zukunft zu vermeiden. Dementsprechend muss das tektonische Spannungsfeld und das Zusammenwirken poro-thermo-mechanischen Prozessen im Bereich des Reservoirs genauer bewertet werden.

Im Vorfeld der vorliegenden Studie beruhte die Interpretation des Spannungsfeldes auf den Daten der Ölexploration der 1950er und 1960er, die überwiegend bis in die känozoischen Schichten reichte. Die Ergebnisse liefern für das gesamte bayrische Molassebecken eine gute Charakterisierung der Orientierung der maximalen horizontalen Spannung (S_H) innerhalb der känozoischen Molassesedimente. Das Spannungsregime konnte jedoch nicht eindeutig bestimmt werden und aufgrund der Tiefenbegrenzung konnten wenige Informationen über das Spannungsfeld innerhalb des derzeit genutzten mesozoischen Oberjura-Reservoirs gewonnen werden. Die seit Beginn der geothermischen Entwicklung im Jahr 2003 aufgezeichneten Bohrlochdaten ermöglichen es nun, zusätzliche Spannungsfeldkomponenten im Oberjura zu untersuchen und das Verständnis des geomechanischen Reservoirverhaltens zu verbessern. Die vorliegende Arbeit gliedert sich in fünf Studien, die die S_h-Magnitude, die S_H-Magnitude und eine mögliche Spannungsrotation im Oberjura-Reservoir sowie das seismische Reaktivierungspotenzial von Störungen untersucht.

Ich beschreibe eine detaillierte Analyse von Formation Integrity Tests (FIT), Leak-Off-Tests (LOT), Zementationsdrücken und Stimulations Drücken aus geothermischen Bohrungen zur Bestimmung der S_h-Magnitude. In einer lithologieabhängigen Untersuchung der S_h-Magnitude kann ich einen sedimentären Einfluss auf den S_h-Gradient ermitteln. Tests innerhalb der mergel-reichen känozoischen Schichten deuten auf ein Minimum des S_{hgrad} von 16.5 MPa km^{-1}, innerhalb des Kalk- bis Mergelstein im Purbeck auf ein Minimum des S_{hgrad} von 15.5 MPa km^{-1} und innerhalb der Karbonate des Oberjuras auf ein Minimalen S_{hgrad} von 14 MPa km^{-1} hin. Darüber hinaus zeigt die Analyse des LOT erstmals ein Abschiebungsregime im zentralen Molassebecken. Bezüglich der Spannungsverhältnisse konnte ich zeigen, dass die horizontale Differenzspannungsgröße ($S_H - S_h$) vertikal von den känozoischen Sedimenten in das Oberjura-Reservoir ansteigt.

Die Interpretation der Image-Logs liefert detaillierte Informationen über das Spannungsregime und die S_H-Orientierung des Oberjura-Reservoirs. Insgesamt wurden an der Bohrlochwand für 10 von 17 Bohrungen Spannungsindikatoren identifiziert, die mit einem Mis-fit Gridding die Bestimmung der S_H-Orientierung ermöglichen. Die Ergebnisse deuten auf eine N-S S_H-Orientierung in fünf Bohrungen, eine Drehung gegen den Uhrzeigersinn von 15° in drei Bohrungen und eine Drehung von 30° und 60° gegen den Uhrzeigersinn jeweils in einer Bohrung. Darüber hinaus ergibt die Interpretation des Versagensmechanismus an der Bohrlochwand ein Strike-Slip-Spannungsregime mit Spannungsverhältnissen von $1,1 < S_H/S_v < 1,56$.

Anschließend wird die im Oberjura-Reservoir beobachtete Spannungsfeldrotation durch numerische Simulationen näher untersucht. Die numerischen Studien verdeutlichen, dass eine Drehung des Spannungsfeldes gegen den Uhrzeigersinn durch im Uhrzeigersinn gedrehte Störungen gegen N000°E verursacht werden kann. Eine Änderung der Festigkeit innerhalb der Deformationszone ändert die lokale Spannungsorientierung für N015°E bis N045°E orientierte Störungen deutlich, während für N060°E bis N090°E orientierte Störungen eine Änderung der Festigkeit einen geringen Einfluss auf die Drehung des Spannungsfeldes hat. Die beobachtete N-S S_H-Orientierung (keine lokale Spannungsrotation) im Bereich der N045°E orientierten Störungszone in Unterhaching lässt darauf schließen, dass im Oberjura-Reservoir eine hohe Differenzspannung vorliegen muss, die somit eine Spannungsrotation entgegenwirkt. Um eine in Sauerlach nachgewiesene Spannungsrotation gegen den Uhrzeigersinn von 30° zu beobachten, muss eine N010°E - N020°E-orientierte Störung vorliegen. Die Kombination aus numerischen Modellierungen und Spannungsfeldbeobachtungen hilft nicht nur Spannungsreorientierung zu erklären, sondern liefert weitere Informationen über das tektonische Spannungsregime.

In der Studie zum Reaktivierungspotenzial konnte ich das Verständnis induzierter Mikroseismizität in Verbindung mit dem geomechanischen Verhalten von Störungsstrukturen im Großraum München verbessern. Dabei konnte ich die S_H, S_h, S_H-Orientierung und μ als die wichtigsten Parameter für die Einschätzung der Erdbebengefährdung von Störungen identifizieren. In diesem Zusammenhang sind Veränderungen der Spannungsfeld-Komponenten und Veränderungen der Störungsparameter die dominierenden Prozesse. Unter kritischen Spannungsbedingungen, wie z.B. am Standort Unterhaching, tritt Mikroseismizität im Bereich der Störungen auf welche durch direkte poro-thermo-elastische Effekte beeinflusst werden. Im weiteren zeitlichen Verlauf kann eine Phase mit aseismischer Verformung eingeleitet werden wodurch die Beobachtung von Mikroseismizität abnimmt. Am Standort Poing weist eine fünfjährige Verzögerung der ersten mikroseismischen Detektion in einer Störungsstruktur mit unkritischen Bedingungen auf langfristige injektionsbedingte Folgen hin. Meine Interpretation verdeutlicht, dass entweder lokale injektionsbedingte poro-thermo-mechanische Effekte eine Spannungsumlagerung auslösen oder eine geochemische Veränderung der Störungsfestigkeit, zu seismischen Ereignissen führen können.

In dieser Arbeit konnte ich ein überarbeitetes Modell für das Spannungsfeld im Känozoikum mit Hinweisen auf ein Abschiebungs- oder Übergangsregime bis hin zu einem Strike-Slip Regime liefern. Darüberhinaus konnten neue Erkenntnisse zur Spannungsmagnitude und dem heterogenen Charakter der S_H-Orientierung im Oberjura-Reservoir

gewonnen werden. Schließlich konnte ich die gewonnenen Spannungsfeldinformationen aus dem Oberjura in eine Reaktivierungspotentialstudie zur Untersuchung der Mikroseismizität von Störungen im Bereich der Injektionsbohrung integrieren. Dieses Verständnis hilft, poro-thermo-mechanische und geochemische Effekte zu bewerten und sie zukünftig für einen weiteren geothermischen Ausbau im Großraum München zu berücksichtigen.

Die für diese Studien verwendete Datenbank umfasste zahlreiche Bohrlochmessungen, die von der Geothermie Allianz Bayern zusammengetragen wurden und die mikroseismischen Lokationen des Bayrischen Erdbebendienst. Die Promotion wurde von der Geothermie Allianz Bayern (GAB), der Energie Baden-Württemberg (EnBW) und dem Helmholzförderprogramm gefördert.

Contents

1

Introduction

"The goals of the energy revolution are not feasible without an conversion of the heat- and cooling sectors to renewables"

Dr. Florian Bieberbach
(CEO of Stadtwerke München GmbH)

Human activities have triggered about 1.0 °C of global warming in 2017 above the pre-industrial level through the emmision of carbon dioxite. The Intergovernmental Panel on Climate Change states that in 2030–2040 the temperature will reach an increase of 1.5 °C (IPCC, 2018). This will affect the intensity and frequency of weather extremes in most inhabited regions: heavy precipitations, droughts and precipitation deficits in some regions (Allen et al., 2018). To limit global warming to a level of 1.5 °C, the main challenge for the future energy market is the replacement of the fossil fuels by climate-neutral renewable energies. Particularly, the heating sector offers a major opportunity to reduce further greenhouse gas emissions. Geothermal Energy makes it possible to supply the district heating infrastructure with constant heat throughout the year without emitting any greenhouse gases (Agemar et al., 2018). By 2040, Munich should be the first German city covering 100 % of its district heating demand from renewables.

This thesis presents the latest findings for the description of the stress field and the geomechanical conditions for efficient drilling, the understanding of the underground fluid flow and a safe reservoir operation of geothermal boreholes in the Bavarian Molasse Basin.

1.1 Hydrothermal Energy in the Bavarian Molasse Basin

The Bavarian Molasse Basin, as part of the North Alpine Foreland Basin, is the most developed region for geothermal use in Germany, with the Cenozoic and Mesozoic units dipping south towards the thrust front. Here, the hydrothermally investigated stratigraphy is the Upper Jurassic / Malm reservoir, which is distributed over the entire Bavarian Molasse Basin and has various variations of hydraulic properties (Birner et al., 2012). South of the Danube river, the Upper Jurassic is strongly affected by karstification and indicates a hydraulic conductivity of 10^{-5} m/s at low reservoir depth. However, southwest of the river Iller, the permeability in the Helvetic facies decreases to $<10^{-8}$ m/s. In the Wasserburg trough, where the Greater Munich Area is located, the permeability is approximately

10^{-5} m/s. Here, the reservoir reaches depths of 2500–4000 m with a temperature level of 90–120 °C and flow-rates (100 to 120 l s^{-1}) that favor geothermal exploitation (Figure 1.1) (STWIVT, 2010).
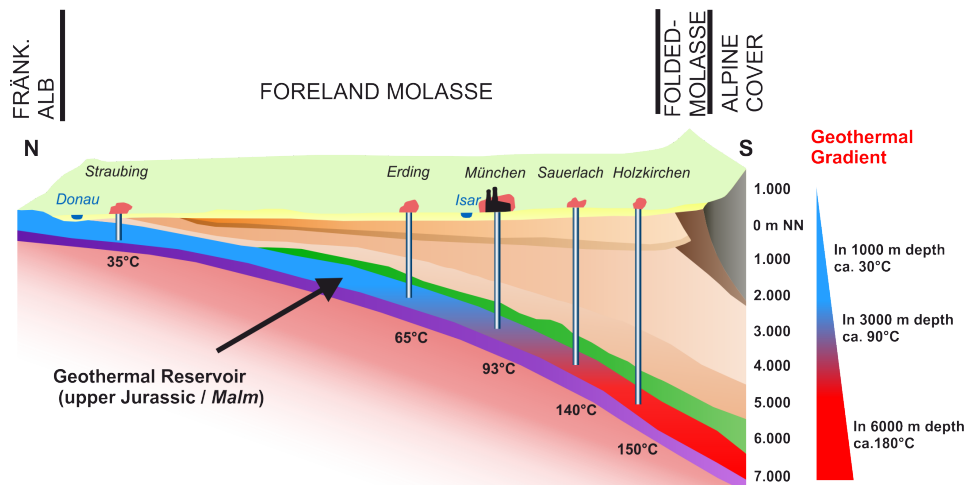
Figure 1.1 – Profile of the Bavarian Foreland Basin with the Upper Jurassic reservoir, depth (u.NN) and the temperature level (kindly provided by F. Flechner / GAB)

These favorable conditions for the heat supply of district heating systems were first recognized in 2003 for the Greater Munich Area. The project of Unterschleißheim (2003) was the first geothermal development in this area, followed by the Riem (2004), Pullach (2005) and Unterhaching (2007) projects. After 2008, the number of projects increased. District heating projects were developed in Unterföhring, Aschheim, Garching and Poing, while the southern projects Dürrnhaar, Kirchstockach and Sauerlach used combined heat and power (Dorsch & Pletl, 2012). Based on the gained experience further successful projects could be realized in Oberhaching/Grünwald (2009), Taufkirchen (2011), Ismaning (2012), Freiham (2015) and Holzkirchen (2016) (Table 1.1). Currently, 17 successful geothermal projects extract heat from the reservoir and mostly feed district heating systems. In total, these projects result in a total flow-rate of 1.6 m^3 s^{-1} and 235.6 MW$_{th}$ thermal and 31 MW$_{el}$ electrical installed capacity (Geotis, 2019). With the "Schäftlarnstraße" project, the Stadtwerke München (SWM) are currently constructing a 50 MW$_{th}$ district heating power plant that supports their plan to realize the "Vision 2040" for the transition to heat generation form renewable energies.

Successful projects in the center of Munich show that the characterization of facies and litho-facies is a essential premise for the further development of the exploration strategy (Boehm et al., 2012; Schneider & Thomas, 2012). To the contrary, unsuccessful projects indicate an incomplete understanding of reservoir properties in the southwestern area of Munich (Mraz, 2019). The intense drilling activity in the last decade has always been accompanied by new developments and the application of innovative technologies for reservoir exploration (Steiner, 2019; Steiner et al., 2014; Ziegler, 2017).

Table 1.1 – List of Geothermal projects in the greater Munich (Geotis, 2019).

Project	In operation since	Utilization	Flowrate	Temperature	Characteristic values			
					P_{th} MW_{th}	E_{th} $GW\,h\,a^{-1}$	P_{el} MW_{el}	E_{el} $GW\,h\,a^{-1}$
Erding	1998	DH	$48\,l\,s^{-1}$	$65\,°C$	7.7	35.58	–	–
Unterschleißheim	2003	DH	$100\,l\,s^{-1}$	$80\,°C$	7.98	42.2	–	–
Riem	2004	DH	$75\,l\,s^{-1}$	$94\,°C$	13	66.5	–	–
Pullach	2005	DH	$110\,l\,s^{-1}$	$107\,°C$	30	57.3	–	–
Unterhaching	2007	P / DH	$140\,l\,s^{-1}$	$124\,°C$	38	85	3.36	9.22
Aschheim	2009	DH	$88.5\,l\,s^{-1}$	$86\,°C$	10.7	66.1	–	–
Garching	2011	DH	$100\,l\,s^{-1}$	$75\,°C$	7.95	31.72	–	–
Oberhaching	2011	P / DH	$140\,l\,s^{-1}$	$135\,°C$	40	94.42	4.3	16.89
Dürrnhaar	2012	P	$130\,l\,s^{-1}$	$135\,°C$	–	–	5.5	35.5
Poing	2012	DH	$100\,l\,s^{-1}$	$85\,°C$	9	34	–	–
Ismaning	2013	DH	$85\,l\,s^{-1}$	$76\,°C$	7.2	33.88	–	–
Kirchstockach	2013	P	$135\,l\,s^{-1}$	$141\,°C$	–	–	7	34.8
Sauerlach	2013	P	$110\,l\,s^{-1}$	$140\,°C$	4	5.31	5	29.25
Taufkirchen	2015	DH	$120\,l\,s^{-1}$	$136\,°C$	40	35	–	–
Unterföhring	2015	DH	$90\,l\,s^{-1}$	$93\,°C$	23	54	–	–
Freiham	2016	DH	$120\,l\,s^{-1}$	$91\,°C$	13	27.6	–	–
Holzkirchen	2018	P / DH	$50\,l\,s^{-1}$	$150\,°C$	24	–	3.4	–
Schäftlarnstraße	u. constr.	DH	–	$100\,°C$	50	–	–	–

P_{th} - installed thermal capacity, E_{th} - annual thermal production, P_{el} - installed electic capacity, E_{el} - annual power production

1.2 Motivation

The development of geothermal projects in urban areas such as the Munich metropolitan area and the high in-situ stress require well developed geomechanical reservoir models (Fjaer et al., 2008; Zoback, 2010). This study is integrated into the Geothermal Alliance of Bavaria (GAB [1]), a research program that improve the competitiveness and the acceptance of this local energy source in the Greater Munich Area. As the complexity of drilling paths increases, a much more accurate understanding of potential sections with wellbore instability is required. The expansion of geothermal heat utilization, especially in inner city areas, must ensure minimal seismic impact in order to maintain the high level of public acceptance. Recently observed seismic events in Unterhaching and Poing (Megies et al., 2017; Megies & Wassermann, 2014) caused some concern and must therefore be understood as a signal to avoid future seismic activity. The combination of the high level of public acceptance, high geothermal potential and a strong local public utility company offers a unique potential for reducing CO_2 emissions through safe use of the geothermal resource.

In general, there is little information about the stress field in the Bavarian Molasse Basin and most studies are based on only few data (Budach et al., 2017; Cacace & Blöcher, 2015; Reinecker et al., 2010; Seithel et al., 2015; Ziegler, 2017). However, in order to develop a

---

[1] Since 2016, the Bavarian State Ministry for Science and Art funds the research project "Geothermal–Alliance Bavaria" (GAB) which is coordinated by the Munich School of Engineering at the Technical University of Munich. An interdisciplinary team of the Technical University of Munich (TUM), the Friedrich-Alexander University Erlangen-Nürnberg (FAU) and the University of Bayreuth is working together on the research of different topics with the common goal to improve the economic efficiency, to minimize the risk of deep geothermal projects and to improve the competitiveness and the acceptance of this local energy source. The aim of the GAB is to combine all aspects of deep geothermal projects from the exploration and characterization of the reservoir to the operation and monitoring of the power plant. This this reason, sub-projects are working on *reservoir characterization*, *PetroTherm*, *operational safety of the thermal water cycle: Scaling and electric submersible pump (ESP)*, *monitoring* and *efficient and flexible power plants*. The GAB project management team made it possible to sign contracts with 12 out of the a total of 17 operators in the Greater Munich Area in order to built-up a database for scientific research. On a discussion platform the scientific community and the operators regularly have the opportunity to exchange their experience.

Table 1.2 – Database of geophysical logs used for the stress field interpretation

Well	Resisitivity Image Log	Oriented Caliper
Ascheim Th1	6 1/8" FMI	-
Dürrnhaar Gt1	8 1/2" HMI	-
Dürrnhaar Gt2	8 1/2" HMI	-
Freiham Th1	8 1/2" CMI	-
Freiham Th2	8 1/2" CMI	-
Ismaning Th1	6 1/8" CMI	-
Ismaning Th2	6 1/8" CMI	-
Kirchstockach Gt1	8 1/2" HMI	-
Kirchstockach Gt2	8 1/2" HMI	-
Pullach Th3	8 3/8" Star Image	-
Riem Th2	6 1/8" HMI	-
Sauerlach Th1	8 1/2" FMI	23" EMS, 16" EMS, 12 1/4" EMS
Sauerlach Th2	8 1/2" FMI	-
Sauerlach Th3	6 1/8" FMI	-
Unterföhring Th1	6 1/8" CMI / HMI	-
Unterföhring Th4	6 1/8" FMI	-
Unterhaching Gt2	9 5/8" FMI	-

FMI - Formation Micro Imager, HMI - High-resolution Micro Imager, CMI - Compact Micro Imager, EMS - Environmental Measurement Sonde

detailed stress model, all data must be integrated into one analysis, providing the possibility to make predictions regarding a future geothermal development strategy with the goal to avoid perceptible microseismicity.

In this PhD-thesis, all accessible borehole data are presented in a high-quality stress field characterization of the Greater Munich Area. In detail, the stress field for the Cenozoic Molasse sediments and the Upper Jurassic limestone reservoir are described. Based on these results, the mechanism of triggered microseismic events are studied by a fault reactivation potential study.

Table 1.3 – Database of the pressure test measurements inside of the well.

Well	Borehole pressure data
Dürrnhaar Gt1	CS 18 5/8" FIT, CS 13 3/8" FIT
Dürrnhaar Gt2	CS 18 5/8" FIT, CS 13 3/8" FIT
Freiham Th1	CS 18 5/8" FIT & Cem. Pres., CS 13 3/8" FIT & Cem. Pres., CS 9 5/8" Cem. Pres.
Freiham Th2	CS 18 5/8" FIT & Cem. Pres., CS 13 3/8" FIT & Cem. Pres., CS 9 5/8" Cem. Pres.
Ismaning Th1	CS 13 3/8" FIT, CS 9 5/8" FIT
Ismaning Th2	CS 13 3/8" FIT, CS 9 5/8"" FIT
Kirchstockach Gt1	CS 18 5/8" FIT, CS 13 3/8" FIT
Kirchstockach Gt2	CS 18 5/8" FIT, CS 13 3/8" FIT
Oberhaching Gt1	CS 13 3/8" FIT
Oberhaching Gt2	CS 18 5/8" FIT, CS 13 3/8" FIT, CS 10 3/8" FIT
Poing Th1	CS 23" FIT, CS 18 5/8" FIT, CS 13 3/8" FIT
Poing Th2	CS 23" FIT, CS 18 5/8" FIT, CS 13 3/8" FIT
Pullach Th1	CS 18 5/8"" FIT, CS 13 3/8" FIT
Pullach Th2	CS 18 5/8" FIT, CS 13 3/8" FIT
Pullach Th3	CS 18 5/8" FIT, CS 13 3/8" FIT
Riem Th1	CS 13 3/8" FIT, CS 9 5/8" FIT, CS 7" FIT
Riem Th2	CS 13 3/8" FIT, CS 9 5/8" FIT
Sauerlach Th1	CS 18 5/8" FIT, CS 13 3/8" FIT
Sauerlach Th2	CS 18 5/8" FIT, CS 13 3/8" FIT
Sauerlach Th3	CS 18 5/8" FIT, CS 13 3/8" FIT
Unterföhring Th1	CS 13 3/8" FIT, CS 9 5/8" FIT
Unterföhring Th2	CS 13 3/8" FIT, CS 9 5/8" FIT
Unterföhring Th3	CS 13 3/8" FIT, CS 13 3/8" LOT, CS 9 5/8" FIT
Unterföhring Th4	CS 13 3/8" FIT & Cem. Pres., CS 9 5/8" FIT, CS 9 5/8" Cem. Pres.
Unterhaching Gt1	CS 16" LOT, CS 13 3/8" FIT, CS 9 5/8" FIT, OH 9 5/8" Stim. Pres.

CS - Casing Shoe, FIT - Formation Integrity Test, LOT - Leak−off Test, Cem. Pres. - Cementation Pressure, Stim. Pres. - Stimulation Pressure

In the framework agreement with the GAB, an almost complete database from the

geothermal projects in the Greater Munich Area could be used for the stress field analysis. A total of 17 Image logs and three oriented caliper logs (EMS) exists for 10 geothermal sites (Table 1.2). The caliper logs are measured within the Cenozoic overburden and the image log data exclusively available in the Upper Jurassic reservoir. In addition, a total of 72 closed borehole pressure measurements are available from 11 sites (Table 1.3). Most of the pressure data was derived from formation integrity tests (FIT) and during cementation jobs (Cem. pres.), with additional data available from one leak-off test (LOT) and one stimulation job (stim. pres.). Lithological logging and daily reports provide data regarding the well conditions.

1.3 Structure of the Thesis

This thesis presents the latest version of the stress field interpretation of the most recently compiled geothermal database in the Greater Munich Area located in the Bavarian Molasse Basin. In addition, a detailed investigation of the reactivation potential provides insights into the complexity of induced microseismic events at geothermal sites. The thesis covers three studies in the main part, which are supplemented by two studies in the appendix. All studies focus on the topic of stress field characterization and its interaction with reservoir operating conditions. In total two studies are published in international journals (Geothermal Energy and Tectonophysics), one is in accepted in Geothermics, one is in preparation for submission and another is a data review of a published article.

Chapter 2 begins with a description of the regional geology of the Bavarian Molasse Basin and then concentrates on the tectonic setting, reservoir hydraulics, the stress field and finally the microseismic observations in the Greater Munich Area.

The next chapter (**Chapter 3**) gives an overview of the fundamentals of rock mechanics. Based on these principles, the techniques used in this study to characterize stress fields are presented (**Chapter 4**). These methods are designed to identify the minimum horizontal stress (S_h), the maximum horizontal stress (S_H), the vertical stress (S_v), and the S_H-orientation, using the interpretation of pressure data and image log data (Seithel et al., 2015) (see Appendix A).

In the main chapters, the first study focus on the S_h magnitude within the Cenozoic and Upper Jurassic, the second on the stress rotation potential and stress regime in the Upper Jurassic reservoir, and the third on the geomechanical application of fault reactivation processes. These studies are supplemented by two further studies on the stress field, which are listed in the appendix. All studies are are presented below:

Lithology correlated S_h assessment based on formation-integrity and leak-off test data in the Bavarian Molasse Basin

In **Chapter 5** the database of formation integrity tests (FIT), cementation pressures (Cem. pres.), leak-off test (LOT) and stimulation pressure (stim. pres.) is reviewed to obtain a new quality controlled data compilation of the intervals within shale, mixed shale/sand and carbonate lithology. In total, 75 measurements were evaluated with respect to the S_h magnitude. The quality assessment results in a database with 46 S_h-measurements from

different lithological units. Within these lithologies different S_h-magnitudes were observed which show a strong lithology dependency of S_h. In the supplementary study presented in Appendix B the shale database is used to discuss the stress regime in the Cenozoic.

Stress rotation in the Bavarian Molasse Basin inferred from borehole data and numerical simulation

The primary observation of the stress field rotation within the Upper Jurassic reservoir (Appendix A) is examined in a total of 17 image logs in the Greater Munich Area (**Chapter 6**). Interpretation of the compressive and tensile borehole failure provides information of the tangential stress distribution in the highly inclined borehole section. Based on the quality ranking of the World Stress Map (WSM) (Tingay et al., 2016) an A-B quality could be assigned to the stress interpretation at 10 boreholes. Finally, a mis-fit gridding was performed on this data to evaluate the S_H-orientation and identify potential stress rotations. In addition, the range of the S_H-magnitude could be determined in 10 intervals from 4 boreholes. Thus, a counterclockwise stress field rotation of maximum 60° and a strike-slip stress regime were determined. Furthermore, geomechanical modeling allows us to discuss the influence of heterogeneous structures on such stress field rotation.

Probability of Fault Reactivation in the Bavarian Molasse Basin

In addition to the stress field investigations, the observation of microseismicity shows that there is a considerable need for research in geomechanical reservoir characterization. In **Chapter 7** the results of the stress field characterization from the first two chapters are integrated into a hazard analysis of seismic reactivation to investigate the interaction of stress field and microseismicity. Thus a methodology was developed which expresses the criticality of faults based on Mohr-Coulomb failure criterion. In order to integrate the characteristic high geological uncertainty, e.g. the stress components, the frictional strength and the cohesion of the fault, a Monte-Carlo simulation was performed, providing the reactivation potential. Frictional fault strength, but also the S_H-orientation could be determined as the most sensitive parameters for the reactivation potential. For the geothermal sites Unterhaching and Poing, the significance of the individual poro-thermo-elastic couplings, geochemical alteration and their effects on the reactivation potential were discussed. On the basis of this analysis I have to recommend the consideration of geomechanical investigations also for seismically inactive regions before and during the operation of geothermal power plants.

Appendix

Stress anomaly in the Bavarian Molasse Basin

The study presented in **Appendix A** is from an early phase of my PhD from 2014 and presents the first stress field characterization approach for the Upper Jurassic reservoir at the Sauerlach site. In the three image logs of the reservoir sections, compressional and tensile borehole failure are interpreted in the highly deviated well sections. The derived

tangential stress distribution is used for a "mis-fit" gridding that allows characterization of the stress field. Sensitivity analysis shows a negligible influence of S_h on the results of the "mis-fit". This study demonstrates for the first time the potential of image log data for the stress field characterization even in the highly heterogeneous Upper Jurassic reservoir of the Bavarian Molasse Basin and is published as

Seithel, R., Steiner, U., Müller, B., Hecht, C. & Kohl, T. (2015): Local stress anomaly in the Bavarian Molasse Basin. – in: *Geothermal Energy* 3 (1), p. 77. – DOI: 10.1186/s40517-014-0023-z.

A NORMAL-FAULTING STRESS REGIME IN THE BAVARIAN FORELAND MOLASSE BASIN? NEW EVIDENCE FROM DETAILED ANALYSIS OF LEAK-OFF AND FORMATION INTEGRITY TESTS IN THE GREATER MUNICH AREA, SE GERMANY.

The database analyzed in Chapter 5 gives the impulse for a collaboration with Dr. Michael Drews (FAU) to better investigate the stress regime within the Cenozoic Molasse sediments. First indications for a normal-faulting stress regime were provided by the disequilibrium compaction trend coming from the pore pressure analysis in Drews et al. (2018). In this study **Appendix B** we also used high quality pressure data from shale-lithology. The basic trends are characterized by FIT and cementation pressure, but the leak-off pressure at Unterhaching Gt1 illustrates the normal-faulting regime at 825 mTVD in the lower Miocene. This study is a collaborative research within the GAB-team and was published as

Drews, M. C., Seithel, R., Savvatis, A., Kohl, T. & Stollhofen, H. (2019a): A normal-faulting stress regime in the Bavarian Foreland Molasse Basin? New evidence from detailed analysis of leak-off and formation integrity tests in the greater Munich area, SE-Germany. – in: *Tectonophysics* 755, pp. 1–9. – DOI: 10.1016/j.tecto.2019.02.011.

2

Geological framework of the Study Area

The Bavarian Molasse Basin is the central part of the north Alpine Molasse Basin, which extends over 700 km from the Swiss Molasse Basin in the West to the Austrian Molasse Basin in the East. It is structured as a typical asymmetric foreland basin filled with up to 5000 m clastic Molasse sediments. These Cenozoic sediments are underlain by 500 m Mesozoic shelf sediments (Bachmann et al., 1987), which represents the Upper Jurassic reservoir.

In the following summary I focus on the geological situation of the Greater Munich Area (50x50 km) (Figure 2.1), which is the main target for today's geothermal development in the Bavarian Molasse Basin. In the following I give a basic geological introduction of the Bavarian Molasse Basin (Chapter 2.1), outline the tectonic situation in the Greater Munich Area (Chapter 2.2), describe the hydrogeological conditions of the geothermal reservoir (Chapter 2.3) and finally explain the knowledge about the stress field (Chapter 2.4) and the recently observed microseismicity (Chapter 2.5).

2.1 Geological background

The stratigraphy of the Bavarian Molasse Basin can be divided into three sections, which are classified according to lithology and formation age: The deepest part is the pre-Mesozoic basement; the Mesozoic / Upper Jurassic and Cretaceous units with mainly carbonates representing the hydro-geothermal reservoir; and the Cenozoic sediments consisting of deep-water sediments in the lower layers and sand and gravel in the shallower layers of the Late Molasse sedimentation cycle (Figure 2.1b.).

The pre-Mesozoic basement has been scarcely explored so far, but it is presumed that there are ENE–WSW oriented troughs (Bachmann et al., 1987; Bachmann & Müller, 1992; Frisch, 1979).

In the Mesozoic (150–135 Ma) the Penninic Ocean opened and in the area of the today's Bavarian Molasse Basin a shelf-water sedimentation took place. During this time the Upper Jurassic, locally called Malm, was deposited, which can be divided regionally into the sedimentation zones of the Swabian, Franconian and Helvetic facies (Meyer & Schmidt-Kaler, 1996). The Swabian facies in the western part of the Bavarian Molasse Basin consists of massive limestone from the Swabian sponge reef and the marl-rich deposits of the Swabian basin (Figure 2.3). In the southwest, the deposits of the shelf sea gradually migrate into the pelagic Helvetic facies with dense bituminous limestone (Selg & Wagenplast, 1990;
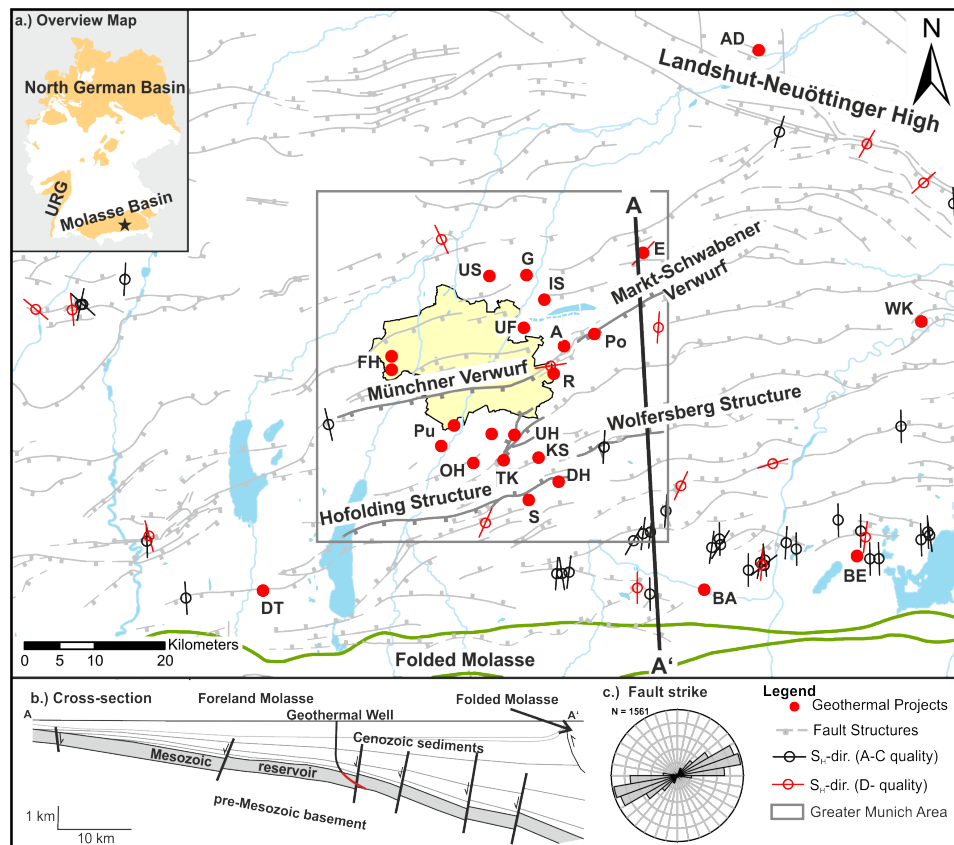
A- Aschheim, BA- Bad Aibling, BE- Bad Enddorf, DT- Dietlhofen,DH- Dürrnhaar, E- Erding, FH- Freiham, G- Garching, IS- Ismanning, KS- Kirchstockach, OH- Oberhaching, PO- Poing, PU- Pullach, S- Sauerlach,TK-Taufkirchen, UF- Unterföhring, UH- Unterhaching, US- Unterschleißheim, WK- Waldkraiburg

Figure 2.1 – Geological map of the central part of the Bavarian Molasse Basin. Map: The fault structures are from the Geothermal Atlas of Bavaria (STWIVT, 2010). Red dots indicate the location of the geothermal power plants. Furthermore, the stress orientation of the World Stress Map Project for the Greater Munich Area is presented (Reinecker et al., 2010) a. Overview map of Germany and the location of the Bavarian Molasse Basin with the project area (asterisk). b. Cross section from A–B with the Cenozoic molasse sediments, the Mesozoic sediments of the Upper Jurassic and Cretaceous representing the geothermal reservoir and the pre-Mesozoic basement. Normal faults indicate an activation period up to the Lower Miocene. In the south the foreland basin is bounded by thrust faults of the folded Molasse section (modified according to Reinecker et al., 2010). c. Stereoplot of faults in the Greater Munich Area.

Stober et al., 2013). The sponge reef platform of the Swabian facies can be continued into the central area of the Bavarian Molasse Basin, where the so-called Franconian facies provide the good reservoir conditions in the Greater Munich Area. Mraz (2019) describes a transition zone from the Helvetic facies in the southwest to the central area of the Bavarian Molasse Basin. This zone might be responsible for less permeable reservoir conditions observed in the southwest of Munich (Figure 2.3).

The sedimentation of the Malm begins in the lower Malm α, β and γ, which consists of marls and marly limestone (Figure 2.4). In a second sedimentation cycle the conditions change and mainly limestone is deposited in the middle Malm δ and ϵ. In the youngest upper Malm ζ, a diversification of the sedimentary environment takes place in shallow water depths (Meyer & Schmidt-Kaler, 1989) and two hyper-facies are formed: The so-called "Bank facies" with typically very thin layers of marl or micritic limestone and the so-called "Mass facies" with thick limestone or dolomitic units and reef structures (Meyer

& Schmidt-Kaler, 1989, Figure 2.4).

The dilatational tectonics caused the formation of normal faults (Bachmann & Müller, 1992) at the end of the Upper Jurassic and earliest Cretaceous period (135 Ma). Thereby the sedimentation conditions changed into a brackish or hypersaline, mostly carbonate "Purbeck" facies with limestone/marl components. Cretaceous deposits completely missing in the western part of the Molasse basin (Figure 2.2). The Upper Cretaceous limestone and marl sediments represent the upper limitation of the geothermal reservoir which include the Malm and Purbeck layers (Lemcke, 1988). At the end of the Upper Jurassic, the Malm platform was subaerially exposed for the first time and erosion and deep karst formation began (Unger & Meyer, 1996).

The beginning of the Molasse evolution is directly linked to the continent-continent collision of the European and the Adriatic plate at the end of the Upper Cretaceous (Schmid et al., 2004). This led to a depression of the European continental margin and to the creation of a deep-sea trench (Frisch, 1979) in which the Turon Claymarl sedimented. During the Late Eocene early Molasse sediments of basal Sandstone and Lithothamnium limestone were deposited (Figure 2.2). A "second" continent-continent collision formed flexure-induced, predominantly basin-parallel normal faults (Ziegler, 1995), which led to rapid subsidence and massive sedimentation of Fish shale and grey Rupelian Marl (33.9–27.82 Ma) (Figure 2.2). At the transition from the Late Oligocene to the Early Miocene (23.03 Ma) the sea level decreases and the intense influx of clastic material leads to the formation of the well-known Baustein Sandstone (Bachmann & Müller, 1992), which is bounded by the lying and the hanging Claymarl of the Chattian (Kuhlemann & Kempf, 2002) (Figure 2.2).
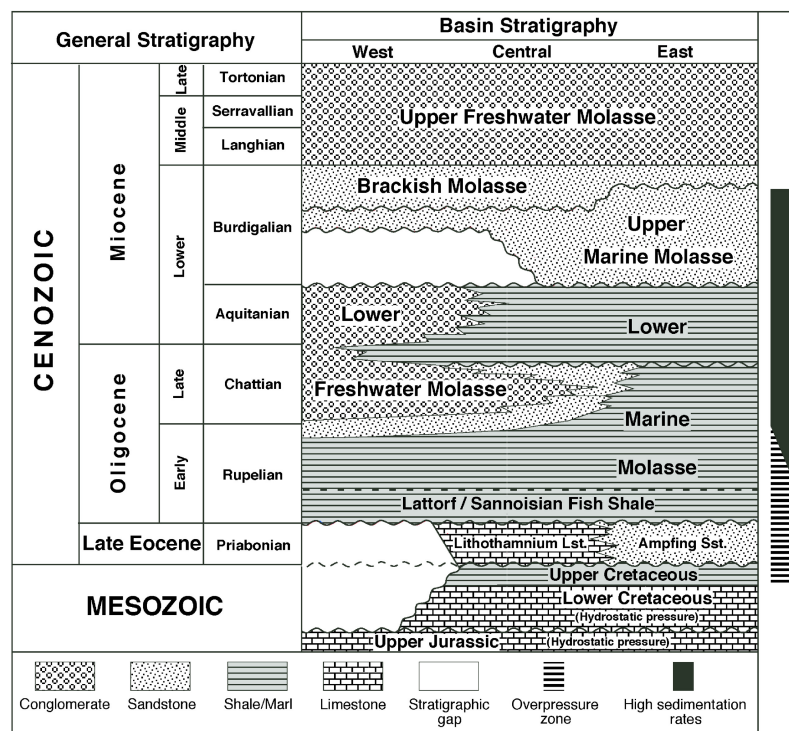
Figure 2.2 – Stratigraphic overview of the Mesozoic and Tertiary sediments of the Molasse sediments (modified after Drews et al., 2018, originate published by Kuhlemann & Kempf, 2002).

A renewed basin-wide transgression during the Early and Middle Miocene (23.03 to

5.33 Ma) results in the sedimentation of interlayered sandstone and claystone of the Upper Marine Molasse Series (Aquitan / Ottnangian) and final sedimentation of the Upper Freshwater Molasse series (Kuhlemann & Kempf, 2002) (Figure 2.2). At the end of the Miocene, the entire German platform was lifted and erosion occurred, resulting in a hydraulic connection between the Malm reservoir and the Danube.

2.2 Structural setting

Most of the fault structures of the Bavarian Molasse Basin indicate a fault pattern parallel to the Alpine thrust front, which is a typical observation for foreland basin structures (Alberta Basin, Swiss Molasse Basin, Apalachian) (Bradley & Kidd, 1991). The predominant tectonics for the formation of fault zones are bending forces in the context of alpine thrusting (Hartmann et al., 2016). Under the load of the advancing Alps the foreland–basin axis migrated to the north, whereby the flexure-induced and predominantly basin-parallel normal faults become younger from south to north (Ziegler, 1995).

The tectonic map published in the geothermal atlas (STWIVT, 2010) shows the faults interpreted by seismic lines at the Lithothamnium limestone (Figure 2.1). In most cases, fault structures have a syn- and antithetic normal fault character with a strike of ENE–WSW (Lemcke, 1988) (Figure 2.1c). These structures dip with 50° to 70° and have a fault throw of 150 to 200 m (Bachmann et al., 1987). But some fault zones, typically with a length of 2.5 to 5 km, change their strike in the direction of NNE–SSW to NE–SW in the area of step-over or transfer zones. To what extent a shortening with compressional forces through the Alps led to the reactivation of old Paleocenic NW–SE / NE–SW striking faults by reverse or strike-slip faulting is under discussion (Ziegler, 1995). Unger (1999b) described a series of strike-slip faults in the eastern part of the Bavarian Molasse Basin. After the drilling of Unterhaching Gt1 it is postulated that it could possibly have an important role in tectonics in the south of Munich (Unger, 2004).

Here, for the Greater Munich Area (Figure 2.1), some selected structures are highlighted. For example, the main structure in the deep underground of Munich in the form of a synthetic normal fault with an offset of up to 200 m. It is to be traced from Unterbrunn in the SW of Munich towards ENE to Riem and is known as "Münchner Verwurf" (Figure 2.1). In Riem this structure turns to NE, splits into several small fault structures and continues with an ENE trend in the area of Poing. Here this structure is known as "Markt-Schwabener Verwurf". In this area structures with a WSW–ENE trend are widely common (Figure 2.1c). The "Hofolding structure" can be traced from the SW part of the study area to the Sauerlach site and Dürrnhaar site as a synthetic normal fault. A special location with a complex structure can be found in Unterhaching, where a scientific 3D-seismic campaign provided detailed information about the underground structure (Lüschen et al., 2014). In this area, one N070°E striking fault zone coming from SE splits-up into a N025°E minor and N045°E major fault zone with N070°E en-echelon, whereas minor fault traces are connected by relay ramps (Budach et al., 2017). This central structure is bounded by two N070°E striking fault zones: The fault zone Unterhaching in the north and the Kirchstockach in the south. All alpine parallel structures can be traced from the Basement over the Mesozoic to the

Cenozoic with a limitation at the Upper Miocene layer (Unger, 1996).

2.3 Hydrogeological setting

In the Bavarian Molasse Basin, the dominat geothermal reservoir is the Upper Jurassic, locally called Malm reservoir, which has an almost constant layer thickness of 500 m and a variation of different lithological facies.

The Upper Jurassic in the southwest of the Bavarian Molasse Basin is characterized by the so-called Helvetic and transition zone (Figure 2.3). These zones are classified as low or extremely low permeable units that do not provide any geothermal reservoir (Mraz, 2019; STWIVT, 2010). Birner et al. (2012) has interpreted a variety of Upper Jurassic well tests and presented the distribution of the hydraulic conductivity in the Bavarian Molasse Basin. The hydraulic conductivity of the Swabian and Franconian facies varies from 10^{-4} m/s in the north at shallow depth to 10^{-7} m/s in the south at great depth (Birner et al., 2012) (Figure 2.3).
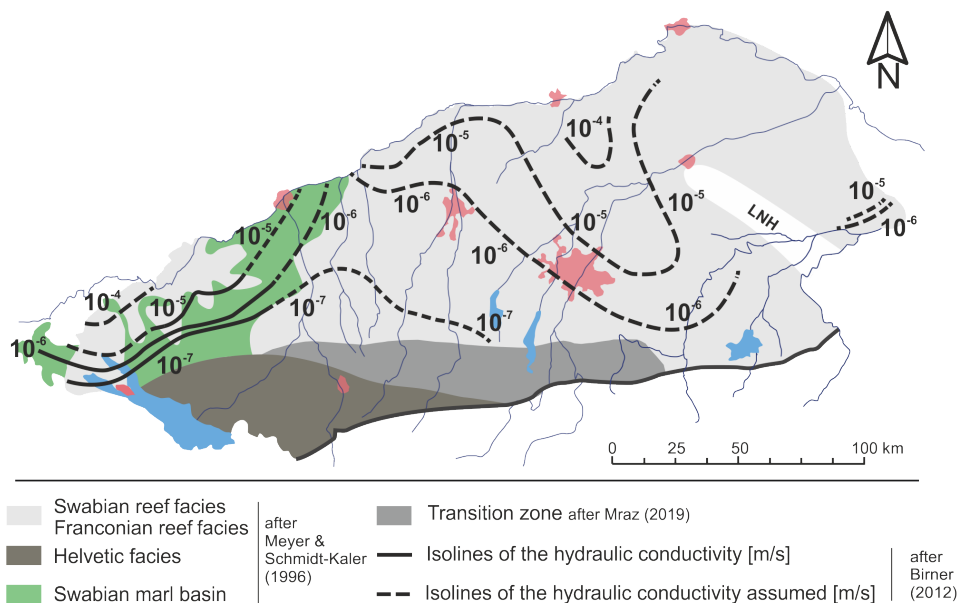
Figure 2.3 – Distribution of hydraulic conductivity and facies of the Upper Jurassic reservoir in the South German Molasse Basin (modified after Birner et al., 2012). The western part of the Molasse Basin is dominated by the Swabian facies, the southwestern part by the Helvetic facies and the central part by the Franconian facies (Meyer & Schmidt-Kaler, 1996). In Mraz (2019) a transition zone is described that can be traced from the Helvetic zone to the southern part of the central Molasse basin. Hydraulically most suitable conditions are observed for the sponge reef platform of the Swabian and Franconian facies (Birner et al., 2012). It should be noted that in the Greater Munich Area a positive trend shows a comparatively high hydraulic conductivity.

In the south, tectonic fractures are preferred flow channels but Stier & Prestel (1991) and Stober et al. (2013) suggested that the dominant process for reservoir hydraulics is the facies-dependent karstification. Recent research describes the Malm reservoir at great depth of the Bavarian Molasse Basin as an inhomogeneous anisotropic karstified and fractured reservoir (Schneider & Thomas, 2012), whose surface area was karstified to a depth of 200−300 m (Koschel, 1991). The groundwater level in the Malm reservoir in the Central Bavarian Molasse Basin is ∼ 225 m below ground level (STWIVT, 2010), which means that

the pore pressure conditions are below hydrostatic conditions. These conditions exist since the Miocene, initiating an influx of CO_2-rich fluid from depth into the reservoir and recently leading to karstification (Lemcke, 1976; Stier & Prestel, 1991).
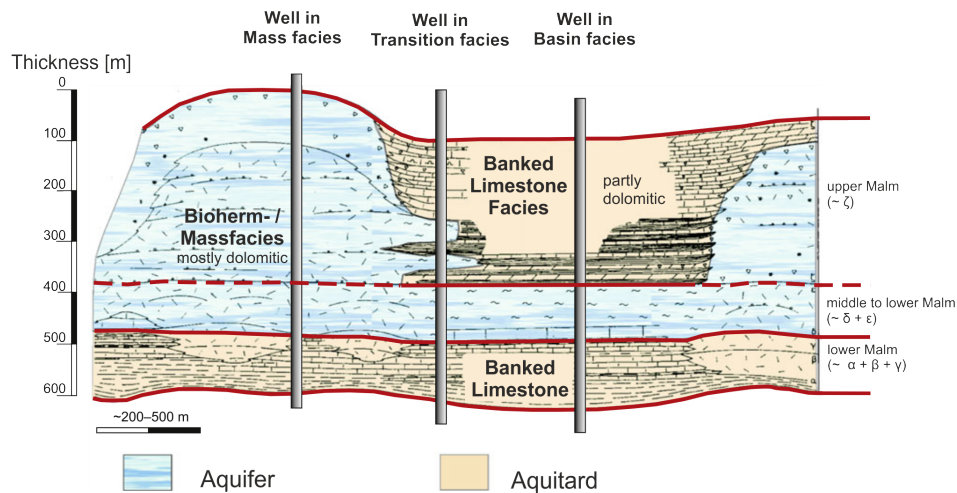
Figure 2.4 – Hydro-stratigraphical classification of the Upper Jurassic (Malm) reservoir modified by Boehm et al. (2012) and originally published by Meyer & Schmidt-Kaler (1996). Boreholes drilled into the Bioherm/ Mass facies of the Malm ζ are highly productive and can be clearly distinguished hydraulically from those of the Banked Limestone facies. In all wells, the middle to lower Malm (Malm δ & Malm ϵ) has good aquifer properties, while the lower Malm (Malm α & Malm β & Malm γ) has bad properties and is characterized as an aquitard.

The reef platform in the Greater Munich Area of the Franconian facies was diversified within the upper Malm (ζ) and partly in the middle Malm (δ and ϵ). Most dolomitic Mass Facies are found in the Malm ζ, δ and ϵ, while the Banked Limestone Facies with only partial dolomitic character are representative for the Malm ζ (Figure 2.4). The lower Malm (α, β and γ) is dominated by banked, partially marl-rich limestones and marls (Boehm et al., 2012).

For the Greater Munich Area, Birner et al. (2012) shows a hydraulic conductivity in the range of 10^{-5} to 10^{-6} m/s (Figure 2.3). The hydraulic properties of the reservoir are mainly dominated by the facies, as it affects the karstification process and the fracture propagation (Stier & Prestel, 1991). E.g. in marl-rich units fracture density decreases and in dolomitic units fracture density increases. Moreover, Boehm et al. (2012) pointed out that additional porosity is to be expected from the dolomitized limestones in the Mass Facies in the Greater Munich Area. Here, the dolomitization provides additional matrix porosity that results from the transformation of calcite into dolomite in the reef structures of the Malm ζ and Malm δ / ϵ (Figure 2.4).

Hydrogeologically, the Malm reservoir exhibits the typical behavior of carbonate aquifers, with a complex interaction of karstification (Stier & Prestel, 1991), fracture and matrix porosity (Lüschen et al., 2014; Steiner et al., 2014).

Boehm et al. (2012), Schneider & Thomas (2012), and Steiner et al. (2014) indicated that geothermal boreholes in the Greater Munich Area can be classified as follows: Boreholes with a long interval of Bioherm / Mass facies and a large amount of dolomite in the upper Malm; boreholes in the transition facies that explore the boundary of a reef structure with Bioherm / Mass facies and Banked Limestone Facies and finally boreholes in the Banked

Limestone Facies with a minor amount of dolomite in the upper Malm (Figure 2.4). Some boreholes in the Greater Munich Area show an extreme karstification in the upper part of the reservoir, which was formed during Cretaceous when the reservoir was at the earth's surface (Unger & Meyer, 1996).

The geologic and hydraulic analysis of the geothermal wells leads to the definition of three types of geothermal reservoir targets: the main targets are the Mass facies with high dolomite content, in addition to the fracture zones in the vicinity of faults and, finally, layers with potential karst formation (Steiner et al., 2014). As the Malm δ / ϵ in the Greater Munich Area consists primarily of Mass facies, an increase of the borehole deviation to 70° from the vertical significantly improves the hydraulics of the boreholes. The Mass facies are decisive for the productivity of the wells, but fault zones and karstified layers allow a drastic increase in the connected reservoir volume. In case of large faults with a vertical offset of ≥50 m the upper Malm should be accessed from the upper block to the lower block to avoid a reduction of the reservoir section.

2.4 STRESS FIELD

The recorded borehole data and structural geological interpretation provide several indications of a strong variation in the stress regime in the Molasse Basin over time (Bachmann et al., 1987; Unger, 1999a). In the Upper Jurassic and in the early Cretaceous the formation of normal faults indicates a normal faulting stress regime, which is interrupted by the uplift process of the south German continental plate at the end of the Cretaceous. The progressive development of the Alpine Orogen and the under-thrusting of the European plate below the Adriatic-African plate leads to the formation of the North Alpine Molasse Basin (35 Ma). Reverse faulting character in the area of the Landshut-Neuöttinger High indicates high compressive stress (Bachmann & Müller, 1992). In the course of the subsequent formation of the Alps, down-bending forces within the European continental plate cause expansion tectonics and reactivation of existing normal faults (Frisch, 1979). This turbulent phase is terminated in the transition from the upper Eocene to the lower Oligocene (33.9 Ma) by a "second" continent-continent collision (Bachmann et al., 1987) with high compressive forces (Ziegler, 1995). In the late Molasse stage postcollision tectonics initiates an orogen-parallel large-scale expansion in the eastern Alps, which reduces the compression character (Frisch et al., 2000).

Geophysical logging in the entire Molasse basin indicate a S_H-orientation perpendicular to the Alpine thrust front (Heidbach & Reinecker, 2013; Reinecker et al., 2010). This stress orientation can be seen for the Greater Munich Area in Figure 2.1a and Figure 2.5a. It should be noted that most of the data comes from the Cenozoic unit and that only the following four sites have a stress interpretation within the Upper Jurassic sediments (Figure 2.5b). In the Schnaitsee 7 well the stress evaluation points to an A-quality and a N147°E S_H-orientation, in Endlhausen 1 a D-quality and a S_H-dir. of N024°E, in Erding 1 a D-quality and a S_H-dir. of N043°E and in Riem Th2 (geothermal project) a D-quality and a S_H-dir. of N082°E (Reinecker et al., 2010). Thus, within the less consolidated Cenozoic sediments the stress orientation is homogeneously N–S oriented, while within the stiff limestone of the

Upper Jurassic there is evidence of a heterogeneous stress pattern.
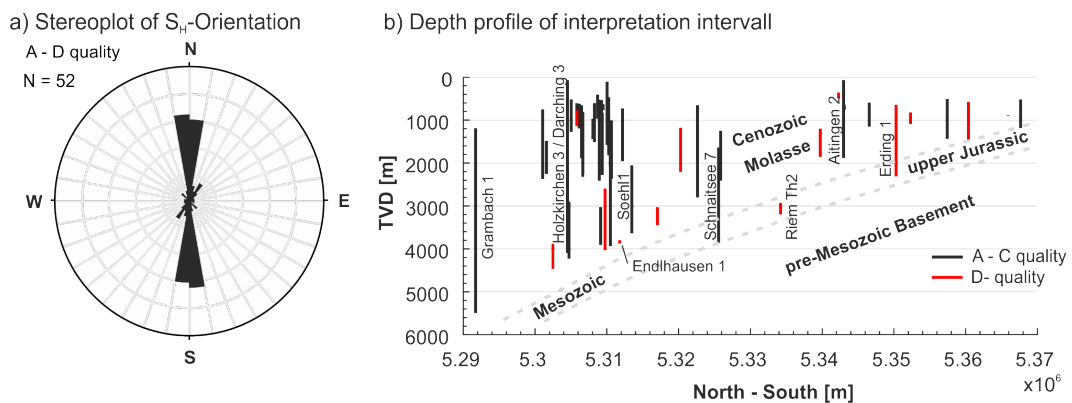
Figure 2.5 – Published stress data of the central Bavarian Molasse Basin for the Greater Munich Area (see Figure 2.1a). a. In this area, the interpretation of 52 wells with at least D-quality from the World Stress Map Project (Reinecker et al., 2010) shows an N–S orientation of the maximum horizontal stress (S_H). b. The depth profile illustrates that almost all interpreted intervals are within the Cenozoic sediments, and only at four locations stress information exists for the Upper Jurassic.

The current stress regime in the Bavarian Molasse Basin is very uncertain but there are indications that it varies locally and over different time periods (Reinecker et al., 2010; Ziegler et al., 2016). In the vicinity of the thrust front, geotechnical measurements in boreholes suggest a compression to strike-slip character and strain accumulation in the folded Molasse (Illies & Greiner, 1978). Within the unfolded Cenozoic sediments in the Bavarian Molasse Basin Reinecker et al. (2010) proposes a transitional strike-slip to normal faulting stress regime, which is also discussed in the Swiss Molasse Basin (Heidbach & Reinecker, 2013). The observed stress anomalies in the Upper Jurassic indicate reduced horizontal differential stress (Reinecker et al., 2010). For the sub-Mesozoic crystalline basement at the geothermal sites Unterhaching and Poing, investigations of the focal mechanisms indicate a current strike-slip faulting regime with a potentially normal faulting component (Megies et al., 2017; Megies & Wassermann, 2014).

As high sedimentation rate associated with increased subsidence rates led to overpressure conditions within the clay sediments of the Oligocene and lower Miocene (Drews et al., 2018). It is known that such conditions strongly influence tectonic stress magnitude as well as borehole and reservoir stability (Fjaer et al., 2008; Zoback, 2010). Overpressure occurs when the compaction of clay-rich sediments exceeds the normal compaction trend. This is the case when the sedimentation rate increases dramatically and the pore pressure cannot diffuse into other layers. Clay-rich layers under overpressure conditions cannot absorb the stress, resulting in a small differential stress magnitude. In the Bavarian Molasse Basin such zones are associated with early Molasse sediments which occur as clay-rich, rapidly consolidated lithological units of the Turonian, Latdorfian, Rupelian and Chattian sequence (Drews et al., 2018). The overpressure potential of these units increases near the thrust front with depth and reaches a hydrostatic level in the north where the sedimentation rate decreased (Drews et al., 2018; Müller et al., 1988). Especially south of Munich, Rupelian and Latdorfian have overpressures of $1.2-1.6\,\mathrm{g\,cm^{-3}}$ equivalent mud weight (EMW). But also in the clay-rich layers of the Cretaceous there is overpressure with EMW-values of $1.2-1.4\,\mathrm{g\,cm^{-3}}$ (Drews et al., 2018).

2.5 Seismic observation

The structural setting and the stress field information indicate that the Bavarian Molasse Basin is a tectonically stable region with minor natural seismicity (Grünthal & Wahlström, 2012). But, some seismic accumulation exists inside of the fold and thrust front near to the Peißenberg mine from the 1970 with $M_{Lmax} = 5$ and from the Bavarian Forest north-eastern of the Bavarian Molasse Basin with $M_{Lmax} = 4$. The earthquake catalog existing since the 1970s own a detection limit of $M_L 2$ which highlights that no natural earthquake of $M_L \geq 2$ could be observed within the Bavarian Molasse Basin.

Despite of the low natural seismicity, few seismic events ($0.8 < M_L < 2.4$) were recorded in the Munich area at the sites Unterhaching, Sauerlach, Kirchstockach, Dürrnhaar and Poing (LIAG, 2017). Unterhaching was the first site where induced microseismicity was detected. Five micro seismic events with a local magnitude $M_L \leq 2$ were observed during the first three years of circulation (Megies & Wassermann, 2014). The seismic events occur mostly as a swarm triggered by a major event ($M_L 2.5$) followed by several micro seismic events ($M_L < 2$) in the area of 400–500 m around the injection well. The analysis of the focal mechanism shows a left lateral slip movement in a strike-slip stress regime, which represents a reactivation of a N45°E major fault zone at the Unterhaching site (Figure 2.6). A depth migration of the events reveals that the rupturing occurs at a depth 1.5 km below the reservoir within the basement.
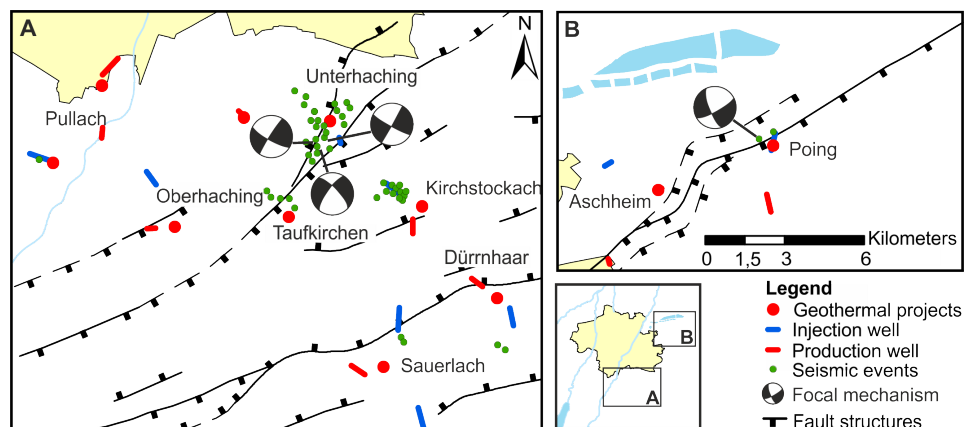
Figure 2.6 – Microseismic events in the Bavarian Molasse Basin. Map of the observation of the microseismic events detected in the greater Munich area to the end of 2017 by Megies & Wassermann (2014) and Megies et al. (2017). Detail Map A and B shows the microseismic events, the production and injection intervals for the accumulation of events with the analyzed focal mechanisms.

At the end of 2016, around four years after starting operations at the Poing site, the first seismic events were observed in the vicinity of the main fault structure "Markt-Schwabener-Verwurf" (Figure 2.6) (LIAG, 2017). Two minor events on 19.11.2016 (M_L 1.3) and 27.11.2016 (M_L 1.0) followed by two additional events on 07.12.2016 (M_L 2.1) and 20.12.2016 (M_L 1.8). About 10 months later another event occurred on 09.09.2017 (M_L 2.1). Since mid-December 2016 further seismic stations were installed and the hypo-central depth could be determined at 1–2 km below the reservoir, inside the basement. The dense network allows the analysis of the focal mechanism of the 20.12.2016 earthquake and indicates a sinistral strike-slip movement with a normal-faulting component (Figure 2.6). In addition to seismicity at

the Unterhaching and Poing site, there are smaller seismic events at the Kirchstockach, Dürrnhaar, Sauerlach, Taufkirchen and Pullach sites (Megies et al., 2017). For all sites, however, there is a common feature that seismicity always occurs in the vicinity of the injection well, approximately 1–2 km below reservoir depth. It appears that the probability of seismic events of magnitude of $M_L > 2$ for the Molasse basin is generally low (only at two sites) and is a very site characteristic phenomena. For a period of 10 years of geothermal use in the Molasse Basin at about 32 wells, only at two sites a total of 8 events with a noticeable magnitude of $M_L > 2$ occured.

The last few years have shown that despite low natural seismicity and tectonically stable conditions, a micro seismic event can be triggered by geothermal use. This underlines the need to intensify the characterization of the stress field, to understand the geomechanical coupling of geothermal reservoir operation and to adapt future development strategies to prevent the release of seismic events.

Principles in Geomechanics

"In the field of solid mechanics, major advances have been observed in understanding the fundamental models of deformation, failure and stability of rocks under conditions where rock stress is high in relation to rock strength." (Brady & Brown, 2006)

In geomechanics, these models are used to investigate the stress-strain behavior of earth material. The key issues are the study of the response of rock material from excavations like building tunnels (Brady & Brown, 2006) or drilling boreholes (Fjaer et al., 2008), enhancing the hydraulic activity of an reservoir e.g by hydraulic stimulation (Cornet, 2015), operating water storage systems (Scholz & Scholz, 2002) or understand reservoir deformation (Zoback, 2010). In the last years several topis concerning rock mechanics came more into the fore especially in connection with induced seismicity due to underground operation. It was realized that the state of underground stress and its modifications due to reservoir related operations have a significant impact on safety and efficiency of exploration. This results in an optimization of the drilling conditions to avoid wellbore failure or to manage uncontrolled fault slip in the course of reservoir operation (Zoback, 2010).

This chapter introduces the basic principles of rock mechanics following the discussion of Cornet (2015), Fjaer et al. (2008), Jaeger et al. (2007), Zang & Stephansson (2010), and Zoback (2010).

3.1 Basic definitions

Stress in the earth's crust is the result of force and strain acting on a rock volume. As traction is a function of the location L and orientation of the plane of interest the stress of a body is represented by its stress tensor (Jaeger et al., 2007). In the simplest form, tectonic stress vector T is the result of a force F acting on a surface A.

$$\vec{T} = \lim_{\Delta A \to 0} \frac{\Delta \vec{F}}{\Delta A} \tag{3.1}$$

The dimension of stress is force F [Newton] $[kg/(m/s^2)]$ per area A $[m^2]$. In a general form the stress tensor describes the forces that acts on all surfaces passing through a given point in a rock volume and can be described by a second- order tensor.

$$\sigma = \begin{bmatrix} \sigma_{xx} & \tau_{xy} & \tau_{xz} \\ \tau_{yx} & \sigma_{yy} & \tau_{yz} \\ \tau_{zx} & \tau_{yz} & \sigma_{zz} \end{bmatrix} \tag{3.2}$$
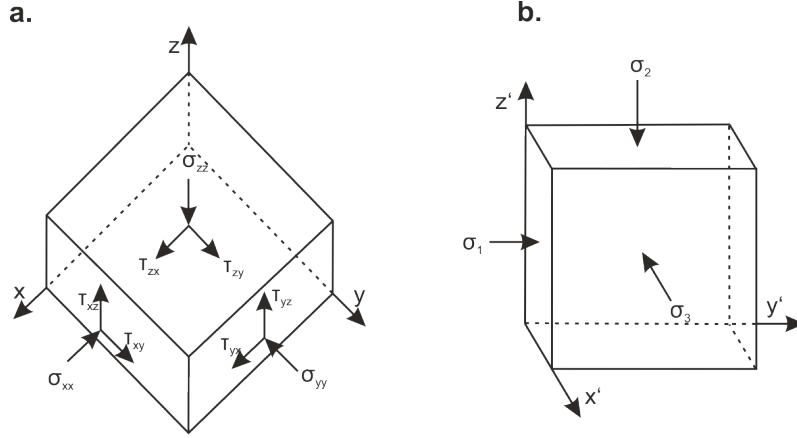
Figure 3.1 – Definition of the stress tensor in a general form a. and b. the principal stress components in the principal stress coordinate system.

The subscripts refer to the orientation of the surface considered and to direction in which the stress component acts. The first row describes the state of stress of a plane perpendicular to the x-axis, the second row perpendicular to the y-axis and the third row perpendicular to the z-axis. Normal stress is denoted with σ_{xx}, σ_{yy} and σ_{zz} and shear components with τ_{xy}, τ_{xz}, τ_{yx}, τ_{yz}, τ_{zx} and τ_{zy} (Figure 3.1a). Equilibrium conditions of forces and the balance of moments of resting bodies enable a reduction of the 9 stress components to 6 independent stress components.

$$\tau_{xy} = \tau_{yx}, \tau_{xz} = \tau_{zx}, \tau_{yz} = \tau_{zy} \tag{3.3}$$

In most geomechanical problems compression is observed, so that compression is reckoned as positive. The Eigenvalues of a stress tensor in the diagonal form describe the principal stress tensor (Figure 3.1b).

$$\sigma = \begin{bmatrix} \sigma_1 & 0 & 0 \\ 0 & \sigma_2 & 0 \\ 0 & 0 & \sigma_3 \end{bmatrix} \tag{3.4}$$

The principal stress components are ordered ($\sigma_1 \geq \sigma_2 \geq \sigma_3$). So, the eigenvector constitutes the transformation of the stress tensor in the general form (Figure 3.1a) to the principal stress coordinate system (Figure 3.1b). At principal stress condition's no shear stress exists ($\tau_{xy} = 0$) thus the principal stress direction (θ) can be calculated in the following form (Jaeger et al., 2007):

$$tan2\theta = \frac{2\tau_{xy}}{\sigma_{xx} - \sigma_{yy}} \tag{3.5}$$

The principal stresses σ_1 and σ_2 are defined as:

$$\sigma_1 = \frac{1}{2}\left(\sigma_{xx} + \sigma_{yy}\right) + \left[\tau_{xy}^2 + \frac{1}{4}\left(\sigma_{xx} - \sigma_{yy}\right)^2\right]^{1/2} \tag{3.6}$$

$$\sigma_2 = \frac{1}{2}\left(\sigma_{xx} + \sigma_{yy}\right) - \left[\tau_{xy}^2 + \frac{1}{4}\left(\sigma_{xx} - \sigma_{yy}\right)^2\right]^{1/2} \tag{3.7}$$

3.2 Linear elasticity

If stress in a rock volume is increased the resulting strain can be expressed by the general form of Hooke's Law.

$$\sigma_{ij} = C_{ijkl} \times \epsilon_{kl} \tag{3.8}$$

where C_{ijkl} is the stiffness tensor with 81 components in an general form and for elastic material it reduced to 2 components. In an idealized isotropic form of the Hooke's Law the stiffness tensor is symmetric and yields:

$$\sigma_{ij} = 2G\epsilon_{ij} + \lambda\epsilon_v\delta_{ij} \tag{3.9}$$

with λ and G of the 1st and 2nd Lamé-Parameters which relates the stress to strain components. G is known as the shear modulus which relates stresses to strain in a state of pure shear. The volumetric amount of strain (ϵ_v) can be related to the change of the hydrostatic stress (σ_p) by

$$K = -\frac{\sigma_p}{\epsilon_v} = \lambda + \frac{2}{3}G \tag{3.10}$$

where K is the bulk modulus and $1/K$ is called compressibility. Considering uniaxial stress in the x-direction, the modulus of elasticity (E) defines the stress-strain relation and the Poisson's ratio (v) the ratio of transverse strain(ϵ_y) to longitudinal (ϵ_x):

$$E = G\frac{3\lambda + 2G}{\lambda + G} \tag{3.11}$$

$$v = \frac{\epsilon_y}{\epsilon_x} = \frac{\lambda}{2(\lambda + G)} \tag{3.12}$$

From equation 3.10 to 3.12 it is clear that when two of the elastic moduli are known all others can be calculated by the equations listed in Table 3.1.

Table 3.1 – Relationship of elastic moduli in isotropic material (see Zoback, 2010).

	K	E	λ	v	G
G,λ	$\lambda + \frac{2G}{3}$	$G\frac{3\lambda+2G}{\lambda+G}$	–	$\frac{\lambda}{2(\lambda+G)}$	–
K,λ	–	$9K\frac{K-\lambda}{3K-\lambda}$	–	$\frac{\lambda}{3K-\lambda}$	$3\frac{K-\lambda}{2}$
K, G	–	$\frac{9K-G}{3K-G}$	$K - \frac{2G}{3}$	$\frac{3K-2G}{2}(3K+G)$	–
G, E	$\frac{EG}{3(3G-E)}$	–	$G\frac{E-2G}{3G-E}$	$\frac{E}{2G} - 1$	–
K, E	–	–	$3K\frac{3K-E}{9K-E}$	$\frac{3K-E}{6K}$	$\frac{3KE}{9K-E}$
λ, v	$\lambda\frac{1+v}{3v}$	$\lambda\frac{(1+v)(1-v)}{v}$	–	–	$\lambda\frac{1-2v}{2v}$
G, v	$G\frac{2(1+v)}{3(1-2v)}$	$2G(1-v)$	$G\frac{2v}{1-2v}$	–	–
v,K	–	$3K(1-2v)$	$3K\frac{v}{1+v}$	–	$3K\frac{1-2v}{2+2v}$
E,v	$\frac{E}{3(1-2v)}$	–	$\frac{Ev}{(1+v)(1-2v)}$	–	$\frac{E}{2+2v}$

3.3 THERMO-PORO-ELASTICITY

Geothermal reservoirs consists of a porous and/or fractured medium where pore pressure and temperature at the production and injection well significantly vary. Most driving forces for transient stress modification are constituted by the linear poro-elasticity and linear thermo-elasticity which can be derived from the constitutive equations by (Zoback, 2010):

$$\sigma_{ij} = 2G\epsilon_{ij} + \lambda\epsilon_v\delta_{ij} - \beta\delta_{ij}P_p - K\alpha_T\delta_{ij}\Delta T \tag{3.13}$$

The poro-elastic component is the 3rd proportion of equation 3.13 which gives a fast effect. If pore pressure exists, the sum of $\epsilon_{xx} + \epsilon_{yy} + \epsilon_{zz}$ is dependent on the inter-connection of the pore system (Nur & Byerlee, 1971). Such inter-connection is described by the Biot-coefficient β, which is a factor of the bulk modulus of the drained rock (K_b) to the bulk modulus of the individual solid grains (K_g) defined as $\beta = 1 - K_b/K_g$ (Biot, 1962). For a rock aggregate without porosity ($\lim_{\phi\to 0} \beta = 0$), pore pressure has no influence on rock behavior. But for a highly inter-connected pore system ($\lim_{\phi\to 0} \beta = 1$) pore pressure has a maximum effect.

The thermo-elastic component is the last summand of equation 3.13 which is a slow process affecting the stress conditions. If temperature decreases, material typically contracts in a linear manner by the factor given by the linear thermal expansion coefficient (α_T) (Cornet, 2015). The thermal induced contraction in isotropic material gives also an isotropic stress reduction without any shear stress. Linear expansion coefficients are highly sensitive to the amount of quartz (Zoback, 2010) and variate from $1.1x10^{-5}$ 1/°C (quartzite) to $5.5x10^{-6}$ 1/°C (gabbro).

3.4 STRESS ON PLANAR STRUCTURES

Most geomechanical problems are related to fractures or fault zones (Brady & Brown, 2006; Jaeger et al., 2007). If a fault is stable or not is highly dependent on the normal (σ_n) and the shear stress component (τ) at this surface.

To study these components in 2-D, I use the transformation in the xy-plane of an arbitrary oriented surface perpendicular to θ (Figure 3.2). The magnitude of the normal component and the shear component can be expressed by

$$\sigma_n = \sigma_{xx}\cos(\theta^2) + \sigma_{yy}\sin(\theta^2) + 2\tau_{xy}\sin(\theta)\cos(\theta) \tag{3.14}$$

$$= \frac{1}{2}(\sigma_{xx} + \sigma_{yy}) + \frac{1}{2}(\sigma_{xx} - \sigma_{yy})\cos(2\theta) + \tau_{yx}\sin(2\theta) \tag{3.15}$$

$$\tau = \sigma_{yy}\sin(\theta)\cos(\theta) - \sigma_{xx}\cos(\theta)\sin(\theta) + \tau_{xy}\cos(\theta^2) - \tau_{yx}\sin(\theta^2) \tag{3.16}$$

$$= \frac{1}{2}(\sigma_{yy} + \sigma xx)\sin(2\theta) + \tau_{xy}\cos(2\theta) \tag{3.17}$$

For the following orientation of θ the shear stress vanishes:

$$\tan(2\theta) = \frac{2\tau_{xy}}{\sigma_{xx} - \sigma_{yy}} \tag{3.18}$$

This equation has two solutions, θ_1 and θ_2 which are called the principal axes of stress.
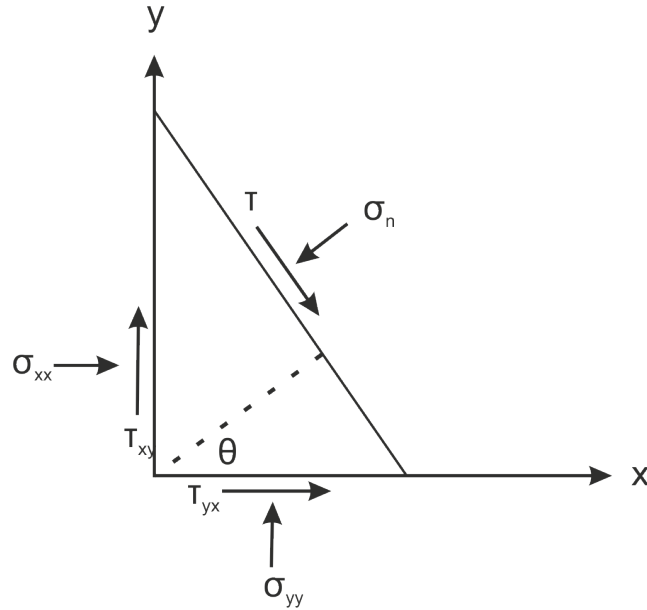
Figure 3.2 – 2D-stress at a xy-oriented plane and a plane rotated by θ from the x-direction. σ_n defines the normal stress, τ defines the shear stress acting on a plane rotated by θ.

The magnitude of these principal stresses are:

$$\sigma_{1/2} = \frac{1}{2}(\sigma_{xx} + \sigma_{yy}) \pm \sqrt{\tau_{xy}^2 + \frac{1}{4}(\sigma_{xx} - \sigma_{yy})^2} \tag{3.19}$$

It is common to reorient the coordinate system that the principal axes are the x- and y-axes. In this case the normal (σ_n) and shear component (τ) on a plane relative to these axes can be described (Zang & Stephansson, 2010):

$$\sigma_n = \frac{1}{2}(\sigma_1 + \sigma_3) + \frac{1}{2}(\sigma_1 + \sigma_2)\cos(2\theta) \tag{3.20}$$

$$\tau = \frac{1}{2}(\sigma_1 - \sigma_2)\sin(2\theta) \tag{3.21}$$

The state of stress can be visualized with the Mohr's circle where the center is at $(\sigma_1 + \sigma_2)/2$ and the radius $(\sigma_1 - \sigma_2)/2$. Largest shear stress occur at a the relative direction of $\theta = \pi/4$ (45°) to the major principal stress orientation (σ_1) (Figure 3.3).

3.5 Rock failure criterion

If differential stress in rocks increase beyond the elastic limit, the material cannot resist the load and deform irreversible(Jaeger et al., 2007). Such failure depend on various conditions like rock properties or stress conditions. Various failure criterion's exists for different failure mode, application or rock type (Fjaer et al., 2008). Fracture types can be classified in tensile - Mode I, in-plane shear - Mode II or out-of-plane shear - Mode III depending on the stress conditions (Scholz & Scholz, 2002). One of the simplest but widely used failure criteria is the Coulomb failure criterion describing Mode II - shear failure.
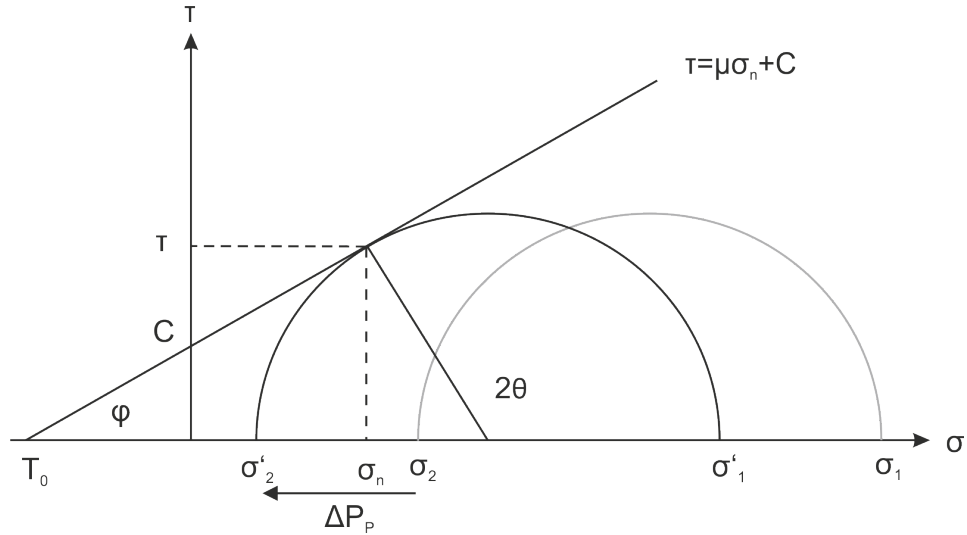
Figure 3.3 – Mohr-diagram with the Coulomb-Failure criterion.

$$\tau = \mu\sigma_n + C \tag{3.22}$$

where it is assumed that the frictional force parallel to this structure (τ) is resisted by the normal stress (σ_n) acting at this structure multiplied by the friction coefficient (μ) (Jaeger et al., 2007). This failure criterion can be easily plotted in the Mohr-Coulomb plot with a linear curve (Figure 3.3) where the y-axis distance is C. The slope of the line is the angle of internal friction (ϕ) which is defined as:

$$\phi = \tan^{-1}\mu \tag{3.23}$$

If a rock fails or not is highly dependent on the effective stress conditions (σ_1' & σ_2') (Jaeger et al., 2007) described by the effective stress theory (Terzaghi, 1962):

$$\sigma_{\text{eff}} = \sigma - P_p \tag{3.24}$$

where the total stress is reduced by the amount of pore pressure (P_p). Figure 3.3 exemplary illustrates the effect of the increasing pore pressure by ΔP_p, which shifts the initial stress conditions (σ_1 & σ_2) (grey) to decreased effective stress conditions (σ_1' & σ_2') (black). If the Mohr-circle of the effective stress (σ_1' & σ_2') intersects the failure criterion shear failure will be initiated (Figure 3.3). The orientation of the failure plane to σ_1' is given by:

$$\beta = 45° + \frac{1}{2}\phi \tag{3.25}$$

In nature the underground rock mass is in most cases fractured and the deformation takes place on these predefined surfaces. Therefore, it is quite challenging to determine a suitable rock strength that in practice will lead to the processing of fault reactivation. To handle such problems the "Slip Tendency" (ST) value describes the frictional resistance of a planar structure for sliding by the ratio of shear (τ) to normal stress (σ_n) (Moeck et al., 2009; Morris et al., 1996).

$$ST = \frac{\tau}{\sigma_n} \tag{3.26}$$

ST is high for critical conditions and low low uncritical conditions.

In underground reservoir operation, the effective stresses in the vicinity of the injection and production well vary due to thermo- poro- elastic effects (see Chapter 3.3) which modify the effective stress compared to the unaffected stress conditions.

To evaluate the seismic potential the distance of the modified effective stress conditions to reach failure is most significant. Such a stress modification can be expressed by the Coulomb-failure function (CFF) (Castillo et al., 2000; Scholz & Scholz, 2002) or the critical pore pressure (P^c_{eff}) (Mildren et al., 2002; Streit & Hillis, 2004; Wiprut & Zoback, 2000b) (Figure 3.4). This effective critical pressure modification (P^c_{eff}) (Mildren et al., 2002; Streit & Hillis, 2004) is defined as the pore pressure to induce slip at the Coulomb-failure criterion.

$$P^c_{eff} = (\sigma_n - P_p) - \left(\frac{(\tau - C)}{\mu}\right) \tag{3.27}$$

An mechanical alteration of the fault parameters will significantly reduce the frictional resistance of the fault structures (Kang et al., 2019). As long as $P^c_{eff} > 0$ fault zones can resist the induced effective stress modification. If P^c_{eff} reaches the failure criterion seismic or aseismic deformation occurs.
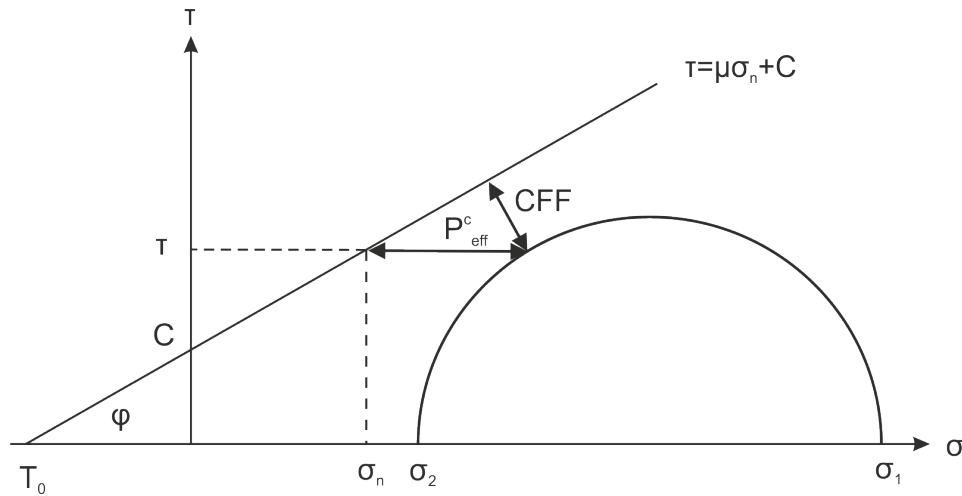
Figure 3.4 – Coulomb failure function (CFF) and critical pressure perturbation (P^c_{eff}) to reach the Coulomb-failure criterion in the Mohr-diagram.

3.6 Elastic stress at cylindrical excavations

At cylindrical excavations, like boreholes, compressive or tensile failure depends on the stress distribution in the cylindrical polar coordinates (r, θ and z) where r represents the distance from the axis, θ is the azimuth angle from the x-axis and z the location along the axis. This is originally described by the so-called "Kirsch" solution (Kirsch, 1898). If one coordinate axes is aligned to a principal stress orientation the stress components ($\sigma_{\theta\theta}$, σ_{rr}, σ_{zz} and $\tau_{r\theta}$) depend on the diameter (R), the internal pressure (p_w) and the principal stress components (σ_x, σ_y, σ_z) (Fjaer et al., 2008):

$$\sigma_{rr} = \frac{\sigma_x + \sigma_y}{2} \left(1 - \frac{R^2}{r^2}\right) + \frac{\sigma_x - \sigma_y}{2} \left(1 + 3\frac{R^2}{r^2} - 4\frac{R^2}{r^2}\right) \cos 2\theta + p_w \frac{R^2}{r^2} \tag{3.28}$$

$$\sigma_{\theta\theta} = \frac{\sigma_x + \sigma_y}{2} \left(1 + \frac{R^2}{r^2}\right) - \frac{\sigma_x - \sigma_y}{2} \left(1 + 3\frac{R^2}{r^2}\right) \cos 2\theta + p_w \frac{R^2}{r^2} \tag{3.29}$$

$$\sigma_{zz} = \sigma_z - 2v \left(\sigma_x - \sigma_y\right) \frac{R^2}{r^2} \cos 2\theta \tag{3.30}$$

$$\tau_{r\theta} = -\frac{\sigma_x - \sigma_y}{2} \left(1 - 3\frac{R^2}{r^2} + 2\frac{R^2}{r^2}\right) \sin 2\theta \tag{3.31}$$

So, failure occurs if the stress conditions exceed the compressive or tensile failure criterion. Figure 3.5 illustrates that the location of compressive failure is aligned to the orientation of σ_y (θ = 90° & 270°) and the location of tensile failure at the orientation of σ_x (θ = 0° & 180°). If the cylindrical polar coordinate system of the excavation is not aligned to the Cartesian coordinate system of the principal stress the distribution of the compressive and tensile failure significantly vary from the principal stress axis (Brudy & Zoback, 1993; Mastin, 1988). For the interpretation of borehole failure in deviated wells an general solution of the stress components is presented by Hiramatu & Oka (1968). A matrix transformation from the originally Cartesian coordinate system of the geographic stresses to the arbitrary oriented cylindrical polar coordinate system of the borehole stresses is considered by Fjaer et al. (2008), Jaeger et al. (2007), and Peska & Zoback (1995).
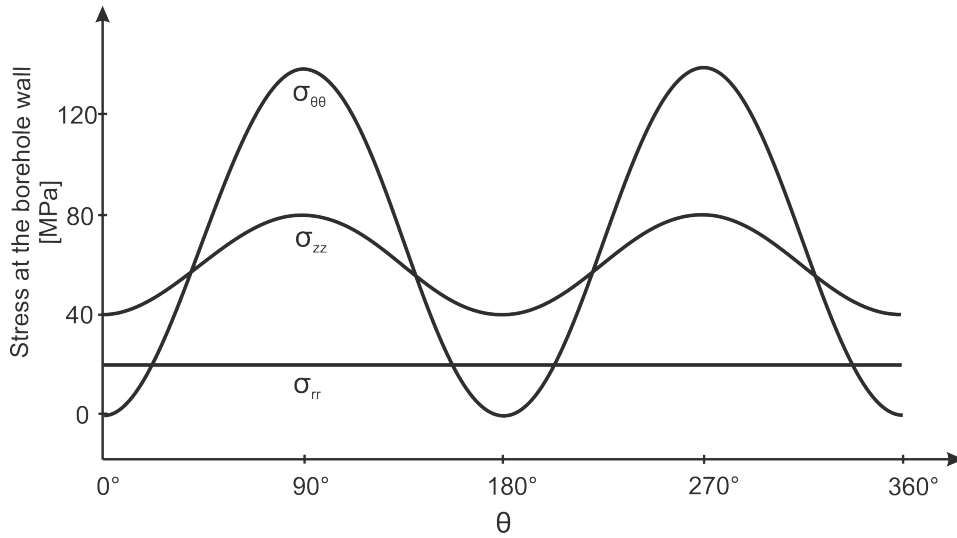
Figure 3.5 – Distribution of the tangential stress ($\sigma_{\theta\theta}$ & σ_{zz}) at the borehole wall.

Stress field analysis in the Bavarian Molasse Basin

This chapter outlines the methods which are used to describe the components of the stress tensor, e.g. the S_H-orientation and the magnitudes of S_v, S_h and S_H. In the World Stress Map project (WSM) stress data are compiled by 42,870 data records and give the best world-wide estimation of the S_H-orientation and the stress regime (Heidbach et al., 2010; Heidbach et al., 2018; Heidbach et al., 2016; Sperner et al., 2003; Zoback et al., 1989). Typical types of stress records in the WSM-database are focal mechanism solutions, geological fault slip data, borehole observations or stress relief measurements. Stress records in the Molasse basin in this study are based on borehole measurements such as geophysical logging and pressure data from enclosed borehole sections and some focal mechanisms solutions from induced microseismicity.

4.1 Tectonic stress field

The stress field can be divided into first-order stresses as a result of forces generated at plate boundaries by e.g. global lithospheric motion (Zoback, 1992) and second-order stresses resulting from lithospheric flexure, e.g. due to glacial loading and unloading or lateral density contrasts (Heidbach et al., 2007; Zoback, 1992). On a local scale, third-order stresses in sedimentary basins are controlled by geological structures (Bell, 1996). On the reservoir scale, active faults, lateral or vertical contrasts in material parameters (for example, salt structures, decoupling horizons) can lead to mechanically modified parameters and deviations of the stress orientation and tectonic regime from the regional or plate-wide stress pattern (Tingay et al., 2006).

According to Anderson (1951), three tectonic regimes can be distinguished based on the magnitudes of the vertical stress (S_v), the maximum horizontal stress (S_H), and the minimum horizontal stress (S_h). In a normal faulting regime (NF) S_v is the maximum principle stress (S_1) (Figure 4.1). It is the intermediate principle stress (S_2) in a strike-slip regime (SS) and the minimal principal stress (S_3) in a thrust faulting regime (TF). In regions with little topography, it is common to assume S_v to be a principal stress.

In areas where no data of the stress magnitude are available, a method known as frictional equilibrium theory can be applied to reduce the range of possible stress ratios (Sibson, 1974). Differential stress magnitudes ($S_1 - S_3$) in the brittle crust are limited by the frictional

strength of faults which are optimally oriented (Jaeger et al., 2007). Byerlee (1978) has shown in laboratory tests that the coefficient of static friction (μ) is independent of the rock type, but depends on the magnitude of normal stress. Accordingly, for normal stress greater than 200 MPa, the coefficient of static friction of $\mu = 0.6$ fits best and for lower normal stress $\mu = 0.85$ can be applied. On the basis of the frictional equilibrium theory, stress polygons for frictionally stable areas in different stress regimes and possible horizontal stresses (S_H and S_h) can be defined (Zoback et al., 2003). The stress polygon in Figure 4.7 represents the stress state for the Upper Jurassic limestone reservoir for a static friction coefficient of $\mu = 0.8$.
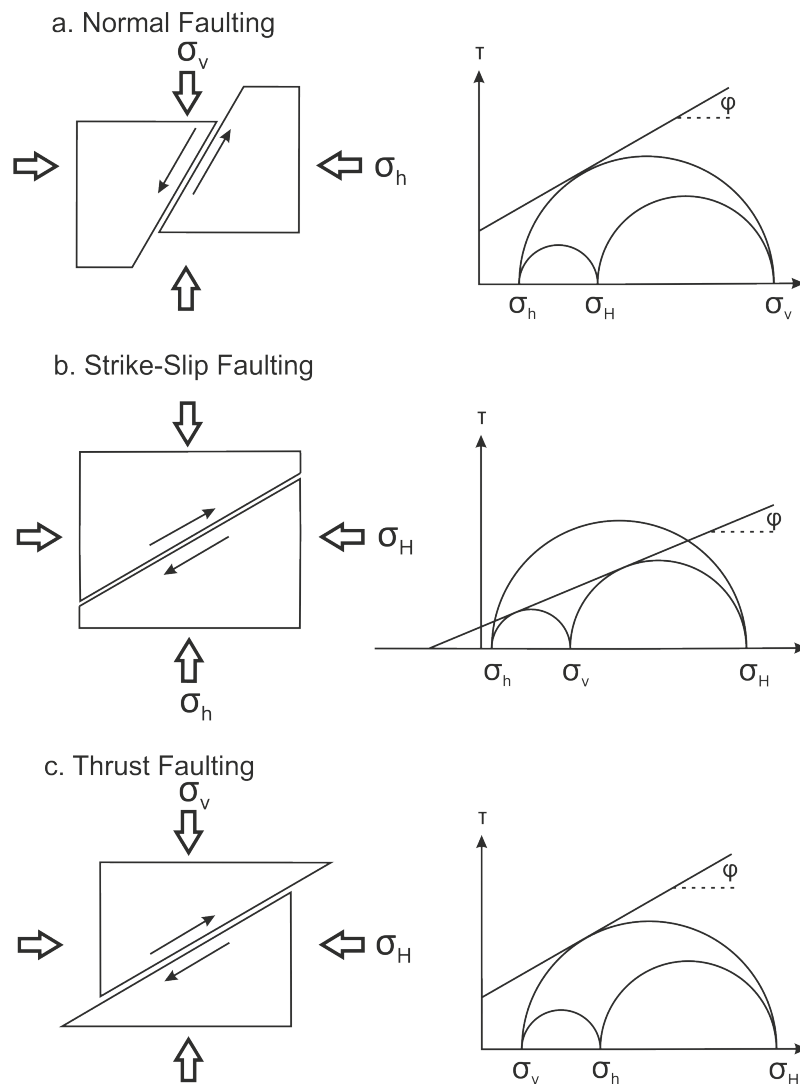
Figure 4.1 – Anderson tectonic state of stress in the crust

The determination of the stress components requires a number of theoretical considerations and a reliable data assessment (Zang & Stephansson, 2010). S_v can be estimated by dividing the subsurface's bulk density ρ_{bulk} into vertical depth intervals dTVD in m, which can be integrated into a vertical stress S_v in Pa at any true vertical depth (TVD):

$$S_v = \int_0^{TVD} \rho_{bulk} \times g \times dTVD \tag{4.1}$$

Where g is the Earth's gravitational acceleration of 9.81 m/s². Pore pressure (P_p) can be estimated by hydraulic pumping tests or pressure measurements. In the Bavarian Molasse Basin pore pressure within the Mesozoic / Upper Jurassic sediments is at hydro-static condition (Birner et al., 2012). But Drews et al. (2018) and Müller et al. (1988) indicate an over-pressure potential within the early Cenozoic clay-sediments of the Turonian, Latdorfian, Rupelian and Chattian sequence.

4.2 Minimal horizontal stress

The minimal horizontal stress (S_h) can be determined from borehole measurements (Hubbert & Willis, 1972; Zoback, 2010) or on the basis of bilateral strain (Eaton, 1969; Zhang & Zhang, 2017). Fortunately the database in the Bavarian Molasse Basin provides pressure data from Leak-off Tests (LOT), Formation Integrity Tests (FIT), cementation jobs and stimulation jobs (see Table 1.3). Using LOTs, the S_h magnitude can be quite well determined because the complete pressure response is used for the evaluation. To the contrary FIT or cementation pressures provide lower bounds for S_h (Zoback et al., 2003). These measurements could be compared to the results from uniaxial stress condition on the basis of a realistic Poisson's ratio (ν) and the vertical stress (S_v).
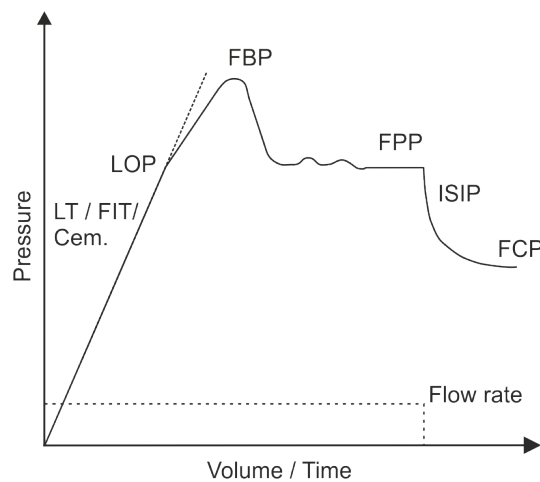
LT - Limit Test; FIT - Formation Integrity Test; Cem. - Cementation pressure; LOP - Leak-off pressure; FBP - Formation Break-Down pressure; FPP - Fracture propagation pressure; ISIP - Instantaneous shut-in pressure; FCP - Fracture closure pressure

Figure 4.2 – Characteristic pressure curve during hydraulic fracturing (modified after Gaarenstroom et al., 1993).

Pressure conditions during LOTs typically indicate a pressure vs. time curve during constant injection volume or flow-rate (Ljunggren et al., 2003). Under these conditions the pressure inside of the borehole increases with a linear trend until the slope decreases at the leak-off pressure (LOP) (see Figure 4.2). The change of the trend is characterized by an increase of the system volume caused by the beginning of hydraulic fracturing. These fractures propagate away from the borehole, perpendicular to S_h and thus give a indication of the S_h-magnitude (Hubbert & Willis, 1972). The so-called fracture breakdown pressure (FBP) occurs when unstable fracture propagation exists. If pumping with constant flow–rate

is continued, pressure drops down and stabilize at the fracture propagation pressure (FPP) which indicates the best measurement of S_h (Hickman & Zoback, 1983). During Formation integrity tests (FIT), cementation jobs (cem. pres.) or stimulation jobs borehole pressure increases but tests are typically aborted at a predefined pressure level during the linear part of the curve (Figure 4.2). So, these tests are significant for the limitation of the minimum magnitude of S_h, but cannot define an upper limit of S_h as no fracturing process occurred (Zang et al., 2012).

4.3 Geomechanical log interpretation

Stress indicators can be interpreted in resistivity Image logs, acoustic Image logs and caliper logs (Bell, 1996; Plumb & Hickman, 1985). In the geophysical borehole database of the Bavarian Molasse Basin caliper measurements from the Cenozoic sediments and resistivity Image logs from the Upper Jurassic reservoir are compiled (see Table 1.2). 4- or 6- arm caliper tools complemented by a GPIT-unit (EMS-tools) measure mechanically the diameter of the borehole and link it with geographical information. The Image logging tool measures the resistivity of the borehole wall in high resolution and displays an oriented borehole resistivity wall image (Ellis & Singer, 2008).

Image log data enable to detect natural fractures by their fracture resistivity contrast to the surroundings as an sinusoidal trace (Figure 4.4c). Completely sinusoidal features with low resistivity (open fractures filled with mud) are distinguished from sinusoidal features, which only show a low resistivity in some areas (partly open fracture filled with mud), and sinusoidal features of higher resistivity than the formation (closed / healed fracture) (Trice, 1999).

Caliper and Image logs are able to map the borehole geometry indicating the distribution of the failure mechanisms at the borehole wall. Compressional failure initiates borehole ovalization (Breakouts) in vertical wells (see Chapter 3.6) when the maximum hoop stress ($\sigma_{\theta max}$) exceeds the rock mass strength (Figure 4.3) (Bell & Gough, 1979; Zoback et al., 1985). For the interpretation of caliper measurements the "SAC" 6-arm caliper interpretation software is used (Wagner et al., 2004). In Image logs borehole ovalization results in a poor quality of resistivity image described as blurry, conductive, symmetrical features (Bell, 1996) (Figure 4.4a). For our analysis each breakout zone is subdivided in 0.5 m intervals of a mean orientation and the Breakout width (ω_{bo}) is determined.

During the drilling process in highly fractured reservoirs, stress rearrangement at the borehole wall can enhance existing fractures where minimal hoop stress $\sigma_{\theta min}$ reaches tensional mode (Figure 4.3). Barton et al. (2009) call these fractures drilling-enhanced natural fractures (DENF). These structures are relatively short segments of fine-aperture natural fractures, which are not visible as complete sinusoidal traces (Figure 4.4c). DENFs are aligned to existing sinusoidal traces and can be fitted by flexible sinusoidal traces (Barton et al., 2009). Due to the interaction of fracture planes and tensile stress, it is sometimes difficult to precisely determine the orientation of the tensile areas with DENFs. In comparison to DENFs, DITFs occur as axisymmetric pairs parallel to the borehole axis. They are formed when the minimal hoop stress ($\sigma_{\theta min}$) reaches the tensile strength (T_o) of
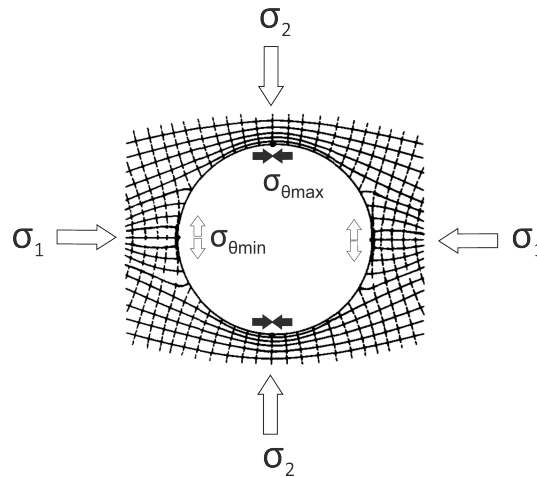
Figure 4.3 – Stress concentration at a borehole oriented along a principle stress orientation with minimal and maximal hoop stress ($\sigma_{\theta min}$ and $\sigma_{\theta max}$) (modified after Zoback, 2010)

the rock mass (Barton et al., 2009) (Figure 4.3) and are promoted by cooling down the well or increasing the mud weight (Davatzes & Hickman, 2010). For wells that are inclined to one principal stress axis, DITF occur as en-echelon sets of fractures (E-DITFs) at a small angle to the borehole axis (Peska & Zoback, 1995). Thus, axial fractures or E-DITF in combination with knowledge of the well trajectory indicate the principal stress direction.

So, stress indicator data give direct indications of the circular distribution of $\sigma_{\theta max}$ from breakout data and $\sigma_{\theta min}$ for DITFs and DENFs. For quality assessment of the stress indicator interpretation the circular statistics are calculated based on Mardia (1972). This statistics gives the mean circular orientation of θ_{min} and θ_{max} with its standard deviation (σ_{st}). This parameter evaluation allows a quality control of the stress indicator data based on the WSM-quality ranking for the interpretation of Breakouts at 6-arm caliper (Reinecker et al., 2016) and the interpretation of Breakouts and DITF at Image logs, (both Tingay et al., 2016).
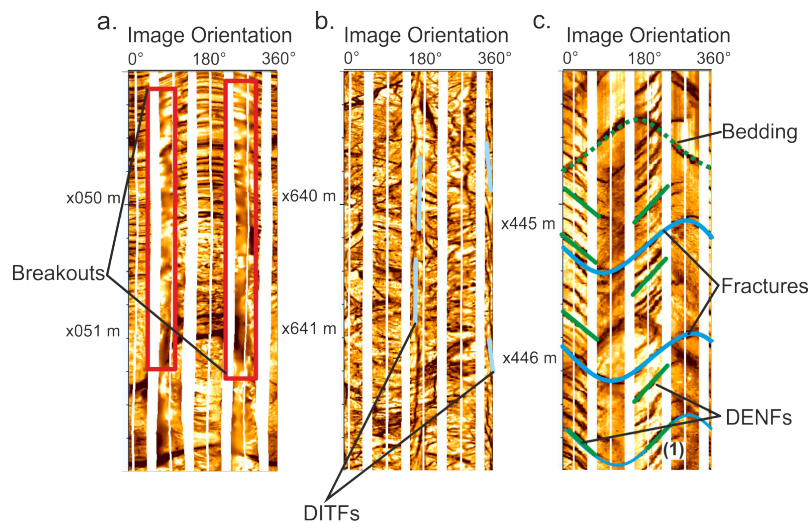
Figure 4.4 – Stress indicators typically observed in Image Logs at the Bavarian Molasse Basin within the Upper Jurassic reservoir (modified after Seithel et al., 2015)

4.4 Borehole failure in deviated wells

If the well is aligned to one principle stress axis the circumferential / tangential ($\sigma_{\theta\theta}$) and radial stress (σ_r) components are described by Kirsch (Kirsch, 1898) (see Chapter 3.6). But most recently drilled wells have inclined well paths where further computations for the stress distribution are needed (Hiramatu & Oka, 1968). According to these computations, the orientation of compressional and tensile borehole failure does not only vary with the stress magnitudes, but also with the orientation of the borehole trajectory relative to the stress tensor (Mastin, 1988). There are several methods described in literature for transforming Cartesian coordinate system of the regional stress into the arbitrary oriented borehole stress in the cylindrical coordinate system (Aadnoy, 1990; Peska & Zoback, 1995; Qian & Pedersen, 1991; Zajac & Stock, 1997).

Peska & Zoback (1995) use a method to determine the direction of the maximal (σ_{tmax}) and minimal tangential stresses (σ_{tmin}) in deviated boreholes for effective stresses ($S_s = S - P_p$). The transformation is based on the "Euler" rotation from the principal stress tensor (S_s) into the stress tensor in the geographic coordinate system (S_g) with a transformation matrix R_s defined as (Note: In Peska & Zoback (1995) this formula is correct, but in Zoback (2010) there is a typing error in one component):

$$R_s = \begin{bmatrix} \cos(\alpha)\cos(\beta) & \sin(\alpha)(\cos(\beta) & -\sin(\beta) \\ \cos(\alpha)\sin(\beta)\sin(\gamma) - \sin(\alpha)\cos(\gamma) & \sin(\alpha)\sin(\beta)\sin(\gamma) + \cos(\alpha)\cos(\gamma) & \cos(\beta)\sin(\gamma) \\ \cos(\alpha)\sin(\beta)\cos(\gamma) + \sin(\alpha)\sin(\gamma) & \sin(\alpha)\sin(\beta)\cos(\gamma) - \cos(\alpha)\sin(\gamma) & \cos(\beta)\cos(\gamma) \end{bmatrix} \tag{4.2}$$

Then, the S_g must be transformed into the cylindrical borehole coordinate system (S_b) by R_b

$$R_b = \begin{bmatrix} -\cos(\delta)\cos(\phi) & -\sin(\delta)(\cos(\phi) & -\sin(\phi) \\ \sin(\delta) & -\cos(\delta) & 0 \\ \cos(\delta)\sin(\phi) & \sin(\delta)\sin(\phi) & \cos(\phi) \end{bmatrix} \tag{4.3}$$

where δ is the borehole azimuth and ϕ is the borehole deviation.

The complete transformation from principal (S_s) to geographic (S_g) and to the borehole coordinates (S_b) is:

$$S_b = R_b\, R_s^T\, S_s\, R_s\, R_b^T \tag{4.4}$$

The state of stress in the cylindrical polar borehole coordinate system (S_b) is referred to an angle θ, which is rotated in clockwise direction from the Bottom of Hole (BOH) or Top of Hole (TOH) along the borehole axis, respectively.

If temperature of the wellbore fluid is smaller than rock temperature, thermal stresses make the stress concentration around the well more tensile. Temperature distribution is a time-dependent effect. Once steady state has been reached the change of the thermal stress component ($\sigma^{\Delta T}$) is (Zoback, 2010)

$$\sigma^{\Delta T} = \frac{\alpha_t E \Delta T}{1 - \nu} \tag{4.5}$$

where α_t is the thermal expansion coefficient, E the Young's modulus and ν the Poisson's ratio.

The following equations describe the cylindrical stress defined by Peska & Zoback (1995).

Note, stress concentration additionally depends on the pressure difference (ΔP) of mud (P_m) and pore pressure (P_p) and the thermal stress ($\sigma^{\Delta T}$) (Zoback, 2010). At cylindrical structures thermal stress acts on the hoop stress ($\sigma_{\theta\theta}$) and the axial stress component (σ_{zz}) (Zoback et al., 2003), resulting in the following equations:

$$\sigma_{zz} = \sigma_{33} - 2\nu\left(\sigma_{11} - \sigma 22\right)\cos 2\theta - 4\nu\sigma_{12}\sin 2\theta - \sigma^{\Delta T} \tag{4.6}$$

$$\sigma_{\theta\theta} = \sigma_{11} + \sigma_{22} - 2\left(\sigma_{11} - \sigma_{22}\right)\cos 2\theta - 4\sigma_{12}\sin 2\theta - \Delta P - \sigma^{\Delta T} \tag{4.7}$$

$$\sigma_{\theta z} = 2\left(\sigma_{23}\cos\theta - \sigma_{13}\sin\theta\right) \tag{4.8}$$

$$\sigma_r = \Delta P \tag{4.9}$$

where σ_{zz} is the stress in axial direction, $\sigma_{\theta\theta}$ the hoop stress, and $\sigma_{\theta z}$ the shear stress. In deviated wells the maximum (σ_{tmax}) and minimum tangential stress (σ_{tmin}) are not aligned to the borehole axis and defined by:

$$\sigma_{tmax} = 1/2\left(\sigma_{zz} + \sigma_{\theta\theta} + \sqrt{(\sigma_{zz} - \sigma_{\theta\theta})^2 + 4\theta_{\theta z}^2}\right) \tag{4.10}$$

$$\sigma_{tmin} = 1/2\left(\sigma_{zz} + \sigma_{\theta\theta} - \sqrt{(\sigma_{zz} - \sigma_{\theta\theta})^2 + 4\sigma_{\theta z}^2}\right) \tag{4.11}$$

In order to determine the orientation of σ_{tmax} ($\theta_{maxmodel}$) and σ_{tmin} ($\theta_{minmodel}$) from TOH, θ is varied in 0.2° steps from 0° to 360°. From this "forward modeling", the compressive σ_{tmax} as well as tensile stresses σ_{tmin} and their orientations ($\theta_{maxmodel}$ and $\theta_{minmodel}$) are determined for a given well trajectory in an arbitrary stress field.
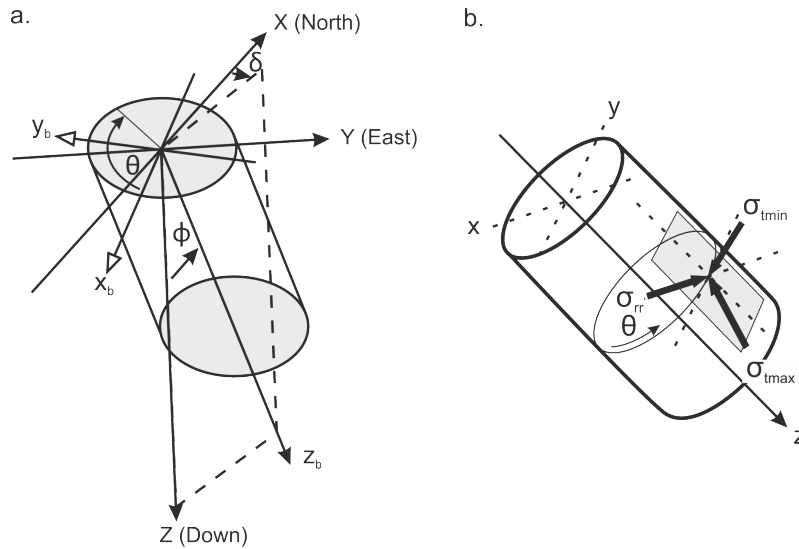
Figure 4.5 – Stress in Cartesian and cylindrical coordinate system. a. Stress transformation from the Cartesian coordinate system of principle stress to the cylindrical polar coordinate system of the borehole stress. b. Stress distribution at the borehole wall in an arbitrary oriented borehole (modified after Peska & Zoback, 1995).

4.5 STRESS ORIENTATION

In vertical wells the S_H-orientation can be directly derived form breakout interpretation. The orientation of maximum hoop stress ($\sigma_{\theta max}$) where breakouts develop is perpendicular to the orientation of the maximum horizontal stress (S_H) (Figure 4.3). Seithel et al. (2015) showed exemplary for one well in the Bavarian Molasse Basin that with increasing borehole deviation ($\phi < 20°$) caliper logs indicate a significant decentralization which disable any breakout interpretation (Reinecker et al., 2016). Mastin (1988) also highlights that stress concentration in deviated wells ($\phi > 20°$) is more and more dependent on the borehole deviation and azimuth. Fortunately, stress indicator data from highly deviated wells, reflects the stress concentration at the borehole wall and can be used for stress field characterization (Barton et al., 1998; Barton et al., 2009; Hickman & Zoback, 2004; Moos & Zoback, 1990; Peska & Zoback, 1995; Schmitt et al., 2012; Schoenball et al., 2016; Seithel et al., 2015; Thorsen, 2011; Wiprut et al., 1997). So, breakouts indicate the orientation of σ_{tmax} and DITF or DENF the orientation of σ_{tmin}.

In highly deviated wells, tangential stress distribution is a function of borehole orientation, tectonic stress regime and S_H- orientation. This situation require a technique to invert the stress field information from borehole stress indicators (Qian & Pedersen, 1991; Schoenball & Davatzes, 2017; Seithel et al., 2015). Here, we apply a grid-search method where the interpreted high quality stress indicators are compared to the modeled stress concentration at the borehole wall for ranges of S_H- orientations and S_H/S_v magnitudes (Seithel et al., 2015). For each stress indicator the reference borehole trajectory at the given depth, combined with the stress field gives the $\theta_{minmodel}$ and $\theta_{maxmodel}$ orientation. The average values of the square roots of the directional differences of the observed (θ_{obs}) vs. modeled stress (θ_{model}) are calculated. For every stress regime, the mean directional difference ($\Delta\theta$), including all stress indicators, is defined.

$$\Delta\theta = \sqrt{\frac{\Sigma\,|\theta_{obs} - \theta_{model}|^2}{N}} \qquad (4.12)$$

Small $\Delta\theta$-values indicate a good match with the modeled stress field (white colors in Figure 4.6) and large $\Delta\theta$-values a poor match (dark colors in Figure 4.6). Seithel et al. (2015) showed that the results of $\Delta\theta$ are minimal sensitive to the S_h-magnitude in a normal faulting and strike-slip faulting regime. Consequently, the S_h-magnitude could be fixed at a best known value of 15 MPa/km for the Upper Jurassic in the Bavarian Molasse Basin. So, by a "mis-fit" gridding all stress cases in the range of $0.5 < S_H/S_V < 1.25$ and the orientation of S_H from N000°E to N180°E were varied and the mean mis-fit ($\Delta\theta$) is calculated (Figure 4.6).

This method enables to interpret stress indicator data in highly deviated wells, if the standard deviation (σ_{st}) of the total stress indicator orientation of a borehole is smaller than 20° and a total length of 35 m of stress indicator are observed. This limitation matches the A–B quality of the WSM-ranking for Image logs (Tingay et al., 2016). In Figure 4.6 the results of the Mis-fit gridding of Sauerlach Th1a (left) can be compared with the results of Sauerlach Th2b (right). It is shown that at Th1a Mis-fit gridding indicates an anti-clockwise rotation of the local maximum horizontal stress by 30° from the regional N000°E S_H-orientation at

a strike-slip stress regime. In contrast Mis-fit gridding of the stress data at the Sauerlach Th2b validate the regional S_H- orientation (Seithel et al., 2015). So, it is possible to evaluate boreholes where stress heterogeneity from local structures dominate and boreholes where the regional trend is verified.
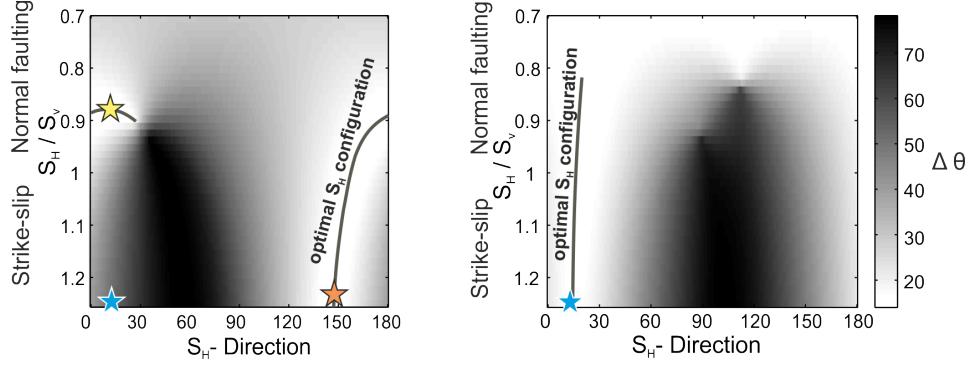
Figure 4.6 – Results of the "mis-fit" gridding to identify the S_H-orientation based on Stress indicator interpretation in highly deviated wells (modified after Seithel et al., 2015)

4.6 Stress Magnitude

There exists two approaches which can be used to determine the magnitude of the maximum horizontal (S_H) and minimum horizontal stress magnitude (S_h) (Aadnoy, 1990; Barton et al., 1998; Barton et al., 1988; Hickman & Zoback, 2004; Moos & Zoback, 1990; Wiprut & Zoback, 2000a; Zoback et al., 2003). One approach is based on the observation of compressive failure / breakouts for the determination of S_H- magnitude and the other is based on tensile failure / DITF or DENF for the determination of S_h- magnitude.

Breakouts occur if stress concentration exceeds the rock strength. Barton et al. (1988) describe a method to determine S_H-magnitude in vertical wells when the uniaxial compressive strength (UCS) and the breakout width (ω_{bo}) is known.

$$S_H = \frac{(UCS + 2P_p + \Delta P + \sigma^{\Delta T}) - S_h(1 - 2\cos 2\omega_{bo})}{1 - 2\cos(2\omega_{bo})} \qquad (4.13)$$

It is well-known that DITF or DENF occur if hoop stress falls below the tensile strength of the rock (Moos & Zoback, 1990). In vertical wells this situation can be used for the determination of the maximal horizontal stress magnitude (S_H) (Brudy et al., 1997).

$$S_H = 3S_h - 2P_p - \Delta P - T_0 - \sigma^{\Delta T} \qquad (4.14)$$

where T_0 is the tensile strength of the rock, ΔP the difference between P_m and P_p and $\sigma^{\Delta T}$ the thermo-elastic stress.

In vertical wells equation 4.13 and equation 4.14 can be used to plot curves describing the stress conditions of compressive (red line in Figure 4.7) or tensile failure (blue line in Figure 4.7) for well-known borehole conditions. Brudy et al. (1997) pointed out that the P_m and $\sigma^{\Delta T}$ corrected value of S_H must be considered to be a lower bound, as tensile failure could be observed without these components.

As described in Chapter 4.4 stress concentration at arbitrary oriented wells is not a linear
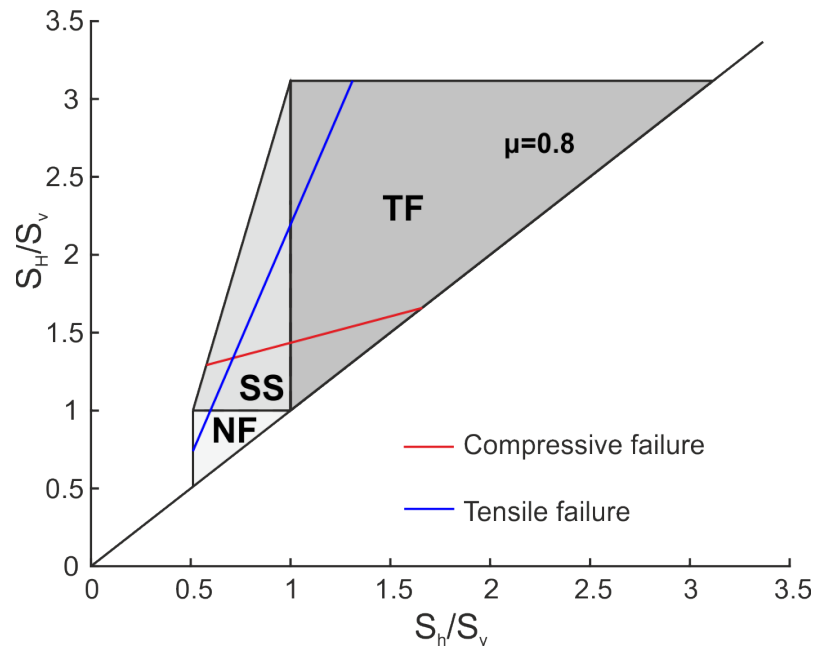
$S_{v\,grad.}$ = 23 MPa/km, E = 40 GPa, UCS = 120 MPa, T_0 = 0 MPa, ω_{bo} = 30°, ν = 0.25, α_T = 1x10^{-6} 1/K, $T_{inj.}$ = 30 °C, $T_{grad.}$ = 0.03 K/m

Figure 4.7 – Stresspolygon for the range of stress in frictional equilibrium at the Upper Jurassic reservoir in the Bavarian Molasse Basin. NF describes the field of the Normal faulting regime, SS the field of Strike-Slip regime and TF the field for Thrust-Faulting regime. The red line indicates the stress limitation for compressional failure and the blue line for tensile failure for the UCS and breakout widths considered here.

combination of S_H and S_h magnitude. So, in deviated wells the maximal principle stress components at the borehole wall are σ_{tmax} and σ_{tmin} that have to be used to determine the borehole failure mechanisms and to investigate the S_H-magnitude. For compressional failure the borehole wall is subdivided into 1°-bins and for each bin the failure conditions are determined based on the UCS and internal friction coefficient according to the tangential borehole wall stress conditions (see Chapter 4.4). The angular width of the failure area is referenced to the observed breakout width (ω_{bo}). This method enables to plot the red line in the stress polygon (Figure 4.7) for the observation of breakouts in an arbitrary well. Tensile failure in deviated wells develop if σ_{tmin} fall below T_0 which enable to plot the blue line into the stress polygon (Figure 4.7).

Thus it is possible to determine the S_H-magnitude for borehole intervals where multiple borehole failures occur and there is a constant borehole orientation. If breakouts with a fixed breakout width (ω_{bo}) are interpreted on image log data, the S_H magnitude can be determined for a realistic range of the UCS. At borehole intervals where both, compressional and tensile, stress indicators are observed the intersection point of both curves describe the state of stress at this section.

Lithology correlated S_h assessment based on formation-integrity and leak-off test data in the Bavarian Molasse Basin

This Chapter describes the complete database of formation integrity tests (FIT), leak-off tests (LOT), pressure protocols during cementation (Cem. Pres.) and stimulation jobs (Stim. Pres.); a quality control and a lithology dependent analysis of the S_h-magnitude. It forms the basis for the close cooperation with Dr. Michael Drews of the Friedich-Alexander University Erlangen-Nürnberg (FAU) for the joint publication of Drews, M. C., Seithel, R., Savvatis, A., Kohl, T. & Stollhofen, H. (2019a): A normal-faulting stress regime in the Bavarian Foreland Molasse Basin? New evidence from detailed analysis of leak-off and formation integrity tests in the greater Munich area, SE-Germany. – in: *Tectonophysics* 755, pp. 1–9. – DOI: 10.1016/j.tecto.2019.02.011.

5.1 Introduction

The Munich area in the Bavarian Molasse Basin is the second largest developed low-enthalpy geothermal field in Europe after the Paris Basin. It is located in the foreland basin north of the Alps with Mesozoic and Cenozoic layers in the underground, dipping south (Bachmann et al., 1987) (Figure 5.1). So far, there are 16 geothermal projects that generate heat and electricity from the Upper Jurassic reservoir with a temperature level in the range of 80 °C to 140 °C and a flow rate of 85 to 140 l s^{-1} (STWIVT, 2010). Within the framework of the "Geothermal Alliance of Bavaria" (GAB) the data of the geothermal projects partners (red dots in Figure 5.1) were collected and provide a spatially almost complete database for scientific research. The determination of the stress field parameters from this database is an important component to avoid wellbore instabilities, to optimize the drilling parameters or to understand the long-term behavior of the reservoir (Fjaer et al., 2008; Zoback, 2010).

The study area is located in the middle Molasse Basin between the eastern and western Molasse Basin, which was intensively explored for oil in the 1950 and 1960. These borehole data were evaluated within the World Stress Map (WSM) Project (Heidbach et al., 2018; Reinecker et al., 2010) and indicate a S_H-orientation perpendicular to the Alpine thrust front. Near the thrust front a compressional stress regime is described (Illies & Greiner, 1978; Reinecker et al., 2010) with decreasing magnitude at increasing distance to the Alpine thrust front (Reinecker et al., 2010). Within the Cenozoic and Mesozoic sediments, numerous

normal faults are interpreted as indicators that a period of normal-faulting character existed (Hartmann et al., 2016). Nevertheless, microseismic events indicate a strike-slip displacement (Megies et al., 2017; Megies & Wassermann, 2014) within or below the Upper Jurassic reservoir and Image log interpretation indicates possible stress rotation (Seithel et al., 2015). For the pore pressure conditions within the Cenozoic Molasse sediments the lithology and depth are crucial (Drews et al., 2018; Drews et al., 2019b; Müller et al., 1988). Such a lithologic layering of stiff and soft sediments typically affects the magnitude of S_h (Gunzburger & Magnenet, 2014; Wileveau et al., 2007; Zhang & Zhang, 2017).

The lithological variation of the Lower Cenozoic (clay/marl-rich) to the Upper Jurassic (limestone) could therefore also control the stress field in the Bavarian Molasse Basin. To improve the knowledge about the poorly known magnitude of S_h, a complete data review in 25 wells and a total of 75 borehole measurements is presented. On the basis of such a broad database, the understanding of the distribution and the order of magnitude of S_h-magnitude can be significantly improved.
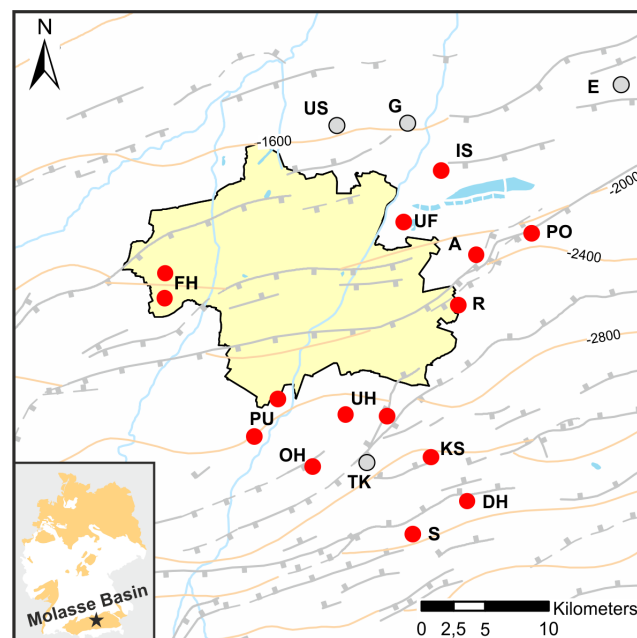
A- Aschheim, DH- Dürrnhaar, E- Erding, FH- Freiham, G- Garching, IS- Ismanning, KS- Kirchstockach, OH- Oberhaching, PO- Poing, PU- Pullach, R- Riem, S- Sauerlach, TK- Taufkirchen, UF- Unterföhring, UH- Unterhaching, US- Unterschleißheim

Figure 5.1 – Map of geothermal sites, fault structures (grey lines) and depth (TVD) of the Upper Jurassic reservoir (STWIVT, 2010). Red circles indicate geothermal projects for which the Geothermal Alliance of Bavaria (GAB) could initiate a research cooperation.

5.2 Geology and Methods

5.2.1 Stratigraphy and lithological variation

Test are usually performed at the casing shoe of the second, third or fourth section at a well-defined lithology with non-permeable sand or claystone. Stratigraphically, these intervals are in the lower or middle Ottnangium (Neuhofenener Schichten or Blättermergel); Aquitan

(Sand-Mergel-Folge); Chatt (Hangende- or Liegende Tonmergel or Sandserie); Turon / Claymarl or the Upper Purbeck (see Figure 5.2).

From a lithological perspective, the lower to middle Ottangnian consists mainly of coarse-grained, sand-sized to pebbel-sized siliclastics, but also with shale-rich sequences (Kuhlemann & Kempf, 2002). Chattian and Aquitan are most likely dominated by shale, while the "Chattian Sands" consists of a heterolithic sequence of alternating sand and shale (Kuhlemann & Kempf, 2002). The Upper Cretaceous is dominated by shale-rich sediments covered by Late Eocene sands and limestones. The lowest deposits on the Upper Jurassic boundary are limestone to dolomite dominated Purbeckian sediments (Bachmann et al., 1987). Basically the lithological units can be divided into pure clay, alternating clay/sand layers and carbonate dominated sediments.
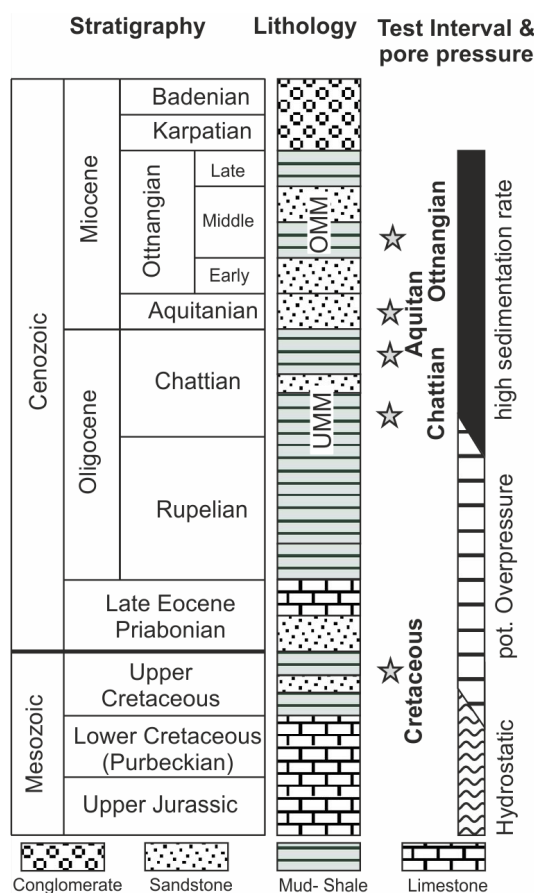
Figure 5.2 – Stratigraphy of the Bavarian Molasse Basin. 1st column stratigraphic overview of the Cenozoic sediment filling (modified after Kuhlemann & Kempf, 2002) and the Mesozoic sediments of the Cretaceous and Upper Jurassic (Bachmann et al., 1987). 2nd column shows the main lithology in each sequence. 3rd column contains the sections that were tested. 4th column indicates zones for hydrostatic, overpressure or underhydrostatic pore pressure conditions (see details in Drews et al., 2018).

The lithological composition of the sediments significantly influences the frictional strength of rocks, which directly limit the differential stresses against which they can resist (Jaeger et al., 2007). Byerlee (1978) has given coefficients of friction of 0.6–0.8 for crustal rocks, a coefficient of friction of 0.21–0.33 for smectite dominated shales and a coefficient of friction of 0.44–0.5 for illite dominated shales. The analysis of Gier (1998) shows that

clay minerals for the eastern Molasse Basin consists mostly of interlayered smectite and illite. Triaxial tests of compacted Cenozoic shales indicate typical coefficients of friction of 0.26–0.47 (Lempp et al., 2010). For marine sedimentary rocks an increasing carbonate content increases the friction coefficient (Kohli & Zoback, 2013). Lithologically the Upper Cretaceous is dominated by shale but the Lower Cretaceous (Purbeckian) by carbonate. Triaxial tests of outcrop samples from the Francian Alp indicate friction coefficients of 0.4–0.44 for the Purbeckian facies and 0.78–0.86 for the Upper Jurassic (Tondera et al., 2013). The friction coefficient of limestone might be sensitive to water saturation, e.g. a micritic limestone indicates $\mu = 0.6$ under dry conditions and $\mu = 0.3$ under wet conditions (Nicolas et al., 2016). Log-based analysis of the rock mechanical parameters of carbonate rocks indicates a dominant dependency of the porosity type where the friction coefficient typically vary from 0.5 for to 0.8 (Ameen et al., 2009). It can be assumed that for the shale-dominated Late Eocene, Oligocene and Early Miocene the friction coefficient is 0.2–0.5, but for the carbonate-dominated Lower Cretaceous and Upper Jurassic friction coefficient increases significantly to 0.6–0.8.

It is known that the pore pressure in the Molasse Basin may reach overpressure conditions, especially near the Alpine thrust front (Drews et al., 2018; Müller et al., 1988). A detailed evaluation of the logging campaigns of oil wells allows a better understanding of the overpressure mechanism and distribution. Drews et al. (2018) has shown that the source of overpressure in the Bavarian Molasse Basin is disequilibrium compaction of shale sediments. It has been demonstrated that the overpressure potential increases with depth and in the direction to the Alpine thrust front. Thus the overpressure potential for the Chattian, Rupelian and Upper Cretaceous increases significantly (Figure 5.2). Up to the Upper Chattian at about 1500 mTVD the pore pressure increases with a hydrostatic gradient. From here the maximal overpressure builds up with a gradient of 20 MPa km^{-1} parallel to the vertical stress (Drews et al., 2018). At depth there is an overpressure potential up to the lower Cretaceous, where the pore pressure conditions change to the "under"- hydrostatic reservoir conditions of the Upper Jurassic (Birner et al., 2012).

5.2.2 S_h measurements

Formation integrity tests (FIT), leak-off tests (LOT), pressure protocols during cementation (Cem. Pres.) or stimulation jobs (Stim. Pres.) are work-over jobs in which borehole pressure increases. The main objective of these pressure tests is to guarantee a safe drilling. The exact evaluation of the borehole pressure, however, also provides in-depth information on the minimum horizontal stress magnitude (S_h) at the test interval.

Pressure conditions during such tests typically indicate a pressure vs. time curve at constant injection volume or flow-rate. Under these conditions, borehole pressure increases with a linear trend until the slope decrease at the leak-off pressure (LOP) (see Chapter 4 Figure 4.2). This trend change is characterized by an increase in system volume due to the beginning of hydraulic fracturing. These fractures propagate away from the borehole wall, perpendicular to S_h. So, a clear LOP is thus the first approximation to the S_h-magnitude in the test interval (Hubbert & Willis, 1972). If the pumping continues with a constant flow, the pressure drops and an unstable fracture propagation occurs at the so-called fracture

breakdown pressure (FBP). This pressure stabilizes at the fracture propagation pressure (FPP), which indicates the best measurement of S_h (Hickman & Zoback, 1983). In formation integrity tests (FIT), cementation jobs (cem. pres.) or stimulation jobs, borehole pressure increases but the tests are typically stopped at a pre-defined pressure level before causing borehole damage. These tests are therefore important for limiting the minimum magnitude of S_h.

Based on the frictional strength of rocks, simple estimates of the effective stress magnitude (σ_h) can be made (Sibson, 1974). The the effective stress ratio of σ_h/σ_v at a lower limit of σ_h is in the frictional equilibrium of the tested lithology (Jaeger et al., 2007). The vertical stress can be easily calculated from the integration of the bulk density (Zoback, 2010). Drews et al. (2018) present a average overburden density of 2300 to 2500 kg m^{-3}. Assuming of hydrostatic conditions, the test results can be compared with lithological properties for a plausibility check of the measured S_h-magnitude (Figure 5.3).

5.3 DATABASE

Due to the extensive geothermal exploration in the greater Munich area, during drilling operations 75 borehole tests (FIT, LOT, Cementation Pressure, stimulation pressure) were recorded. For reasons of confidentiality and competition, the borehole are listed alphabetical as A - K. Pressure data has been carefully collected and analyzed from daily reports, final drilling reports, cementation reports or personal communications from the mining authority. In total there are 56 FIT, 15 Cem. Pres., one LOT with LOP, FBP and FPP and one stimulation pressure.

FIT are available from almost all wells for the casing shoe in the second and third section (Table 5.1). LOTs are not mandatory by the mining authority and involve the risk of undesired fracturing and intensive mud-losses. Therefore, these data are only available for the Unterhaching Gt1 well (K1). FIT and LOT are typically performed after cementation when a new casing shoe (CS) has been placed to check the planned mud pressure for the next section. When the cement plug is cured, a length of 10–20 m is drilled to access the next formation and perform the pressure test. With FIT and LOT, the borehole pressure is increased by closing the annulus and pumping mud at a constant flow rate into the borehole. The pressure at the top of the borehole is measured, which can be easily transferred to bottom hole pressure with the well mud weight assuming static conditions. For FIT, typically the borehole conditions during the maximum pressure period are listed in the drilling reports, while for LOT the entire pressure curve can be recorded and interpreted. Cementation also causes increased borehole pressure conditions, but measurement of wellhead pressure and interpolation to overall depth lead to a variety of systematic errors. More recent cement jobs additionally provide a dynamic and static pressure (Dyn. Cem./Stat. Cem.) based on pressure modeling with cement weight, injection pressure and fluid dynamics. The database of cementation jobs does not show any cement losses, which make them comparable with the FIT pressure data. Acid stimulation jobs typically do not provide a pressure signal, but for Unterhaching Gt1 (K1) pressure signal was recorded within the reservoir during a packered stimulation job.

Table 5.1 – Borehole tests, e.g formation integrity tests (FIT), leak-off tests (LOT), cementation pressure (Cem. Pres.) or stimulation pressure (Stim. Pres.) of A-and B-quality stress measurements.

Well	Type	TVD [m]	Stratigraphy	Lithology	S_h [MPa]	S_{hgrad} [MPa/km]	σ_h [MPa]	σ_v [MPa]
A1	FIT	957	UMM, Aquitan	Shale	16.2	16.9	5.80	11.17
A1	FIT	2187	UMM, Chatt	Shale	37.2	17.0	12.79	24.89
A2	FIT	973	UMM, Aquitan	Shale	16.5	17.0	5.18	10.60
A2	FIT	1008	UMM, Aquitan	Shale	15.8	15.6	4.00	10.98
B1	Cem. dyn.	750	OMM, low. Ottnang	Shale	12.2	16.3	4.12	8.83
B1	FIT	755	OMM, low. Ottnang	Shale	11.9	15.7	3.50	8.67
B1	Cem. dyn.	1702	UMM, Chatt	Shale	28.2	16.6	9.84	20.04
B1	FIT	1706	UMM, Chatt	Shale	26.9	15.8	7.49	19.08
B1	Cem. dyn.	2150	Purbeck	Limestone	29.6	13.8	7.90	26.78
B2	Cem. dyn.	750	OMM, low. Ottnang	Shale	12.2	16.3	4.12	8.83
B2	FIT	753	OMM, low. Ottnang	Shale	11.9	15.8	3.30	8.42
B2	Cem. dyn.	1600	UMM, Chatt	Shale	26.3	16.4	9.02	18.84
B2	FIT	1605	UMM, Chatt	Shale	25.2	15.7	6.59	17.63
B2	Cem. dyn.	2034	Purbeck	Limestone	28.9	14.2	8.77	25.74
D1	FIT	983	UMM, Aquitan	Sand \Limestone	15.1	15.4	4.20	11.28
D1	FIT	2154	UMM, Chatt	Sand \Limestone	32.1	14.9	7.99	24.51
D2	FIT	2174	UMM, Chatt	Sand \Limestone	32.5	15.0	7.99	24.52
E1	FIT	1884	UMM, Chatt	Sand \Limestone	30.7	16.3	12.23	24.03
E2	FIT	805	OMM, low. Ottnang	Shale \Sand	14.5	18.0	6.59	10.27
E2	FIT	1920	UMM, Chatt	Sand \Limestone	34.6	18.0	15.72	24.49
E2	FIT	3314	Purbeck	Limestone	51.4	15.5	18.86	42.26
F1	FIT	652	OMM, mid. Ottnang	Shale	9.7	14.9	2.83	7.80
F1	FIT	1638	UMM, Chatt	Sand \Limestone	25.3	15.5	6.85	18.48
F2	FIT	1801	UMM, Chatt	Sand \Limestone	32.3	17.9	11.99	20.32
G1	FIT	719	OMM, mid. Ottnang	Sand \Limestone	12.3	17.1	4.70	8.61
G1	FIT	1802	UMM, Chatt	Shale	29.1	16.2	8.99	20.50
G2	FIT	770	OMM, mid. Ottnang	Shale	12.8	16.7	4.30	8.84
G2	FIT	1915	UMM, Chatt	Shale	32.6	17.0	11.33	21.98
H1	FIT	635	OMM, mid. Ottnang.	Shale	10.8	17.0	3.60	7.10
H1	FIT	1651	UMM, Chatt	Shale	29.7	18.0	11.42	18.95
H1	FIT	2578	Purbeck	Limestone	46.4	18.0	11.13	29.34
H2	FIT	631	OMM, mid. Ottnang	Shale	10.7	17.0	3.73	7.24
H2	FIT	1662	UMM, Chatt	Shale	29.9	18.0	11.00	18.59
I2	FIT	2301	UMM, Chatt	Sand \Limestone	33.7	14.6	7.29	25.51
J2	FIT	619	OMM, mid. Ottnang	Sand \Limestone	8.7	14.0	2.10	7.41
J3	FIT	673	OMM, low. Ottnang	Shale	10.6	15.7	3.00	7.59
J4	Cem. dyn.	681	OMM, low. Ottnang	Shale	11.6	17.0	4.87	8.68
J4	FIT	684	OMM, low. Ottnang	Shale	10.6	15.5	3.00	7.85
J4	Cem. dyn.	1618	UMM, Chatt	Shale	27.0	16.7	11.10	20.64
J4	FIT	1621	UMM, Chatt	Shale	24.8	15.3	6.49	18.29
K1	FBP	825	OMM, low. Ottnang	Shale	14.0	17.0	5.70	10.28
K1	LOP	825	OMM, low. Ottnang	Shale	13.3	16.2	5.00	10.28
K1	FPP	825	OMM, low. Ottnang	Shale	12.9	15.6	4.55	10.28
K1	FIT	1345	UMM, Aquitan	Shale	21.3	15.9	8.00	17.02
K1	FIT	3022	upper Cretaceous	Shale	48.0	15.9	18.09	38.24
K1	Stim. Pres.	3234	upper Jurassic	Limestone	43.7	13.5	11.99	41.24

TVD- True vertical depth, S_h - minimal horizontal stress, σ_h - effective horizontal stress, σ_v - effective vertical stress

The majority of the pressure tests were performed at a depth of 500–1200 mTVD or 1500–2200 mTVD, respectively. Stratigraphically, these units are located at the Miocene Upper Marine Molasse (OMM) or the Oligocene Lower Marine Molasse (UMM). These layers are characterized on a local level by alternating sedimentary conditions from deep water clay to shelf sandstones (Figure 5.2). To better characterize the lithological situation during the tests, the lithology is subdivided into pure shale (green), a mixture of shale/marl/sand (yellow) or pure limestone (blue) based on the drilling reports (Figure 5.3).

Typically, the measured S_h-magnitude varies depending on the lithological characterization (Gunzburger & Magnenet, 2014; Wileveau et al., 2007) or pore pressure conditions (Zoback, 2010). To identify data that do not meet the lithological characterization and pore pressure conditions, we perform a plausibility check.

5.4 Results

5.4.1 Quality control and identification of outliers

Frictional limitation of S_h under consideration of characteristic friction coefficients of lithology and comparison with other tests under similar conditions, the test results are classified in A-, B- and C- quality. Tests with A- and B- quality indicate realistic stress values and C- quality indicates stress values that are disproved by stress measurements with higher values.

Figure 5.3 shows all stress measurements in a depth profile, each marked by its lithology (green - clay, yellow - sandstone and blue - limestone) and test type (cycle - FIT, cross - LOP, square - Cem. Pres. and star - stim. Pres.). For characteristic pore pressure conditions and friction coefficients between $0.2 < \mu < 0.6$ the frictional equilibrium defines the yellow curves for S_h. The data marked in red are classified with C- quality with low confidence.

The uppermost data, above 500 mTVD, are excluded from the database due to uncertain consolidation conditions in the Karpatian. The LOT at 825 mTVD from the Early Ottnangian with a shale-dominated lithology points to a S_{hgrad} of at least 16 MPa km^{-1} at an A- quality. Based on this stress measurement several Tests in C1, C2, F2, J1 and J3 were excluded due to low FIT.

In A1, A2 and D1 FIT data at about 1000 mTVD in the Aquitan with alternating shale and sand reveal a S_{hgrad} of ~17 MPa km^{-1}. With these tests the data from boreholes I1, I2, I3 and D2 at the same stratigraphy and lithology are excluded.

The data points in C1 (1260 mTVD), C2 (1340 mTVD), J1 (1460 mTVD) and J2 (1430 mTVD) for the middle Chattian could also be excluded, since the two FITs in H1 and H2 give a S_{hgrad} of ~18 MPa km^{-1} at 1650 mTVD under comparable lithological conditions. Within the Early Chattian, the test in well J3 (1700 mTVD) with a S_{hgrad} of 13 MPa km^{-1} was excluded from the dataset due to a FIT in J4 with 15 MPa km^{-1}.

Cementation jobs always specifies two pressure levels (static and dynamic). Due to the differences of the analyzed pressure level, the static cementation with low pressure are excluded from the database (see 1700 and 2150 mTVD at B1, 1600 and 2030 mTVD at B2). Note, cementation pressure in B1 (2150 mTVD) and B2 (2030 mTVD) were measured in the

lower Cretaceous in limestone dominated sections.

For the Upper Cretaceous, lower Cretaceous (Purbeck) and Upper Jurassic a total of 8 pressure tests exists. Two static cementation pressures were excluded from the database. Two tests in H1 and K1 were tested in a shale-rich lithology of the Upper Cretaceous and Purbeck, indicating a S_{hgrad} of 16–18 MPa km^{-1}. The sequences dominated by limestone have two dyn. Cem. each with 14 MPa km^{-1}, one stimulation with 13.5 MPa km^{-1} and one FIT with 15.5 MPa km^{-1}.

Note that the existing database of pressure tests are not primarily designed to measure S_h. Therefore, most tests are stopped far before the leak-off pressure is reached and do not provide high quality stress measurements. This analysis, which includes stratigraphic and lithological data, allows you to identify outliers and limit the database to 46 stress measurements with the highest reliability (Table 5.1).
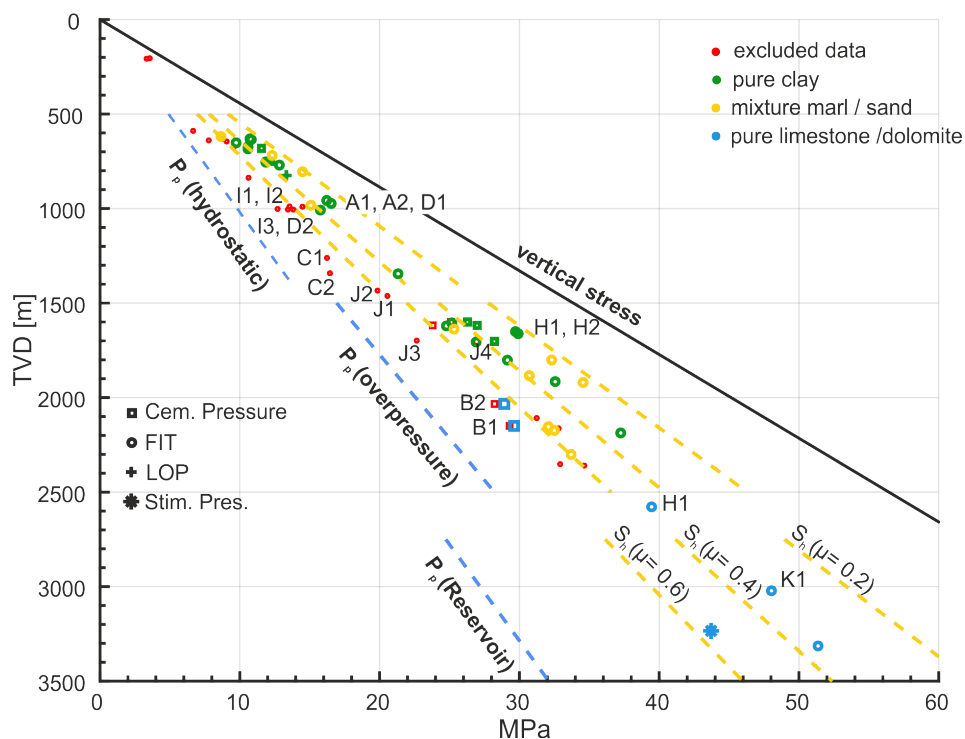
Figure 5.3 – Depth profile of the quality-checked stress data in relation to the frictional equilibrium. Red dots represents the excluded data points because the quality for the stress interpretation is insufficient. The measured stress magnitude is compared with the frictional equilibrium ($\mu = 0.2$, $\mu = 0.4$, $\mu = 0.6$) for hydrostatic ($TVD < 1500m$ / Miocene), overpressure ($1500m < TVD < 2500m$ / Oligocene) and under-hydrostatic conditions for the Lower Cretaceous and Upper Jurassic.

5.4.2 Stratigraphical variation of S_h

For each stratigraphical subunit (Ottnangian / Aquitan, Chattian and Cretaceous / Upper Jurassic) the S_h-magnitude can be calculated from frictional equilibrium with different friction coefficients, pore pressure and mean overburden density. Thus, the magnitude of S_h is evaluated for $0.2 \leq \mu \leq 0.8$, hydrostatically, slightly overpressured, under-hydrostatically and a mean overburden density of 2300 to 2500 kg m^{-3} (Figure 5.4). In the Ottnangian / Aquitan (Figure 5.4a) there is only one A- quality stress measurement of a LOP in the middle Ottnangian – at 16 MPa km^{-1}. Most of the FIT in this layer scatters around this value or

an even higher S_{hgrad} up to 18 MPa km^{-1}. Based on these results, the frictional strength of these layers can be determined in the range of $0.2 \leq \mu \leq 0.4$. Therefore, the minimum of S_{hgrad} is 16 MPa km^{-1}, but more realistic is 18 MPa km^{-1}.

With increasing depth and especially with decreasing distance to the Alpine thrust front the potential of overpressure increases (Drews et al., 2018; Drews et al., 2019b; Müller et al., 1988). Even in the area of Munich at the Chattian sequence a slight overpressure of 1.15 g cm^{-3} is observed (Drews et al., 2018). In Figure 5.4b the influence of such an overpressure in the Chattian on S_h is compared with the test results. The Upper and lower Chattians are dominated by shale, indicating a minimum S_{hgrad} of 15 to 17 MPa km^{-1}. The lithology in the middle Chattian is dominated by alternating sand and shale. Tests in this lithology scatter from 15 to 18 MPa km^{-1}, but there is no correlation between pore pressure and S_h.
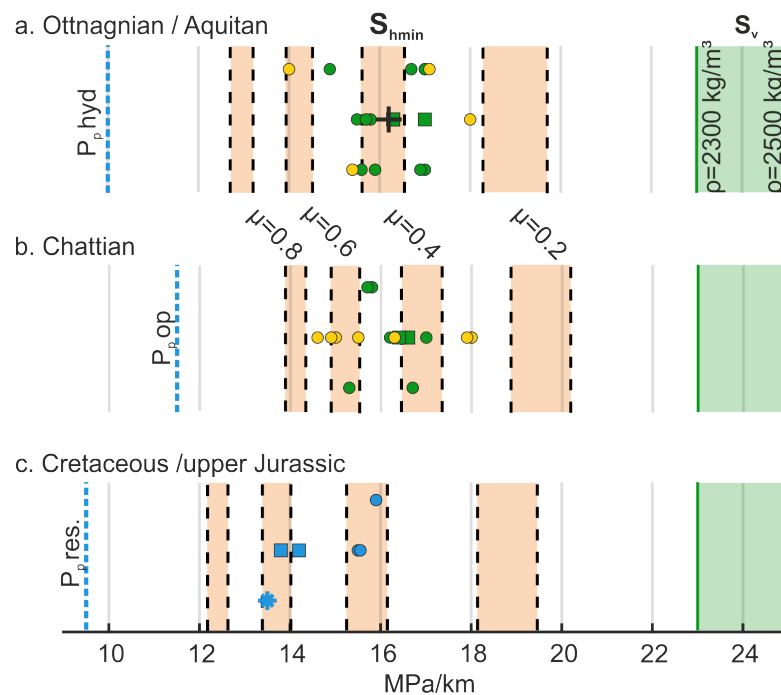
Figure 5.4 – Quality-checked stress data for the Miocene Ottnagnian / Aquitan, the Oligocene Chatt, the Upper Cretaceous and Upper Jurassic. The range of confidence of S_h for an overburden density interval of 2300 to 2500 kg/m³ and coefficients of friction of $\mu = 0.2$, $\mu = 0.4$, $\mu = 0.6$ and $\mu = 0.8$.

For the Upper Cretaceous only one FIT is available in a shale-dominated lithology at S_{hgrad} (15.9 MPa km^{-1}), which is comparable to the lower limit of S_h of the Chattian shales. In the limestone dominated lower Cretaceous (Purbeck) there are two cementation pressure from H1 and H2, indicating a minimum S_{hgrad} of 13.8 and 14.2 MPa km^{-1} and $\mu_{max} \sim 0.6$. In addition, there are two FITs from H1 and E2 that indicate a minimum S_{hgrad} of 15.5 MPa km^{-1} for a marl-rich carbonate and indicate $\mu_{max} \sim 0.4$. From the Upper Jurassic a packered stimulation pressure exists suggesting a minimum S_{hgrad} of 13.5 MPa km^{-1} and $\mu_{max} \sim 0.6$. In general, the increasing friction coefficient of limestone dominated rocks reduces the S_{hgrad} for frictional equilibrium. The tests allow to determine a minimum S_{hgrad} of ~ 14 MPa km^{-1} for dolomite dominated rocks and a minimum of S_{hgrad} of 15.5 MPa km^{-1} for marl-rich carbonates.

5.4.3 Lithological variation

The results of the plausibility checked database (Table 5.1) can also be analyzed as a function of their lithology-dependent friction coefficients. Figure 5.4 shows the effective horizontal (σ_h) and vertical stress (σ_v) for each test for pure shale (a), mixture of marl and sand (b) and pure limestone or dolomite (c). The pore pressure refers to the mud weight during the test and vertical stress to the average overburden density of $2300 \, \text{kg} \, \text{m}^{-3}$ (Drews et al., 2018).

The tests on pure shale lithologies show friction coefficients between 0.2–0.5 with an accumulation at $\mu = 0.4$ (Figure 5.4a). A- quality test of the LOP at the Unterhaching site, indicates a stress gradient of $16 \, \text{MPa} \, \text{km}^{-1}$ with $\mu \sim 0.4$. All tests excluded from the database (C- quality) indicate a small S_h-magnitude, as they were aborted at a predefined pressure level and therefore do not reach leak-off. These tests therefore result in a higher friction coefficient than tests that reach higher pressure. Within the Molasse sediments of the eastern Molasse Basin inter-layered clay minerals of smectite and illite are observed (Gier, 1998). Morley et al. (2018) suggests that the friction coefficient of smectite-rich shales is in the range of 0.1–0.3, but with increasing carbonate content friction coefficient may increase (Kohli & Zoback, 2013). Usually clay-rich lithologies of inter-layered smectite and illite have a friction coefficient of $0.2 \leq \mu \leq 0.5$. Thus, the database shows a much lower friction coefficient for the tests in the shale layers at 0.2–0.4 than generally suggested by Byerlee (1978) for crustal rocks. This would also affect the minimum S_{hgrad} of 15.5 to $19.8 \, \text{MPa} \, \text{km}^{-1}$ over the range of S_{vgrad} of $23–25 \, \text{MPa} \, \text{km}^{-1}$. Note that these values refer to hydrostatic conditions and frictional equilibrium. If the lithology is under maximum overpressure ($P_{pop} = 17 \, \text{MPa} \, \text{km}^{-1}$), the S_{hgrad} may reach a maximum value of $22 \, \text{MPa} \, \text{km}^{-1}$ ($\mu = 0.2$) or $20.4 \, \text{MPa} \, \text{km}^{-1}$ ($\mu = 0.4$).

Plausibility checked database for lithologies with marl and sand fractions show no cluster formation at certain friction coefficients (Figure 5.4b). Most tests come from the sandy sequence of the Chatt, where fine interlayers of clay and sand dominate. These tests do not reach any leak-off which result in a significant scatter of the tested pressure value. The friction coefficients of these tests vary between 0.2–0.6, whereas thin interlayers of clay or low pressure tests may influence the strong scatter.

Pressure measurements for carbonate (limestone and dolomite) dominated intervals are rarely available. In the Purbeckian limestone there are two cementation pressures and two FIT (Figure 5.4c). The cementation pressures scatter at an equivalent friction coefficient of 0.6, FIT at 0.4 and stimulation pressure at 0.65. Lithological logging indicate that limestoen and marl components dominate at the depth at which the FITs were tested.These changes my result in reduced rock friction. Whereas in the cementation jobs and stimulation job at pure limestone shows potentially higher friction coefficients. In addition, triaxial tests of Purbeckian rocks demonstrate friction coefficients of 0.4 and, for Upper Jurassic rocks, friction coefficients of 0.6 (Ameen et al., 2009; Tondera et al., 2013), both corresponding to our database.
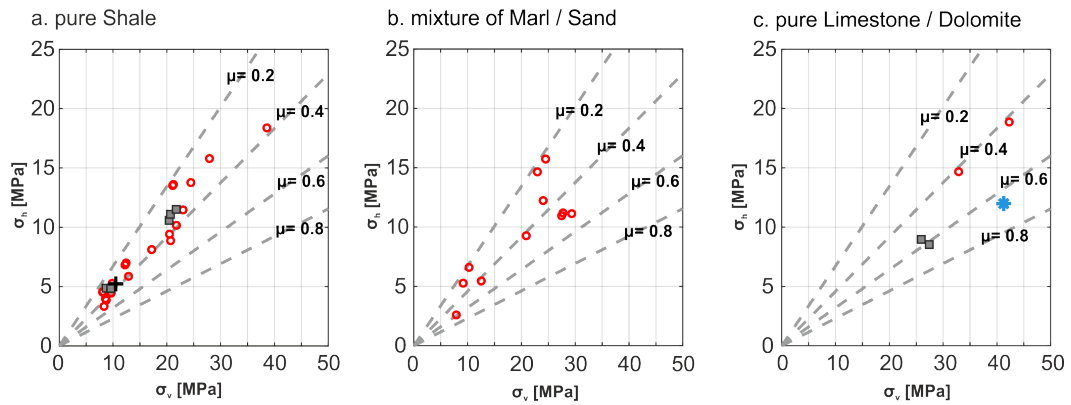
Figure 5.5 – Frictional strength and effective horizontal (σ_h) and vertical stress (σ_v) for pure shale in a., a mixture of marl and sand in b. and pure limestone or dolomite in c. Red circles identify formation integrity tests (FIT), gray square cementation pressure, blue star stimulation pressure and the black cross leak-off test data.

5.5 IMPLICATION FOR THE STRESS REGIME

All test data yield a minimum principle stress (S_1) that is less than the expected range of vertical stress (S_v). Thus a predominant thrust-faulting regime for the Cenozoic basin fill in the central part of the Molasse basin can be excluded, since S_v is always S_1 in the normal-faulting or S_2 in the strike-slip faulting regime. The analysis of the S_h-measurements points to a lithological control, which indicates a clear stiffness contrast between the clay-rich and the carbonate lithology. The friction coefficient for the clay-rich layers is in the range of 0.2–0.4 (Figure 5.5a) and for the carbonate-dominated layers at 0.6 (Figure 5.5c).

Applying the stress polygons based on the resulting friction coefficients provides a realistic range of differential stress for a normal-faulting (NF), strike-slip (SS) and thrust faulting regime (TF) (Figure 5.6). For clay-rich lithology, the leak-off test at Unterhaching Gt1 indicates a S_{hgrad} of 16.5 MPa km^{-1} at 825 mTVD. The stress polygon for $\mu = 0.4$ shows that this value is the lower limit where a normal-faulting or a transtensional stress regime exists (red dashed line Figure 5.6). The analysis of the complete pressure curve of the LOT at Unterhaching Gt1 can be used to determine the S_H-magnitude (Haimson & Fairhurst, 1970). So the magnitude of S_H at 825 mTVD is 15.1 MPa, S_v =19 MPa and the ratio of S_H/S_v = 0.79 (Drews et al., 2019a)(black star in Figure 5.6a). Such a stress ratio defines a normal-faulting stress regime within the Cenozoic sediments at 825 mTVD. The occurrence of Cenozoic normal faults in the central part of the Bavarian Molasse Basin (Hartmann et al., 2016) underpins that such a normal-faulting stress regime was present at least in the Miocene. Also the disequilibrium compaction trend of the overpressure data indicates a normal-faulting regime by vertical initiated loading (Drews et al., 2018; Drews et al., 2019b).

Stress measurements for the Cretaceous and Upper Jurassic carbonate lithology are only available in a few wells (Figure 5.4c), but they indicate a friction coefficient in the range of 0.4–0.6 (Figure 5.5c). Literature data support this range of friction coefficients (Ameen et al., 2009; Nicolas et al., 2016; Tondera et al., 2013), but also refer to the strong influence of marl components, which could be responsible for the low friction coefficient of 0.4 in Cretaceous rocks. Figure 5.6b shows the stress polygon for carbonates at 0.6 < μ < 0.8. In addition, the
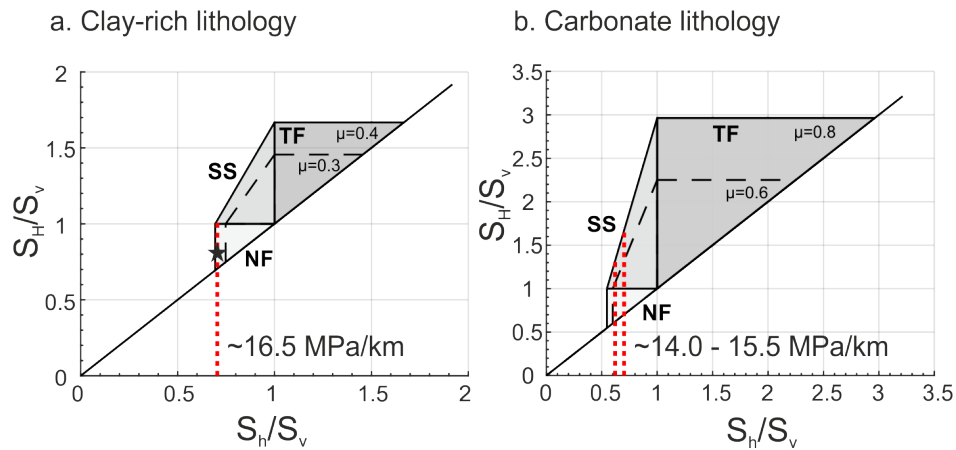
Figure 5.6 – Stress polygon with the fields for a normal-faulting (NF), strike-slip faulting (SS) and thrust-faulting (TF) stress regime for a clay-rich and the carbonate dominated lithology. a. Stress polygon for $\mu = 0.4$ and $\mu = 0.3$ with S_{hgrad} analyzed from the LOT at Unterhaching Gt1 at 825 mTVD (red line). The black asterisks represent the state of stress published by Drews et al. (2019a). b. Stress polygon for $\mu = 0.8$ and $\mu = 0.6$ with the S_{hgrad} interpreted from cementation and FIT data.

results of the cementation pressure ($14\,\text{MPa\,km}^{-1}$) and the FIT ($15.5\,\text{MPa\,km}^{-1}$) are shown in the red dotted lines. These lines demonstrate that under these conditions the state of stress could be a normal-faulting or strike-slip faulting regime (Figure 5.6b). Unfortunately, additional stress measurements are missing for the Cretaceous and Upper Jurassic. Budach et al. (2017) and Megies & Wassermann (2014) discusses such a transitional normal-faulting / strike-slip faulting stress regime, which is supported by the observed stress rotation at the Sauerlach site (Seithel et al., 2015).

A simplified model for the vertical variation of the stress regime in the central part of the Bavarian Foreland Molasse Basin suggests that it varies from a normal-faulting regime in the Cenozoic basin fill (as presented in this study and Drews et al., 2019a), into a transition zone (normal-faulting to strike-slip stress regime) in the sub-Molasse Mesozoic sediments (Budach et al., 2017; Seithel et al., 2015) to a strike-slip stress regime in the crystalline basement (Megies & Wassermann, 2014).

5.6 Conclusion

A detailed analysis of the available database of geothermal wells in the greater Munich area reduces the number of qualitatively good tests from 72 to 46. Most of the excluded tests indicate a lower pressure level at comparable lithology and depth. We could show that lithology significantly controls the S_h-magnitude. Most tests on the clay-rich Cenozoic layers indicates a minimum S_h of $16.5\,\text{MPa\,km}^{-1}$, which is in frictional equilibrium with $0.2 < \mu < 0.4$. A minimum S_{hgrad} of $15.5\,\text{MPa\,km}^{-1}$ is observed in the limestone to marl dominated Purbeck and a minimum S_{hgrad} of $14\,\text{MPa\,km}^{-1}$ at the Upper Jurassic. These S_{hgrad} are in frictional equilibrium with $0.4 < \mu < 0.6$. The database does not contain any test data where a significant influence of the overpressure can be proven. The stress field analysis results in a normal-faulting stress regime for the clay-dominated sequences at 825 mTVD in the central Molasse basin. The Upper Jurassic carbonate-dominated sequences

lack reliable stress measurements, but other studies suggest a normal-faulting to strike-slip faulting stress regime. As long as the database does not provide a better understanding of the stress field in the Cenozoic, Cretaceous and Upper Jurassic sequences, further studies are needed to capture the stress field with its variation in the Bavarian Molasse Basin.

6

STRESS ROTATION IN THE BAVARIAN MOLASSE BASIN INFERRED FROM BOREHOLE DATA AND NUMERICAL SIMULATION

This Chapter is in preparation for submission as Seithel, R., Niederhuber, T., Röckel, L., Müller, B. & Kohl, T. (2019b): Stress rotation in the Bavarian Molasse Basin inferred from borehole data and numerical simulation. – in: *preparation for submission.*

ABSTRACT

In the Munich area the favorable reservoir conditions of 100–$140\,\mathrm{l\,s^{-1}}$ flow rates at temperature levels reaching $140\,°\mathrm{C}$ are most favorable for the continuous development of geothermal utilization. In recent years, however, microseismicity has led to public concern and has initiated new scientific investigations. Besides the quantification of the regional stress components, it is essential to study the its local reorientation from the general N-S trend as an essential factor for the reactivation of microseismicity.

Borehole breakouts or drilling induced fractures have been used from image logs for evaluation of the stress orientation. The database of geothermal drillings in the Greater Munich Area contains 17 image logs. The evaluation of image log data from the Upper Jurassic reservoir shows a large number of compressive and tensile borehole failures with an good quality in 10 wells. Misfit gridding of these data identified significant counterclockwise local stress rotation whereas no stress rotation is indicated in other wells. In addition, analysis of the failure mechanism at 9 borehole intervals indicates a strike-slip stress regime.

Generic numerical modeling shows large stress rotations within weak fault structures with a clockwise orientation from the north. Stress reorientation magnitude at N015°E to N045°E oriented fault structures is higher than at N070°E to N090°E oriented fault structures, which trend more or less perpendicular to the regional maximum horizontal stress orientation. This study also underlines that no stress rotation at N025°E to N045°E trending faults indicates high differential stress conditions. Furthermore, the observation of stress reorientations in combination with numerical modeling and other geological borehole data supports the interpretation of the tectonic environment.

6.1 INTRODUCTION

In underground mining, the in-situ state of stress is crucial to understand the mechanical behavior of rocks, to ensure safe drilling operation, to improve the knowledge of the reservoir hydraulics and mitigate induced seismic events (Zoback, 2010). Evidence for horizontal tectonic stress rotation is seen on different spatial and temporal scales: Rotation of stresses on 100 km scale at old continental rifts, such as Brazil, due to density contrasts (Zoback & Richardson, 1996) and at the Peace River Arch due to stiffness contrast (Bell & Lloyd, 1989); for several fault structures in oil fields on a scale of several km (Yale, 2003) and borehole scale (Barton & Zoback, 1994). Temporal stress orientation and magnitude changes were observed in The Geyers (Martínez-Garzón et al., 2014) and Soultz-sous-Forêts (Schoenball et al., 2014), both linked to geothermal activities. As any deviation from a general stress trend can have a significant impact on the assessment of the stability of the underground technical operation (tunnels, drillholes etc.) or the seismic hazard, its quantification is decisive for the underground operations. In reservoir engineering it will have consequences on e.g. placement of secondary production wells or hydraulic fracture propagation (Nelson et al., 2005; Zoback, 2010)

The stress field is evaluated on global scale (Heidbach et al., 2018), on basin scale (Kastrup et al., 2004; Reinecker et al., 2010; Reiter & Heidbach, 2014) or on local reservoir scale (Lin et al., 2010; Seithel et al., 2015; Zhang et al., 1994). Any analysis of the stress orientation patterns highlights typically the variation of S_H on a regional or local scale (Heidbach et al., 2007; Zoback, 1992). The stress field is typically determined by the three principal stress magnitudes S1, S2 and S3 and their alignment (Jaeger et al., 2007). In a normal-faulting stress regime the vertical stress (S_v) is maximum with the two minor horizontal stress components ($S_v > S_H > S_h$). Similarly, thrust faulting stress regimes ($S_H > S_h > S_v$) or strike−slip stress regime ($S_H > S_v > S_h$) were defined (Anderson, 1951). The tectonic regime can provide limitations on the differential stresses ($S1 − S3$), beeing particularly important for fault reactivation.

Fault zones typically consist of a centered, localized core and a broad damage zone with different strengths than the surroundings (Billi et al., 2003; Childs et al., 1996; Gudmundsson et al., 2010; Michie et al., 2014; Sibson, 1977). The increasing permeability is focused within the highly fractured damage zone (Agosta & Kirschner, 2003; Caine et al., 1996) with reduced strength (Bauer et al., 2015; Faulkner et al., 2010; Faulkner et al., 2003; Heap & Faulkner, 2008).

Basic explanations for stress heterogeneities in the vicinity of geological structures are provided by Martin & Chandler (1993) and Yale (2003). Sonder (1990) and Zoback (1992) discuss the influence of material contrasts, geometry and differential stress quantities on the stress reorientation at a geological structure by superposition of regional stress and local stress fields. Several studies focus on the boundary effects at lateral discontinuities or at fault tips where significant local stress rotations and stress concentrations are present (Homberg et al., 1997; Sassi & Faure, 1997; Spann et al., 1994; Su & Stephansson, 1999).

Here we examine the Greater Munich Area for stress rotation due to its impact on possible seismicity. The investigations take into account natural stress reorientations e.g.
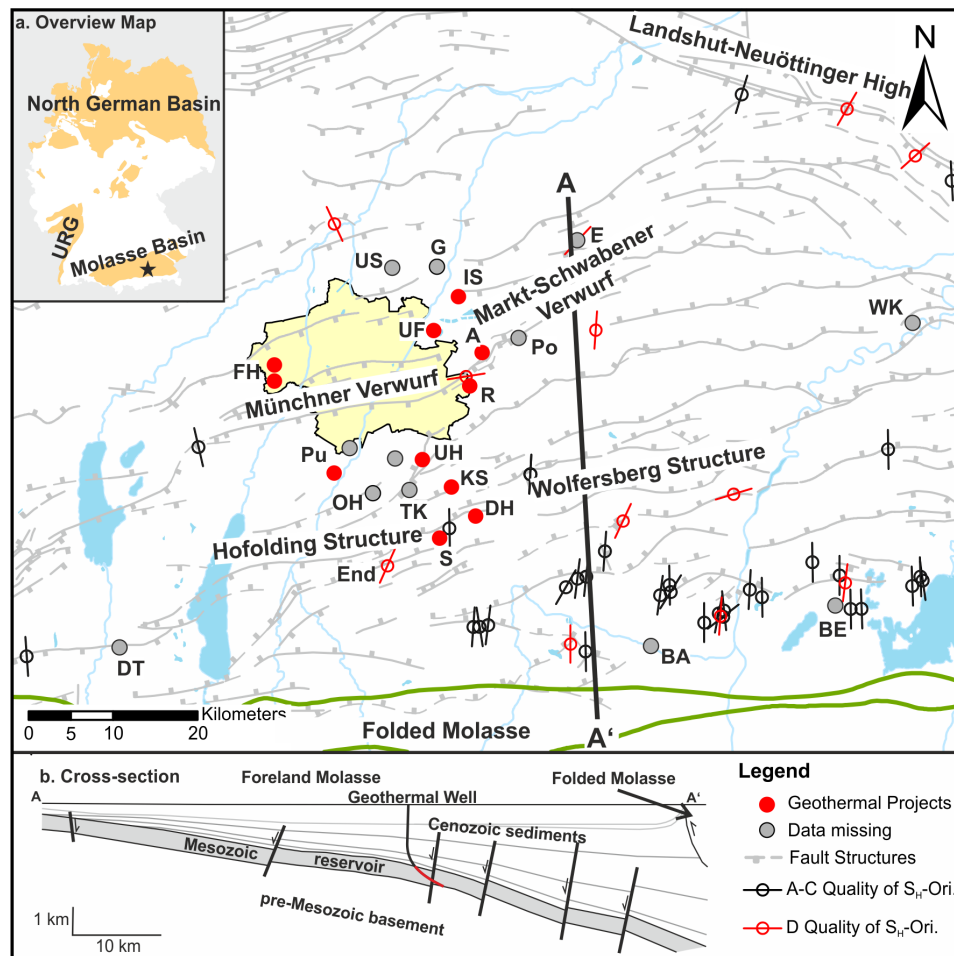
A- Aschheim, BA- Bad Aibling, BE- Bad Enddorf, DT- Dietlhofen, DH- Dürrnhaar, E- Erding, End- Endlhausen, FH- Freiham, G- Garching, IS- Ismanning, KS- Kirchstockach, OH- Oberhaching, PO- Poing, PU- Pullach, S- Sauerlach, TK- Taufkirchen, UF- Unterföhring, UH- Unterhaching, US- Unterschleißheim, WK- Waldkraiburg

Figure 6.1 – Map of the locations of geothermal projects in the Greater Munich Area for image log evaluation. Grey lines show the fault structures from the Geothermal Atlas (STWIVT, 2010). The stress symbol marks the S_H-orientation from the World Stress Map (WSM) (Reinecker et al., 2010) with A-C quality (black symbols) and D quality (red symbols). Points locate geothermal projects, red for available image logs in the Upper Jurassic and grey if no data is available. a. Overview map of the geothermal provinces in Germany. b. Cross section of the Bavarian Molasse Basin (modified according to Reinecker et al. (2010)). It shows the typical well path of the geothermal wells with the open-hole section in red in the Mesozoic Upper Jurassic reservoir.

at the location of the geothermal project of Sauerlach (Seithel et al., 2015), whereas the potential for induced stress reorientations is discussed in Seithel et al. (2019a). The Greater Munich Area is the most developed region in Germany for geothermal use. In total, there are 17 projects that produce geothermal brine from the Upper Jurassic reservoir for district heating or electricity generation with a flowrate of 80–140 l s^{-1} and a temperature level of 80–150 °C. In most projects, fault zones as well as reef and basin structures in the Upper Jurassic geothermal reservoir are the most important well targets (Figure 6.1b), which have been identified as key geological features for local stress reorientation (Faulds et al., 2011; Gudmundsson et al., 2010).

In this study, we present the new stress database that includes 17 geothermal wells in the Greater Munich Area. This characterization aims at supporting the future developments by quantifying the effects of stress orientation and magnitude within the Upper Jurassic

reservoir in the Bavarian Molasse Basin. By using numerical approaches these can be discussed in terms of geometry, material contrast and differential stress magnitude. In order to study the stress field and to understand possible effects, the method of stress field interpretation based on the image log data is explained and the database is described in detail (Chapter 6.3). Subsequently, the results of the stress field interpretation in relation to the determination of the stress field rotation in the Upper Jurassic are briefly explained (Chapter 6.4). Furthermore, a numerical model with a heterogeneous zone (Chapter 6.5) allows to describe such a stress field rotation. On the basis of this numerical approach, the results of the stress field analysis of borehole data could be discussed (Chapter 6.6), which provides further information of the stress field characteristic.

6.2 TECTONIC SETTING

The Greater Munich Area is located in the Bavarian foreland basin, where the Upper Jurassic hydrothermal reservoir dip to the south and reaches a depth of 2000 m (near Munich) – 4000 m (south of Munich). The geothermal reservoir was formed as a carbonate platform with reef and basin structures ensuring the high flow rates of the numerous geothermal projects (Boehm et al., 2012; Meyer & Schmidt-Kaler, 1989). In the course of the Alpine thrust, the carbonate platform was lowered by the formation of fault structures (Bachmann & Müller, 1992; Frisch, 1979) and a regional accumulation of the Cenozoic deep-water sediments (Ziegler, 1995).

Most fault structures in this area are normal faults aligned parallel to the Alpine orogen (Bachmann & Müller, 1992). In the Greater Munich Area fault structures are mainly dominated by the ENE-WSW trend, but can vary locally to a NNE-SSW trend (e.g. Unterhaching) (Figure 6.1).

A basin-wide stress field characterization, mostly within the Cenozoic sediments, shows a consistent N000°E S_H-orientation (Figure 6.1) over the entire Bavarian Molasse Basin (Reinecker et al., 2010), while at the Sauerlach site local stress field anomalies within the Upper Jurassic reservoir could be detected (Seithel et al., 2015). A simplified model for the vertical variation of the stress regime in the central part of the Bavarian Foreland Molasse Basin suggests a normal-faulting stress regime in the Cenozoic basin fill up to 2–3 km (Drews et al., 2019a). This regime may have changed to a transitional zone from normal-faulting to strike-slip stress regime in the Upper Jurassic reservoir (Budach et al., 2017; Seithel et al., 2015) and a strike-slip stress regime in the crystalline basement (Megies & Wassermann, 2014). Lack of reliable S_h data at the geothermal reservoir has let to estimating a stress gradient of S_h-gradient of 15 MPa km^{-1} (Seithel et al., 2015). Compaction trend studies of the Cenozoic filling show an average overburden density of 2300 kg m^{-3}, corresponding to a S_v-gradient of 23 MPa km^{-1} (Drews et al., 2018).

During the geothermal development in the recent years, the image log database has been greatly extended. This offers the possibility to investigate stress components (Brudy & Zoback, 1998; Moos & Zoback, 1990; Peska & Zoback, 1995; Wiprut & Zoback, 2000a), stress anomalies (Seithel et al., 2015) or the interaction of fault strength contrast with stress field anomalies (Sahara et al., 2014).

6.3 Data analysis

6.3.1 Geomechanical log interpretation

Electrical borehole imaging provide detailed information about the failure of wells used to assess stress orientation and magnitude at depth. The borehole wall may show failure in compression as well as tension, depending on the deviation of the borehole from vertical, the in-situ stress field and the lithological units (Barton & Moos, 2010). Compressional failures, mainly referred to as breakouts (BO), are observed as blurry, conductive, symmetrical elements on the electrical image logs indicating borehole enlargements (Bell, 1996). Drilling induced tensile fractures (DITF) are axially symmetric parallel to the borehole axis and drilling enhanced natural fractures (DENF) are relatively short segments of fine-aperture natural fractures that are not visible as complete sinusoidal traces (Barton & Moos, 2010). These elements are stress indicators that arise when the minimal tangential stress on the borehole wall is less than the tensile strength of the rock (Brudy & Zoback, 1998). Breakouts occur when the maximum tangential stress exceeds the rock strength (Zoback et al., 1985). These features indicate the orientation α at the borehole wall for compressive and tensile failure which is measured in highly inclined wells from top of hole (TOH).

Table 6.1 – Summary of stress indicator data for compression (Breakout) and tensile wellbore failure – Drilling induced Tensile Fractures (DITF) and Drilling-enhanced natural fractures (DENF) – from 17 logging intervals within the Upper Jurassic. Note, the high borehole inclination implies the stress indicator orientation (α) relative to TOH. The data marked with grey indicate a total length (ΣL) >35 m and a standard deviation (σ_{st}) < 20° that meets the requirements for at least A - C class from the quality ranking of the WSM catalog for image log interpretation (Tingay et al., 2016).

Well	Depth [mTVD]	BO ΣL [m]	α [TOH]	σ_{st}	ω_{bo}	Quality	DITF No.	α [TOH]	σ_{st}	DENF No.	α [TOH]	σ_{st}	Total Tensile Failure ΣL [m]	Quality
A1	2112–2591	28	17°	25°	30°	C	64	105°	18°	17	121°	18°	40.5	**B**
DH1	3491–3926	–	–	–	–	–	–	–	–	33	65°	14°	16.5	D
DH2	3526–4114	35	83°	9°	28°	**C**	30	19°	20°	–	–	–	15	D
FH1	2150–2518	19	129°	22°	29°	D	–	–	–	10	175°	4°	5	D
FH2	2018–2447	–	–	–	–	–	170	12°	12°	31	177°	8°	100.5	**A**
IS1	1886–2195	–	–	–	–	–	–	–	–	–	–	–	–	–
IS2	1765–1906	–	–	–	–	–	–	–	–	–	–	–	–	–
KS1	3330–3837	106	89°	6°	34°	**A**	87	18°	26°	226	176°	37°	156.5	D
KS2	3352–3787	63.5	114°	14°	29°	**B**	106	66°	22°	9	71°	25°	57.5	C
PU3	2968–3505	–	–	–	–	–	83	11°	36°	–	–	–	41.5	D
R2	2509–2746	–	–	–	–	–	85	105°	23°	–	–	–	42.5	C
S1	3739–4177	141	114°	14°	36°	**A**	82	41°	21°	394	28°	13°	238	B
S2	3571–4086	40	92°	14°	40°	B	823	172°	10°	492	174°	11°	657.5	**A**
S3	3872–4430	3.5	105°	13°	33°	D	178	180°	22°	676	177°	33°	427	D
UF1	1943–2512	9	135°	4°	26°	D	–	–	–	384	25°	12°	192	**A**
UF4	2011–2335	46	97°	18°	30°	B	85	2°	14°	9	1°	8°	47	**B**
UH2	2956–3577	65	103°	24°	29°	C	37	9°	12°	42	8°	11°	39.5	**B**

A – Aschheim, DH – Dürrnhaar, FH — Freiham, IS — Ismaning, KS — Kirchstockach, PU – Pullach, R – Riem, S – Sauerlach, UF – Unterföhring, UH – Unterhaching

Peska & Zoback (1995) describe the effective stress conditions at the borehole wall in deviated wells with a tensor transformation from the Cartesian to the cylindrical coordinate system. The technique for inverting the orientation and magnitude of S_H from the observation and geometry of wellbore failures was presented in earlier studies (Davatzes & Hickman, 2010; Sahara et al., 2014; Schoenball et al., 2016; Schoenball et al., 2017; Seithel et al., 2015; Zajac, 1997). In this study, we use the misfit-gridding technique of Seithel et al. (2015) to identify a stress field rotation. Here the mean value of the square roots of

the directional differences of the observed vs. modeled stress is calculated for the total number of stress indicators of a borehole. This value indicates the quality described here as mis-fit with small values (white) and high values (black) for a selected S_H-orientation and S_H/S_v-magnitude. For the gridding technique stress range (S_H/S_v), limited by the stress polygon, and the S_H-orientation are varied, resulting in a mis-fit distribution indicating the "best" solution with white colors (Figure 6.2).

In addition, the stress indicators described above allow reservoir stresses to be determined by modeling the effective stress conditions on the borehole wall and comparing them with compression or tension borehole failure (Barton & Moos, 2010; Peska & Zoback, 1995; Wiprut & Zoback, 2000a). Compression failure indicates stress conditions exceeding the rock strength (UCS). Thereby, the maximum horizontal stress can be estimated from the observed breakout width (ω_{bo}). Tensile failure is indicative of stress conditions that reach tensile rock strength (T_o) as a function of the thermal conditions in the borehole. On this basis, characteristic curves for compression and tensile failure can be drawn into the stress polygon (Zoback, 2010). These curves can be plotted for several estimations of UCS given a range of stress magnitude (Figure 6.3a). At the intersection point of the curve for compressional and tensile failure both conditions are fulfilled and the local stress magnitude in reservoir depth can be determined (Wiprut & Zoback, 2000a) (Figure 6.3b).

6.3.2 Data base

The locations of the available Image log data from geothermal wells in the Greater Munich Area are shown in Figure 6.1. In the central part of Munich, e.g. at Ismaning site (IS), Unterföhring site (UF), Freiham site (FH), Aschheim site (A) and Riem site (R), the Upper Jurassic reservoir is at 2000–2500 mTVD (Table 6.1). The boreholes south of the "Münchner Verwurf" e.g. at Dürrnhaar site (DH), Kirchstockach site (KS), Pullach site (PU), Sauerlach site (S) and Unterhaching site (UH) reach the Upper Jurassic reservoir at 3000–4000 mTVD (Table 6.1). In total, electrical image logs from 17 wells in the Greater Munich Area are available for the interpretation of BO, DITF and DENF (Table 6.1). The borehole failure zones are subdivided into individual 0.5 m long intervals and describe a circumferential alignment of borehole failure at the borehole wall (α) from Top of Hole. Based on the total length (ΣL) and the standard deviation (σ_{st}) of the complete stress indicators of each well, the results of the stress interpretation can be classified into A-, B-, C-, D- or E-quality of the WSM catalog ranking system for image log interpretation (Tingay et al., 2016). To ensure the quality of the stress interpretation, only borehole failure data of at least B/C quality corresponding to $\Sigma L > 35$ m and $\sigma_{st} < 20°$ are used. For 10 wells, the interpretation of stress indicator meets this criterion (data set marked in gray in Table 6.1). Tensile failure occurs with A- quality in FH2, S2 and UF1 and B- quality in A1, UF4 and UH2. In comparison, S1 and KS1 show compressive failure with A- quality, KS2 with B- quality and DH2 with C-quality.

6.4 STRESS PATTERN

6.4.1 STRESS ORIENTATION

For the stress inversion the compressive and tensile failures are considered separately and only the dataset with the higher quality is used for each borehole. Figure 6.2 shows the results at the 10 wells of breakouts (DH2, KS1, KS2, S1) and DITF / DENF (A1, FH2, S2, UF1, UF4, UH2) using the misfit-gridding that indicates the stress regime and S_H-orientation for minimum misfit (white colors). In Figure 6.2a for A1, the minimum mis-fit is at N000°E and N180°E S_H- orientation, both indicating a N-S oriented stress field. But in Figure 6.2b for DH2, the minimum mis-fit is at N160°E S_H- orientation, indicating a counter clockwise stress rotation from the regional N-S oriented stress field. On one hand A1, FH2, S2, UF1 and UH2 confirm the N000°E S_H-orientation, on the other hand DH2, KS1 and UF4 observe a 15° counterclockwise reorientation. An S_H rotation of 30° counterclockwise is observed at S1 and even an S_H-rotation of 60° counterclockwise at KS2.
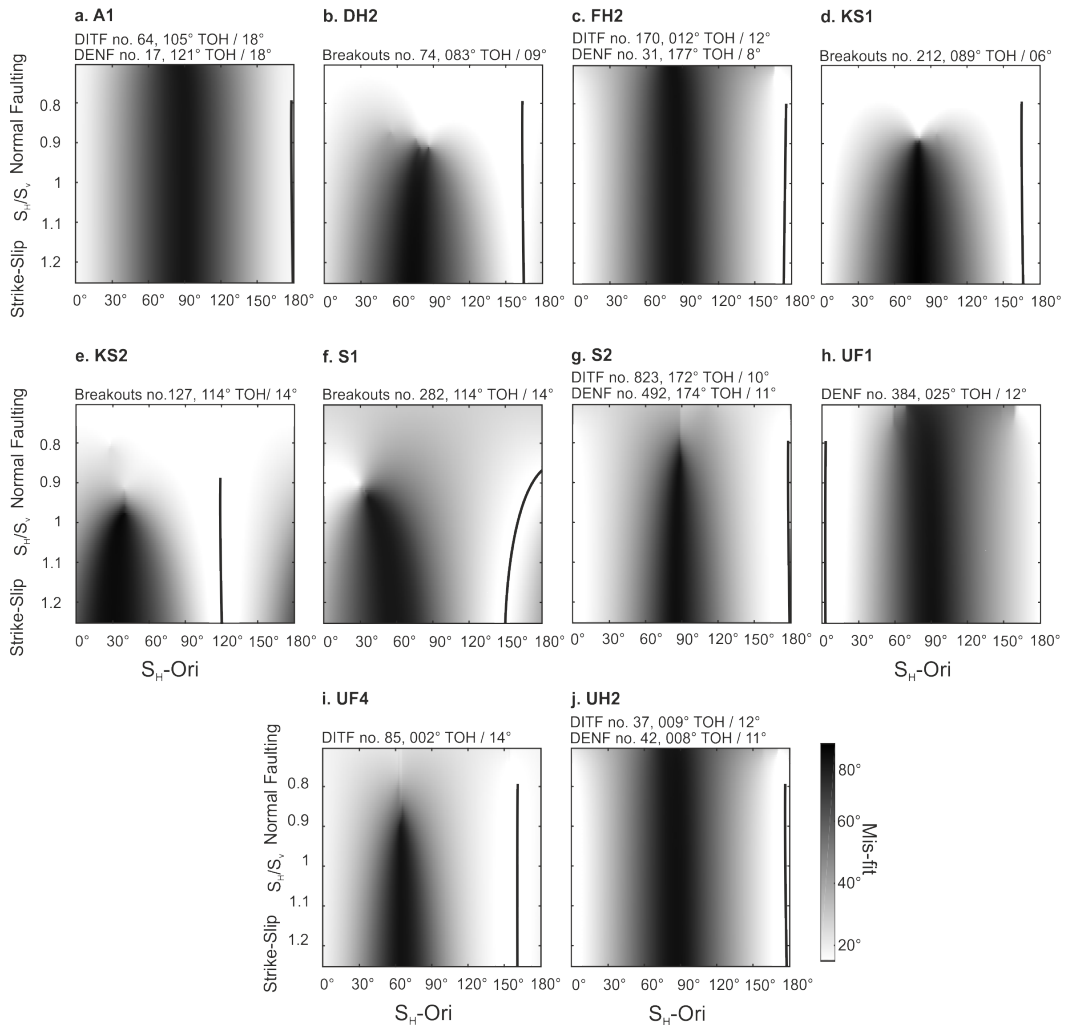
Figure 6.2 – Misfit grid results of the data set with good data quality (wells marked with grey in Table 6.1). The white to grey colors indicate low to high misfit values for a stress magnitude (S_H/S_v 0.7 − 1.25) and S_H-orientation (N000°E to N180°E). The ratio of S_H/S_v indicates a stress change from a normal ($S_H/S_v < 1$) to strike-slip stress regime ($S_H/S_v > 1$) and the S_H-orientation clockwise from north. The black line indicates the state of stress for the minimal misfit of the observed stress indicators and the modeled stress orientation.

6.4.2 STRESS MAGNITUDE

The estimation of stress magnitude requires identifying depth intervals with a uniform borehole orientation and a high quality of stress indicators. A total of 9 intervals of sufficient quality (> 25 borehole failures with a standard deviation (σ_{st}) less-than 15° (Table 6.2) are identified from DH2, KS1, KS2, S1 and S2. For these intervals, the mean breakout width (ω_{bo}) is between 26° to 40° and the interval length between 60 to 420 m (Table 6.2). In total, there are six intervals in which compression failure (DH2 – 3930 m & 4230 m, KS2 – 3950 m & 4210 m, S1 – 4130 m & 4295 m) and three intervals (KS1 – 3950 m, S1 – 4495 m , S2 – 4135 m) are observed with both compression and tensile failure beeing predominant.

Table 6.2 – Intervals of high quality stress indicators (σ_{st} < 15° & No. > 25) for the calculation of the stress magnitude. Unique observation of breakouts, compressive failure (Comp.) determine a stress range for frictional equilibrium μ = 0.8 and S_h/S_v = 1; Parallel observation of breakouts, DITF and DENF describing compressive (Comp.) and tensile (Tens.) failure.

Well	Mean Depth [mMD]	Length [m]	Fail. Mech.	Breakouts No.	σ_{st}	ω_{bo}	DITF No.	σ_{st}	DENF No.	σ_{st}	Stress Magnitude S_H/S_v 100 MPa	120 MPa	140 MPa
DH2	3930	60	Comp.	34	7°	26°	–	–	–	–	1.16–1.30	1.28–1.41	1.39–1.52
	4230	60	Comp.	30	6°	29°	–	–	–	–	1.11–1.29	1.22–1.39	1.35–1.48
KS1	3990	420	Comp. & Tens.	190	6°	35°	56	5°	91	10°	1.20	1.31	1.45
KS2	3950	190	Comp.	92	10°	30°	–	–	–	–	1.17–1.27	1.26–1.35	1.35–1.42
	4210	300	Comp.	28	10°	28°	–	–	–	–	1.15–1.27	1.23–1.37	1.32–1.43
S1	4130	260	Comp.	175	13°	36°	–	–	–	–	1.15–1.36	1.30–1.45	1.42–1.56
	4295	80	Comp.	80	13°	36°	–	–	–	–	1.11–1.30	1.24–1.40	1.36–1.49
	4495	330	Comp. & Tens.	26	9°	31°	-	-	323	14°	1.11	1.23	1.35
S2	4135	230	Comp. & Tens.	51	15°	40°	141	12°	–	–	1.22	1.40	1.55

DH – Dürrnhaar, KS – Kirchstockach, S – Sauerlach
Stress magnitude is based on an uniaxial compressive stress (UCS) (100 MPa, 120 MPa and 140 MPa) and breakout width (ω_{bo} = 30°) and tensile strength (T_0 = 0 MPa)

The stress calculations at the borehole wall are carried out for deviating boreholes according to the approach presented in Peska & Zoback (1995) and Wiprut & Zoback (2000a). This enables the modeling of compression failure based on the Mohr-Coulomb failure criterion with an average observed breakout width of ω_{bo} = 30° (Table 6.2), μ_{int} = 0.8 and an uniaxial strength (UCS) in the range of 100–140 MPa (Tondera et al., 2013) (Figure 6.3a/b). Each red line in Figure 6.3a represents the stress state for an assumed UCS. Typically, the fissured rock mass has no tensile strength (T_0 =0 MPa), resulting in the blue line for tensile failure in Figure 6.3b/left. When both types of failure are observed at an interval, the intersection (red dot) of the compression and tension failure lines describes the magnitude of reservoir stress (Figure 6.3b/right).

In Figure 6.3a, the left stress polygon describes the stress magnitude for compression failure (red dashed line) of the interval of KS2 at a depth of 3950 mMD. Figure 6.3a/right shows the S_H/S_v- ratio for those six intervals for UCS of 100 MPa in the range 1.11–1.36 (white area), for UCS of 120 MPa in the range 1.22–1.41 (light gray) and at UCS of 140 MPa in the range of 1.32–1.56 (gray) (Table 6.2). Figure 6.3b/left shows the result of compression and tension failure in the stress polygon for the interval S1 – 4495 m. The intervals at KS1 – 3990 m, S1 – 4495 m and S2 – 4135 m show an S_H/S_v- ratio in the range of 1.11–1.22 (UCS = 100 MPa), 1.23–1.40 (UCS = 120 MPa) and 1.35–1.55 (UCS = 140 MPa) (Figure 6.3b/left).

According to Anderson (1951) the analysis of the stress magnitudes allows the estimation

of the tectonic stress regime. From the interpretation of the borehole failure interpretation for the nine considered intervals, a strike-slip faulting regime with of S_H/S_v ratios between 1.11 and 1.56 can be derived (Figure 6.3). The vertical stress gradient of 23 MPa km^{-1} (Drews et al., 2018; Drews et al., 2019b; Seithel et al., 2015) and the ratio of $S_h/S_v = 0.65$ (Seithel et al., 2015) give an absolute S_h-magnitude at 4000 mTVD of 60 MPa. In addition, the results of this study show an S_H in the range from 102 to 143 MPa and a horizontal differential stress ($S_H - S_h$) between 42–83 MPa.
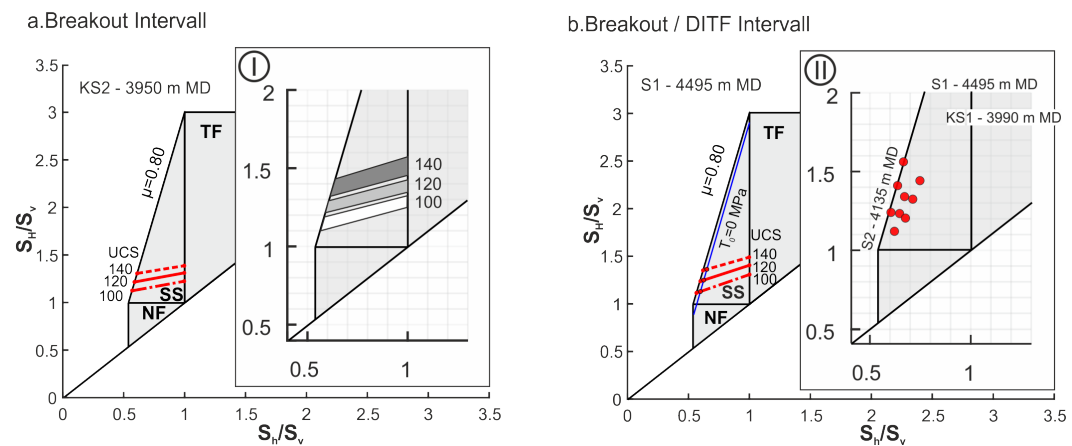
Reference Parameters: $S_{v\ grad.} = 23$ MPa/km, $\omega_{bo} = 30°$, $v = 0.25$, $E = 40$ GPa, $\alpha_T = 1 \times 10^{-6}$ 1/K, $T_{inj.} = 30\,°$C, $T_{grad.} = 0.03$ K/m

Figure 6.3 – Stress magnitude in the Upper Jurassic reservoir, calculated from (a.) compression failure intervals and (b.) compression and tension failure intervals. According to Wiprut & Zoback (2000a), curves for compression and tension failure on the borehole wall can be drawn in the stress polygon on the basis of $\mu = 0.8$. For Breakout intervals the red lines for the stress states are drawn (a. & b.) under the compression failure using the Mohr-Coulomb criterion for a breakout width ($\omega_{bo} = 30°$), $\mu = 0.8$ and various uniaxial compressive strengths (UCS) (100 MPa, 120 MPa, 130 MPa). Blue lines describe the stress state when the minimum tangential stress is less than the tensile strength ($T_0 = 0$ MPa) and Drilling Induced Tensile Fractures (DITF) and Drilling Enhanced Natural Fractures (DENF) occur. The insert Figure I shows the stress range for compression failure for all intervals (Table 6.2) based on UCS = 100 MPa (white area), UCS = 120 MPa (light grey area) and UCS = 140 MPa (grey area). Inlay Figure II shows the intersection point (red dot) for compression and tensile failure for UCS = 100 MPa, 120 MPa and 140 MPa.

6.4.3 OBSERVATION OF STRESS ROTATION

Seithel et al. (2019a) cites stress rotation as one possible effect for the reactivation of existing fault structures in the Bavarian Molasse Basin. In the central part of the Bavarian Molasse Basin, the available information is mainly available from oil drilling in the 1950s and 1960s, which concentrated on the Cenozoic sediments (Figure 6.4b). This depth limitation is responsible for the current gaps in knowledge about the stress field in the Upper Jurassic reservoir. However, the newly added geothermal database provides image log data from the reservoir section of 17 boreholes in the Greater Munich Area. After a quality control, an extraordinary database for stress interpretation is available for ten wells.

Interestingly, compressive and tensile failures show a strong depth dependency, i.e. BO are usually observed at depths below 2800 mTVD (DH2, KS1, KS2, S1, S2, UH2) and DITF at shallower depth intervals (A1, FH2, UF1, UF4) (Figure 6.4b). Therefore, the in-situ stress magnitude from 2800 mTVD is large enough to cause compressional borehole failure. Frequently observed total mud losses in the Upper Jurassic reservoir and the replacement

of mud by pure water dramatically change the temperature conditions. Such processes reduce the tangential stress and can result in thermally amplified tensile borehole failure (e.g. A1, DH2, KS1, KS2, PU3, R2, S3) (Brudy & Zoback, 1998).

The wells with A-C quality of the WSM database show a consistent N000°E S_H-orientation within the Cenozoic sediments (Figure 6.4b). Stress interpretations within Mesozoic sediments from the WSM database exists for Endlhausen 1 (S_H-dir. N024°E / D-quality), Erding1 (S_H-dir. N043°E / D-quality) and Riem2 (S_H-dir. N082°E / D-quality) (Figure 6.1, which have only a D- quality and indicate a heterogeneous stress orientation (Reinecker et al., 2010). Our data from DITF and DENF at A1, FH2, S2, UF1 and UH2 also show a N000°S ± 15° S_H-orientation (Figure 6.4a). However, BO data (DH2 and KS1) and DITF (UF4) describe a counterclockwise stress rotation of 15° (N165°E). The BO data in S1 show a counterclockwise stress rotation of 30° (N150°E) and in KS2 of 60° (N120°E) (Figure 6.4a). This changes the homogeneous N-S S_H-orientation from the interior of the Cenozoic sediments to a heterogeneous S_H orientation within the Upper Jurassic reservoir (Figure 6.4b).

Stress rotation is predominantly related to heterogeneous reservoir structures characterized by density contrasts or variation of mechanical parameters (Sonder, 1990; Zoback, 1992). The inner structure of the Upper Jurassic consists of non-uniformly distributed petrophysical parameters due to an variation of porous reef, laminated basin sediments (Meyer & Schmidt-Kaler, 1989) and fault structures with high fracture density (Heap & Faulkner, 2008; Sahara et al., 2014). Such local material heterogeneities influence the characteristic of the stress field in the environment or within these structures (Sahara et al., 2014; Yale, 2003). These heterogeneities and the associated influence of stress rotations are investigated in detail below by numerical modeling.
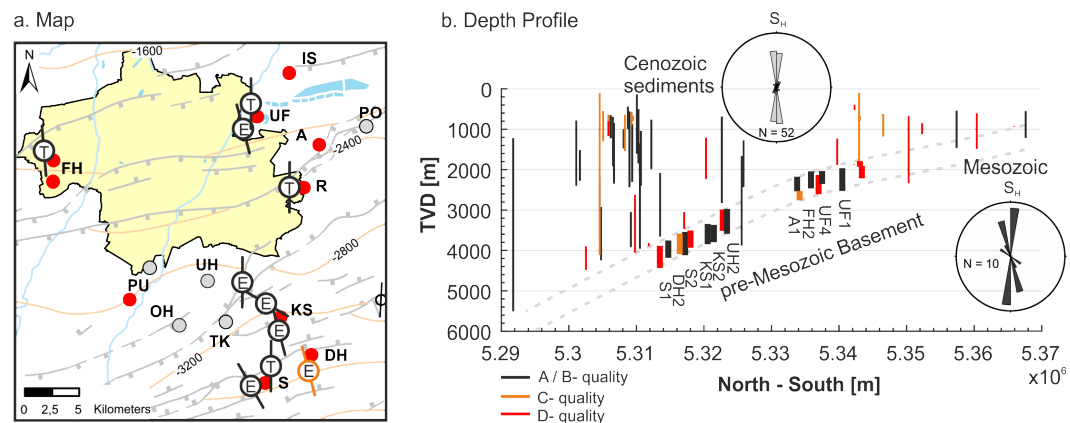
A-Aschheim, DH- Dürrnhaar, FH-Freiham, G- Garching, IS- Ismanning, KS- Kirchstockach, OH-Oberhaching, PO- Poing, PU-Pullach, S- Sauerlach,TK- Taufkirchen, UF- Unterföhring, UH- Unterhaching, US- Unterschleißheim

Figure 6.4 – a. Map of stress orientations: A- or B- quality data of stress orientation are marked by black symbols, T shows the interpretation of tensile failure (DITF/ DENF) and E shows the interpretation for borehole enlargement (Breakouts). b. Depth profile of the recorded interval for the stress field interpretation for the central Bavarian Molasse basin. World Stress Map (WSM)-data (thin line) are mainly available at the Cenozoic sediments (Reinecker et al., 2010), the image log data of the geothermal boreholes (thick line) are only available in the Upper Jurassic reservoir. The intervals are color coded according to quality: A- & B- quality in black, C-quality in orange and D- quality in red (Tingay et al., 2016).

6.5 NUMERICAL MODEL

The case study from the southern area of Munich shows the horizontal stress rotation within the Upper Jurassic reservoir. Zoback (1992) indicates that the intensity of horizontal stress rotation is very sensitive to geometry, local stress change and the differential stress magnitude. To investigate the amount of horizontal stress rotation, a horizontal 2D-plane strain model was chosen, referenced the stress state at 4000 mTVD. Stress rotation counterclockwise, e.g. in S1 and KS2, indicates a weakening zone aligned in the first-quadrant from N000°E to N090°E (Bell, 1996). To evaluate the amount of stress rotation (γ) within the Upper Jurassic reservoir, we changed the contrast of fault to matrix stiffness (R), the differential stress ($S_H - S_h$) and the geometry of heterogeneity in a realistic range.

6.5.1 MECHANICAL MODEL

The model boundaries are aligned parallel to the S_H- and the S_h-orientation (Figure 6.5a). The fault length and width are adjusted so that boundary effects within the heterogeneity are kept low (Homberg et al., 1997; Spann et al., 1994). The dimension of the numerical model is 5000 m by 5000 m with a central 50 m wide and 1000 m long fault. The model was structured in such a way that the fault orientation could be varied from N000°E to N090°E in 5°-steps. The partial differential equation of the equilibrium forces for a linear elastic rheology of absolute stress (without pore pressure) is solved by Abaqus standard. Within the fault, plane strain quad-elements (CPS4) with a mesh size of 5 m were selected, outside the fault, plane strain trias-elements (CPS3) with a mesh coarsening to 100 m at the boundary were selected. The total number of elements of the model is approximately 42'000.

A Young's modulus of 40 GPa and a Poisson's ratio of 0.25, which are characteristic for the Upper Jurassic limestone reservoir, were used as material properties (Tondera et al., 2013). For the fault, the Young's modulus was systematically varied between 4 GPa and 40 GPa, resulting in a material contrast $R = E_{Fault}/E_{Matrix}$ between 0.1 and 1. Strong faults are marked by $R = 1$ and weak faults by $R = 0.1$. The Poisson's ratio was kept constant at 0.25.

The boundary conditions at the eastern and western borders allow a displacement parallel, but not perpendicular to the model boundaries. The stress inside the model results from displacement boundary conditions (e.g. Dirichlet) in the west and south following the approach of Hergert et al. (2015) and Reiter & Heidbach (2014) (Figure 6.5a). The calibration of the model is performed for the values S_H and S_h with an adapted iterative calibration procedure for the displacement boundary conditions (Ziegler et al., 2016). To cover the realistic range of stress states, we use differential stresses corresponding to a normal-faulting (Figure 6.6a), transtensional (Figure 6.6b), less compressive strike-slip (Figure 6.6c), and a compressive strike-slip stress regime (Figure 6.6d). The Abaqus2Matlab-Tool (Papazafeiropoulos et al., 2017) enables automatic adaption of the model parameters and post-processing methods. Thus it is possible to perform numerous model runs (190 per stress case) to vary the material properties and orientations of the fault.

In the following analysis, the stress in the fault center (black point in Figure 6.5b) is
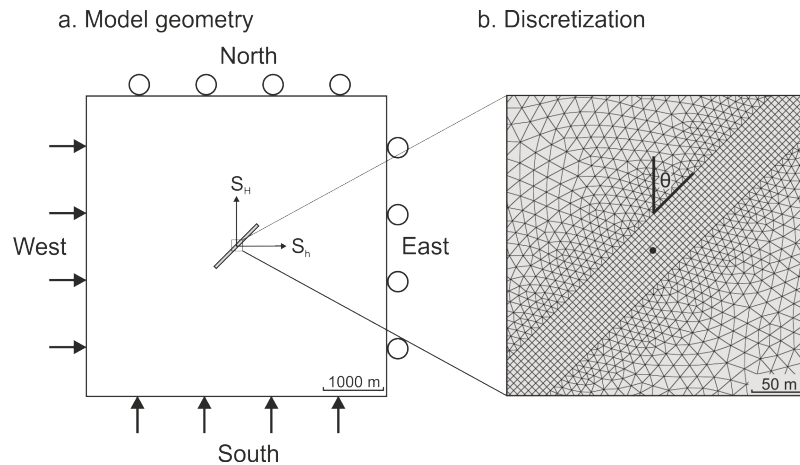
Figure 6.5 – Model geometry and discretization. a. Model geometry with an extension of 5000 m x 5000 m and a central fault structure with an dimension of 1000 m x 50 m. The southern (S_H-direction) and western (S_h-direction) boundaries are displaced so that the principal stress components are calibrated outside of the fault. On the north and east side, roller boundary conditions are applied to fix the model in S_h- and S_H-direction, respectively. b. Detailed view of the discretization with quad elements (CPS4) inside of the fault and trias elements (CPS3) outside of the fault. The black dot shows the reference point for considering the stress rotation.

considered. The local principal stresses (S_{Hloc}, S_{hloc}) at this point are compared with the regional stress orientations to obtain the local stress rotation (γ). Negative values indicate counterclockwise rotation, positive values clockwise rotation (Figure 6.6).

6.5.2 STRESS ROTATION RESULTS

The stress rotation (γ) is investigated within the heterogeneous structure at the reference point (black dot in Figure 6.5b) as a function of the material contrast (R), the orientation of the structure with respect to the regional stress (θ) and the stress field magnitude (Figure 6.6). Each curve in Figure 6.6 shows the magnitude of stress rotation (γ) for a material contrast (R) depending on the orientation of the structure (θ). In Figure 6.6a-d, these curves are plotted for increasing differential stress magnitudes corresponding to a transition from a normal-faulting to a more compressive strike-slip stress regime.

In general, the stress rotation increases with increasing material contrast. The maximum principal stress at the reference point within a weak fault with a high material contrast ($R = 0.1$) is perpendicular to the lateral boundary of the fault. If the material contrast is lower e.g. at strong faults ($R > 0.9$), the stress orientation within the structure is aligned to the regional S_H-orientation (no stress rotation). The stress rotation depends on the orientation of the fault with respect to the regional maximum horizontal stress: There is no rotation within faults perpendicular to S_H. When faults are parallel to S_H the local stress orientation can be rotated by up to 90° depending on material contrasts. The grey dashed line in Figure 6.6 divides the cases where the stress rotates in more or less perpendicular orientations to the fault and the cases where the resulting maximum stress is more parallel to the regional S_H.

The amount of horizontal stress rotation (γ) depends on the initial differential stress ($S_H - S_h$). In case of a material contrast $R = 0.6$, for a $S_H - S_h$ of 32 MPa in a transtensional

stress regime γ is up to 32° (Figure 6.6b). With constant material contrast and increasing $S_H - S_h$ to 42 MPa, the possible stress rotation γ decreases to a maximum of 23° (Figure 6.6c) and with increasing $S_H - S_h$ of 83 MPa to a maximum of 15°. In general it can be observed that with increasing differential stress the amount of S_H-rotation and the influence of the material contrast decrease.
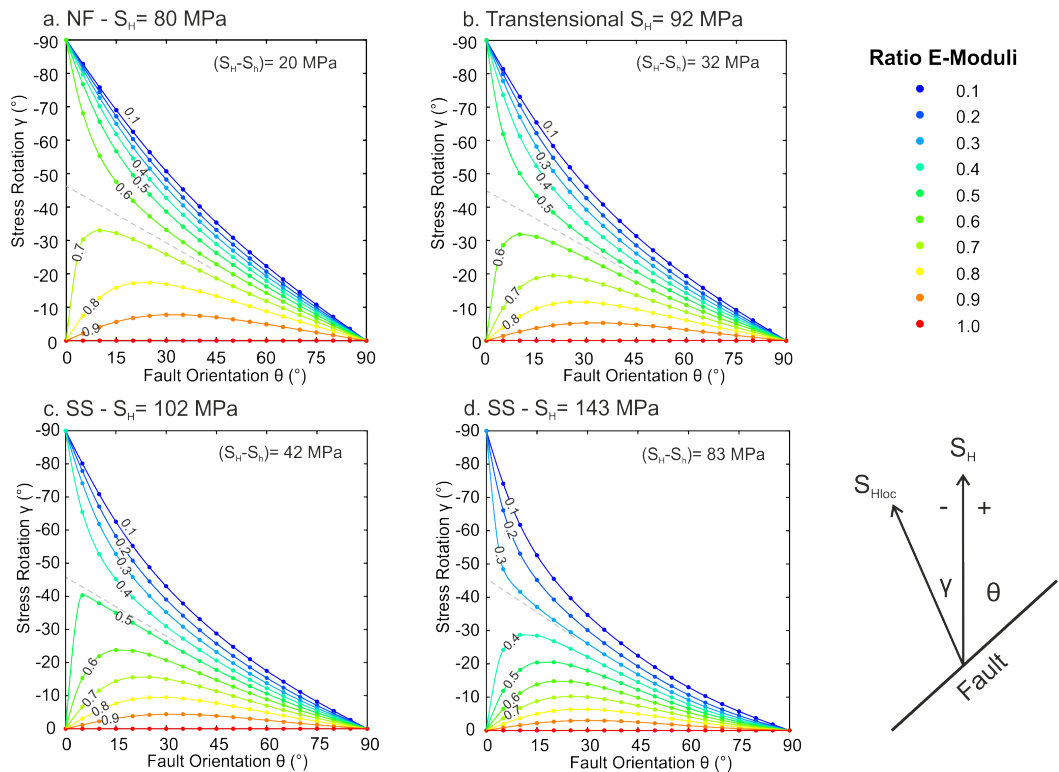
Figure 6.6 – Stress rotation (γ) of the local S_H (S_{Hloc}) inside of a heterogeneous structure at 4000 mTVD. Material contrast is expressed by the ratio of the Young's modulus of the matrix and the fault. Blue lines indicate high contrast of weak faults, red lines express less contrast. Fault orientation (θ) is varied from N000°E to N090°E direction. Stress conditions are variated from a. normal-faulting regime (S_v = 92 MPa, S_H = 80 MPa, S_h = 60 MPa), b. transtensional regime ($S_H = S_v$ = 92 MPa, S_h = 60 MPa), c. less compressive strike-slip regime (S_H = 102 MPa, S_v = 92 MPa, S_h = 60 MPa) and d. high compressive strike-slip regime (S_H =143 MPa, S_v = 92 MPa, S_h = 60 MPa).

6.6 Discussion

The numerical model of stress rotation as a result of stiffness contrasts shows that stress rotation increases at faults with increasing material contrasts or decreasing stiffness and decreasing differential stresses.

Previous studies indicate a normal-faulting to strike-slip faulting stress regime for the Munich area with very constant N–S S_H- orientations, especially in the Cenozoic sediments (Drews et al., 2019a). In the reservoirs, which are often associated with fault structures, stress reorientations were observed in some wells. The uniform N-S S_H-orientation within the Cenozoic sediments could indicate that within the sedimentary layers lateral stiffness contrasts are low, corresponding to the sedimentary environment of deepwater sediments, or that the structures with different material properties are E-W oriented, perpendicular to the regional stress field.

In contrast, the stress rotations observed at the Upper Jurassic reservoir show local heterogeneous material contrasts that potentially reflect the complex reservoir structure with fault, reef and basin structures. Analysis of the logging data indicates that stress rotation occurs in some wells and not in others.

At the Unterhaching site the geological model (Budach et al., 2017; Lüschen et al., 2014) (violet lines in Figure 6.7a) shows a N025°E and N045°E fault trend and the image log interpretation at UH2 gives a N000°E S_H-orientation without any rotation in the vicinity of the fault. Based on the numerical model, the absence of stress rotation in the Unterhaching fault could be explained by a strong fault (high R-value) or high differential stresses. We assume a weak fault with R of at least 0.6–0.4 for the Unterhaching fault structure. If the fault is characterized by this material contrast, a counterclockwise stress rotation of at least 20°-30° can be observed for differential stress between 42 and 80 MPa. This interpretation results in higher differential stresses. In the case of Unterhaching with S_v =92 MPa and S_h =60 MPa, a horizontal differential stress of >40 MPa leads to a strike-slip tectonic regime, which is proven by the analysis of focal mechanisms interpreted for microseismic events near the UH2 borehole.
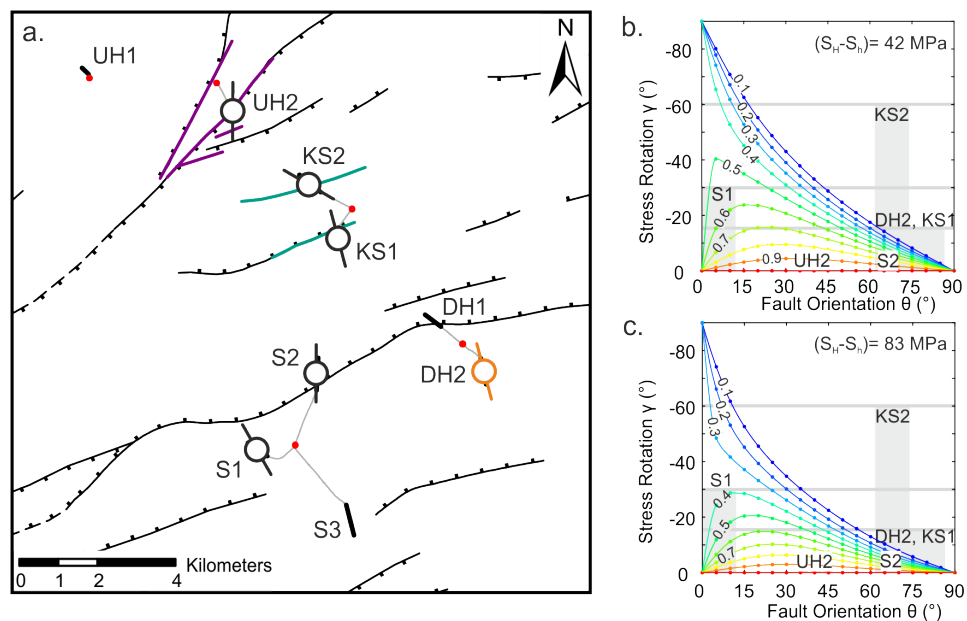
Figure 6.7 – Stress rotation observation and local structural setting. a. Map of stress orientation (A-B quality black, C- quality orange) (this study) and fault structures from the geothermal atlas of Bavaria (STWIVT, 2010) which are added by the local structures at Unterhaching (purple) (Lüschen et al., 2014) and Kirchstockach (turquoise). In b. & c. the numerical results for differential stress of 42 MPa and 82 MPa are added by the observation of stress rotation and a characteristic fault setting.

Stress field characterization of the southern sites at S2, DH2 and KS1 indicates only a very small counterclockwise stress rotation of 0° to 15° to the general trend. The structural model of the geothermal atlas (STWIVT, 2010) shows that all wells were drilled at the N070°E – N080°E striking structures (Figure 6.7a). The results of our modeling confirm the observations from the image log data. For structures that are aligned almost perpendicular to the maximum horizontal stress (S_H), a small stress rotation is to be expected even for weak faults (Figure 6.7b/c).

At S1 a counterclockwise stress rotation of γ =30° was interpreted in a strike-slip regime

(Seithel et al., 2015). Note that this well is drilled into a zone between two N070°E striking normal faults (Figure 6.7a), where there are several indications of a deformation zone. Numerous breakouts occur in the upper 500 m open hole section within the Upper Jurassic reservoir. In addition, north-striking "cross-fracturing" is detected. Both observations potentially reflect a dominant material contrast or a deformation zone that was not mapped by the seismic data (Seithel et al., 2015). Based on our numerical model, a counterclockwise stress rotation indicates a clockwise oriented structural zone from the S_H-orientation. Based on the numerical model, at differential stresses of 40 MPa and $R = 0.5$, a maximum stress rotation of $\gamma = 30°$ can occur for faults oriented N025°E, or at 80 MPa differential stress and $R = 0.4$, the faults are in the trend N010°E. The latter corresponds to the north-striking "cross-fracturing".

The stress field characterization at the Kirchstockach site shows a counterclockwise stress rotation of 15° at KS1 and 60° at KS2. For both wells, the current interpretation of the structural setting results in two parallel, N070°E striking, normal faults (green line in Figure 6.7a). The S_H-orientation at KS1 can be explained by a rotation due to the greatest stiffness contrasts at faults oriented N070°E. Obviously, the 60° counterclockwise stress reorientation at KS2 is far too large for the currently known structural setting (Figure 6.7c). Therefore, our model does not explain the observed stress orientation. A fault structure with an orientation of N150°E would be required.

6.7 CONCLUSION

The characteristics for stress reorientation as determined from stress observations and numerical modeling. Using new logging data from the Munich area we have investigated tectonic stress orientations which do not show stress field rotation at the wells A1 (Aschheim site), FH2 (Freiham site), S2 (Sauerlach site), UF1 (Unterföhring site), UH2 (Unterhaching site) and detectable stress field rotation at S1, DH2 (Dürrnhaar site), KS1 (Kirchstockach site), KS2 and UF4. Furthermore, we found that the rotation of the stress field is much more frequent in the southern/deep boreholes than in the shallower boreholes in the urban area of Munich. Numerical modeling shows that counterclockwise stress rotation can be explained as a result of weak fault structures occurring at 10° to 45° with respect to the maximum principal stress orientation. From this combined analysis we conclude with respect to potential stress rotation, stress regimes and structural framework:

⬦ The material contrast in the deformation zones leads to larger local stress reorientations for fault structures aligned between N015°E to N045°E with respect to the regional maximum horizontal stress orientation (N-S in Molasse basin), while less stress reorientations are to be expected for faults trending between N070°E and N090°E.

⬦ The observed N-S S_H- orientation (no local stress rotation) at the N045°E oriented fault zone in UH2 indicates that there must be a high differential stress within the Upper Jurassic reservoir that prevents stress rotation.

⬦ For the counterclockwise 30° stress rotation observed in S1, our study shows that such rotation is feasible if there is a N010°E – N020°E oriented fault with reduced stiffness.

⬦ At the Kirchstockach site, the wells show different counterclockwise stress reorien-

tation (15° in KS1 and 60° in KS2). The observation of the 60° stress rotation in KS2 could not be explained by stiffness reduction at the N070°E fault zones, but these fault zones could explain the rotation in KS1.

⋄ The combination of numerical modeling results and stress observations can not only help to explain the stress reorientations at some of the sites, but also provides further information on the tectonic stress regime (relative stress magnitudes). For example, in Unterhaching the high differential stress identified in this study is only possible in a prevailing strike slip regime.

This study shows that the combination of observed and modeled local stress rotations (γ), estimation or knowledge of structural framework, some reasonable assumptions about horizontal differential stress magnitudes and material contrasts can be used to characterize the tectonic stress field. Based on these results, the stress rotation potential and the horizontal differential stress magnitude can be investigated and the assessment of the seismic reactivation potential of fault structures improved. On this basis, the use of the geothermal reservoir in the Greater Munich Area can be further expanded in the future and safe operation can be ensured.

Probability of Fault Reactivation in the Bavarian Molasse Basin

Abstract

In the Bavarian Molasse Basin, especially in the greater Munich, geothermal exploration of the hydrothermal Upper Jurassic reservoir is rapidly expanding. Until now, little seismic reservoir response is observed, only at two out of 16 sites seismic events with $M_L > 2$ were detected: at Unterhaching, in 2008, six events with $M_L > 2$ occurred soon after the onset of circulation; at Poing, in 2016, 5 years after circulation started, two events with $M_L \sim 2.1$ occurred, both located near the injection well.

The analysis of the reactivation potential allows to connect seismicity to fault structures. In the Bavarian Molasse Basin, fault structures generally exhibit low seismic reactivation potential, as long as they trend ENE–WSW. By Monte-Carlo simulation, the geological uncertainty and the sensitivity of the individual parameters are quantified. They show that critically pre-stressed fault segments, e.g. at Unterhaching, combined with minimum change of the hydraulic reservoir conditions can lead to a dramatic increase of the reactivation potential of seismicity. For uncritical fault segments, e.g. at the Poing site, two self-enforcing effects are discussed which increase the reactivation potential over time: first, stress field modification by thermo-hydraulic effects and, second, fault alteration by carbonate dissolution can reduce the fault friction and cohesion. Both effects increase the sensitivity of the reactivation potential to the fault friction and can bring previously uncritical fault segments to critical state.

Finally, the possible impact of coupled thermo-hydro-mechanical and chemical processes at hydrothermal systems on the reactivation potential is highlighted: at fault segments with high reactivation potential hydro-mechanical effects may dominate whereas at low reactivation potential thermo-mechanical processes can potentially yield to a slow rotation of the stress field.

7.1 INTRODUCTION

The Bavarian Molasse Basin and therein especially the Greater Munich Area (30 x 30 km) is under a continuous development. In the meantime, it is after the Paris Basin (Laplaige et al., 2005), the second largest developed hydro-geothermal field in continental Europe. Close to Munich, the geothermal fluids are produced from the Upper Jurassic Mesozoic aquifer (Figure 7.1b), at depths between 2000–2500 m, temperatures of 80–100 °C and with high flow-rates (100–140 l s^{-1}). This hydrothermal resource is used for district heating in the urban area. To the south of Munich, the aquifer is at depths of 3000–4000 m and temperatures increase to more than 120 °C, which enables power production (Birner et al., 2012). These favorable conditions led to a first geothermal development phase from 2003, with the project of Unterschleißheim (2003), followed by the projects of Riem (2004), Pullach (2005) and Unterhaching (2007). After 2008, the number of projects increased. District heating developed at Unterföhring, Aschheim, Garching and Poing, combined power and heat generation projects at Dürrnhaar, Kirchstockach and Sauerlach (Dorsch & Pletl, 2012). Thanks to the experience gained, additional successful projects were realized in Grünwald (2009), Taufkirchen (2011), Ismaning (2012), Freiham (2015) and Holzkirchen (2016), with the wish to optimize the heat and power plant operation (Figure 7.1).

Currently, 16 geothermal projects extract heat from the reservoir, mostly used for district heating. In total, these projects produce a circulation rate of 1.6 m^3 s^{-1} and a thermal and electrical installed capacity of 235.6 MW$_{th}$ and 31 MW$_{el}$, respectively (Agemar et al., 2014).

The intense development in the Munich area is now accompanied by an increasing scientific program. As such, the Geothermal Alliance Bavaria (GAB) consisting of academic institutions in Bavaria aims at assisting to better managing the production plan. In the Greater Munich Area only at two geothermal sites few seismic-events have led to public perception. However, concerning the onset of seismicity there are marked differences: at the Unterhaching site microseismicity was detected already during the first years of operation (2008) whereas at the Poing site the onset of microseismicity and perceived seismicity was around 5 years after the begin of geothermal circulation (Megies et al., 2017).

Indeed, it appears difficult to explain how the circulation of fluids in permeable layers at flow rates as high as 100 l s^{-1}, with wellhead injection pressure in the order of only 10 bar and in a seismically quiet area can induce seismicity. Under these conditions it is also challenging to monitor the temporal evolution of injection parameters, however, at Pullach, Unterhaching and Taufkirchen a decreasing injection pressure is observed (Baumann et al., 2017; Wolfgramm et al., 2015). It seems that such processes are linked to carbonate dissolution which is common at the Upper Jurassic reservoir (Ueckert & Baumann, 2019) but could not be monitored at Poing.

Microseismic observations in the context of reservoir operation are widely common and mostly are explained by fault structures with a high reactivation potential (Ellsworth, 2013; Evans et al., 2012; Grünthal, 2014). Induced seismic events from geothermal injection are generally observed where the local stress field is changed by fluid injection or petrophysical parameters are modified (i.e. Gaucher et al. (2015) and Schoenball et al. (2014)). It is well-know that the probability for induced seismicity depends on the stress field, pore

pressure perturbation, time-dependent stress modification and the presence and mechanical characteristic of fault structures.

Herein, we present a model to statistically evaluate the influence of petrophysical parameters and in-situ stress changes on the stress conditions at faults. To integrate the uncertainty of the geological and mechanical parameters at reservoir depth, we apply a statistical approach assessing the probability for fault reactivation (Schoenball et al., 2017; Walsh & Zoback, 2016). The calculations are based on the critical pore pressure for fault reactivation P^c_{eff} (Mildren et al., 2002; Streit & Hillis, 2004). Using Monte-Carlo simulation the distribution of P^c_{eff} define a statistically based reactivation potential at an injection pressure P^{ref}_p. Finally, the impact of key model parameters e.g. the maximum to minimum horizontal stress ratio S_H/S_h, S_H- orientation, fault friction μ and cohesion C is investigated to study the effect of stress field rearrangements and geochemical alteration processes in the context operation induced seismicity in the Bavarian Molasse Basin.

7.2 Geological framework

The Bavarian Molasse Basin is part of the North Alpine Foreland Basin stretching 700 km in E-W and 130 km in N-S direction. The lithological sequence can be subdivided in the youngest Cenozoic Molasse sediments, the Mesozoic Upper Jurassic reservoir (grey layer in Figure 7.1b) and the pre-Mesozoic basement. During tropical climate in the Upper Jurassic, the today geothermal highly productive limestone reservoir sediments had been deposited consisting of thin-bedded marl and thick-bedded limestone or dolomitic units as well as porous reef structures (Meyer & Schmidt-Kaler, 1989). During foreland basin development with dilatational tectonics the Upper Jurassic layers where tectonically subsidized resulting in a dominant structural southward dipping (Bachmann et al., 1987) and the formation of the dominant normal fault pattern striking parallel to the Alpine Orogen (see Figure 7.11c) (Bachmann & Müller, 1992).

7.2.1 Structural setting

In the Bavarian Molasse Basin E-W trending, alpine parallel, strongly dipping fault structures can be traced from the Basement, to the Mesozoic, up to the Cenozoic in the upper Miocene part (Unger, 1996). As such, interpretation from well data indicate dip angles of 70°–80° and seismic interpretation highlight sub-vertical fault structures (Budach et al., 2017).

The tectonic map at the Cenozoic base published in the geothermal atlas (STWIVT, 2010) shows faults based on seismic lines (Figure 7.1). The faults are synthetic and antithetic normal faults striking ENE-WSW (Figure 7.1c). A secondary NNE-SSW to NE-SW orientated fault set with a limited length of 2.5–5 km exists at step-over or transfer zones (e.g. Unterhaching structure).

In the fault map, dominant structures in the Greater Munich Area are highlighted by bold lines in Figure 7.1. The main structure in the deep underground of Munich is a synthetic normal fault with an offset up to 200 m. It is traced from Unterbrunn in the SW of Munich
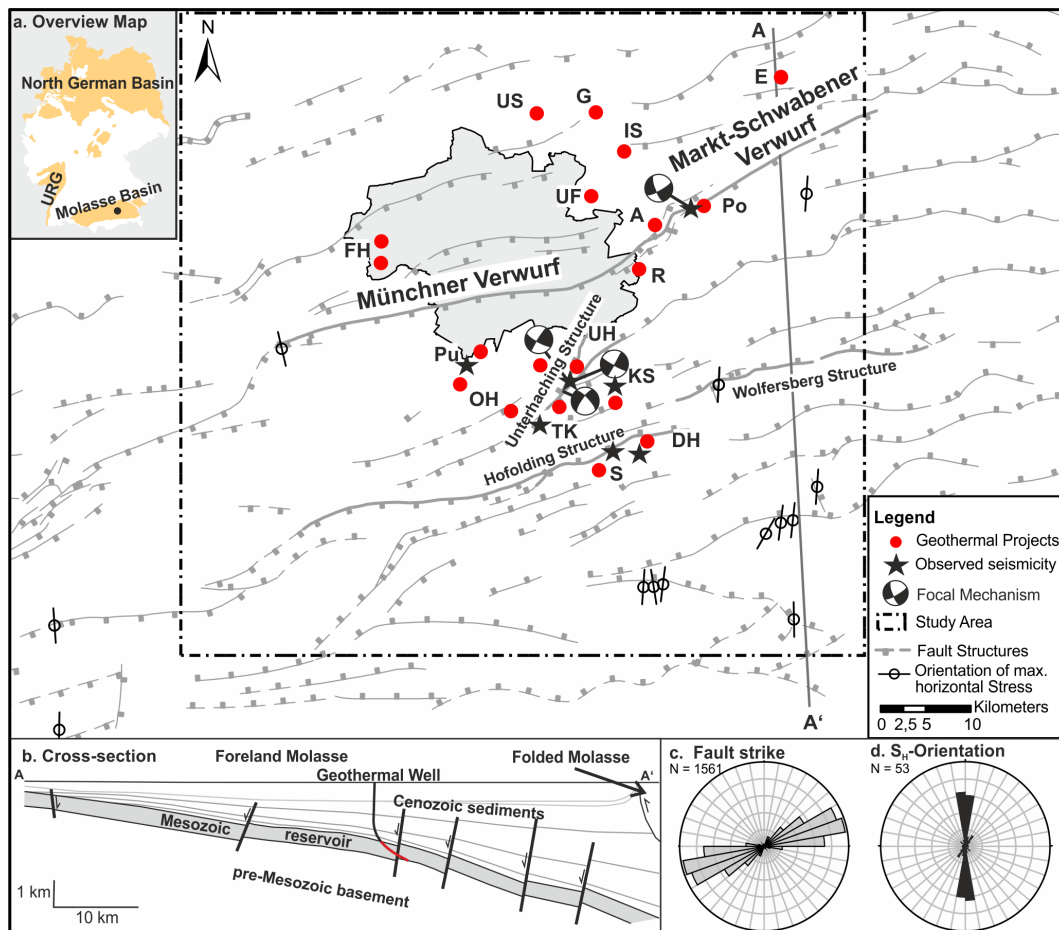
A- Aschheim, DH- Dürrnhaar, E- Erding, FH- Freiham, G- Garching, IS- Ismanning, KS- Kirchstockach, OH- Oberhaching, PO- Poing, PU- Pullach, S- Sauerlach,TK- Taufkirchen, UF- Unterföhring, UH- Unterhaching, US- Unterschleißheim

Figure 7.1 – Study area and tectonics: Map of the Greater Munich Area with the considered geothermal projects (red points), the location of microseismic events (black stars) and analyzed focal mechanisms (Megies et al., 2017), see details in Table 7.1. The fault structures are taken from the Geothermal Atlas (STWIVT, 2010) and the stress orientations from the World Stress Map (WSM) project (Reinecker et al., 2010); a. Overview map of the geothermal provinces in Germany (Schulz et al., 2009). b. North-South oriented cross-section in the eastern part of the study area (modified after Reinecker et al., 2010 with the Cenozoic Molasse sediments, the Mesozoic Upper Jurassic reservoir (grey), the pre-Mesozoic basements and the roughly E-W striking normal faults, Black line sketch a typical Geothermal well path with the open-hole section (red section) in the Upper Jurassic reservoir c. Strike direction of major faults within the study area; d. Orientation of S_H from the WSM-data with better than D-quality.

in the ENE direction to Riem and known as "Münchner Verwurf". At Riem, it turns to NE, splits up into several smaller faults, and continues to the NE with an ENE trend along Poing where it is named "Markt-Schwabener Verwurf". WSW-ENE striking structures are frequently observed and reached e.g. by the injection well at Poing. A complex structure is located at the Unterhaching site where a scientific 3D-seismic campaign provided detailed information of the underground structure (Lüschen et al., 2014)). There, a 70° striking fault zone coming from the SE splits into a 25° minor and 45° major fault zone with 70° striking en-echelon minor faults which are connected over relay ramps (Budach et al., 2017). This central structure is used for injection at the Unterhaching site and bounded by a 70° striking fault in the south which is used for injection of the Kirchstockach geothermal site.

7.2.2 SEISMICITY

In 2008 a $M_L = 2.4$ earthquake was probably induced by the geothermal exploitation at Unterhaching and was the first seismic event in the Greater Munich Area felt by the nearby population (Megies & Wassermann, 2014). On the basis of the seismic catalogue such hazard was not foreseen. The seismic catalogue for Germany exhibits minimal background seismicity for the Bavarian Molasse Basin (Leydecker, 2009), as well as the seismic catalogue of the Bavarian earthquake service (BES) did not contain any natural seismic event in the Greater Munich Area since 1970, i.e. $M_L > 2.0$ according to the sensitivity of the regional seismological network. The mechanisms to induce seismicity in this highly permeable layer at wellhead injection pressure of approximately 10 bar are broadly discussed. The present paper will contribute further arguments to this.

Since this Unterhaching earthquake in 2008, the seismic monitoring of the Greater Munich Area has been improved. Regulations require the installation of at least one seismometer at each geothermal site and in case of local seismic events with $M_L \geq 1.5$ (or peak ground velocity $\geq 0.1 \mathrm{mm\,s^{-1}}$) of minimum four additional stations.

Besides regulatory actions, the MAGS1 (2010–2013) and subsequent MAGS2 (2013–2017) projects allowed to better characterize the seismicity, mainly in the southern part of Munich area. As a result, a catalogue of all local seismic events in the Greater Munich Area between 2008 until end of 2017 was established. This catalogue, however, exhibits spatially varying magnitude of completeness. In the southern area of Munich, below the sites Pullach, Oberhaching, Unterhaching, Taufkirchen, Kirchstockach and Dürrnhaar, M_L down to −0.36 can be currently detected which is a significant improvement since 2008. In the inner and northern part of Munich, the magnitude of completeness reaches 1.0 to 1.5 (Megies et al., 2017).

Table 7.1 summarizes the main characteristics of the seismicity, recorded in the vicinity of the geothermal sites. Figure 7.1 shows that most of the – detected – seismicity is occurring either in the south of Munich or close to Poing. All eight catalogue events with $M_L \geq 2.0$ have been recorded at the Unterhaching (UH) and Poing (PO) sites. Seismic events with $M_L \leq 2.0$ were recorded at the Kirchstockach (KS), Dürrnhaar (DH), Sauerlach (S), Taufkirchen (TK) and Pullach (Pu) sites (Megies et al., 2017). At all locations seismicity was located near the injection well and approx. 1–2 km below the reservoir depth.

Six seismic events with $M_L \geq 2.0$ were detected during the first three years of circulation at Unterhaching (UH) (Megies & Wassermann, 2014). The major event ($M_L = 2.4$) was followed by events within a radius of 400–500 m to the injection well given location errors between 100 and 500 m. The focal mechanisms highlight sinistral strike-slip displacements. The depth distribution indicates a rupturing plane up to 1.5 km below the reservoir (Megies et al., 2017). At Unterhaching, the injection well targeted the vicinity of a main fault zone with an offset of 160 to 200 m favoring injection pressure decrease in the highly conductive Malm layer close to the well (Wolfgramm et al., 2007).

End of 2016, at the Poing (PO) site, around five years after launching the circulation, first seismic events were observed nearby the injection well Poing Th1 at the "Markt-Schwabener-Verwurf". Two minor events ($M_L = 1.3/1.0$) on 19/11/16 and 27/11/16, were

Table 7.1 – Earthquake catalogue from 2008 to the end of 2017 provided by the Bavarian Earthquake service in the MAGS2-project.All events concentrate on seven sites, always near the injection well, with a maximum magnitude of 2.4. The catalogue may be biased by the varying magnitude of completeness over the greater Munich area. Due to the relatively dense networks around Unterhaching and Poing, many microseismic events could be detected there and at the neighboring sites.

Project	First detection	Strongest Event / #	Description
Unterhaching (UH)	10.02.2008	$M_L 2.4$ / 657	27 events $M_L \geq 1.0$, six events $M_L \geq 2.0$, near inj. well, decreasing magnitude
Taufkirchen (TK)	19.07.2012	$M_L 0.3$ / 11	During circulation test at inj. well
Kirchstockach (KS)	23.08.2012	$M_L 0.8$ / 33	30 mirco events $M_L \geq 0.8$, near inj. well
Sauerlach (S)	19.06.2014	$M_L 1.2$ / 2	$M_L 0.7$ and $M_L 1.2$, big uncertainty
Pullach (PU)	21.02.2015	$M_L - 0.4$ / 1	Near inj. well
Oberhaching (OH)	01.02.2016	$M_L 0.5$ / 3	Near inj. well
Dürrnhaar (DH)	31.07.2016	$M_L 1.3$ / 10	Big uncertainty
Poing (PO)	19.11.2016	$M_L 2.1$ / 21	18 detected events, two events with $M_L 2.1$

followed by two events ($M_L = 2.1/1.8$) on 07/12/16 and 20/12/16. Focal mechanisms of the 20/12/16 event indicates a sinistral strike-slip displacement with a normal faulting component. Since the initial installed seismic network yields location errors of up to 1000 m additional seismic stations have been installed since mid-December 2016 reducing the location error of up to 500 m. Note, Th1 is the only well where the pre-Mesozoic basement is reached. Around 10 months later, on 09/09/17, an additional event ($M_L = 2.1$) occurred.

7.2.3 Stress field

The state of stress in the Bavarian Molasse basin is dominated by a N-S S_H- orientation (Heidbach et al., 2010) as derived from the analysis of petroleum and geothermal wells (Reinecker et al., 2010; Seithel et al., 2015). Additional information about the stress orientations and tectonic regimes from focal mechanism was provided by the MAGS1 and MAGS2 projects and indicates a strike-slip stress regime in which S_H magnitude exceed the S_v magnitude (Megies et al., 2017).

The N-S oriented S_H reflects the push of the Alps along the alpine thrust front. Furthermore, thrust deformation in the Peißenberg mine (Illies & Greiner, 1978) indicates that compressive stresses are maximum next to the Alpine thrust front. The low natural seismicity (Grünthal & Wahlström, 2012), the missing active thrust faulting structures (Hartmann et al., 2016) and the normal fault structures (Bachmann & Müller, 1992; Unger, 1999a) indicate a decreasing S_H-component within the undeformed foreland basin. In a more detailed view, variations of the regional S_H-trend in the Upper Jurassic sediments are observed at Riem and Sauerlach (Reinecker et al., 2010; Seithel et al., 2015). Yale (2003) argued that such variations in the S_H-orientation can be induced by mechanical heterogeneities at fault structures or poro-/thermo-/elastic coupling in the vicinity of injection wells (Ziegler, 2017). Such processes are subsequently defined as stress rotation, which characterize any difference of the S_H-orientation from the regional trend.

Combining pressure test data, borehole failure mechanisms and the concept of stress

limitation by frictional strength, Seithel et al. (2015) presented a stress model for the Upper Jurassic in the Bavarian Molasse Basin (Table 7.2). S_h is analyzed from pressure data of drilling operations and indicating a S_h-gradient of $15 \pm 1 \, \mathrm{MPa \, km^{-1}}$ at reservoir depth. Analysis of the compaction trend within Cenozoic sediments indicates a S_v-gradient of $23 \pm 2 \, \mathrm{MPa \, km^{-1}}$ (Drews et al., 2018). From hydraulic tests the reservoir pore pressure P_p of the low mineralized reservoir fluid has been determined to be at under-hydrostatic level (Birner et al., 2012). Table 7.2 illustrates the results from two test cases for a frictional equilibrium with friction coefficients of $\mu = 0.6$ and $\mu = 0.8$, respectively. From the S_h/S_v ratio of 0.66 the values for the S_H/S_v ratios range between $1.25 < S_H/S_v < 1.55$ in other words, a horizontal differential stress $(S_H - S_h)$ between 54.3 MPa–81.9 MPa at a depth of 4000 mTVD is most likely.

Table 7.2 – Stress data for Stress Case I and Stress Case II at a reference depth of 4000 mTVD (see details at Seithel et al., 2015).

Stress Case	I	II
P_p [MPa]	38	38
S_v at 4000 mTVD [MPa]	92	92
S_h/S_v	0.66	0.66
S_h at 4000 mTVD [MPa]	60.7	60.7
S_H/S_v	1.25	1.55
S_H at 4000 mTVD [MPa]	115	142.6
$S_H - S_h$	54.3	81.9

S_h – minimal horizontal stress, S_H – maximal horizontal stress, S_v – vertical stress and the reservoir pore pressure P_p

7.3 METHODS

The general fault setting in the Molasse basin is oriented perpendicular to S_H indicating a low opening character of the faults (see Figure 7.1c and d). In a fractured hydrothermal system this might lead to low transmissivity of the faults. However, in the heterogeneously segmented karstified limestone of the Upper Jurassic, the faults represent the main reservoir structures with very high permeability. Given the low natural seismicity, these faults seem to be not favorably oriented for failure. The seismic reactivation potential, RP, of fault structures is described by applying a failure criterion to the state of stress of a planar structure (Moeck et al., 2009). Herein, we quantify the RP, by assigning a probability for reactivation for a statistical parameter set based on an individual fault strength (fault friction and cohesion) and stress field parameters (S_H, S_h, S_v, P_p and S_H-orientation), to investigate the mechanism of fault reactivation in the Bavarian Molasse Basin.

7.3.1 REACTIVATION POTENTIAL

Due to the well-known uncertainty of geological and mechanical parameters at reservoir depth, we vary the parameter settings to calculate the absolute value of the critical pore pressure for failure. The statistical approach enables to handle the critically of fault structures based on a statistical distribution of the parameters and from a sensitivity analysis the most sensitive parameters can be determined. The probability of RP (i.e. fault reactivation to quantify the criticality of fault structures) is calculated by a Monte-Carlo simulation of

the critical pore pressure based on a normal distribution of the parameters (Schoenball et al., 2017; Walsh & Zoback, 2016). Along each fault segment the comparison of the calculated RP with the seismicity enables to study the influence of the dominant processes like stress field rotation, increasing differential stress or fault alteration.

The RP is based on the critical pore pressure P_{eff}^c of individual fault segments describing the potential pressure modification to reach the Mohr-Coulomb failure envelope (Figure 7.2b) (Mildren et al., 2002; Streit & Hillis, 2004).

$$P_{eff}^c = (\sigma_n - P_p) - \frac{\tau - C}{\mu} \tag{7.1}$$

Here, normal stress σ_n and shear stress τ are functions of the strike of the fault β with respect to North and the state of stress described by S_H, S_h, S_v. The mechanical parameters of the fault are described by friction coefficient μ and cohesion C. P_p is the reservoir pore pressure. High RP values indicate favorably oriented fault segments for failure, low RP values indicate no expected failure.

To quantitatively assess the implication on β in the study area at a reference depth of 4000 mTVD, the fault traces from the Bavarian Geothermal Atlas (STWIVT, 2010) are discretized into equally spaced intervals of 450 m length (total 1561 fault sections with $\Sigma L = 700\,000$ m). Since the exact dip angle of the steeply dipping faults (see Chapter 7.2.1) is only available at a small part of the investigation area, a uniform reference fault dip of $\phi = 80°$ was assumed. For the statistical approach the parameter set is varied (i.e. S_H, S_h, S_v, P_p and S_H- orientation, μ, C, φ).

For the sensitivity analysis (see Chapter 7.4.2), normal distributions specific to each parameter have been used. This could however be adopted when large number of observations would be available. They constitute the basis for the Monte-Carlo simulation run with a predetermined number of 10'000 iterations (see Figure 7.2a). For each iteration, the P_{eff}^c-values along each fault segment is calculated with Eq.(7.1) (Figure 7.2b). So, for each fault segment, the P_{eff}^c-distribution of the parameter statistics gives a cumulated density function, which quantifies the probability of failure for each fault segment at a specific over-pressure level (Figure 7.2c). The RP-value for each fault segment is extracted from the cumulated density function using a reference pressure P_p^{ref}, taken herein as $P_p^{ref} = 20$bar (Figure 7.2c), the corresponding maximum pressure increase at reservoir depth nearby the injection well.

7.3.2 Parameter sensitivity

The parameter sensitivity represents the kernel of the statistical approach by calculating the individual impact of each parameter to P_{eff}^c. As a reference value, we use the derivative with respect to each parameter (Pannell, 1997). A derivative of '0' indicates no sensitivity, positive value stabilizing and negative value destabilizing effect.

Figure 7.3a illustrates the derivative on the basis of the reference parameter set (Figure 7.3b) for each parameter for the strike direction β with respect to North between N000°E to N090°E. Additionally, we show the derivative function by each parameter of P_{eff}^c in Figure 7.3b. Note that there is a 90° symmetry in the parameter sensitivity.
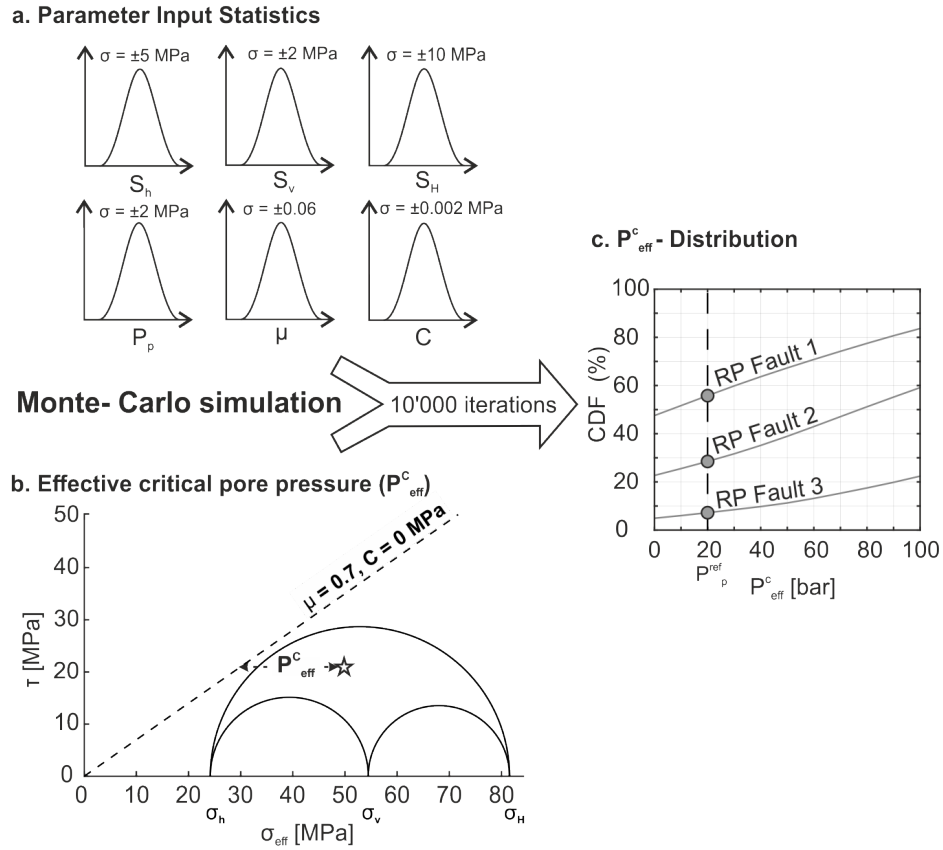
Figure 7.2 – Workflow for the calculation of the reactivation potential RP. a. Normal distribution of each parameter used as input in the Monte-Carlo simulation (10'000 iterations). b. Calculation of the critical pore pressure P_{eff}^c for each iteration of the Monte-Carlo simulation e.g. for stress Case I (Table 7.2). c. Cumulated Density Function (CDF) of P_{eff}^c results of the Monte-Carlo simulation for Fault 1, 2 and 3. Picking the reactivation potential RP for each fault segments from the CDF-curve for the reference maximum pressure increase at reservoir depth (P_p^{ref} = 20 bar).

It is obvious that μ yields the strongest effect at N045°E (Figure 7.3a). As expected, highest destabilizing effect for S_H is observed at N030°E and highest stabilizing effect at N090°E. In contrast, S_h own a permanent stabilizing effect for the reference parameter set with a maximum at N030°E and no effect at N090°E. The sensitivities of both stress components S_H, S_h are solely dependent on μ and β. Whereas, P_p exhibits the most important destabilizing effect with a parameter independent constant '-1' derivative. The derivative of C is $^{(-1)}$ without any dependency of β (see Figure 7.3b), e.g. with $\mu^{(-1)}$ = 1.67 at the reference parameter set.

The strike-slip stress field sensitivity analysis indicates no effect of S_v and ϕ. Note that the modification in the reference parameter set (e.g. stress field, μ, C) will change the results in Figure 7.3. The highest sensitivity for S_H and S_h is observed at the N030°E and for μ it is at N045°E. Destabilizing effects remain most significant around a $30° - 45°$ between the orientation of S_H and β.

The sensitivity analysis provide the basis for a classification into 1st-order (μ), 2nd-order (S_H, S_h, P_p and C) and 3rd-order (S_v, ϕ) parameters (Figure 7.3a). Based on the data analysis (see Chapter 3.2) a realistic range of the standard deviation for the parameters was chosen (i.e. ±10 MPa for S_H, ±5 MPa for S_h and ±0.06 for μ, ±2 MPa for S_v, ±2 MPa for P_p and
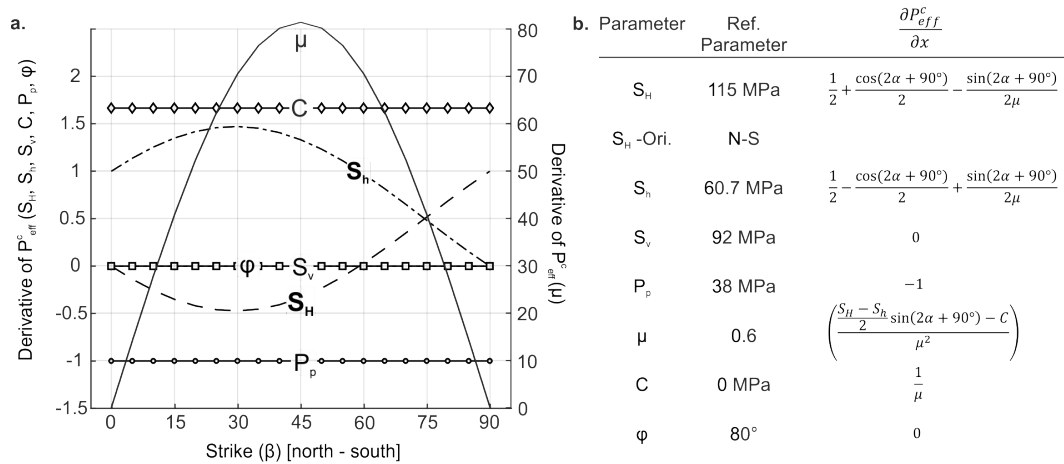
Figure 7.3 – Sensitivity to P^c_{eff} to characterize the key parameters based on the reference parameter setting. a. The derivative of P^c_{eff} for each parameter is used as an indicator for sensitivity. A positive derivative indicates fault stabilization; a negative derivative indicates destabilization. There exists a significant direction dependency of the sensitivity for the stress components S_H, S_h and μ. Besides, there is no variation for the sensitivity P_p and C for strike. Note there is no sensitivity at all of ϕ and S_v for the strike–slip stress field. b. Table of the reference parameter set and the derivative of the parameters. The orientation of faults is here defined as direction of the dip α. μ represents 1st order sensitivity, S_H, S_h, P_p and C 2nd order sensitivity and ϕ and S_v 3rd order sensitivity.

±0.002 MPa for C). According to the classification P^c_{eff} is highly sensitive to the S_H, S_h, μ and C parameters, which therefore constitute the key parameters to investigate. Next, we present the sensitivity of the key parameters represented by Stress Case I & II, μ and C towards the angular RP-values.
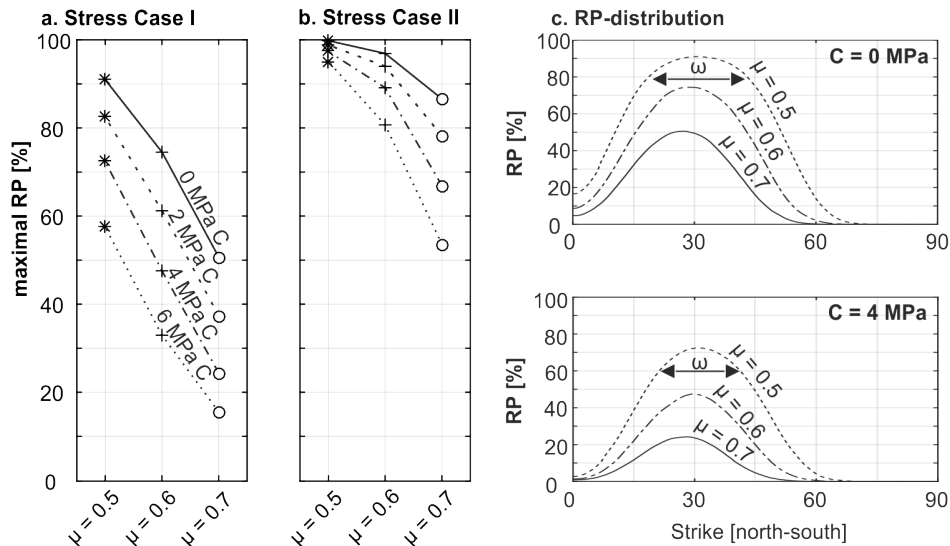
Figure 7.4 – Maximal reactivation potential RP in reference to the friction coefficient μ and the cohesion C for Stress Case I (a.) and II (b.). c. Angular distribution of the reactivation potential RP for cohesion C of 0 MPa and 4 MPa in dependence to fault friction μ of 0.5, 0.6 and 0.7 for the reference parameter set (see Figure 7.3b).

7.4 Reactivation potential analysis

7.4.1 Stress magnitude and fault mechanics

In Figure 7.4a and b, the magnitude of RP is analyzed as a function of Stress Case I & II and the fault mechanical parameters in the range of $0.5 < \mu < 0.7$ and $0 < C < 6$. From Stress Case I to Stress Case II, the horizontal differential stress $(S_H - S_h)$ increases from 54 MPa to 83 MPa, respectively. Based on the reference parameter set in Figure 7.3b (Stress Case I with $\mu = 0.6$ and $C = 0$ MPa), RP decreases from 75 % to 32 % at $C = 6$ MPa (Figure 7.4a)., RP decreases from 90 % to 58 % (Δ32 %) when $\mu = 0.5$ and from 50 % to 15 % (Δ35 %) when $\mu = 0.7$. It is obvious that decreasing μ or C will dramatically increase the maximal RP.

Comparing Stress Case I (Figure 7.4a) with Stress Case II (Figure 7.4b), the increase of the differential horizontal stress increases the maximal RP, e.g. from reference parameter set 75 % to 95 % (Stress Case II, $\mu = 0.6$ and $C = 0$ MPa). Under Stress Case II (Figure 7.4b), the influence of C is highly dependent on μ by a sensitivity factor of $\mu^{(-1)}$ (Figure 7.3b).

Figure 7.4c shows the angular RP-values (N00°E–N090°E) in dependence of the highly coupled parameters μ and C for the reference parameter set. For a decreasing μ, the angular width ω of high RP-values increases. This observation is more pronounced in a fault without cohesion ($C = 0$ MPa) than in a fault with cohesion ($C = 4$ MPa).

Fault friction μ is the most sensitive factor for high RP-values at 45° between S_H and β and the differential stress $S_H - S_h$ is most sensitive at 30° between S_H and β (Figure 7.3a). Additionally, μ is the most sensitive parameter with a self-intensifying effect due to the $\mu^{(-2)}$ in the denominator of the derivative function (Figure 7.3a/b). So the magnitude of RP can be calculated with μ, C and $S_H - S_h$ in an angular distribution in reference to the local S_H-orientation (Figure 7.6).

7.4.2 Stress rotation and regional distribution

The angular distribution of RP is highly dependent on the strike of the fault segments β and potential stress rotation. Using the reference parameter set (Figure 7.3b), a maximum RP-value of 78 % at N030°E is observed. Applying a potential stress rotation of about ±20°, the angular RP distribution is compared to the 1561 fault sections in the Greater Munich Area to analyze the influence of a rotated stress field on the magnitude of RP (Figure 7.6). Additionally, a map of the RP-values for all fault sections in the study area presents the most sensitive fault segments for reactivation in the reference parameter set (Figure 7.5).

Figure 7.6a indicates a limited overlap of the main fault structures with the highest RP-values under a N-S stress field. Only the rarely occurring N030°E oriented fault structures show high RP-values. Therefore, the majority of the faults which has an orientation of N070°E–N090°E possesses low RP-values.

Generally, a clockwise stress field rotation (e.g. up to 30°) significantly affects the RP-value of fault segments which strike N030°E–N060°E (Figure 7.6a). On the contrary, a counter-clockwise stress rotation reduces RP-values for these fault segments. Clockwise rotation of S_H to N020°E decreases the number of fault sections with low RP ($<$10 %) to 30 % and increases the number of faults with high RP ($>$50 %) (Figure 7.6b), e.g. this stress
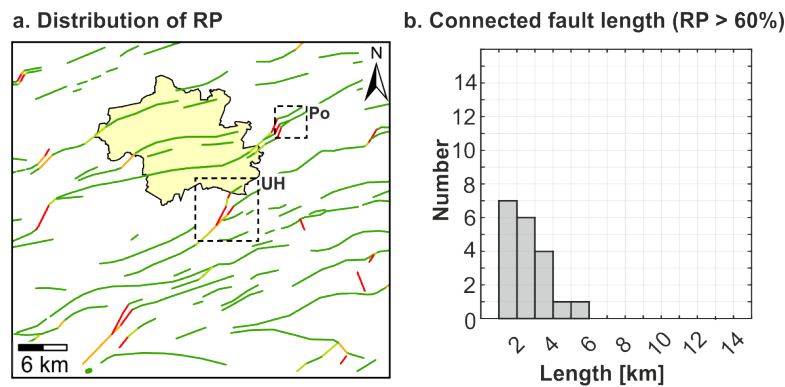
Figure 7.5 – Reactivation potential RP of faults in the study area for the reference parameter set (see Figure 7.3b) a. Map view of the RP scaled between 0 % (green) and 80 % (red). Marked regions in the maps indicate the area for the case studies (PO- Poing, UH- Unterhaching and S- Sauerlach). b. Histogram of the fault length with RP >60 %.

rotation increases the RP of N050°E fault orientations from primarily 25 % to over 78 %.

Overall, 80 % of the fault segments in the reference parameter set show RP-values smaller than 10 % (Figure 7.6b). Only very localized connected fault segments with RP-values > 60 % exist, e.g. at the Unterhaching structure or at the transition of the "Münchner-Verwurf" to the "Markt-Schwabener-Verwurf" (Figure 7.5a). In total, there are 7 connected fault segments with RP > 60 % and a maximal length of 2 km, 6 with a maximal length of 3 km and 4 with a maximal length of 4 km (Figure 7.5b).

This shows that the RP study for seismic characterization is highly dependent on the local settings. In the next chapter, we focus our discussion on the three geothermal sites, Unterhaching, Kirchstockach and Poing.

7.5 Case studies

Fault zones in the Bavarian Molasse Basin indicate a general low RP, which is in accordance with the observation of minor natural seismicity (Grünthal & Wahlström, 2012). Only at two locations, a total of eight seismic events with M_L > 2 have been observed as a reservoir response to injection. The MAGS catalogue indicates at these sites clustering of the seismicity near the injection wells. Furthermore, seismicity is aligned to adjacent fault zones and localized within the upper section of the basement. Based on the previous parameter studies, the RP of fault zones will be calculated for the reference parameter set (Figure 7.3b) and discussed at the light of microseismic observation, the operation conditions and the structural setting at the Unterhaching, Kirchstockach and Poing sites.

7.5.1 Unterhaching site

At the Unterhaching geothermal site, the majority of the observed microseismic events occurred during the first three years of circulation. It started with a magnitude two event and a subsequent microseismic swarm (Megies et al., 2017). The site uses one production-well (black line) with a flow-rate of 140 l s⁻¹ and a temperature of 123 °C (Agemar et al., 2014) located at the northwestern part of the "Unterhaching structure", and one injection-well

a. Influence of stress rotation

b. Distribution of RP at the fault sections
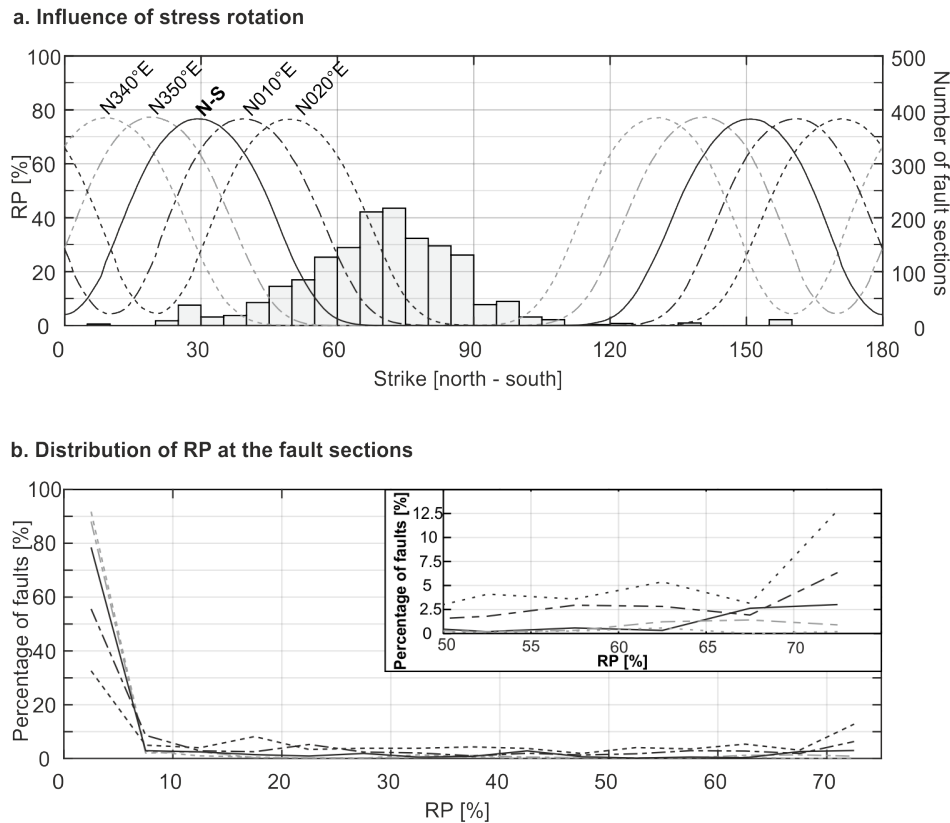
Figure 7.6 – Reactivation potential RP for the reference parameter set (see Figure 7.3b) a. Influence of stress rotation from N340°E to N020°E on the RP-values. Histogram as a function of the strike of the fault section in the study area. b. Distribution of the RP-values for the fault section in the study area. The N030°E–N050°E striking fault structures get higher RP for anti-clockwise stress rotation.

(blue line) crossing the well-known southeastern "Unterhaching structure" (Figure 7.7a). The N045°E striking fault, splits up into a N025°E minor, N045°E major and small en-echelon N070°E faults (Budach et al., 2017). Most induced events are directly aligned to the N045°E oriented fault structure targeted by the injection well Gt2 and could be located at 200 m – 900 m below the reservoir in the basement (Megies et al., 2017). Focal mechanisms indicate sinistral strike-slip displacement (Figure 7.7a). The RP (78 %) show that theses faults are at critical conditions for the reference parameter set (Figure 7.7b). Thus, only minimal perturbations of the effective stress conditions induced by circulation could reactivate these faults. Furthermore, minor stress changes could result from hydraulic poro-elastic coupling that can be observed in a rock volume in the vicinity of the injection well (Schoenball et al., 2014). The coupled high sensitivity of μ, S_H and S_h at these critical fault orientations (Figure 7.3a) shows that any operation-induced modification of the effective S_H- or S_h-magnitude can increase the RP. Occurrence of seismic events during the early phase of circulation supports this interpretation of the reactivation of a close to critically pre-stressed N045°E oriented fault segment by injection-induced hydraulic poro-elastic effects.

7.5.2 Kirchstockach site

At the Kirchstockach geothermal site, south of Unterhaching, the MAGS seismic catalogue contains a total of 33 induced microseismic events with $M_L < 0.8$ (not shown in Figure 7.7a)
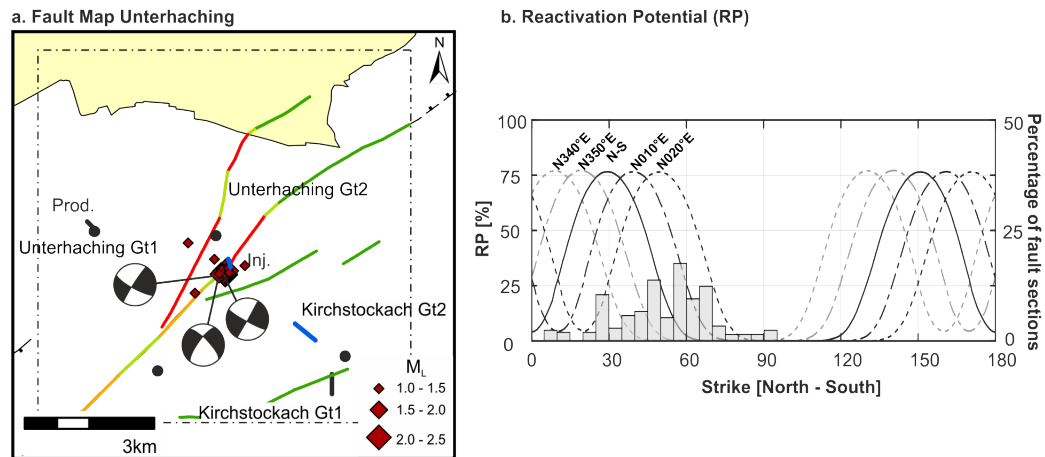
Figure 7.7 – Case study at the Unterhaching site for the reference parameter set (see Figure 7.3b). a. RP on the faults is scaled between 0 % (green) and 80 % (red). Black dots locate the well site (Unterhaching is drilled from two well sites, Kirchstockach from one), bolt black lines highlight the open hole section for production, blue bolt line the open hole section for injection and red symbols microseismic events with $M_L \geq 1$. b. Angular RP-distribution for stress rotation and histogram of the local fault strike.

and a significant location error (>500 m) (Megies et al., 2017). The events are located in the area of the injection well, but the seismic cloud indicates no connection to the neighboring N070°E Kirchstockach fault with generally low RP-values (0 % and 20 %). This low level of seismicity is in good agreement with the low angular sensitivity of μ, S_H and S_h for the reference parameters at N070°E (Figure 7.3a), which limits possible injection-induced effects on RP and major shear reactivation.

7.5.3 Poing site

The seismicity at the Poing site is characterized by a temporal delay. Five years after circulation started, first seismic activity was observed 1–2 km below the reservoir within the basement, at the western end of the "Markt-Schwabener Verwurf" (Figure 7.8a). After another 9–10 months, a second phase of seismic activity was observed in westward direction. The local fault structure is the western tail of the dominant N050°E–N060°E striking "Markt-Schwabener-Verwurf" which finally turns to the south (N020°E) next to the Aschheim Th1 well (Figure 7.8a). One well produces 85 °C hot water with a flow-rate of 100 l s^{-1} from the south, the second well injects cold water with $\Delta T = 35$ K into the "Markt-Schwabener-Verwurf". The seismic events are located along this structure, nearby the injection well with a location error of 100 m–500 m. Two events ($1.0 \leq M_L \leq 1.5$) in the north show location errors of 1.1 km and 2.9 km because the number of seismic stations was limited during the first detected events (Megies et al., 2017). A network improvement decreases the location error of the subsequent events. Focal mechanisms indicate a sinistral strike-slip displacement with a normal faulting component at N050°E–N060°E (Figure 7.8a), which agrees with a reactivation of this part of the "Markt-Schwabener-Verwurf". For the reference parameter set, the highest RP-values (RP 50 %–75 %) are observed at N020°E to N040°E near the production well of Aschheim Th1 and the lowest RP-values (RP < 10 %) at N050°E–N080°E, where the microseismicity was observed (Figure 7.8a). The P^C_{eff}-values for the fault segments with RP<10 % show an almost constant distribution at low RP-values (e.g.

see Fault 3 in Figure 7.2c).
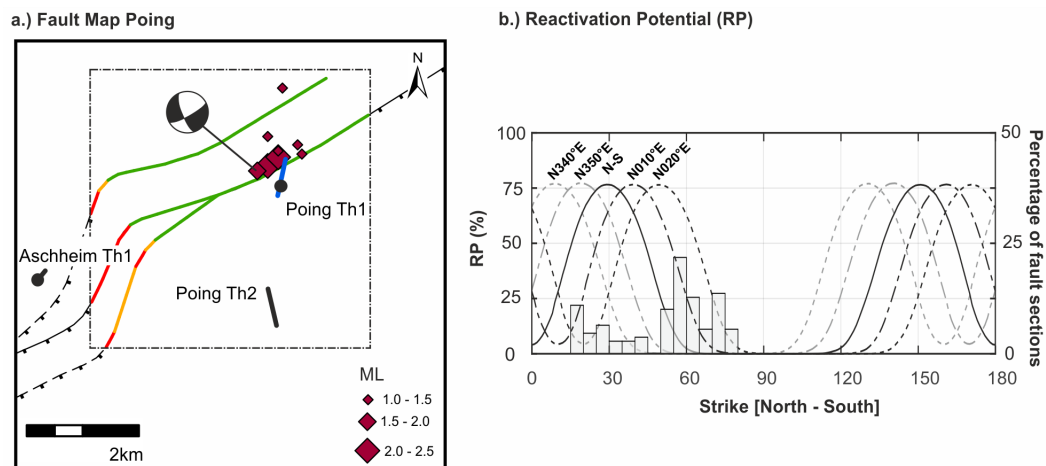
Figure 7.8 – Case study at the Poing site for the reference parameter set (see Figure 7.3b). a. RP on the faults ranges between 0 % (green) and 80 % (red). The black dots show the well site (Poing and Aschheim wells were drilled from one well site), the large black lines highlight the producing zones (note the Aschheim Th1 is nearly vertical), the large blue line highlights the open-hole section for injection and the microseismic events are shown in red with $M_L \geq 1$ b. Angular RP-distribution for stress rotation and histogram of the local fault strike.

Based on Reinecker et al. (2010), the regional S_H-orientation of the reference parameter set is proven, however there exists several indications for heterogeneous S_H-orientation within the Upper Jurassic reservoir or even deeper (Seithel et al., 2015). Note that stress field anomalies in the Bavarian Molasse Basin are detected at depth >2800 mTVD and no local information of the stress orientation at the Poing site exists.

The parameter study for the reactivated fault segment (N050°E–N060°E) shows highest sensitivity to μ, no sensitivity to S_H magnitude and dominant sensitivity to S_h magnitudes (Figure 7.3a). Since there is a direct connectivity to the basement through the injection well at the Poing geothermal site, the pressure changes from injection could be concentrated to the width of the fault zone. The poro-elastic coupling between stresses and increasing pore pressure could again lead to stress reorientations. However, these rotations – depending on the permeability at the location – could already occur at the early phases of the circulation and lead to a generally more critical stress state.

The temporal effect could result from two additional components (Kang et al., 2019): alteration of μ due to widely distributed dissolution and precipitation processes at the cold side of the geothermal doublet (Nitschke, 2017), and thermal stresses developing around the injection well.

7.6 DISCUSSION

The dissolution capacity of carbonate minerals is depending on the temperature difference, geochemical signature and reservoir lithology and will strongly affects the dissolution process near the injection well (Baumann et al., 2017). Such processes were detected e.g. at Pullach, Taufkirchen and Unterhaching, but no studies exists for the Poing site. Therewith, dissolution can change the reservoir permeability as well as the fault parameters in reservoir units with time. Our analysis indicates that for the reference parameter set

and faults without cohesion (e.g. $\mu = 0.7$ and $C = 0$ MPa) the RP-value, at a fault strike of N050°E − N060°E, is 0 % − 12 %. An alteration of the fault strength, which could decrease the coefficient of friction to 0.5 would drastically increase the RP-value to 70 % (Figure 7.4c). On the other hand, lower friction coefficient will also decrease the amount of strain energy stored in the matrix leading to lower elastic energy release in earthquakes (Kang et al., 2019). Such processes could explain the decline of microseismicity at the Unterhaching site after three years of injection.

Thermo-elastic effects along the cold water flow-path, at the geothermal reservoir, near the injection well, could potentially change the deviatoric stress (Segall & Fitzgerald, 1998) and lead to stress reorientations. Compared to hydraulic effects, these are slow processes which can be characterized by a transient and constant phase at a stable thermal front (Taron & Elsworth, 2009), and can initiate time-dependent local stress rotations (Ziegler, 2017). As shown in Figure 7.8b, stress changes by a minimum clockwise rotation of 20° results in an increase of the RP-values, at N060°E, up to 60°. The sensitivity study demonstrates that for such rotated stress conditions the sensitivity to μ increases and dramatically enhances the effect of altered fault zones. After operation started, physical processes can be separated by short-term like poro-elastic and mid-term like thermo-elastic effects (Taron & Elsworth, 2009). For the Upper Jurassic reservoir, it is demonstrated that the poro-elastic process is one order smaller than the thermo-elastic process which both stabilize after several years, however, the effects of geochemical dissolution would have an increasing impact (Rühaak et al., 2017). Our modelling highlights that, at the Poing injection well, induced fault alteration and thermo-elastic effects, by reservoir temperature change, potentially increase the RP-value of the fault structure to critical conditions.

At critical fault conditions, e.g. at the Unterhaching site, even minor stress changes resulting from poro-elastic coupling could be sufficient to trigger microseismicity (Schoenball et al., 2014). Stress modification is highly dependent on the permeability of the injection zone. This could mean that the injection zone at the Unterhaching site is presumably hydraulically connected with the low permeable basement over the major fault zone. Only at Poing, it is documented that the injection well reaches the basement. Goertz-Allmann et al. (2017) argue that induced seismic events are most likely below reservoir units inside of the under-burden basement. For the seismicity related to Arbuckle waste-water injection in the U.S.A.m it is concluded that pressure disturbances above the basement can reach and reactivate the basement faults at greater distance to the injection well (Schoenball et al., 2017). Despite of the high permeability of the Upper Jurassic reservoir and the small potential for increased pore pressure, it has to be clarified how far injection induced poro-thermo-elastic effects can be transferred into the basement.

7.7 Conclusion

The Bavarian Molasse Basin is one of the most favorable area in Europe for geothermal utilization. The geothermal development must, however, be accompanied by the development of detailed risk studies, especially in highly populated cities such as Munich and despite very good hydraulic properties of the reservoir.

In this context, our assessment of reactivation potential highlights the sensitivity of stress field modification and alteration processes at underground structures. As such, the knowledge of parameters like S_H, S_h and μ is of high importance to quantify seismic hazard associated with fault structures.

Given the observed seismicity pattern at the geothermal sites, our study can be considered to be a backward hazard analysis. On critically stressed faults, e.g. at the Unterhaching site, poro-elastic effects are sufficient to induce microseismic events during the first years of circulation. Injection induced perturbations of S_H, S_h or μ highly affect the RP-value. Given the – currently known – rather uncritical situation at Poing, longer term effects such as delayed stress field rotation by thermo-elastic effects and/or fault weakening by carbonate dissolution may also lead to fault failure. But after years of operation and the release of some microseismic events, e.g. at the Unterhaching site, a decline of seismicity is observed. However, more in-depth investigations are required in this context, especially concerning the evolution of stored strain energy. Additionally, approaches to model these processes and estimate their associated effects on the reactivation potential of the fault system of the greater Munich underground should be developed.

In future, we recommend to consider such RP-analysis at the earliest development stage of any geothermal project exploiting the Upper Jurassic reservoir. In this intensively utilized reservoir, long-term temperature and permeability monitoring as well as deformation – including seismicity – monitoring can build-up a scientific knowledge database, and cooperation of scientists with operators will maintain the high level of acceptance for this future-oriented technology.

Acknowledgements

8

Conclusion and Outlook

Based on the IPCC's formulated aim to regulate the climate warming to 1.5 °C (IPCC, 2018), the Munich Municipal Utility (SWM) has formulated the goal to cover the district heating demand of 100 % from renewable energies and to avoid any CO_2 emission. The required amount of heat is supplied with geothermal energy from the Upper Jurassic hydrothermal reservoir.

The Munich area is the second most developed region in terms of geothermal energy in Europe, with a significant higher potential for upgrading. However, frequent delays in the development of the reservoir within the Cenozoic Molasse sediments often increase drilling costs to unpredictable levels. Such problems are often caused by differential sticking, stuck pipe or problems setting the casings which indicates a number of open questions about well integrity (Seyberth, 2019). The high level of public acceptance of the geothermal use was partly disturbed by the release of microseismic events at several geothermal sites. Despite of the favorable conditions for non-pressured geothermal reservoir operation in the greater Munich, the unexpected microseismic events require a re-thinking of the reservoir operation concept by incorporating geomechanical approaches. As mentioned by Fjaer et al. (2008) and Zoback (2010) for use and sustainability of deep wells, geomechanical borehole and reservoir behavior during drilling and operation is essential to avoid unpredictable risks.

The decisive factor for safe and efficient reservoir operation is the detailed determination of the stress tensor components. Earlier studies are based on results from the 1950 and 1960 hydrocarbon exploration campaigns that limited the available database to the S_H-orientation (Reinecker et al., 2010). Only recently, data for geomechanical assessments have been gained in geothermal projects. Thus, and also due to the low natural seismicity there is less information about the stress regime and the S_v, S_h and S_H- components in the Bavarian Molasse Basin.

This study focuses on the description of the stress field based on the recorded and compiled geothermal exploration database in the last 15 years. It provides a unique regional database of formation integrity tests, leak-off pressures and cementation pressures (Table 1.3) that allows to interpret the S_h-magnitude for different stratigraphic and lithological units. In addition, one leak-off test allows an interpretation of the stress regime and the S_H-magnitude within the Cenozoic sediments. The Image log database (Table 1.2) measured in the Upper Jurassic reservoir provides insights into the stress regime and S_H-orientation within the geothermal reservoir surrounding the injection and production well. A geome-

chanical investigation of the reactivation potential at fault structures for geothermal sites discusses possible mechanisms to release induced microseismic events.

8.1 Major findings for the stress field in the Bavarian Molasse Basin

The objective of the first study (Chapter 5) was the detailed analysis of formation integrity tests (FIT), leak-off tests (LOT), cementation pressures and stimulation pressures from geothermal wells (Table 1.3) to assess the quality of the stress field determination. This evaluation resulted in a restriction of the entire database from 72 to 46 measurements. The remaining data set shows the highest significance for the interpretation of the S_h-magnitude. If for comparable lithologies and depths several tests had been available the results of the higher S_h-magnitudes have been selected. This selection is justified by the fact that the tests are often stopped at low pressures.

The lithology dependent analysis of the S_h-magnitude indicates a control factor of the sedimentological composition for the S_h-magnitude. Most tests on the clay-rich Cenozoic strata indicate a minimum S_h of 16.5 MPa km^{-1}, on the limestone to marlstone of Purbeck a minimum S_{hgrad} of 15.5 MPa km^{-1} and on the Upper Jurassic carbonates a minimum S_{hgrad} of 14 MPa km^{-1}. Assuming frictional equilibrium and hydro-static pore pressure, these stress gradients result in a friction coefficient of $0.2 < \mu < 0.4$ for the clay-rich Cenozoic layers and $0.4 < \mu < 0.6$ for the carbonate- dominated Mesozoic layers.

The detailed analysis of the LOT at 825 mTVD from the clay-rich Cenozoic layers yields a normal-faulting stress regime in the central Molasse basin (Appendix B). The data base lacks further LOTs which could quantitatively limit the significance of the depth and spatial distribution of the stress regime. But this study can disprove that the highly compressive character of the Cenozoic within the thrust front (Greiner & Lohr, 1980; Lemcke, 1973; Lohr, 1978; Reinecker et al., 2010) extends from the folded Molasse far into the foreland basin (see Figure 1.1). Drews et al. (2019a), Drews et al. (2018), Müller & Nieberding (1996), and Müller et al. (1988) claim that the overpressure within the lower Cenozoic layers is caused by disequilibrium compaction, indicating that the maximum principal stress at the time of compaction was vertical (S_v). Furthermore, seismic mapping of Cenozoic normal faults suggests that a normal-faulting stress regime was present during the Cenozoic history (Hartmann et al., 2016).

In the second study (Chapter 6), the Image log database (Table 1.2) was interpreted to analyze the distribution of borehole failure mechanism and derive stress field information for the Upper Jurassic reservoir. Borehole breakouts indicate a compression failure mechanism, drilling-induced tensile failure and drilling-enhanced natural fractures indicate tensile failure at the borehole wall. In total, A-& B-quality stress indicators were identified for 10 out of 17 wells, enabling high quality mis-fit gridding for the S_H-orientation. The results show an N–S S_H-orientation in five wells, a counterclockwise rotation of 15° in three wells and a rotation of 30° and 60° counterclockwise each in one well. In addition, the interpretation of the borehole failure mechanism gives a strike-slip stress regime in the Upper Jurassic reservoir with $1.1 < S_H/S_v < 1.56$.

The high-quality stress indicators (A-& B-quality) from this study confirm the observation of stress rotation in the Upper Jurassic from previous studies (Reinecker et al., 2010). Subsequently, the stress heterogeneity within the Upper Jurassic reservoir was further investigated in a numerically based sensitivity study. Here a geomechanical model is exposed to the stress state at a reference depth of 4000 m, the heterogeneous structure is characterized by a reduced stiffness and is rotated by a defined angle to the S_H-orientation. Based on various stiffness contrasts and orientations of the heterogeneous structure, type curves for the investigation of stress rotation in the Upper Jurassic reservoir are discussed.

Numerical studies show that counterclockwise rotation of the stress field can be caused by fault structures rotating clockwise of N000°E. The stiffness reduction at the deformation zones significantly changes the local stress orientation at N015°E to N045°E oriented fault structures, whereas at N060°E to N090°E structures the stiffness reduction has a minor effect on the stress field rotation.

The observed N–S S_H-orientation (no local stress rotation) at the N045°E oriented fault zone in Unterhaching indicates that there must be a high differential stress within the Upper Jurassic reservoir that prevents stress rotation. For the observation of a counterclockwise 30° stress rotation observed in Sauerlach, our study shows that such rotation is feasible if there is a N010°E - N020°E oriented fault with reduced stiffness. The combination of numerical modeling results and stress observations can not only help to explain the stress reorientations at some of the sites, but also provides further information on the tectonic stress regime (relative stress magnitudes). For example, in Unterhaching the high differential stress identified is only possible in a prevailing strike-slip regime.

The scientific basis of this study results from Heidbach et al. (2010) and Reinecker et al. (2010), in which a homogeneous N-S oriented stress field with a considerable compressive stress component within the Cenozoic Molasse sediments was formulated. Since geothermal development began in 2003, a significant amount of new borehole data has been collected. With the newly available database, I was able to gain the following new insights into the characterization of the stress field in the Bavarian Molasse Basin for the Greater Munich Area:

- ⋄ Within the Cenozoic filling I was able to show that a transtensional strike-slip to normal-faulting stress regime with a homogeneous N-S S_H-component exists.
- ⋄ Analysis of borehole failure in Image logs of the Upper Jurassic reservoir shows a strike-slip stress regime and a heterogeneous stress field orientation in some wells.
- ⋄ The horizontal differential stress magnitude ($S_H - S_h$) is increasing from the Cenozoic to the Upper Jurassic.
- ⋄ Local variations of the S_H-orientation and numerical analysis of the stress rotation show that stiffness contrast in fault structures as wells as strong variations of the petrophysical reservoir parameters seem to be responsible for the heterogeneous stress field in the Upper Jurassic.

8.2 Geomechanical significance for the geothermal reservoir utilization

Geothermal operation in the Bavarian Molasse Basin must, be accompanied by the development of detailed risk studies, especially in highly populated cities such as Munich despite very good hydraulic properties of the reservoir. In this context, the assessment of the reactivation potential is of great importance and depend on stress field changes and alteration processes at subsurface structures. The sensitivity analysis performed in the third study emphasizes the understanding of parameters such as S_H, S_h and μ, which are of great importance for the evaluation of the seismic hazard of fault structures.

This study can be considered as an analysis for preliminary study of a risk analysis for the observed seismicity pattern at the geothermal sites of the Bavarian Molasse Basin. In the case of critically stressed faults, e.g. at the Unterhaching site, poro-elastic effects are sufficient to produce microseismic events even under the good hydraulic conditions in the Upper Jurassic. However, after years of operation and the triggering of some microseismic events, e.g. at the Unterhaching site, a decrease in seismicity can be observed. This can be the result of an underground stress relief by microseismic deformation or a shift of the deformation mode from seismic to aseismic deformation. In view of the – currently known – rather uncritical situation at Poing, long-term effects such as delayed stress field rotation due to thermo-elastic effects and/or fault weakening due to carbonate dissolution can lead to a failure.

Such microseismicity, as observed in the Bavarian Molasse Basin, can be induced at the injection well by changing the effective stress (Segall & Fitzgerald, 1998; Taron & Elsworth, 2009), altering the fault zone parameters by carbonate dissolution capacity of the injection fluid (Baumann et al., 2017), or mechanically changing the friction parameters by releasing microseismic deformation (Kang et al., 2019). In this context, however, more in-depth investigations are necessary, especially with regard to the developments of the stored strain energy.

In order to understand the processes that trigger microseismicity in the Bavarian Molasse Basin, it is of great importance to improve the depth and spatial resolution of the seismic network. Past research projects show significant site-dependent location errors of seismic events (Megies et al., 2017; Megies & Wassermann, 2013). Only at two sites (Poing and Unterhaching) can this location error be reduced and the earthquake location determined at 500 to 1000 m below the reservoir.

The earthquake location in the basement and the minimal pressure impulse at the injection well in the Upper Jurassic raises some open questions. If a fault zone is under critical stress conditions, e.g. at the Unterhaching site, even minor stress changes due to poro-elastic coupling may be sufficient to trigger microseismicity (Schoenball et al., 2014). However, the effective change in stress is strongly dependent on the permeability of the injection zone. This can be interpreted in such a way that the injection zone at the Unterhaching site is probably hydraulically connected to the low-permeable basement via the main fault zone. Only at Poing is it documented that the injection well reaches into the basement. Goertz-Allmann et al. (2017) argue that induced seismic events are most

likely to occur below reservoir units within the basement. For seismicity in connection with Arbuckle waste-water injection in the USA, it is concluded that pressure perturbations above the basement can reach and reactivate basement faults at a greater distance from the injection well (Schoenball et al., 2017). Despite the high permeability of the Upper Jurassic reservoir and the lower potential of increased pore pressure, it must be clarified to what extent injection-induced poro-thermo-elastic effects can be transferred into the basement.

Until this study, few geomechanical research was conducted, as minimal natural seismicity was observed in the Bavarian Molasse Basin and the highly productive reservoir is dominated by lithofacies porosity or secondary dolomitization without significant injection pressure. On the basis of Reinecker et al. (2010) a homogeneous N-S oriented stress field was assumed and thus most fault structures in the Bavarian Molasse Basin (oriented WSW-ENE) were considered with less potential for seismic reactivation. However, since the operation of geothermal energy in Unterhaching in 2008 triggered microseismicity for the first time, there is public interest in a better understanding of the reactivation process of seismic deformation. The key insights for a secure reservoir operation are:

◇ The homogeneous N-S oriented S_H-component is useful at the regional scale, but at the local scale the stress rotation could be most significant near reservoir structures and the injection well.

◇ Under critical fault conditions, e.g. at Unterhaching site, the seismic deformation in the fault structure area, which may be triggered by direct poro-thermo-elastic effects, changes into a phase with aseismic deformation.

◇ At the Poing site, the time delay of five years of the first microseismic detection at a fault structure with uncritical conditions indicates long-term injection-related effects.

◇ Possible local injection induced thermo-elastic effects can cause a stress rearrangement or the geochemical dissolution can change the fault strength, both potentially leading to seismic deformation.

This thesis underlines the importance of the existence of a good stress field database to better define the stress magnitudes and the stress rotation and thus the fault reactivation potential. Furthermore, seismic network optimization could help to provide a well-suited microseismic catalogue for the spatial interpretation of the focal mechanism solutions, providing additional information on the stress field. The fault reactivation and the frictional strength strongly depends on the fault parameters. Geochemical alteration processes or deformations, cause time-dependent changes of fault parameters, that also influence the probability of seismic events.

We propose a model approach to capture these processes and estimate the associated effects on the reactivation potential of the Munich underground fault system. For the future, we recommend that such an analysis be considered at the earliest stage of any geothermal project.

In this intensively used reservoir, long-term temperature and permeability monitoring as well as deformation and seismicity investigations can contribute to a better understanding of the coupled reservoir processes. Through the cooperation of scientists with operators, the high level of acceptance and development of this forward-looking technology can be further expanded.

Stress anomaly in the Bavarian Molasse Basin

Abstract

Background: The characterization of fault zones in the Bavarian Molasse Basin plays a major role for further geothermal reservoir development. Hence, their identification, geological origin, and hydraulic characterization are discussed extensively.

Methods: Stress indicators and fractures are interpreted from image and caliper logs of three highly deviated wells at the Sauerlach site. We transform the identified stress field into the borehole coordinate system and compare the observed orientation to the modeled stress field which assumes a homogeneous borehole surrounding.

Results and discussion: High breakout occurrence, cross-cutting fractures, and a fracture orientation from N–S to NNE–SSW are observed in Sauerlach Th1. In Sauerlach Th2 and Th3 fractures strike primarily ENE–WSW and N–S to NNE-SSW. Drilling-enhanced natural fractures and drilling-induced tensile fractures are observed in all three wells and indicate the orientation of tensile stress at the borehole wall. In Sauerlach Th2 and Th3 stress transformation indicates a S_H-dir. ∼ N010°E in a strike-slip stress regime. The modeled stress orientations match the observed orientations within the well Sauerlach Th1 if either S_H-dir. is N320°E in a strike-slip regime or S_H-dir. is N010°E in a normal faulting regime.

Conclusion: This approach improves the detection of the local stress field especially for non-vertical wells, which has, in combination with the fracture pattern, a major impact on the hydraulic system of the geothermal reservoir.

Keywords: Fault zone; Stress regime; Stress indicator; Borehole wall; Static friction coefficient

A.1 Background

The use of geothermal energy in the Bavarian Molasse Basin started in the late 1990s when first district heating projects emerged. To encourage further development of geothermal energy use, the Bavarian Geothermal Atlas was published in 2004. Indeed, this led to

an increased exploration activity for heat and power generation. For geothermal district heating projects, an incentive program followed on the national level, resulting in a total of 12 successfully developed district heating projects with an installed thermal capacity of 141.1 MW$_{th}$ so far. After the first power generation project in 2004, three more projects followed after 2008/2009 in the area south of Munich, the installed capacity being 22.6 MW$_{el}$ and 42 MW$_{th}$ (Dorsch & Pletl, 2012; GTV, 2014).

The Bavarian Molasse Basin offers favorable conditions for the utilization of geothermal energy. Among a total number of 46 wells, 44 were operated successfully. The initial exploration strategy focused on faults and fault zones. They were identified mainly based on old seismic industry data showing an offset of significant reflectors especially at the base of the Tertiary strata. With advancing reservoir knowledge resulting from the evaluation of the drilled geothermal wells and the acquisition of new seismic data, the lithofacial aspects of the Malm reservoir were studied. The findings were incorporated in the exploration strategy (Boehm et al., 2012; Lüschen et al., 2014). Nevertheless, the two failed drillings still give rise to questions with respect to diagenetic processes, along with dolomitization as well as hydraulically active fractures and faulting. A key aspect towards an improved evaluation of reservoir rock properties of the Malm is the integration of stress field parameters, since critically stressed fractures are known to be more often hydraulically active than uncritically stressed fractures (Barton et al., 1995).

It is well known that the major geothermal provinces are located at structurally favorable settings dominated by step-over / transferring, overlapping or terminating normal faults. They are preferably striking parallel to the maximum horizontal stress (Faulds et al., 2011). The majority of the Molasse Basin fault zones identified are ENE–WSW-trending normal faults (Lemcke, 1988). In relation to the roughly N–S oriented maximum horizontal stress (Reinecker et al., 2010), the N–S or NNE–SSW (~ N30°E) oriented fracture systems show a high tendency to develop tensile or shearing character. Recent seismic investigations revealed inhomogeneities near normal faults, which may have a significant impact on the hydraulic properties of the reservoir (Lüschen et al., 2014).

In order to study fracture systems, stress indicators, and facies structures within the reservoir image logs can be used (Hickman & Zoback, 2004; Shamir & Zoback, 1992). This study covers three wells of the Sauerlach site with highly deviated reservoir sections. Their fracture sets as well as stress indicators (Drilling Induced Tensile Fractures (DITF), Drilling-enhanced Natural Fractures (DENF), and Breakouts (BO)) are interpreted in the image logs. For highly deviated wells, in-situ stress interpretation based on stress indicators is carried out by transforming the regional stress field into the wellbore coordinate system. Our approach is to compare the observed orientations from the different stress indicators with the calculated (modeled) stress orientations. For the regional stress field we generally assumed a strike-slip stress regime (Reinecker et al., 2010). The difference between the orientation of the interpreted stress indicators and the calculated stress distribution in the well can be determined. By varying the stress regime, the difference between the observed and calculated stress direction is minimized to study the local stress field near the wells.
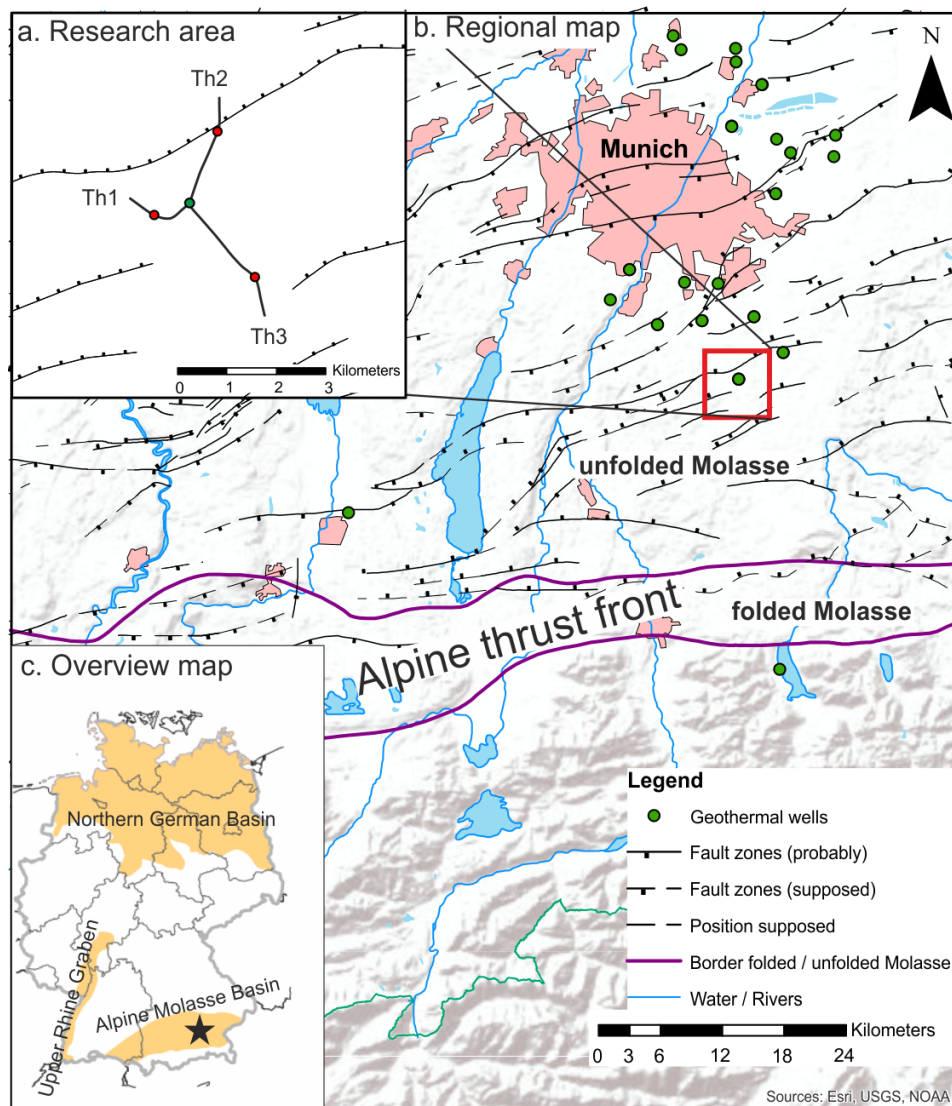
Figure A.1 – Study area and tectonic background. a. Map with well trajectories of Th1, Th2, and Th3 and the top of the reservoir section marked by red points as well as fault zones of the Geothermie Atlas (STWIVT, 2010). b. Map of the region south of Munich with the tectonic sections of the unfolded and folded Molasse Basin, geothermal wells, and the fault zones found in the tertiary structures of the Geothermie Atlas. c. Overview map from Geotis (Schulz et al., 2009) and the investigation area marked by a black asterisk.

A.2 Technical data and geological situation

A.2.1 The Geothermal Sauerlach Project

We analyzed data from the geothermal project at Sauerlach which is situated southeast of Munich. It is one of the biggest heat- and power-supplying geothermal projects in Germany (GTV, 2014) and is operated by the Munich utility company Stadtwerke München. Three wells, two for injection (Sauerlach Th2 and Th3) and one for production (Sauerlach Th1), were drilled in 2008 and 2009. The production yield is $110\,\mathrm{l\,s^{-1}}$ with a temperature of $140\,°C$ from the 4 km deep reservoir (Pletl et al., 2010). Under present conditions, an about $4\,\mathrm{MW_{el}}$ of electrical power and a maximum heat production of $4\,\mathrm{MW_{th}}$ ($4\,\mathrm{GW\,h\,a^{-1}}$) are supplied. The plant has been connected to the grid since spring 2014.

All three wells are drilled from one drill pad with a nearly vertical orientation down

to 1000 m depth. Starting with the third well section, they are inclined in the direction of the reservoir targets: Sauerlach Th1 is oriented to NW–SE (N300°E) with an inclination between 50°–60° (from the vertical) and reaches the reservoir at a depth of 3739 mTVD (Figure A.1a / red point). Sauerlach Th2 reaches the reservoir at 3571 mTVD (Figure A.1a / red point) and is directed towards N (N0°E) with an inclination between 40°–60°. Sauerlach Th3 reaches the reservoir at 3872 mTVD and is oriented to SSE (N160°E) (Figure A.1a / red point) with an inclination between 35°–60°.

Directly after drilling, 6-arm caliper (Schlumberger EMS-GR) and image logs (Schlumberger FMI) were measured to image the borehole wall. In addition, drilling safety tests, such as formation integrity tests (FIT), and the reports of cementation jobs revealed borehole pressure data indicating the lower bound of the minimum principle stress magnitude.

Well test analysis shows a considerably higher productivity of Sauerlach Th1 compared to Sauerlach Th2 and Th3, although permeability values of the reservoir in all three wells were similar. A dominant radial flow regime underlines the significance of matrix porosity to reservoir characterization in all three wells during expansion of the depression cone. However, additional to its better productivity, Sauerlach Th1 stands out with its very high negative skin effect at the very beginning of pumping, which is an indicator of a good hydraulic connection between the borehole and the reservoir (Savvatis, 2014).

Table A.1 – Database for structural and stress interpretation of well logs.

Well	Tool	Hole Diameter	Hole azimuth / inclination	Depth intervall (MD)	(TVD)
Th1	EMS-GR (6-arm caliper)	23″	vertical	49 m–987 m	49 m–987 m
	EMS-GR (6-arm caliper)	16″	vertical	982 m–2351 m	982 m–2351 m
	EMS-GR (6-arm caliper)	12″	vertical to 230°–290°/45°	2346 m–3990 m	2351 m–3739 m
	FMI	8 1/2″	300°/45°–60°	3981 m–4757 m	3739 m –4177 m
Th2	FMI	8 1/2″	0°/45°–60°	4025 m–4850 m	3571 m–4086 m
Th3	FMI	6 1/8″	160°/45°–60°	4343 m–5490 m	3872 m–4438 m

A.2.2 Reservoir geology

The Upper Jurassic (Malm) forms the major hydrothermal reservoir in the Bavarian Molasse Basin. In the Munich area it reaches depths between 2000 to 4000 m, while the thickness is about 550 m. With temperatures between 80 to 140 °C and a low salinity, favorable conditions exist for heat and power generation (STWIVT, 2010). The Malm is located below the Bavarian Molasse Basin as part of the North Alpine Foreland Basin. The Bavarian Molasse Basin evolved as a typically wedge-shaped foreland basin from the Upper Eocene to the Upper Miocene in response to Alpine tectonics accompanied by erosion and uplift (Kuhlemann & Kempf, 2002).

Hydrogeologically speaking, the Malm exhibits the behavior typical of carbonatic aquifers, with a complex interaction of karstification, fracture, and matrix porosity, where structural and lithofacial properties determine the productivity of the wells (Lüschen et al., 2014; Steiner et al., 2014).

The Malm lithology is characterized by two major sedimentation cycles with marls and marly limestones in Malm alpha and gamma and predominantly limestones in Malm beta

and delta/epsilon. Within the younger Malm zeta, a diversification of the sedimentary environment took place (Meyer & Schmidt-Kaler, 1989). During the latest Jurassic and earliest Cretaceous, sedimentation changed to a brackish or hypersaline "Purbeck" facies. Since these units are both carbonatic and cannot be separated in the seismic data, the latter is considered as a part of the Malm reservoir (Lemcke, 1988).

Regarding the lithofacies of the Malm, two types of hyper-facies are distinguished: The so-called "bedded facies" with typically thin-bedded marly or micritic limestones and the so-called "mass facies" with thick-bedded limestone or dolomitic units and reef structures. Boehm et al. (2012) pointed out that in the Munich region, favorable reservoir properties can be expected from dolomitized limestones in the mass facies of the Malm zeta and in the Malm delta/epsilon due to parts having a favorable matrix porosity. In addition, the massy dolomitized limestones tend to have karstification potential (Stier & Prestel, 1991) and also show a higher fracture density under structural impact due to more brittle properties.

Structurally speaking, the Bavarian Molasse Basin has undergone different tectonic stages of compressive and extensive regimes (Ziegler, 1987). The tectonic map at the base Tertiary published in the geothermal atlas (STWIVT, 2010) shows a dominant WSW–ENE system in the Munich area (Figure A.1b). It consists mainly of antithetic normal fault systems with displacements of up to 150 m, which are oriented parallel to the Alpine Orogen due to basin subsidence as well as subduction in the south (Bachmann et al., 1987). During the Upper Miocene, the compressive regime started with thrust faulting forming the folded Molasse with still a high pore pressure declining into the unfolded northern foreland (Müller et al., 1988).

It is still being discussed where and to what extent the younger alpine tectonics affects the unfolded foreland, since fracture porosity can be influenced significantly by the activity of faults. Previous publications of Betz & Wendt (1983) and Illies et al. (1981) presented conjugated lineament sets from satellite imagery in the western and Unger (1999a) described a set of strike-slip faults in the eastern part of the Bavarian Molasse Basin. Kraemer (2009) identified strike-slip faults in the SW of Munich close to the Alpine forefront. Megies & Wassermann (2014) analyzed recent seismic activity and concluded a NW–oriented strike-slip movement who identified a N20°–45°E fault system from 3D seismic measurements (Lüschen et al., 2014).

The present-day maximum horizontal stress orientation in the Bavarian Molasse Basin is roughly perpendicular to the strike of the Alpine front, indicating that the first-order, far field tectonics in Western Europe is less dominant in the area than the second- and third-order stress pattern (Tingay et al., 2006). A regional study of the stress field in the Bavarian Molasse Basin based on breakout analysis by Reinecker et al. (2010) revealed a rather homogeneously distributed N–S-oriented S_H with a dominating strike-slip or thrust faulting stress regime.

For the WSW–ENE-oriented fault systems, a limited reactivation potential can be assumed. The hydraulic potential of these faults probably is also limited. Consequently, faults related to a strike-slip regime as identified by the analysis of focal mechanisms of seismic events (Megies & Wassermann, 2014) would also be of importance to geothermal exploration.

A.3 STRESS DATA ANALYSIS

A.3.1 DETERMINATION OF THE LOCAL STRESS FIELD

The stress field can be divided into first-order stresses as a result of forces generated at plate boundaries by e.g. global lithospheric motion and second-order stresses resulting from lithospheric flexure e.g. due to glacial loading and unloading or lateral density contrasts (Zoback, 1992). On a local scale, third-order stresses in sedimentary basins are controlled by geological structures (Bell, 1996). On the reservoir scale, active faults, lateral or vertical contrasts in material parameters (for example, salt structures, decoupling horizons) can lead to mechanically modified parameters and deviations of the stress orientation and tectonic regime from the regional or plate-wide stress pattern (Tingay et al., 2006).

According to Anderson (1951), three tectonic regimes can be distinguished based on the magnitudes of the vertical stress (S_v), the maximum horizontal stress (S_H), and the minimum horizontal stress (S_h). In a normal faulting regime (NF) S_v is the maximum principle stress (S_1). It is the intermediate principle stress (S_2) in a strike-slip regime (SS) and the minimal principal stress (S_3) in a thrust faulting regime (TF). In regions with little topography, it is common to assume S_v to be a principal stress.

In areas where no data of the stress magnitude are available, a method known as frictional equilibrium theory can be applied to reduce the range of possible stress ratios (Sibson, 1974). Differential stress ($S_1 - S_3$) magnitudes in the brittle crust are limited by the frictional strength of optimally oriented faults (Jaeger et al., 2007). Byerlee (1978) has shown in laboratory tests that the coefficient of static friction (μ) is independent of the rock type, but depends on the magnitude of normal stress. Accordingly, for normal stress greater than 200 MPa, the coefficient of static friction of $\mu = 0.6$ fits best and for lower normal stress $\mu = 0.85$ can be applied. On the basis of the frictional equilibrium theory, stress polygons for frictionally stable areas in different stress regimes and possible horizontal stresses (S_H and S_h) can be defined (Zoback et al., 2003). In Figure A.4a the stress polygon for both static friction coefficients ($\mu = 0.6$ and $\mu = 0.85$) is shown. The determination of the stress components requires a number of theoretical considerations and a reliable data assessment. The S_v component can be estimated from the density of the overburden. Pore pressure (P_p) can be estimated by hydraulic pumping tests or pressure measurements in the wells and S_h can be estimated from the vertical stress by making certain assumptions (e.g. no lateral strain), if measurements, such as mini-fracs or leak-off tests are not available (Hubbert & Willis, 1972; Zoback, 2010). If FIT or cementation reports are available, it is also possible to calculate a minimal value for the least principal stress, which helps to define a lower limit of the stress gradient (Zoback et al., 2003).

In this study, stress-induced phenomena, such as DITF, DENF, and BO recorded at the borehole wall by both FMI and 6-arm caliper logs were used. The stress state in a borehole with its circumferential / tangential ($\sigma_{\theta\theta}$) and radial stress (σ_r) components are described by Kirsch (Kirsch, 1898) for a vertical well. For inclined wells, further computations with an analytical solution for the stress distribution are needed (Hiramatu & Oka, 1968). According to these computations, the orientation of BO and DITFs does not only vary with the stress magnitudes, but also with the orientation of the borehole trajectory relative to the stress

tensor (Mastin, 1988). Peska & Zoback (1995) described a method to determine the direction of the maximal (σ_{tmax}) and minimal tangential stresses (σ_{tmin}) in deviated boreholes for effective stresses ($S_s = S - P_p$). It consists in a transformation of the principal stress tensor (S_s) into the stress tensor in the geographic coordinate system (S_g) using the transformation matrix R_s. Then, S_g is transformed into the cylindrical borehole coordinate system (S_b) by R_b. The complete transformation from principal (S_s) to geographic (S_g) and to the borehole coordinates (S_b) is:

$$S_b = R_b \, R_s^T \, S_s \, R_s \, R_b^T \tag{A.1}$$

The stress state in the cylindrical borehole coordinate system (S_b) is referred to an angle θ, which is rotated in clockwise direction from the Bottom of Hole (BOH) or Top of Hole (TOH) along the borehole axis, respectively. The following equations describe the cylindrical stress defined by Peska & Zoback (1995). Note the correction required for the Poisson's ratio (ν) and the pressure difference (ΔP) between mud pressure and P_p (Zoback, 2010):

$$\sigma_{zz} = \sigma_{33} - 2\nu \left(\sigma_{11} - \sigma 22\right) \cos 2\theta - 4\nu \sigma_{12} \sin 2\theta \tag{A.2}$$

$$\sigma_{\theta\theta} = \sigma_{11} + \sigma_{22} - 2\left(\sigma_{11} - \sigma_{22}\right) \cos 2\theta - 4\sigma_{12} \sin 2\theta - \Delta P \tag{A.3}$$

$$\sigma_{\theta z} = 2\left(\sigma_{23} \cos \theta - \sigma_{13} \sin \theta\right) \tag{A.4}$$

$$\sigma_r = \Delta P \tag{A.5}$$

where σ_{zz} is the stress in axial direction, $\sigma_{\theta\theta}$ the stress tangential to the borehole, and $\sigma_{\theta z}$ represents the shear stress. The maximum (σ_{tmax}) and minimum tangential stresses (σ_{tmin}) are defined by:

$$\sigma_{tmax} = 1/2 \left(\sigma_{zz} + \sigma_{\theta\theta} + \sqrt{\left(\sigma_{zz} - \sigma_{\theta\theta}\right)^2 + 4\theta_{\theta z}^2}\right) \tag{A.6}$$

$$\sigma_{tmin} = 1/2 \left(\sigma_{zz} + \sigma_{\theta\theta} - \sqrt{\left(\sigma_{zz} - \sigma_{\theta\theta}\right)^2 + 4\sigma_{\theta z}^2}\right) \tag{A.7}$$

In order to determine the angles of σ_{tmax} and σ_{tmin}, θ is varied in 0.2° steps from 0° to 360°. This enables us to determine the direction of the maximum of σ_{tmax} ($\theta_{maxmodel}$) and the minimum of σ_{tmin} ($\theta_{minmodel}$). From this "forward modeling", the compressive σ_{tmax} as well as tensile stresses σ_{tmin} and their orientations ($\theta_{maxmodel}$ /$\theta_{minmodel}$) are determined for a given well trajectory in an arbitrary stress field (see Chapter A.4.2). For the Sauerlach well trajectories, the stress distributions is calculated for the well surface and compared to stress indicators like DITFs, DENFs, and BOs. This "stress inversion" is applied in Chapter A.3.1.

A.3.2 STRESS INTERPRETATION APPROACH

Information on the stress distribution in the Sauerlach project area was derived from oriented caliper measurements with EMS-GR-tools available for the 1st, 2nd, and 3rd sections of Sauerlach Th1 and from image measurements from FMI-tools for all three wells of the reservoir section (see also Table A.1). Oriented caliper tools measure mechanically the diameter of the borehole and link it with geographical information. The FMI-tool measure the resistivity of the borehole wall in high resolution and display an oriented

borehole resistivity wall image on this basis.

In image log data natural fractures can be detected by their fracture resistivity contrasting to the surroundings and sinusoidal trace. Completely sinusoidal features with low resistivity (open fractures filled with mud) are distinguished from sinusoidal features, which only show a low resistivity in some areas (partly open fracture filled with mud), and sinusoidal features of higher resistivity than the formation (closed / healed fracture) (Trice, 1999). Since the distribution of fracture orientation identified from the image log depends on the angle ($d°$) between the fracture plane and the well trajectory, a bias correction for the fracture density, called "Terzaghi correction", is applied (Terzaghi, 1965). As a threshold for bias correction it is used a value of $d° < 15°$. BO occur when σ_{tmax} exceeds the rock mass strength. They occur in the direction of maximum tangential stress θ_{max} (Bell & Gough, 1979). These structures can be detected by caliper or image logs or borehole televiewer tools. For the present study, the "SAC" 6-arm caliper interpretation software was used (Wagner et al., 2004) and the criteria given by Reinecker et al. (2016) for 4-arm caliper tools were adapted to the 6-arm caliper tools. Averaging was performed using the circular statistics of Mardia (1972). BO analysis in image log data were described as blurry, conductive, symmetrical features (Figure A.2a) by Bell (1996).

During the process of drilling in highly fractured reservoirs, stress rearrangement at the borehole wall can enhance existing fractures in the direction of σ_{tmin} (θ_{min}). Barton & Moos (2010) call these fractures drilling-enhanced natural fractures (DENF). These structures are relatively short segments of fine-aperture natural fractures, which are not visible as complete sinusoidal traces (Figure A.2c). DENFs are aligned to existing sinusoidal traces and can be fitted by flexible sinusoidal traces (Barton & Moos, 2010). Due to the interaction of fracture planes and tensile stress, it is sometimes difficult to precisely determine the orientation of the tensile areas with DENFs. In comparison to DENFs, DITFs occur as axisymmetric pairs parallel to the borehole axis. They are formed when σ_{tmin} reaches the tensile strength of the rock mass (Barton & Moos, 2010) and are promoted by cooling down the well or increasing the mud weight (Davatzes & Hickman, 2010). For wells that are inclined to one principal stress axis, DITF occur as en-echelon sets of fractures (E-DITFs) at a small angle to the borehole axis (Peska & Zoback, 1995). Thus, axial fractures or E-DITF in combination with knowledge of the well trajectory indicate the principal stress direction. Petal-centerline fractures are features which develop during the drilling process in front of the drill bit in the plane of S_H due to enhanced tensile stress. They can propagate into DITFs. The difference is that they develop as complex, non-planar features that typically are not coaxially oriented to the borehole (Davatzes & Hickman, 2010). These features might be, but not used in the dataset and can be responsible for data scattering of drilling induced features.

In this study, we focus on DENFs and DITFs identified in the Sauerlach wells to analyze the orientation of σ_{tmin} (θ_{min}) and BO in order to determine the orientation of σ_{tmax} (θ_{max}) in the borehole coordinate system. These data observed are finally compared to the modeled stresses as described above (Chapter A.3.1) and discussed.
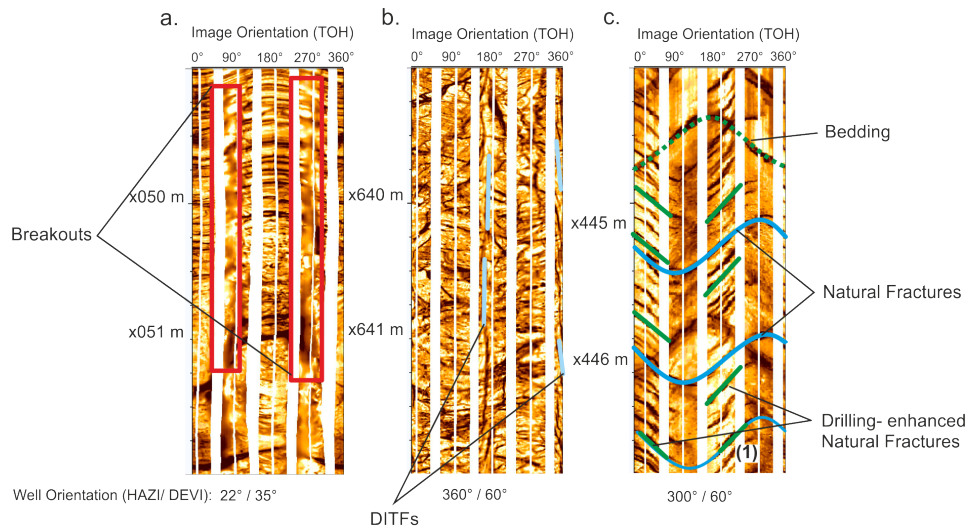
Figure A.2 – Typical stress indicators found in FMI logs. a.) Axially oriented breakouts with blurry appearance in the directions of 90° and 270° TOH. b.) Drilling-induced tensile fractures (DITFs) occurring as axial fractures in the directions of 180° and 355° TOH parallel to one principal stress. c.) Drilling-enhanced natural fractures (DENF) appear as inclined non-continuous fractures (green line) next to continuous natural fractures (blue sinusoidal curve) in the directions of 190° and 15° TOH. (1) shows the alignment of these features to existing natural fractures. Bedding planes (green dotted sinusoidal curve) crosscutting the fracture planes are unaffected by stress-induced borehole wall features.

A.3.3 STRESS REGIME

The orientation of the identified BO as derived from the interpretation of the 6-arm caliper measurements in Sauerlach Th1 is presented in Figure A.3. From the top to 500 mTVD, numerous washout zones can be seen, which limit the interpretation and cannot be included in the results. From 500 mTVD to 2600 mTVD, clearly identifiable BO zones exist. An inclination built-up beginning from 2400 mTVD to more than 20° from vertical, however, makes further BO interpretation due to severe tool decentralization impossible (Figure A.3). The 220 BOs identified with a total length of 625 m indicate an S_H-direction of approximately N–S ($N7.5°E \pm 9°$).

The section where image logs are acquired ranges from a depth of 3700 to 4100 mTVD. This open-hole section is highly deviated and covered by mainly Cenozoic compacted sand and clay stones. For this coverage no density measurements were performed. Thus, for these sedimentary layers we assume a mean density of 2300 kg m^{-3} (Fjaer et al., 2008). At reservoir level (4000 mTVD) S_v will be 92 MPa with a stress gradient of 23 MPa km^{-1} (cf. Figure A.4b). Due to low topography and investigations of focal mechanisms (Megies & Wassermann, 2014) the vertical stress can be considered as a principal stress at the Sauerlach site.

Pore pressure measurements were conducted after drilling at 3450 mTVD and reveal a static P_p of 31.6 MPa 550 m above the reservoir and a groundwater level of 225 m below surface. To extrapolate P_p to reservoir depth (4000 mTVD) a low mineralized model water with $\rho = 1.000\,227$ g cm^{-3} (10 °C, 1 bar) is used. So the P_p can be extrapolated to 37 MPa (0.4 S_v) at a depth of 4000 mTVD, which results in a gradient of 9.814 MPa km$^{-1} - 2.25$ MPa (Figure A.4b).
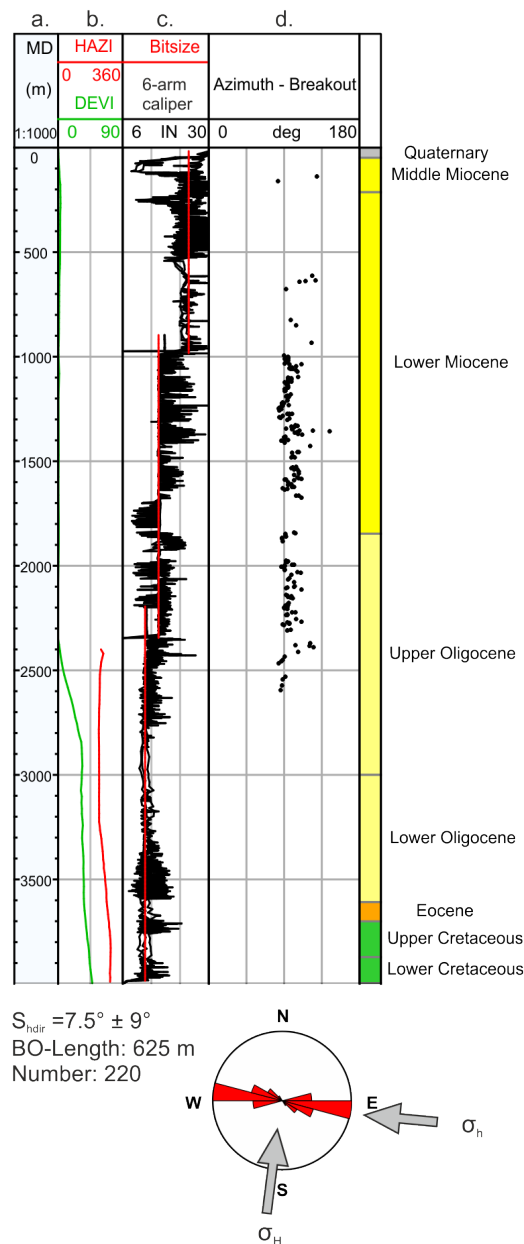
Figure A.3 – Breakout data measured by oriented six-arm caliper tools in the 1st, 2nd, and 3rd sections of well Th1. Column a.) Well trajectory data, the 1st and 2nd sections are nearly vertical, in the 3rd section well inclination is increased to 45° with an azimuth of 230°– 290°. Column b.) Caliper diameter (black lines) and bitsize diameter (red line), the bitsize decreases from 23″ in the 1st section to 16″ in the 2nd section and 12″ in the 3rd section. Column c.) Breakout azimuth (0°– 180°) determined with the 'SAC' software (Wagner et al., 2004), increasing well inclination at 2700 mMD makes breakout interpretation impossible because of tool decentralization. Column d.) Stratigraphic units: Upper Freshwater Molasse (OSM), middle Miocene to upper Lower Miocene (50 m – 500 m) is characterized by numbers of washouts; Upper Marine Molasse (UMM) at the middle Lower Miocene (500 m – 800 m), good well stability and less breakouts are observed; Lower Freshwater Molasse (USM), the middle Lower Miocene to the Lower Oligocene (800 m – 2800 m), clear breakout orientation, high number of breakouts.

Technical drilling operations like FIT and cementation pressures from the Sauerlach drillings help to estimate the lower boundary of S_h within the Molasse sediments. In Figure A.4b test pressures are illustrated as S_h/FIT and S_h/Cem. They show a mean S_h gradient of about 15.5 MPa km^{-1} (Figure A.4b).

S_H is determined by applying the stress polygon method (Zoback et al., 2003). For a given depth (here, we use the mean reservoir depth of 4000 mTVD), the gradients of S_v, P_p (introduced in the previous paragraphs), and the static friction coefficient (μ) give the frictional limits for S_H as well as S_h for each stress regime (NF, SS, TF) (Figure A.4a). According to Jaeger et al. (2007), the stress limits for optimally oriented faults can be described by the static friction coefficient, as it is exemplarily done for $\mu = 0.6$ (lower static friction coefficient according to Byerlee (1978).

$$\frac{S_1 - P_p}{S_3 - P_p} = \left[(\mu^2 + 1)^{1/2} + \mu \right]^2 \tag{A.8}$$

for $P_p = 0.4 S_v$, $\mu = 0.6$

$$S_1 + 0.85 * S_v = 3.12 * S_3 \tag{A.9}$$

For normal-faulting ($S_v > S_H > S_h$), strike-slip faulting ($S_H > S_v > S_h$), and thrust-faulting ($S_H > S_h > S_v$), the limits can hence be defined as:

$$S_h = 0.58 S_v \qquad (S_1 = S_v; S_3 = S_h) \qquad (NF) \tag{A.10}$$

$$S_H = 3.12 S_h - 0.85 S_v \qquad (S_1 = S_H; S_3 = S_h) \qquad (SS) \tag{A.11}$$

$$S_H = 2.27 S_v \qquad (S_1 = S_H; S_3 = S_v) \qquad (TF) \tag{A.12}$$

In Figure A.4a the stress polygon for a static friction coefficient of 0.6 (black dotted line) and for a static friction coefficient of 0.85 (black solid line) is illustrated. This method defines values for S_h (0.52 S_v for $\mu = 0.85$; 0.58 S_v for $\mu = 0.6$) which are smaller than the values measured with FIT and cementation pressures (0.65 S_v) (red dotted line). Using $\mu = 0.85$, the stress polygon shows higher possible magnitudes of S_H, if $\mu = 0.6$. Lower values of S_H are obtained for the same S_h/S_v. For the S_h magnitude analyzed based on FIT and cementation reports ($S_h = 0.65 S_v$), S_H magnitudes between 1.25 S_v (for $\mu = 0.6$) and 1.5 S_v (for $\mu = 0.85$) are obtained. Several authors give insights into the stress regime in the Bavarian Molasse Basin and describe it as being dominated by strike-slip or thrust-faulting (Illies et al., 1981; Reinecker et al., 2010), whereas local stress anomalies/perturbations (see Riem Th2 in Reinecker et al. (2010) indicate similar magnitudes of S_H and S_h.

For the following analyses, the stress regime is defined at the intersection point of the lower boundary of Sh and the stress polygon for $\mu = 0.6$ (blue asterisk in Figure A.4a). The stress gradient for S_h is 15.5 MPa km^{-1}, for S_v 23 MPa km^{-1}, and for S_H 28 MPa km^{-1}. With regard to the stress orientation, BO data confirm the pervasive N–S orientation of S_H (Reinecker et al., 2010).

A.3.4 Identified natural fractures and drilling-induced stress indicators

For the natural fractures analyzed according to the methods described in chapter A.3.2, a Terzaghi correction was applied. The Rose diagrams of the fracture orientations are
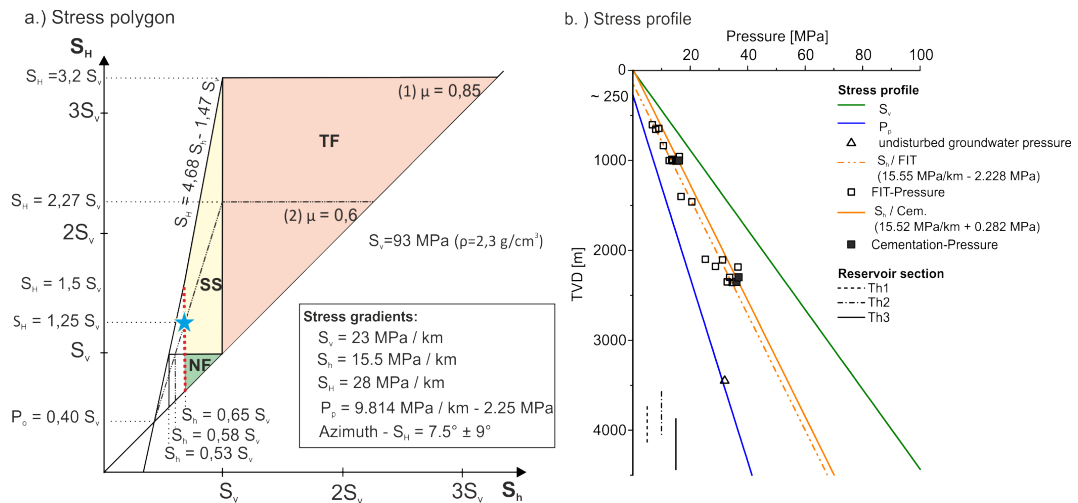
Figure A.4 – Stress field investigations. a.) Stress polygon for a reservoir depth of 4000 mTVD. Different stress regimes are illustrated (NF - Normal-Faulting (green), SS - Strike-Slip Faulting (yellow), TF - Thrust-Faulting (red)) with differential stress ratios (1) for $\mu = 0.85$ (solid line) and (2) for $\mu = 0.6$ (dotted line). The red dotted line describes the lower threshold for S_h as obtained from FIT and cementation pressure data. The blue asterisk shows the stress tensor combining both stress polygons for $\mu = 0.6$ as well as $\mu = 0.85$ and the S_h values resulting from FIT and cementation pressures. b.) Stress profiles: Pore pressure (P_p) for a groundwater level of 225 m and a pressure measurement at 3450 mTVD result in a gradient of 9.814 MPa km^{-1} – 2.25 MPa; Vertical stress (S_v) for a mean density of the overburden of 2.3 g cm^{-3}; Minimal horizontal stress (S_h) gradients for the FIT data in the greater Munich area (S_h/FIT) and minimal horizontal stress gradient from cementation pressures at the Sauerlach wells (S_h/Cem.); Reservoir sections for Th1, Th2, and Th3 (black dotted and solid lines).

illustrated in Figure A.5 and statistical data presented in Table A.2. The results of Sauerlach Th2 and Th3 show a bi-directional distribution in a main fracture set directed towards the ENE–WSW and a secondary orientation towards the N–S to NNE–SSW. In contrast to this, Sauerlach Th1 shows a singular natural fracture set directed N–S to NNE–SSW. Both fracture sets are inclined by 70° to 90°. In Sauerlach Th1 oriented to N300°E (see Figure A.5 black arrow) the N–S fracture set exhibits an angle of $d° = 60°$ and the ENE–WSW fracture set has an angle of $d° = 30°$. Therefore the bias correction could be applied. In Sauerlach Th2 and Th3 oriented to N0°E and to N160°E (see Figure A.5 black arrow), by contrast, the angle of the NNE–SSW fracture set is $d° = 0° - -15°$, while that of the ENE–WSW fracture set is $d° = 80°$. In these wells bias correction can be applied for the ENE–WSW fracture set but due to $d°$–values below the critical limit of 15° this correction cannot be applied to the NNE–SSW fracture set.

It has to be mentioned here that fracture interpretation in Sauerlach Th1 is of limited quality between 4000 m and 4390 mMD due to extensive intersection of different fracture orientations, which is called cross-fracturing (Figure A.6a). This implies a partly low fracture density, although a highly fractured or deformed reservoir can be observed in the image log. In the transition zone of the alternating strata of dolomite and limestone to a compact limestone in the mass facies (4350 mMD), the fracture density increases and cross-fracturing disappears. Such a change in fracture density is frequently observed in the Malm section of geothermal wells. This is also observed in Sauerlach Th2 and Th3 in the transition area to the compact deep dolomite units in the mass facies (4600 mMD - Sauerlach Th2; 5000 mMD - Sauerlach Th3). BO indicating drilling-induced stress occur in Sauerlach Th1 with a mean azimuth of 115° ± 14° to TOH in the upper part of the reservoir

Table A.2 – FMI interpretation data from the Sauerlach Th1, Th2 and Th3. Logged length describe the reservoir depth where the image log is measured. The number and orientation for picked fractures, as well as the number, total length and orientation for Drilling induced fractures (DITF), Reopen natural fractures (RENF) and Breakouts (BO) is measured.

		Sauerlach Th1	Sauerlach Th2	Sauerlach Th3
Logged length(m)		776	825	1147
Fractures	Number	1660	823	158
	Orientation (North)	N–S, NNE–SSW	ENE–WSW; NNE–SSW	ENE-WSW; NNE–SSW
DITF	Number	70	961	2460
	Total length (m)	21	207	61
	Orientation (TOH)	38.5° ± 16.5°	176.3° ± 9.6°	1.52° ± 15.7°
RENF	Number	378	492	621
	Total length (m)	66	105.5	130
	Orientation (TOH)	27.2° ± 11.2°	173.9° ± 10.4°	179.9° ± 15.3°
BO	Number	212	80	7
	Total length (m)	95	24	2.6
	Orientation (TOH)	113.9° ± 14.4°	92.0° ± 14.4°	104.8° ± 12.9°

between 4050 m and 4390 mMD, where cross-fracturing dominates (Figure A.6a). Deeper than 4390 mMD, the drilling process leads to a reactivation of intense fracturing and DENF occur with a direction of 27° ± 11°TOH (Figure A.5a). In Sauerlach Th2 the direction of DITFs and DENFs is 176° ± 9.6° TOH / 173.9° ± 10.4°. Additionally, BOs can be found in a short area between 4020 m and 4140 mMD with an orientation of 95° ± 14° TOH (Figure A.5). In Sauerlach Th3 mainly DENFs occur over the whole reservoir interval with an orientation of 179.9° ± 15.3° TOH (Figure A.6).

A.4 Interpretation and discussion of results

A.4.1 Fracture system and tectonic environment

Fractures connected to normal faults form networks which are often sub-parallel to fault zones, resulting in a WSW–ENE oriented fracture set in the Molasse Basin. Indeed, the fractures in the Sauerlach wells Th2 and Th3 show this orientation (Figure A.5b/c). Sauerlach Th1, by contrast, is oriented between two terminating normal faults and shows a unimodal fracture set distribution between N 350°– 010°E (Figure A.5a), although fractures oriented towards the WSW–ENE would be partly affected by observation bias.

Near to fault zones fracture density frequently increases and rock mass strength is reduced. In general, fault zones possess a complex structure so that it is hard to identify them solely from borehole data. Additional indication of a fault may be found in the upper part of Sauerlach Th1 (4000 to 4390 mMD). It is dominated by cross-fracturing which is difficult to identify, but shows a deformed rock mass. The lower part (4390 to 4760 mMD) does not exhibit any deformation and only tension fractures occur. Typically, the Malm carbonates show a high rock mass strength reflected by a good well stability in Sauerlach Th2 and Th3 (Figure A.6 b/c), but cross-fracturing and the high breakout frequency between 4000 to 4390 mMD in Sauerlach Th1 indicate cataclastic rocks and a reduced rock strength (Figure A.6a).

Since no further direct information on the structural setting around Sauerlach Th1, e.g. from 3D seismic data, is available, the fracture system as a single source of information could
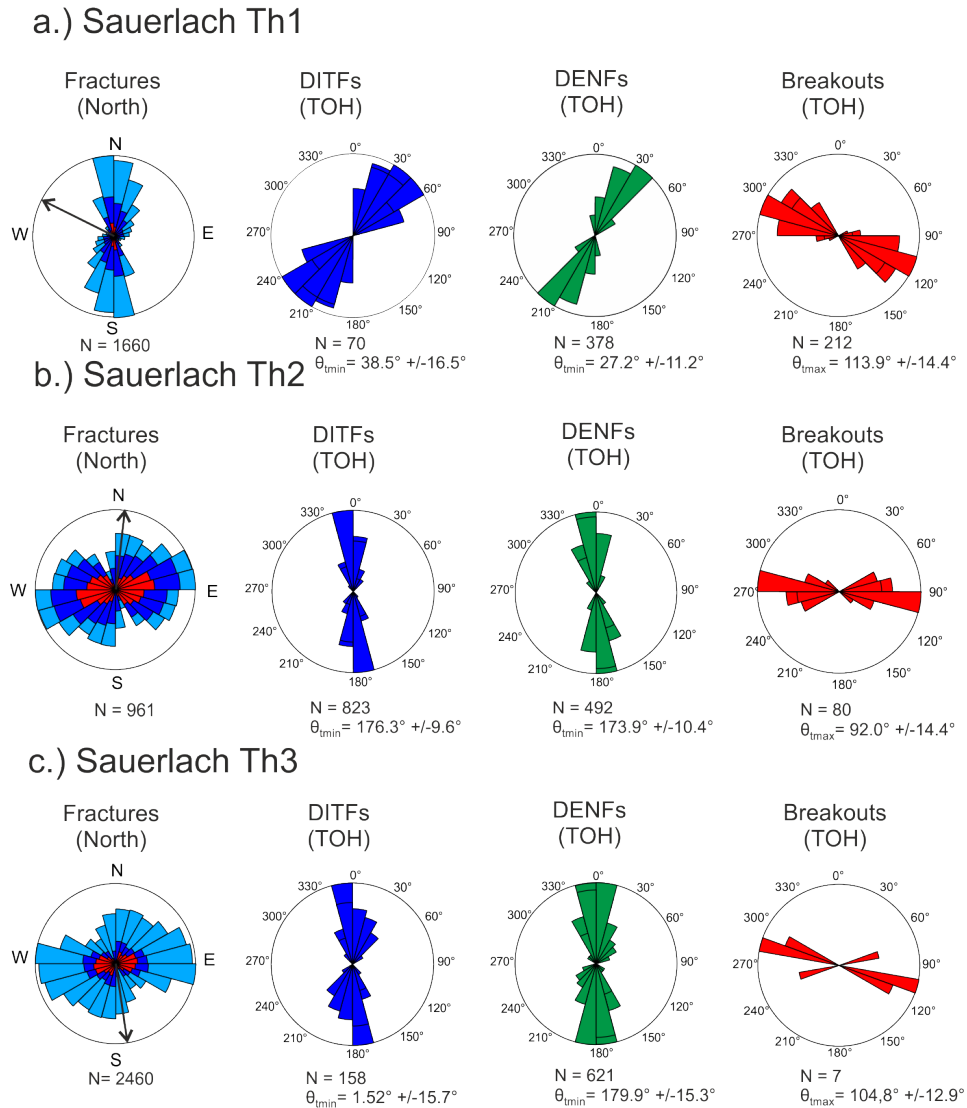
Figure A.5 – Data obtained from interpreting the FMI logs of Sauerlach Th1, Th2, and Th3. First column: Rose display of the Terzaghi-corrected fractures related to the geographic coordinate system. Light blue colors indicate partly conductive or partly open fractures, dark blue colors conductive or open fractures, and red colors resistive or healed fractures (Trice, 1999). The black arrow indicates the mean well orientation in the logged interval and N the total number of fractures. Second column: Drilling-induced tensile fractures (DITF) in the borehole coordinate system relative to the Top of Hole (TOH). N indicates the number and θ the mean orientation with standard deviation. Third column: Drilling-enhanced natural fractures (DENF). Fourth column: Breakout (BO) data. All stress indicator data are measured in the borehole coordinate system against TOH due to high well inclination in the reservoir sections.

indicate an N–S-oriented fault zone. However, an N–S-oriented fault system has not yet been discussed for the Bavarian Molasse Basin. When considering strike-slip environments (Lüschen et al., 2014; Megies & Wassermann, 2014) with faults oriented to N 020°–045°E, however, such a fault system may exist, since fracture in strike-slip fault zones are not always oriented parallel to the fault zone (Sylvester, 1988).

A.4.2 Stress indicators and modeled stress directions

The wellbore trajectory and the stress field control the state of stress at the wellbore wall and the occurrence of BOs, DENFs, and DITFs (see Chapter A.3.2). The input stress magnitudes of our model approach are shown in Figure A.4b (see Chapter A.3.3). Figure A.6 presents the results of $\theta_{minmodel}$ (blue line) and $\theta_{maxmodel}$ (red line) with the picked BOs, DENFs, and DITFs.

Moreover, Figure A.6a shows a mismatch between the orientation of observed features and those assuming a strike-slip regime. The mismatch differs in two distinct sections: (i) between 4000 to 4380 mMD, there is a significant offset between $\theta_{maxmodel}$ and θ_{max} of 35°–45° (Figure A.6/Sauerlach Th1) and (ii) between 4038 to 4760 mMD, the offset is shifted by a mean of 15° to 30° with respect to TOH.

In contrast to this, the observed θ_{max} from BOs and θ_{min} from DENFs and DITF in Sauerlach Th2 correlate well with the modeled stress orientations and confirm the stress conditions assumed for modeling (Figure A.6/Sauerlach Th2). The data set of Sauerlach Th2 is considered to be representative due to the low standard deviation and high number of stress indicators in the well interval (BO, DENF, and DITF). Modeled stress orientations in Sauerlach Th3 generally confirm the assumed stress regime with DITF and DENF (Figure A.6/Sauerlach Th3), however few BOs to localize θ_{max} can be interpreted.

The observations made, in combination with modeling, suggest local stress changes in the vicinity of the wells. The wells oriented north (Sauerlach Th2) and south (Sauerlach Th3) exhibit a strike–slip stress regime with S_H oriented N–S. The modeled stress distribution of Sauerlach Th1 oriented NW–SE differs. The mismatch between observed and modeled data requires a critical review of potentially influencing factors and will be discussed in the following sections.

A.4.3 Sensitivity study of Sauerlach Th1 and Th2

Heterogeneous structures, such as highly fractured zones or locally changed lithological composition in the reservoir, can have an influence on the local stress regime and stress trajectories (Bell, 1996; Homberg et al., 1997). Depending on the distance to the fault or its properties, the direction and the magnitude of the maximum horizontal stress can significantly vary in the vicinity of these structures (Hickman & Zoback, 2004; Shamir & Zoback, 1992).

The direction and the stress regime based on the stress indicators are investigated to identify the local stress field in the vicinity of the wells. The depth (TVD) and the well trajectory at the position of every stress indicator are included and the angle $\theta_{maxmodel}$ as well as $\theta_{minmodel}$ (see chapter A.3.1) are calculated. For every stress regime, the average
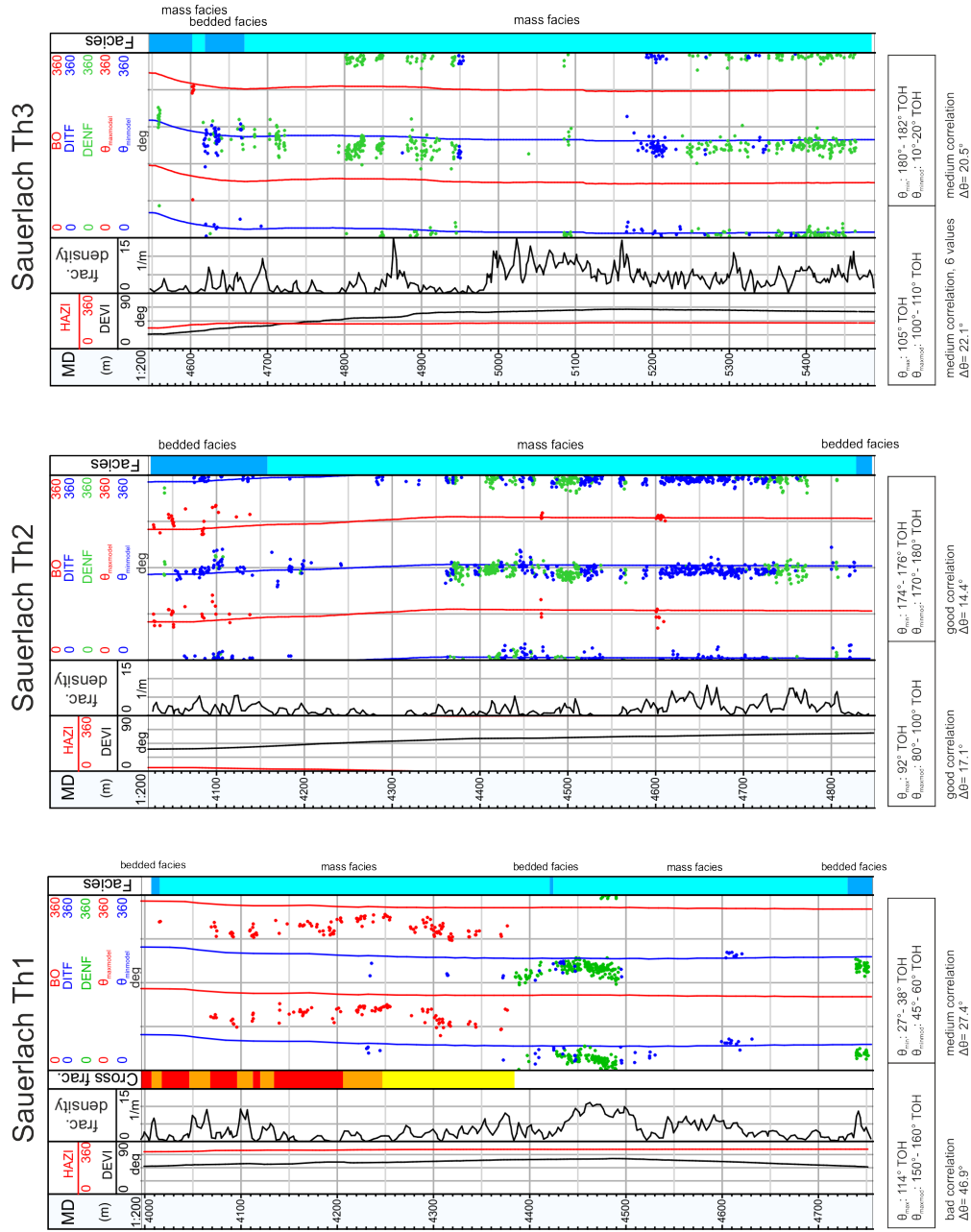
Figure A.6 – Comparison of the stress indicators and the modeled tangential stress. First column: Well inclination (0°–90°) relative to the vertical (black line), well azimuth (000° to 360°)(red line). Second column: Corrected fracture density calculated in 5 m steps from 0 to 15 m and interpreted cross-fracturing in well Th1. Third column: Stress indicators (blue - drilling-induced tensile fractures, green-drilling-enhanced natural fractures, red - breakouts) and the direction of $\theta_{maxmodel}$ (red line) and $\theta_{minmodel}$ (blue line) for a strike-slip stress regime with a N–S-oriented S_H. All angles are measured in the borehole coordinate system with the θ-angle (0°–360°) relative to TOH. Fourth column: Facies interpretation with mass- and bedded facies. The boxes show the mean direction of the observed (θ_{max} & θ_{min}) and modeled stress indicators $\theta_{maxmodel}$ & $\theta_{minmodel}$) and the difference between the observed and modeled orientations ($\Delta\theta$). These data indicate that a strike-slip stress regime with an N–S-oriented S_H predominates in the wells Th2 and Th3, but not in well Th1.

values of the square roots of the directional differences of the observed (θ_{obs}) vs. modeled stresses (θ_{model}) are calculated. For every stress regime, the mean directional difference ($\Delta\theta$), including all stress indicators, is defined.

$$\Delta\theta = \sqrt{\frac{\Sigma\,|\theta_{obs} - \theta_{model}|^2}{N}} \tag{A.13}$$
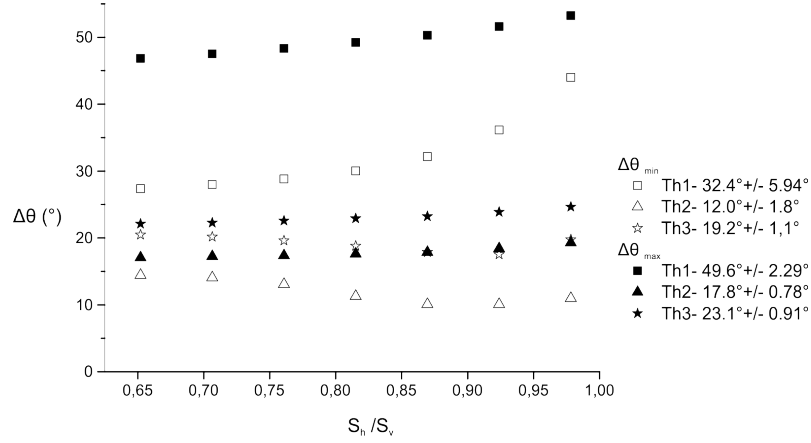
Figure A.7 – Mean difference between the modeled and observed stress orientations ($\Delta\theta$) for varied minimal horizontal stresses. θ_{min} from DITF and DENF as well as θ_{max} from BO are compared to the modeled directions ($\theta_{maxmodel}$, $\theta_{minmodel}$) in (a.) a normal-faulting ($S_H = 0.9 S_v$) (b.) a strike-slip stress regime ($S_H = 1.25 S_v$) for a variable S_h-magnitude. The value of $\Delta\theta$ is calculated to evaluate the consistency of the model (see Chapter A.4.3). The S_h/S_v ratio's independence of the stress distribution results in constant $\Delta\theta$-values and low standard deviations. In the normal faulting regime (a.) the $\Delta\theta$- values for Th1, Th2 and Th3 are particularly constant for different S_h/S_v-ratios. Such constant $\Delta\theta$-values are also seen in the strike-slip regime (b.) for Th2 and Th3. The data of Th1 in b.) illustrate a change for increasing S_h/S_v ratios, but the standard deviation is even lower than 6°. These results show that the S_h/S_v- ratio do not have a significant impact in stress distribution in the well. So further analysis will be based on fixed S_h/S_v-ratios with modified S_H-magnitude and S_H-orientation.

This value can be used to better describe the validity of a stress model applied to stress indicators. First, the influence of the S_h magnitude is studied by varying its magnitude. In a second step the magnitude and the orientation of S_H are varied and S_h is kept constant.

To study the influence of S_h, the magnitudes of S_H and S_v are kept constant in a strike-slip regime ($S_H = 1.25 S_v$) (Figure A.7b) and the magnitude of S_h is varied from low values (0.65 S_v) to higher values (S_v). In the same way the influence of S_h on stress distribution in a normal-faulting regime is verified ($S_H = 0.9 S_v$; $S_h < 0.9 S_v$) (Figure A.7a). Figure A.7 illustrates the $\Delta\theta$ values for S_h/S_v ratios at θ_{max} and θ_{min}. In a strike-slip regime the standard deviations for different S_h values are between 0.8° to 6° (Figure A.7b), in a normal-faulting regime (Figure A.7a) these values are between 0.5° to 4° and emphasize that the S_h-magnitude do not have a significant impact on stress distribution at the borehole wall. Thus, in the following consideration S_h will be kept constant to simplify the analysis.

In the next step the influence of the S_H-direction as well as of the S_H-magnitude on $\Delta\theta$-values for compressive stress indicators is analyzed. Here, the focus lies on the wells Th1 and Th2 because of the large numbers of stress indicators. As illustrated in Figure A.7, S_h has a small influence on $\Delta\theta$. It is concluded that it remains unaffected by stress perturbations

and is kept constant at 0.65 S_v. The direction of S_H is rotated clockwise from N000° – 180°E (North to South) and the stress regime is varied from a normal-faulting regime with nearly isotropic horizontal stress ($S_H = 0.7S_v$) to a strike-slip faulting regime ($S_H = 1.25S_v$). This variation can be traced in the stress polygon from the blue asterisk to the lower limit of the red dotted line (Figure A.4a).

Figure A.8 shows the $\Delta\theta$ values for compressive stress indicators (BO) in Th1 and Th2 as a function of S_H orientation and S_H magnitude. White areas define stress regimes with $\Delta\theta$ values lower than 20°. Grey to black areas indicate high $\Delta\theta$ values of up to 70°. Consequently, the white areas represent stress regimes with the best agreement of observed and modeled data.

In Sauerlach Th1 the observations do not correlate with the assumed strike-slip stress regime which is marked by the blue asterisk for low values of $\Delta\theta$. The best fit is marked by the black line (Figure A.8 / Sauerlach Th1). A good fit between model and data is obtained for either a rotation of 40° to a direction of N150°E in a strike-slip regime ($S_H > S_v$) (Figure A.8 /orange asterisk) or for unperturbed stress orientations (S_H-dir. N010°E) by a reduction of S_H. The latter indicates a stress regime change to an intermediate strike-slip / normal-faulting regime ($S_H = S_v$) or a normal-faulting regime with $S_H = 0.85S_v$ (Figure A.8/ yellow asterisk).

The best fit for well Sauerlach Th2 shows that without stress rotation (S_H-dir. N 010°E) the observed stress indicators can be modeled in a strike-slip regime ($1.25S_v > S_H > S_v$), intermediate strike-slip / normal-faulting regime ($S_H = S_v$) or a normal-faulting regime ($S_v > S_H$) (Figure A.8/ Sauerlach Th2). The line of best fit correlates well with a strike-slip stress regime with a N–S-oriented S_H marked by the blue asterisk in Figure A.4. It is worth mentioning that in Sauerlach Th2 for $S_H/S_v < 0.8$ (normal-faulting regime) the results are independent of the S_H-orientation. Therefore, it is not possible to deduce a preferential stress orientation.

Stress modeling indicates that stress indicators observed in Sauerlach Th1 show the influence of local stress perturbations. Stress magnitude determination is based on the existence and the orientation of breakouts, but we did not use e.g. breakout depths and width in combination with strength to estimate the stress magnitude. For additional analysis, geomechanical data and logging information, such as acoustic logs, cored sections, and extended pressure tests, are required.

A.4.4 Conceptual model at the Sauerlach site

According to Illies et al. (1981) and Reinecker et al. (2010), the stress regime in the Bavarian Molasse Basin is primarily influenced by the alpine orogeny and oriented accordingly perpendicular to it (N–S to NW–SE). Breakout interpretation in the Sauerlach wells based on the caliper data in the Cenozoic sediments from 500 to 2600 mTVD reveals a mean S_H direction of N 007.5° ± 9°E. The total breakout length (625 m) and total logged interval with breakout zones (2100 m) give a ratio of 0.30 and indicate a mean differential stress for breakout formation. This phenomenon is interpreted by Illies et al. (1981) and Reinecker et al. (2010) to be an indicator of a strike-slip or thrust faulting regime and also the focal mechanisms analysis (Megies & Wassermann, 2014) support this interpretation.
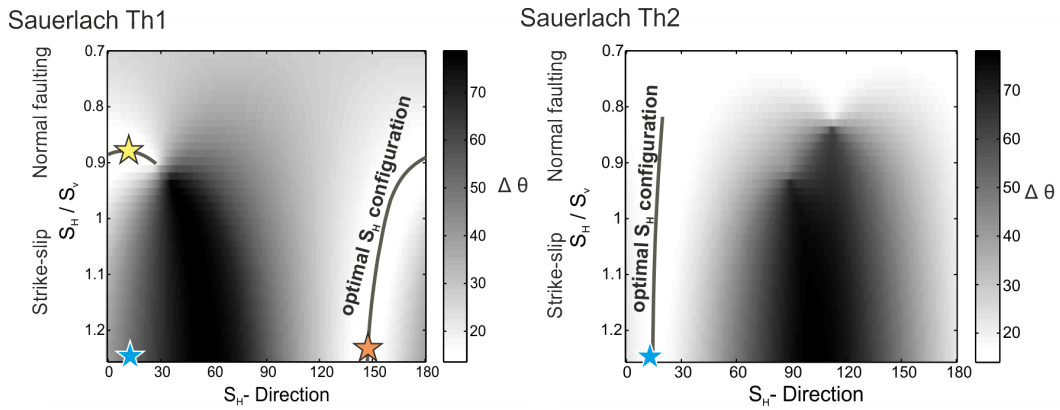
Figure A.8 – Differences of the modeled and observed stress indicators for a varied direction and stress regime. The vertical (S_v) and the minimum horizontal stresses (S_h) are kept constant (0.65 S_v), the stress direction and the magnitude of the maximum horizontal stress (S_H) are changed (S_H-dir.: 000°–180°, S_H: 0.7–1.25 S_v). The location of the strike-slip stress tensor is shown by the blue asterisk. The colors illustrate the mean difference ($\Delta\theta$) between the observed and modeled maximum tangential stresses. Th1 shows a rotation of the stress regime (orange asterisk) or a change in the stress regime to normal-faulting (yellow asterisk) fits our observation best. In Th2 the strike-slip regime with a N–S-oriented S_H is confirmed, but this analysis also suggests that stress direction is independent in a normal-faulting regime.

The number and total length of breakouts within the Cenozoic sedimentary layers in Sauerlach Th1 (Figure A.3) is much higher than in the Malm reservoir in Sauerlach Th1, Th2 and Th3 (Table A.2). This can be the result of lower tangential compressive stress due to the well trajectory, a changed stress regime or higher rock strength in the Malm reservoir. Nevertheless, the analysis of stress indicators orientation indicate an N–S oriented S_H with a strike-slip character for the wells Sauerlach Th2 and Th3. According to our stress inversion, a transitional strike-slip / normal-faulting ($S_v = S_H$) or a normal-faulting regime ($S_H < S_v$) might exist when judging from the stress data. We therefore conclude a strike-slip to normal-faulting regime where the compressional character decreases with depth due to higher vertical stress gradients in comparison to the horizontal stress gradients. The absence of stress rotation with depth points to significantly different horizontal stress magnitudes as also observed by Reinecker et al. (2010).

Our stress inversion in Sauerlach Th1 indicates either a normal faulting regime ($S_v > S_H$) with S_H oriented to N010°E or a rotation of S_H oriented to N150°E in a strike-slip stress regime ($S_H > S_v$). Compared to the observations in Sauerlach Th2 and Th3, this would indicate a regionally perturbed stress field of 2nd or 3rd order stress patterns. Such a perturbed stress field at the Sauerlach site is not a unique phenomenon in the Molasse Basin, according to Reinecker et al. (2010) at least 10 wells indicate a locally rotated stress field. Within the geothermal reservoir in the Bavarian Molasse Basin, units with a perturbed stress field can either be linked to lithofacial homogeneous bodies (e.g. reef complexes) with a significant size or tectonic structures, as e.g. observed in a set of combined strike-slip / extensional fault system with several en-echelon normal faults building several small relay ramps (Lüschen et al., 2014). Consequently, wells drilled into the normal faults, such as Sauerlach Th2 and Th3, may exhibit a fracture set that differs significantly from that of Sauerlach Th1 which is drilled in-between two terminating normal faults.

The identified mainly N–S to NNE–SSW oriented fractures in Sauerlach Th1 are either influenced from a dilatational tendency in a normal-faulting regime with an N–S oriented

S_H (Figure A.9/ white arrows in Case II), or a shearing character in the rotated strike-slip stress regime (Figure A.9/ shear movement in Case I). In both scenarios the fractures would have an opening character and provide a good hydraulic activity. Therefore, the above presented structural concept goes along with the observations during the early stage of pumping tests corresponding with a high negative skin effect indicating a good connectivity of Sauerlach Th1 to the reservoir (see Chapter A.2.1). From this perspective it is presumed that these open fractures contribute to the high productivity of the well by a low turbulent inflow into the borehole.

Compared to the fractures in Sauerlach Th2 and Th3 which are mainly oriented ENE–WSW they are identified to be closing within the observed stress field. Therefore it seems that these are unfavorable for geothermal targeting though a significant displacement along with faulting was initially encountered in the seismic data.
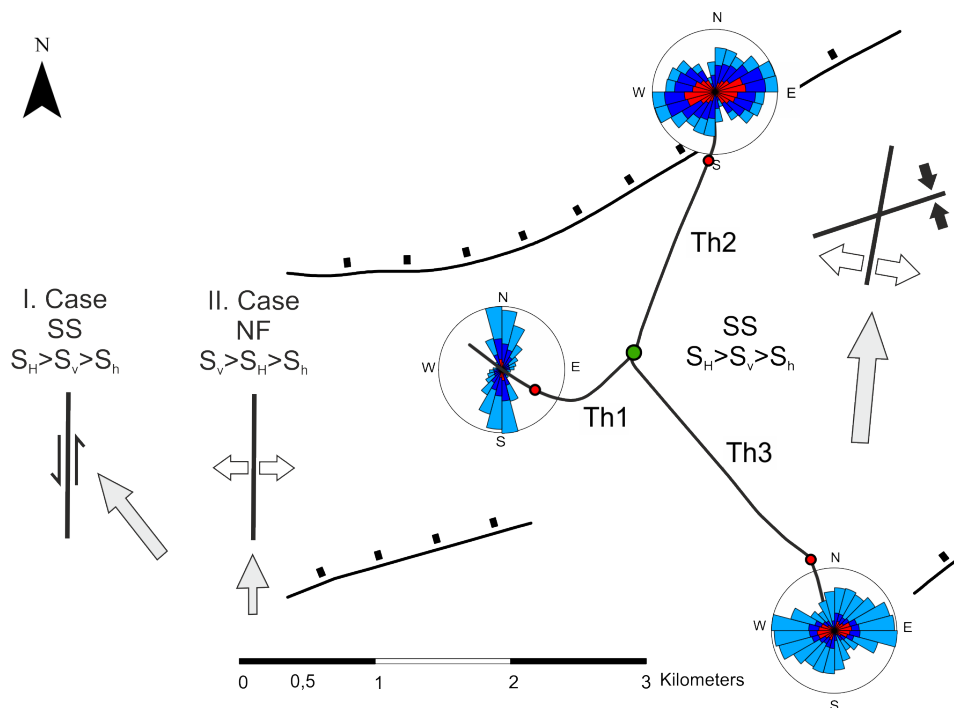
Figure A.9 – Stress field interpretation near the well Th1 and the stress pattern in Th2 and Th3. Gray arrows present the orientation of the maximum horizontal stress. Here, local variations of a strike-slip regime (SS) and a normal faulting regime (NF) can be observed. For well Th1, a local perturbation of the stress regime is observed and determined to be strike-slip and S_H oriented to 320° (Case I) or normal faulting regime with S_H oriented towards the N–S (Case II). In Th2 and Th3 the strike-slip regime is observed with S_H having an N–S orientation. The rose diagram illustrates the fracture sets. The principal fracture set in Th1 for stress state Case I indicates a high shear tendency. For Case II, these fracture sets exhibit a dilatational tendency (white arrows). Fracture sets in Th2 and Th3 show a dilatational tendency (white arrows) (NNE–SSW) as well as a closing tendency (black arrows) (ENE–WSW) in the strike-slip stress regime.

A.5 Conclusion

The stress analysis made within the framework of this study has shown that the strike-slip stress regime with a N–S-oriented S_H can be found in the Cenozoic layers in one well (Sauerlach Th1) and even in the Malm reservoir in two other wells (Sauerlach Th2 and Th3). Stress inversion of the breakout data measured in the Malm reservoir of Sauerlach Th1 and

Th2 indicates a perturbed stress regime for Sauerlach Th1. The fracture systems within the Malm reservoir of Sauerlach Th2 and Th3, both drilled towards the WSW–ENE faults, have a predominant WSW–ENE orientation. In contrast Sauerlach Th1, drilled between the northern and southern WSW–ENE fault zones exhibits an N–S to NNE–SSW-oriented fracture system. This tectonic situation can lead to consequences for the hydraulic system for both inferred stress regimes: In a stress regime with nearly N–S oriented S_H the N–S to NNE–SSW oriented fracture system, which is dominant in the Sauerlach Th1 but very minor seen in Sauerlach Th2 and Th3, can have a dilatational character (Figure A.9/white arrows in Case I). In a strike-slip stress regime with N150°E oriented S_H the N–S to NNE–SSW oriented fracture planes will reach highest shear stress (Figure A.9/shear movement in Case I) and most likely experience shear movement In both cases the fracture aperture might be increased leading to better hydraulic connectivity. This is supported by the fact, that Th1 has a higher productivity. Overall, the identified stress effects help us to understand the hydraulic properties of the well Sauerlach Th1 compared to the wells Sauerlach Th2 and Th3. In this study we could assess the stress distribution in highly-deviated wells at the Sauerlach site. The approach chosen, however, is not site-specific and can be transferred to other wells. The ability to identify and precisely locate stress perturbations can improve the predictability of hydraulic performance and thus, contribute to a better assessment strategy.

Authors' contributions

RS carried out the data analysis, modeling, and wrote the manuscript. US and BM participated in analyzing the results and in drafting the manuscript. TK initiated the study, participated in the design, coordination, and quality control of the project and in drafting the manuscript. CH completed the data set and was involved in drafting the manuscript.

Acknowledgments

A Normal-Faulting Stress Regime in the Bavarian Foreland Molasse Basin? New evidence from detailed analysis of leak-off and formation integrity tests in the greater Munich area, SE Germany.

Abstract

Leak-off and formation integrity test data from the central part of the Bavarian Foreland Molasse Basin have been investigated in detail to infer information about the stress regime of the Cenozoic basin fill. The detailed analysis of leak-off test data from the Bavarian Foreland Molasse Basin and lithology-dependent analysis of leak-off test and formation integrity data is the first of its kind in a published study. Only test data from shale-rich sequences have been considered. All data yield minimum principal stresses that are smaller than an estimated vertical stress range. In combination with critical stress and frictional equilibrium theory, the data indicate that the stress regime in the Greater Munich Area and possibly the far-field stress regime of the Bavarian Foreland Molasse Basin are most likely of an extensional nature (normal-faulting stress regime). Under the assumption of frictional equilibrium, a friction coefficient between 0.2 to 0.4 best explains failure in shale-dominated sections of the central part of the Bavarian Foreland Molasse Basin and can be used to estimate the minimum horizontal stress S_{Hmin}. However, even in the spatially restricted domain of the Greater Munich Area the stress regime might vary towards a strike-slip stress regime; most likely in the vicinity of fault zones and \or due to variations in mechanical rock strength. The results of this study have great impact and relevance to improved planning of drilling campaigns, future numerical modeling and the general understanding of the evolution of the Bavarian Foreland Molasse Basin. Additional leak-off tests and extended

leak-off tests are recommended to fully unravel the spatial variation and geologic control factors of the stress regime of the entire Bavarian Foreland Molasse Basin.

KEYWORDS: North Alpine Foreland Basin; Bavarian Foreland Molasse Basin; stress regime; leak-off test; minimum principal stress

B.1 INTRODUCTION

Subsurface stresses are important mechanical parameters in the Earth's crust, driving deformation, fault formation and reactivation, compaction and thus also hydraulics and fluid flow in the subsurface (e.g. Zoback, 2010). Understanding of the geological development of the subsurface, designing of wellbores and associated extracting and injecting of fluids critically depends on the understanding of subsurface stresses. Subsurface stresses can be generally described by three principal stress components S_1, S_2 and S_3, where $S_1 \geq S_2 \geq S_3$ (e.g. Jaeger et al., 2007). In case of the vertical stress S_v being one of the three principal stresses, the remaining stresses become the maximum horizontal stress S_{Hmax} and the minimum horizontal stress S_{Hmin}. If the vertical stress S_v is the maximum principal stress, an extensional or normal-faulting stress regime is present. Accordingly, a compressional or thrust-faulting stress regime is present, if S_v is the minimum principal stress. $S_{Hmax} > S_v > S_{hmin}$ characterizes a strike-slip stress regime.

The stress regime of Central Europe, including the Bavarian Foreland Molasse Basin, has been subject to various studies in the past (e.g. Gölke & Coblentz, 1996; Greiner & Lohr, 1980; Grünthal & Stromeyer, 1986; Grünthal & Stromeyer, 1992; Heidbach et al., 2007; Lohr, 1969; Lohr, 1978; Müller et al., 1997; Müller et al., 1992; Reinecker et al., 2010; Seithel et al., 2015; Ziegler et al., 2016). For the Bavarian Foreland Molasse Basin, orientations of the maximum horizontal stress S_{Hmax} are fairly well understood and have been previously determined by analysis of borehole breakouts (Reinecker et al., 2010; Seithel et al., 2015) and numerical studies, both on the regional (Gölke & Coblentz, 1996; Grünthal & Stromeyer, 1986; Grünthal & Stromeyer, 1992) and local (Ziegler et al., 2016) scale. Borehole breakout studies and larger scale numerical studies, addressing the stress field of Central Europe, show that the predominant orientation of S_{Hmax} is roughly perpendicular to the associated orogenic thrust-fronts, mimicking the resulting intraplate horizontal compression (Gölke & Coblentz, 1996; Grünthal & Stromeyer, 1986; Grünthal & Stromeyer, 1992; Heidbach et al., 2007; Heidbach et al., 2018; Müller et al., 1997; Müller et al., 1992; Reinecker et al., 2010). In case of the Bavarian Foreland Molasse Basin, S_{Hmax} is roughly represented by a N–S orientation (Reinecker et al., 2010), which fits with the regional crustal stress pattern of the World Stress Map database (Heidbach et al., 2018). Nevertheless, the magnitudes of horizontal stresses and the resulting regional stress regime(s) of the Bavarian Foreland Molasse Basin are not well understood in their entirety. Gölke & Coblentz (1996) deduced from numerical modeling of the European plate, that the regional stress field in Central Europe is characterized by uniform compression, which might be completely compensated by buoyancy effects in the vicinity of the Alps. Due to a general increase of seismic velocities towards the Alps, Lohr (1978), Greiner & Lohr (1980) and Lemcke (1973) interpreted that a thrust-faulting to strike-slip stress regime might be present in the Cenozoic fill of the

Bavarian Foreland Molasse Basin. However, this increase in seismic velocities might also be controlled by lithological effects and the general deepening of the Bavarian Foreland Molasse Basin from north to south (Lohr, 1978). Compressive deformation structures in the Peissenberg mine (~60 km SW of Munich) are indicators of a thrust-faulting stress regime Illies & Greiner (1978). Based on the findings in the Peissenberg Mine and the apparent large horizontal differential stresses necessary to induce borehole breakouts, Reinecker et al. (2010) also suggested a strike-slip to thrust-faulting stress regime. However, it should be noted that the Peissenberg Mine is located right at the border between the North Alpine Thrust Front (Subalpine Molasse) and the up-tilted part of the Bavarian Foreland Molasse Basin (c.f.Grottenthaler, 2009) and therefore does not necessarily represent the stress state of the undeformed part of the Bavarian Foreland Molasse Basin.

Seismic mapping by Hartmann et al. (2016) of Cenozoic, but presently likely inactive normal faults, which strike parallel to the North Alpine Thrust Front, indicates that a normal-faulting stress regime has been present during the Cenozoic history of the Bavarian Foreland Molasse Basin. Based on horizon flattening and analysis of incremental fault throws of seismically mapped faults in the pre-Molasse Upper Jurassic at the Unterhaching wellsite (<10 km South of Munich), (Budach et al., 2017) interpreted a strike-slip to normal-faulting stress regime is likely present below the Cenozoic basin fill. Focal mechanism interpretation of induced (not tectonic) microseismicity from geothermal injection wells in the Greater Munich Area point toward presence of a strike-slip stress regime in the crystalline basement, underlying the Molasse Basin (Megies & Wassermann, 2014). Drews et al. (2018), Drews et al. (2019b), Müller et al. (1988) and Müller & Nieberding (1996) argued that overpressure in the Bavarian Foreland Molasse Basin rather originated from high sedimentation rates than lateral stresses and compression, suggesting a vertical or sub-vertical maximum principal stress at the time of Cenozoic (Early Oligocene to Lower Miocene) overpressure build-up.
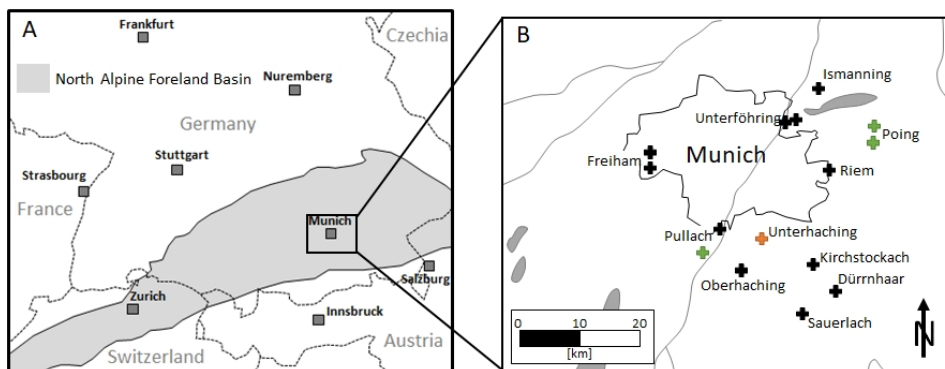
Figure B.1 – Location of the study area and used wells. A: Location of the North Alpine Foreland Basin (grey shading) and the study area (black box) after Drews et al. (2018). B: Zoom into the study area around Munich. The crosses mark the wells used in this study (orange and green crosses = leak-off and formation integrity test data disclosed in table 1; black crosses = additional formation integrity test and cementation pressure data).

Seithel et al. (2015) used anonymized formation integrity tests from the Greater Munich Area to estimate through assumption of frictional equilibrium (using a standard friction coefficient of 0.6), that a strike-slip stress regime is prevailing in the Greater Munich Area. However, through probabilistic analysis of stress-indicators and fracture orientations

present in the wellbores of the Sauerlach deep geothermal project, Seithel et al. (2015) also interpreted that the stress regime in the Mesozoic basement sediments can switch from the interpreted original strike-slip stress regime towards a normal-faulting stress regime due to the presence of faults. Likewise, Ziegler et al. (2016) used formation integrity test data from the Greater Munich Area and results from leak-off test data of the Unterhaching Gt 1 well to numerically study the stress regime of the Greater Munich Area, also under the assumption of a critically stressed crust and frictional equilibrium. Hereby, Ziegler et al. (2016) interpreted that a strike-slip stress regime is likely present in the Cenozoic basin fill, but also suggested that a normal-faulting stress regime was possible. They showed that the numerical results critically depend on the calibration data, which were not set into relation to the lithological composition of the tested formations and, in the case of the Unterhaching Gt 1 leak-off test, were based on personal communication only.

The variety of interpretations regarding the stress regime of the Bavarian Foreland Molasse Basin is mostly due to the unknown influence of lateral compression related to the Alpine orogenesis. Recent numerical studies, addressing the stress magnitude variations in fold-and-thrust-belt systems and their foredeeps (Gao et al., 2018; Obradors-Prats et al., 2017), and analogue studies of fold-and-thrust-belt systems (Couzens-Schultz & Azbel, 2014) suggest that a normal-faulting stress regime should be predominantly present in central parts of foredeeps and foreland basins of fold-and-thrust-belt systems. Herby, lateral compression only plays a major role very proximal to the respective thrust-front and at shallow depths.

A significant factor of uncertainty in studies, which rely on frictional equilibrium and critical stress theory, is given by the generic use of standard friction coefficients (e.g. 0.6 or 0.85; c.f. Byerlee, 1978) for the upper part of the Earth's crust. However, the coefficient of friction varies depending on the lithological composition. For example, it has been shown by field data and laboratory studies that shale friction coefficients are significantly lower than the average of the Earth's upper crust (e.g. Byerlee, 1978; Gaarenstroom et al., 1993; Hagke et al., 2014; Kohli & Zoback, 2013; Morley et al., 2018; Stump & Flemings, 2002).

Additional uncertainty related to the determination of the stress regime of the Bavarian Foreland Molasse Basin is due to the variety of investigated scales and locations. For example, the present day stress regime of the central part of the Bavarian Foreland Molasse Basin might vary between the Cenozoic basin fill and the Mesozoic sub-Molasse sediments and underlying basement (Budach et al., 2017; Megies & Wassermann, 2014; Seithel et al., 2015; Ziegler et al., 2016). Variations on different scales or adjacent to fault zones are also likely (Seithel et al., 2015). In addition, the uncertainty of the stress regime of the Bavarian Foreland Molasse Basin is also owed to the fact that many data sets rely on indirect measurements of stress magnitudes (e.g. seismic velocities, borehole breakouts and numerical modeling).

Although recent access to in-situ measurements, such as leak-off test and formation integrity test data of deep geothermal wells from the Greater Munich Area, provided first insights into the far-field stress regime of the Bavarian Foreland Molasse Basin (c.f. Seithel et al., 2015; Ziegler et al., 2016), a detailed study on an actual pressure build-up dataset of leak-off test data and incorporation of the lithological composition of the tested formations

is yet missing. The analysis of leak-off test and formation integrity test data within the lithological context would allow for a much more definite analysis of these data and subsequent interpretation of the stress regime. In this study, results and interpretations of leak-off test, formation integrity test and cementation pressure data and their implications for the recognition of the present day stress regime of the Cenozoic basin fill of the central part of the Bavarian Foreland Molasse Basin will be presented for the first time. Thereby, only tests performed in shale-rich sequences were considered to allow for comparability of the test data. Also, a full analysis of leak-off test data from the Bavarian Foreland Molasse Basin will be presented.

B.2 Geological setting

The Bavarian Foreland Molasse Basin is located to the north of the Eastern Alps and between Lake Constance in the west and Upper Austria in the east. The northern limits of the Bavarian Foreland Molasse Basin are outlined by the Danube river incision. The Bavarian Foreland Molasse Basin is part of the North Alpine Foreland Basin, which is the peripheral foredeep of the Alps and started to form in the context of continent-to-continent collision of the Adriatic and European plates in Eocene/Oligocene times (e.g. Pfiffner, 1986; Schmid et al., 2004). The basin fill of the Bavarian Foreland Molasse Basin therefore comprises Cenozoic "Molasse" sediments of Eocene to Late Miocene age (Kuhlemann & Kempf, 2002). In the Greater Munich Area the lithological composition is mostly limestone for the thin Eocene section. Shales dominate the Oligocene and Lowermost Miocene (Aquitanian), except for the so called "Chattian Sands" of the Upper Oligocene, a heterolithic sequence of alternating sand and shale packages. Lower Miocene (Burdigalian) to Late Miocene (Tortonian) sediments are mostly coarse-grained and sand-sized to pebble-sized, but also comprise some shale-rich sequences (Kuhlemann & Kempf, 2002). The Cenozoic basin fill overlies Mesozoic siliciclastic and calcareous basement sediments and finally crystalline basement rocks of the European plate (Bachmann et al., 1987).

B.3 Methods and data

Hydraulic fracturing experiments, such as leak-off tests (LOT), can be used to determine the minimum principal stress present in the subsurface (c.f. Zoback, 2010). Thereby, the pressure is increased in an isolated well section with open formation (usually below a casing shoe) by pumping drilling fluid into the isolated section. Usually, pressure initially increases linearly with constantly increased volume of the pumped fluid until the leak-off point (LOP) is reached. The LOP is the first diversion from the linear pressure build-up and marks the formation of a hydraulic fracture. Continuation of pumping will yield a maximum pressure, the formation breakdown pressure (FBP). FBP marks the point where unstable fracture propagation away from the wellbore occurs (c.f. Zoback, 2010). Further pumping at constant rate might result in a decrease in pressure, which eventually stabilizes to the fracture propagation pressure (FPP). FPP is usually very close to the minimum principal stress S_3 (for a more detailed review on leak-off tests, see Zoback, 2010). A formation

integrity test (FIT) is performed in the same way as a LOT, but stops on the linear part of the pressure build-up curve and before the LOP is reached. Hence, FITs only provide a lower bound of the minimum principal stress. However, in combination with LOTs performed in formations with comparable lithological composition, FITs can also provide valuable information about the minimum principal stress. The maximum horizontal stress S_{Hmax} cannot be measured in the deeper subsurface with conventional methods. Without an estimate of S_{Hmax} it can only be determined, whether a thrust-faulting stress regime is present or not (provided S_{Hmin} and S_v can be sufficiently estimated). For shallow leak-off tests (<2000 m below ground level), the method of Haimson & Fairhurst (1970) can be used to calculate S_{Hmax} from leak-off test data:

$$S_{Hmax} = 3 \times S_{Hmin} - FBP - P_p + T_0 \qquad (B.1)$$

Where P_p is the pore pressure of the formation and T_0 is the tensile strength of the formation. Here, a tight borehole wall is assumed, which separates the formation pressure from the mud pressure, which is generally the case in shale-rich sequences. In equation B.1, the compressive stresses S_{Hmax} and S_{Hmin} as well as FBP are in positive notation, while the tensile strength T_0 is a negative (c.f. Fjaer et al., 2008). Generally, tensile strength (or cohesion) of shales is very low or even negligible (c.f. Zoback, 2010). Even for highly compacted/cemented shales with porosities of less than 5 %, Wang et al. (2017) showed through laboratory measurements that shale tensile strength can be as low as 3 MPa. For effective stresses less than 10 MPa or depths < 1 km, tensile strength of shales has been found to range between 0 to 5 MPa (c.f. Morley et al., 2018). Theoretically, T_0 cannot exceed the difference between S_{Hmin} and FBP (c.f. Fjaer et al., 2008).
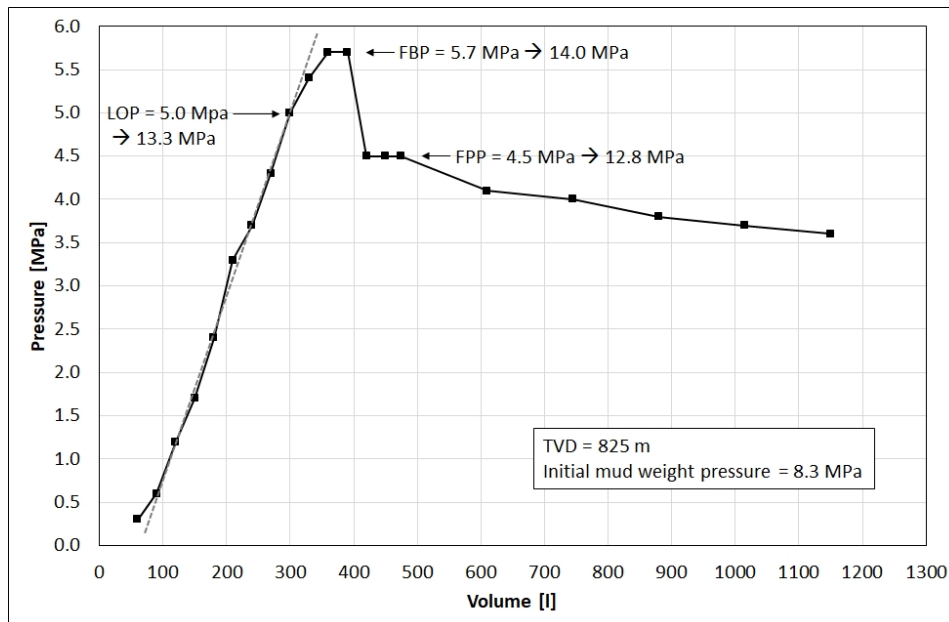
Figure B.2 – LOP = leak-off pressure, FBP = formation break-down pressure, FPP = fracture propagation pressure, TVD = true vertical depth.

Estimates of S_v, S_{Hmax} and S_{Hmin} then permit to assess the present-day stress regime. S_v can be estimated by dividing the subsurface's bulk density ρ_{bulk} into vertical depth

intervals dTVD in m, which can be integrated into a vertical stress S_v in Pa at any true vertical depth (TVD):

$$S_v = \int_0^{TVD} \rho_{bulk} \times g \times dTVD \tag{B.2}$$

Where g is the Earth's gravitational acceleration of 9.81 m/s². No density data is available for any of the wells included in this study. However, in sedimentary basins the density profile (here we use a 1 m depth interval) of the subsurface can be approximated by an Athy-type porosity decay function (Athy, 1930) modified for vertical effective stress σ_v (c.f. Heppard & Cander, H.S., Eggertson, E.B., 1998; Hubbert & Rubey, 1959; Scott & Thomas, 1993):

$$\varphi = \varphi_0 \times exp\left(-\sigma_v/C\right) \tag{B.3}$$

Where φ is the fractional porosity, φ_0 is the fractional porosity at the Earth's surface and C is a constant. According to Drews et al. (2018), who calibrated equation B.3 to density and velocity data of petroleum wells, φ_0 can be set to 0.3 and C to 31 MPa⁻1 for the Bavarian Foreland Molasse Basin (with σ_v in MPa). For an upper bound porosity profile (lower bound density and vertical stress profiles), which represents a pure shale overburden, φ_0 can be set to 0.4 (Drews et al., 2018). The bulk density ρ_{bulk} profile of the subsurface can be obtained from the modeled porosity profile, using an average grain density ρ_{grain} of 2700 kg/m³ and a formation water density ρ_{water} of 1000 kg/m³:

$$\rho_{bulk} = \rho_{grain} \times (1 - \varphi) + \rho_{water} \times \varphi \tag{B.4}$$

In combination with two principal stress components, assumption of frictional equilibrium and a critically stressed crust might be used to infer the actual stress regime, if the friction coefficient was constrained sufficiently (c.f. Zoback, 2010). Thereby, the friction coefficient μ is related to the minimum and maximum principal stresses S_1 and S_3 as follows:

$$\frac{\sigma_1}{\sigma_2} = \frac{S_1 - P_p}{S_3 - P_p} = \left[(\mu^2 + 1)^{0.5} + \mu\right]^2 \tag{B.5}$$

Where σ_1 and σ_3 are the maximum and minimum principal effective stresses (principal stress minus the pore pressure P_p), respectively. Average values of the friction coefficient μ range between 0.6–0.85 for the Earth's crust (c.f. Byerlee, 1978; Zoback, 2010). However, the friction coefficient is lithology-dependent (c.f. Zoback, 2010). Despite most of the tested rocks by Byerlee (1978) produced friction coefficients in the range of 0.6 to 0.85, his measurements on shale samples yielded friction coefficients between 0.21 and 0.33 for Montmorillonites (smectite) and 0.44 and 0.53 for illite samples. Smectite-rich clays are more common in shallow-buried, younger sediments (such as the Cenozoic basin fill of the Bavarian Foreland Molasse Basin), while illite-rich shales have likely seen higher temperatures, which are necessary to transform smectite to illite through hydroxide loss (e.g. Colton-Bradley, 1987). Mixed-layer clays might therefore have friction coefficients in the range of 0.2 and 0.5. Accordingly, Kohli & Zoback (2013) have experimentally derived friction coefficients around 0.4 for carbonate and organic-rich shales. LOT and pore pressure

data from the North Sea yielded increasing effective stress ratios (σ_3/σ_1) with depth and overpressure, translating to shale friction coefficients around 0.4 and 0.25 at 1000 to 3000 m depth below the seafloor, respectively (Gaarenstroom et al., 1993). Stump & Flemings (2002) inferred friction coefficients below 0.1 from laboratory measurements of smectite-rich samples from the Gulf of Mexico, which is in agreement with field data from the same area. Morley et al. (2018) give a review of friction coefficients for different mineralogical compositions of shales and suggest friction coefficients between 0.1–0.3 for smectite-rich, shallow-buried shales. Unfortunately, laboratory measurements of shale friction coefficients are not available for the Bavarian Foreland Molasse Basin. Clay mineralogy of Cenozoic shales of the Bavarian Foreland Molasse Basin is also not well constrained, yet. However, Gier (1998) reports similar smectite and illite contents of clay-rich Cenozoic samples from the Upper Austrian part of the North Alpine Foreland Basin. In addition, Hagke et al. (2014) suggest friction coefficients below 0.1 for shale detachments of the Swiss Alps, based on critical taper analysis.

In order to assess the stress regime of the Bavarian Foreland Molasse Basin, LOT, FIT and cementation pressure data from shale-rich Cenozoic strata of 22 deep geothermal wells in the Greater Munich Area have been investigated (Figure B.1). LOT and FIT data of the Unterhaching Gt 1, Poing Th1, Poing Th2 and Pullach Th3 wells are fully disclosed in this study (Table B.1). The data from the remaining 18 wells have been anonymized for confidentiality reasons. The data are analyzed to derive information about the stress regime of the Bavarian Foreland Molasse Basin. According to geological well reports, mud logs and cutting descriptions, all LOTs, FITs and cementation pressures selected for this study have been recorded in shale-dominated sections to ensure comparability between the different data points.

B.4 Results and discussion

B.4.1 The Unterhaching Gt1 leak-off test at 825 mTVD

An excellent dataset is given by a fairly shallow LOT, taken at 825 m true vertical depth (TVD) in the Unterhaching Gt 1 well (~ 10 km south of Munich). The well is located in a central position of the Bavarian Foreland Molasse Basin, and therefore potentially representing the far-field stress conditions of the Bavarian Foreland Molasse Basin (c.f., Figure B.1). Hydrostatic pressure conditions are present at the depth of the LOT, as supported by the low initial mud density of 1.025 g/cm³. The LOT has been taken in a shale-dominated stratigraphic section of the Upper Burdigalian (Lower Miocene). The LOT data shows a typical pressure response to the injected volume with an initial linear build-up and a first diversion at 13.3 MPa or 5 MPa above the initial mud weight pressure of 8.3 MPa (Figure B.2). This point marks the leak-off point (LOP). The maximum pressure before formation break-down (FBP) was reached at 14 MPa or 5.7 MPa above the initial mud weight pressure (Figure B.2). A fracture propagation pressure (FPP) can be interpreted at the first indication of a steady state system around 4.5 MPa above the initial mud weight pressure (Figure B.2), which corresponds to an absolute pressure of 12.8 MPa. Here, it is assumed that FPP is

representative for the minimum principal stress at 825 mTVD. A vertical stress estimate
at 825 mTVD yields 18.3 MPa ($\phi_0 = 0.3$, $C = 31 MPa^{-1}$, c.f. equation B.3), whereas a lower
bound estimate ($\phi_0 = 0.4$, $C = 31 MPa^- 1$, c.f. equation B.3) would yield a vertical stress
of 17.1 MPa. A constant bulk density of the subsurface of 2600 kg/m³ would return an
upper bound vertical stress of 21 MPa. All values obtained from the LOT (LOP, FBP and
FPP) are significantly lower than the estimated vertical stress range, implying that either a
normal-faulting or strike-slip stress regime is present at 825 mTVD at the Unterhaching Gt
1 well location.

Constructing the stress polygon (c.f. Zoback, 2010) for the Unterhaching Gt 1 LOT at
825 mTVD implies a strike-slip stress regime is present in case of a critically stressed crust
and a standard average friction coefficient of 0.6 (see star in Figure B.3A). However, assuming
a friction coefficient of 0.4 indicates critically stressed conditions in a normal-faulting stress
regime (Figure B.3B). Since the test was performed in shale-dominated strata, a friction
coefficient of 0.4 is much more in concordance with field data and laboratory studies on
shale friction coefficients and effective stress ratios (e.g. Byerlee, 1978; Gaarenstroom et al.,
1993; Stump & Flemings, 2002) than a standard friction coefficient of 0.6 or higher. A
normal-faulting stress regime is also supported by estimation of the maximum horizontal
stress S_{Hmax}, following the method of Haimson & Fairhurst (1970), which is independent of
the friction coefficient. Assuming no tensile strength of the shale dominated stratigraphy,
the resulting estimate of S_{Hmax} is around 16.3 MPa (Figure B.3). Since tensile strength T_0 is
a negative term in equation B.1, the assumption of no tensile strength provides an upper
limit of S_{Hmax}, when using the method after Haimson & Fairhurst (1970). Assuming a
maximum absolute tensile strength of 1.2 MPa derived from the difference between FBP and
FPP yields a S_{Hmax} of 15.1 MPa. Both estimates of S_{Hmax} are less than the estimated vertical
stress range between 17.1 MPa and 21 MPa, supporting the presence of a normal-faulting
stress regime.

B.4.2 Leak-off test, formation integrity test and cementation pressure data of the Greater Munich Area

Besides the Unterhaching Gt 1 LOT at 825 mTVD, FITs and cementation pressures of
additional 21 wells and a deep LOT with lower quality from the Unterhaching Gt 1 well
were analyzed (Table B.1; Figure 4). Since FITs only provide a lower boundary of the
minimum principal stress, we have only chosen FITs, which were performed in lithological
units (here: shales) comparable to the LOTs of the Unterhaching Gt 1 well. So, the FIT and
cementation pressure results can be set into the context of the more reliable LOT data and
can be used to provide additional insights into the stress regime of the Cenozoic basin fill
of the central part of the Bavarian Foreland Molasse Basin.

Investigation of the relationship between the maximum and minimum principal effective
stresses can provide information about the friction coefficient μ, if a critically stressed
environment is assumed (c.f. Zoback, 2010). Since a friction coefficient of 0.4 and a normal-
faulting stress regime were interpreted from the Unterhaching Gt 1 LOT at 825 mTVD, the
minimum principal effective stress would be the minimum horizontal effective stress σ_{Hmin},
while the maximum principal effective stress would be the vertical effective stress σ_v. Effec-
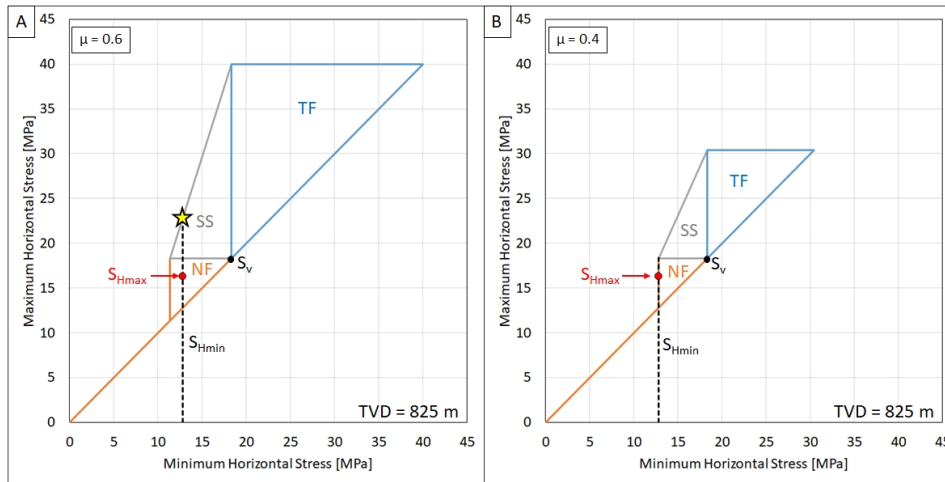
Figure B.3 – Stress polygon analysis (c.f. Zoback, 2010) of the leak-off test at 825 m at the Unterhaching Gt 1 well location. A and B: Stress polygons for the Unterhaching Gt 1 leak-off test at 825 mTVD assuming a friction coefficient of $\mu = 0.6$ (A) and $\mu = 0.4$ (B), respectively. The dashed lines mark the value of the minimum horizontal stress S_{Hmin} derived from the leak-off test. In A, the intersection with the stress polygon is marked by a yellow star. S_v = vertical stress, S_{Hmax} = estimated maximum horizontal stress (after Haimson & Fairhurst, 1970). NF = normal-faulting stress regime, SS = strike-slip stress regime, TF = thrust-faulting stress regime. Under critically stressed conditions, panel A would represent a strike-slip-stress regime, while panel B would represent a normal-faulting stress regime.

Table B.1 – Disclosed leak–off test and formation integrity test data used in this study.

Well name	TVD [m]	Strat. Unit	Test type	MW [g/cm³]	σ_v [MPa]	σ_{Hmin} [MPa]
Unterhaching Gt1	825	M. Mioc.	LOT	1.03	9.60	4.74
Unterhaching Gt1	1345	L. Mioc.	LOT*	1.10	16.27	7.32
Poing Th1	207	M. Mioc.	FIT	1.09	2.29	1.30
Poing Th1	652	M. Mioc.	FIT	1.08	7.48	3.34
Poing Th1	1688	U. Oligoc.	FIT	1.16	20.89	8.77
Poing Th2	205.5	M. Mioc.	FIT	1.06	2.26	1.55
Poing Th2	632	M. Mioc.	FIT	1.09	7.24	2.56
Poing Th2	1801	U. Oligoc.	FIT	1.15	22.44	14.65
Pullach Th3	2108	U. Oligoc.	FIT	1.10	25.00	7.46

TVD = true vertical depth, MW = initial drilling mud weight, σ_v = vertical effective stress, σ_{Hmin} = minimum horizontal effective stress, LOT = leak–off test, LOT* = leak–off test with multiple pressure build–ups (here the first build–up pressure has been taken), FIT = formation integrity test.

tive stresses can be easily estimated by subtracting pore pressure from the principal stress. In the Bavarian Foreland Molasse Basin, pore pressure is known to follow a hydrostatic gradient down to 1500 mTVD (c.f. Drews et al., 2018). Below 1500 m, overpressure might start to build up in Late Oligocene (Chattian) strata with a minimum vertical effective stress of 20 MPa (c.f. Drews et al., 2018). In this study, pore pressure in Chattian shales below 1500 m has been estimated from the average drilling mud weight (1.15 g/cm³) of wells with test data in this depth range (Figure B.4). A detailed look at all data in a pressure-depth profile reveals FIT data, which are most likely yielding too low minimum principal stresses, since other tests at similar depths and in the same litho-stratigraphic units yielded higher minimum principal stresses (Figure B.4). These tests have not been considered in the following analysis (see red circles in Figure B.4 for excluded data).

All remaining test data yield minimum horizontal effective stresses that are below the respective vertical effective stresses (Table B.1, Figure B.5A) and are therefore either implying a normal-faulting or strike-slip stress regime. Assuming frictional equilibrium
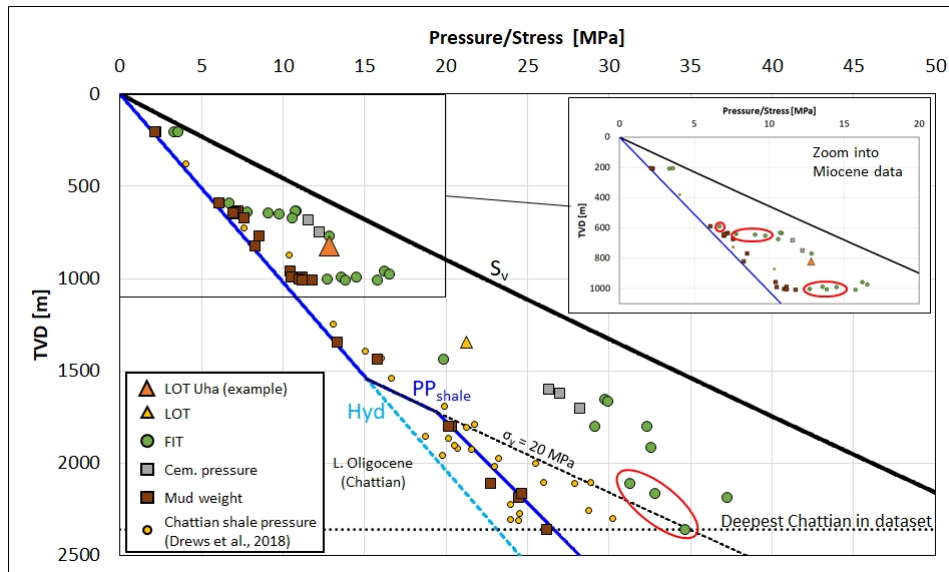
Figure B.4 – Pressure and stress vs. depth including all data used in this study. The inset represents a zoom into the shallower part of the dataset (TVD <1100 m; $pressure/stress$ < 20 MPa). Leak-off test, formation integrity test and cementation pressure data are represented by orange and yellow triangles, green dots and grey squares, respectively. The respective drilling mud weights are displayed as brown squares. Yellow dots represent the range of Chattian shale pore pressures derived from seismic velocities (from Drews et al., 2018). The formation integrity tests framed by red circles are likely too low and were excluded in further analysis. TVD = true vertical depth, S_v =vertical stress after Drews et al. (2018), Hyd = hydrostatic pore pressure, PP_{shale} = estimated shale pore pressure, σ_v = vertical effective stress.

and a normal-faulting stress regime, as interpreted from the Unterhaching Gt 1 LOT at 825 m, yields typical shale friction coefficients between 0.2–0.4 for more than 90 % of the data (Figure B.5A).

Assuming frictional equilibrium, a constant friction coefficient for all data and S_{Hmin} being the minimum principal stress, allows for an estimate of the theoretical maximum principal stress S_1. (c.f. Zoback, 2010). Thereby, any variation from the actual vertical stress gives insight into the likelihood of either being in a normal-faulting or strike-slip stress regime. Figure B.5 B-D illustrates the difference between the theoretical maximum principal stress S_1 as calculated from frictional equilibrium (using S_{Hmin} values from all LOT, FIT and cementation pressure data and friction coefficients of 0.3, 0.4 and 0.6, respectively) and the estimated vertical stress S_v (ϕ_0 = 0.3, C to 31 MPa^{-1} , c.f. equation B.3). In order to address the uncertainty related to the vertical stress estimate, lower and upper bound differences have been calculated, representing vertical stress profiles based on the shale compaction trend from Drews et al. (2018) (ϕ_0 = 0.4,C to 31 MPa^{-1}, c.f. equation B.3) and a constant bulk density of 2600 kg/m³, respectively. Data plotting between these vertical stress bounds would suggest a normal-faulting stress regime is most likely present, provided the assumed friction coefficient was representative. Data points plotting above the upper vertical stress bound would either represent a strike-slip stress regime, higher than estimated pore pressures, or a smaller friction coefficient. Data points plotting below the lower vertical stress bound would indicate test data, which yielded too low minimum principal stresses, e.g. FITs, which stopped significantly before reaching the leak-off point. Except for a few data points, which plot below the lower vertical stress bound, most data are

within the vertical stress bounds for a friction coefficient of 0.3, indicating a normal-faulting stress regime as most likely solution (Figure B.5B). For a friction coefficient of 0.4 (Figure B.5C), as derived from the Unterhaching Gt 1 LOT, the large majority of data points plot between the vertical stress bounds, which would support the hypothesis of the presence of a normal-faulting stress regime in the Greater Munich Area. The data between 1500 and 2000 m, plotting above the upper vertical stress bound, might represent a strike-slip stress regime, an underestimation of overpressure or friction coefficients < 0.4. Applying a friction coefficient of 0.5 to estimate S_1, results in most data points plotting above the upper vertical stress bound (Figure B.5D). In this case, a strike-slip stress regime would be more likely, and the results of the LOT of the Unterhaching Gt 1 well were not representative. However, shale friction coefficients of 0.5 or higher are unusually high for mixed illite-smectite-rich shales (c.f. Byerlee, 1978; Gaarenstroom et al., 1993; Kohli & Zoback, 2013; Morley et al., 2018; Stump & Flemings, 2002), or imply a much lower smectite content than observed in the adjacent Upper Austrian part of the North Alpine Foreland Basin (c.f. Gier, 1998). Also, the fairly shallow Unterhaching Gt 1 LOT at 825 mTVD provides a high quality data base case for presence of a normal-faulting stress regime and, under the assumption of frictional equilibrium, points towards a friction coefficient of 0.4 (or less). Nevertheless, friction coefficients < 0.1, as reported previously for the detachments of the Subalpine Molasse (Hagke et al., 2014), cannot be supported for shales of the undeformed part of the Bavarian Foreland Molasse Basin, but might be present at greater depths and \or where overpressure magnitudes are comparable to the Subalpine Molasse (c.f. Drews et al., 2018; Müller et al., 1988).

In addition to the uncertainty related to the vertical stress estimation, local variations of the stress regime towards a strike-slip stress regime (c.f. Seithel et al., 2015), yet undetected overpressured sections or unresolved lithological variations might also be causes of diversion from the Unterhaching Gt 1 base case LOT. Most important, it has to be pointed out that FITs only provide a lower bound of the minimum principal stress, which might bias the interpretation depending on the assumed friction coefficient. This definitely appears to be the case for data points plotting below the lower bound in Figure B.5B. The remaining LOT, FIT and cementation pressure data show very similar stress ratios and frictional behavior as the LOT at 825 mTVD in the Unterhaching Gt 1 well (Figure B.5A), though.

B.4.3 Implications for the stress regime of the Bavarian Foreland Molasse Basin

The results of the lithology-dependent analysis of LOT, FIT and cementation pressure data indicate that a normal-faulting stress regime is most likely present – at least in the central part of the Bavarian Foreland Molasse Basin. Since all test data yield minimum principal stresses, which are less than the estimated range of vertical stress, presence of a predominant thrust-faulting stress regime can be excluded for the Cenozoic basin fill of the central part of the Bavarian Foreland Molasse Basin. Therefore, the results of this study provide a valuable update of previous studies, which were either lithologically unconstrained (Reinecker et al., 2010; Seithel et al., 2015) and \or used indirect methods to investigate the stress regime (Reinecker et al., 2010; Ziegler et al., 2016) and interpreted a strike-slip to thrust-faulting
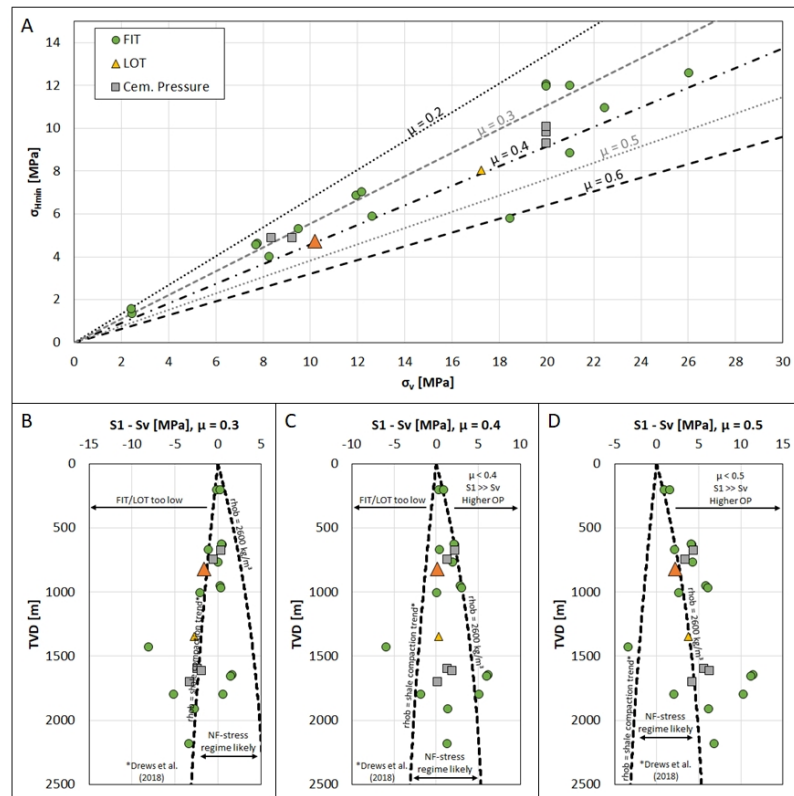
Figure B.5 – Analysis of cementation pressures, formation integrity and leak-off test data of all wells used in this study. A: Minimum horizontal effective stress (σ_{Hmin}) vs. vertical effective stress (σ_v). The dotted, dashed-dotted and dashed black and grey lines indicate where data points would plot in case of a critically stressed crust and friction coefficients of $\mu = 0.2$, $\mu = 0.3$, $\mu = 0.4$, $\mu = 0.5$ and $\mu = 0.6$, respectively. The legend also applies to figures B-D. B-D: Difference of theoretical maximum principal stress S_1 and modeled vertical stress S_v assuming a friction coefficient of 0.3, 0.4 and 0.5 for all data points, respectively. The left dashed black line represents the difference between a lower bound vertical stress for a pure shale lithological column and the modeled vertical stress, while the right dashed black line represents the difference between an upper bound vertical stress (assuming a constant bulk density ρ_b of 2600 kg/m³) and the modeled vertical stress. Vertical stress has been modeled using equation B.3 (c.f. Drews et al., 2018). Data plotting left of the lower vertical stress bound indicate FITs, which were stopped too early before leak-off. OP = overpressure.

stress regime (Reinecker et al., 2010) or a strike-slip stress regime (Seithel et al., 2015; Ziegler et al., 2016). The presence of Cenozoic normal faults in the central part of the Bavarian Foreland Molasse Basin (Hartmann et al., 2016) underpins that a normal-faulting stress regime has been present at least in Miocene times. In the Bavarian Foreland Molasse Basin, overpressure generation is dominated by vertical loading-induced disequilibrium compaction (Drews et al., 2018; Drews et al., 2019b). In a strike-slip or even compressional stress regime, lateral stress should strongly influence or even dominate compaction or overpressure formation, which does not appear to be the case in the undeformed part of the Bavarian Foreland Molasse Basin (Drews et al., 2018). Together with results from recent generic numerical studies (Gao et al., 2018; Obradors-Prats et al., 2017), it can therefore be speculated if the interpreted normal-faulting stress regime in the central part of the basin can be extrapolated to the entire undeformed part of the Bavarian Foreland Molasse Basin. However, the stress regime might be increasingly influenced by lateral stresses

towards the geological boundaries of the Bavarian Foreland Molasse Basin (Lohr, 1978; Reinecker et al., 2010), such as the crystalline basement exposure in Eastern Bavaria and in particular towards the North Alpine Thrust Front (Subalpine Molasse) to the south of the Bavarian Foreland Molasse Basin (Müller & Nieberding, 1996; Müller et al., 1988). Also, a positive shale velocity anomaly in the north–western part of the Bavarian Foreland Molasse Basin (Drews et al., 2018) might be related to either uplift and \or increased lateral compression against the Swabian Alb. Access to LOT data in the remainder of the basin would be necessary to investigate the spatial distribution of stress magnitudes and stress regime variations in the entire Bavarian Foreland Molasse Basin. Until then, a predominant strike-slip or even thrust-faulting stress regime cannot be excluded for the areas, which are outside of the central part of the Bavarian Foreland Molasse Basin investigated in this study.

Most likely, the stress regime also varies on smaller scales, for example in the vicinity of fault zones (Seithel et al., 2015). An increased influence of lateral stress on the most shallow stratigraphic units of foreland basins of fold-and-thrust-belt systems has been recently suggested by hydromechanical numerical studies (Gao et al., 2018; Obradors-Prats et al., 2017) and discussed for the Bavarian Foreland Molasse Basin (Ziegler et al., 2016) and Central Europe (Gölke & Coblentz, 1996). Also, several studies suggested presence of a normal-faulting to strike-slip stress regime in the Mesozoic sub-Molasse sediments Budach et al. (2017) and Seithel et al. (2015) and a strike-slip stress regime in the crystalline basement (Megies & Wassermann, 2014) of the central part of the Bavarian Foreland Molasse Basin. A simplified model for the vertical variation of the stress regime in the central part of the Bavarian Foreland Molasse Basin might therefore be given by presence of a normal-faulting stress regime in the Cenozoic basin fill (as presented in this study), which converges towards a strike-slip stress regime in the crystalline basement (Megies & Wassermann, 2014)) with a transition zone (normal-faulting to strike-slip stress regime) in the sub-Molasse Mesozoic sediments (Budach et al., 2017; Seithel et al., 2015).

B.4.4 Implications for drilling and fluid extraction in the Greater Munich Area

The Greater Munich Area in the central part of the Bavarian Foreland Molasse Basin is Germany's most active hydrothermal heat and energy province. Although the production of hot water is from the Mesozoic (Upper Jurassic) sub-Molasse sediments, the new insights into the stress regime of the Cenozoic basin fill have relevance to deep drilling in the Greater Munich Area: many deep geothermal wells experienced wellbore stability problems in the Cenozoic section. Understanding the stress regime is a key input for wellbore stability studies and for optimizing both casing and drilling mud weight programs prior to drilling. For example, under the assumption of a normal-faulting stress regime (based on the results of this study) and frictional equilibrium, the derived shale friction coefficients between 0.2 and 0.4 can be used to estimate S_{Hmin} or "fracture gradient" to predict (prior to drilling) the maximum drilling mud weight before drilling fluid losses are induced. The results of this study therefore can contribute to minimizing non-productive time and associated additional costs due to wellbore stability problems or drilling fluid losses. Presence of a

normal-faulting stress regime in the Cenozoic basin fill also supports the hypothesis that a normal-faulting to strike-slip stress regime is present in the Mesozoic basement sediments in the Greater Munich Area (Budach et al., 2017; Seithel et al., 2015), which is important for an improved reservoir management.

B.5 Conclusion

Leak-off test, formation integrity test and cementation pressure data have been investigated in detail and with respect to the lithological composition of the tested formations to infer information about the stress regime of the central part of the Bavarian Foreland Molasse Basin. Thereby, only tests performed in shale-rich formations have been considered. In that way, the following conclusions can be drawn:

- ⬦ A normal-faulting stress regime is most likely present in the Cenozoic basin fill of the central part (Greater Munich Area) of the Bavarian Foreland Molasse Basin.
- ⬦ Assuming a critically stressed crust, a normal-faulting stress regime and together with an estimate of the vertical stress S_v, a friction coefficient between 0.2 and 0.4 can be used to estimate S_{Hmin} in shale-dominated strata of the central part of the Bavarian Foreland Molasse Basin.
- ⬦ Incorporation of the lithological composition of the tested formation is important for understanding the frictional equilibrium on the basis of formation integrity test and leak-off test data.
- ⬦ On smaller scales, variations of the stress regime cannot be excluded, e.g. in the vicinity of fault zones and due to variations in mechanical rock strength.
- ⬦ Additional studies in other areas of the basin, using high quality leak-off test data, are required to fully unravel the stress regime variations of the entire Bavarian Foreland Molasse Basin.

References

Aadnoy, B. S. (1990): Inversion Technique to Determine the in-Situ Stress Field from Fracturing Data. – in: *Journal of Petroleum Science and Engineering* 4 (2), pp. 127–141. – DOI: 10.1016/0920-4105(90)90021-T.

Agemar, T., Suchi, E. & Moeck, I. (2018): Die Rolle der tiefen Geothermie bei der Wärmewende: Wie Deutschland die 60% erneuerbare Wärme bis 2050 schaffen könnte. – ed. by LIAG. – Hannover.

Agemar, T., Weber, J. & Schulz, R. (2014): Deep Geothermal Energy Production in Germany. – in: *Energies* 7 (7), pp. 4397–4416. – DOI: 10.3390/en7074397.

Agosta, F. & Kirschner, D. L. (2003): Fluid conduits in carbonate-hosted seismogenic normal faults of central Italy. – in: *Journal of Geophysical Research: Solid Earth* 108 (B4), n/a–n/a. – DOI: 10.1029/2002JB002013.

Allen, M. R., Dube, O. P., Solecki, W., Aragón-Durand, F., Cramer, W., Humphreys, S., Kainuma, M., Kala, J., Mahowald, N., Mulugetta, Y., Perez, R., Wairiu, M. & Zickfeld, K. (2018): Framing and Context. – in: *Global Warming of 1.5°C*. – ed. by IPCC.

Ameen, M. S., Smart, B. G., Somerville, J., Hammilton, S. & Naji, N. A. (2009): Predicting rock mechanical properties of carbonates from wireline logs (A case study: Arab-D reservoir, Ghawar field, Saudi Arabia). – in: *Marine and Petroleum Geology* 26 (4), pp. 430–444. – DOI: 10.1016/j.marpetgeo.2009.01.017.

Anderson, E. M. (1951): The Dynamic of Faulting and Dyke Formation with Application to Britain. – Edinburgh: Oliver and Boyd.

Athy, L. F. (1930): Density, porosity and compaction of sedimentary rocks. – in: *AAPG Bulletin* (14), pp. 1–24.

Bachmann, G. H., Müller, M. & Weggen, K. (1987): Evolution of the Molasse Basin (Germany, Switzerland). – in: *Tectonophysics* 137 (1-4), pp. 77–92. – DOI: 10.1016/0040-1951(87)90315-5.

Bachmann, G. H. & Müller, M. (1992): Sedimentary and structural evolution of the German Molasse Basin. – in: *Ecologae Geologicae Helvetiae* 85 (3), pp. 519–530. – DOI: 10.5169/seals-167019.

Barton, C. A., Zoback, M. D. & Moos, D. (1995): Fluid-flow along potentially active faults in crystalline rock. – in: *Geology* 23 (8), pp. 683–686. – DOI: 10.1130/0091-7613(1995)023<0683:Ffapaf>2.3.Co;2.

Barton, C., Castillo, D. A., Moos, D., Peska, P. & Zoback, M. D. (1998): Characterising the Full Stress Tensor Based on Observations of Drilling-Induced Wellbore Failures in Vertical

and Inclined Boreholes Leading to Improved Wellbore Stability and Permeability Prediction. – in: *APPEA Journal*, pp. 29–53.

Barton, C., Moos, D. & Tezuka, K. (2009): Geomechanical wellbore imaging: Implications for reservoir fracture permeability. – in: *AAPG Bulletin* 93 (11), pp. 1551–1569. – DOI: 10.1306/06180909030.

Barton, C. & Moos, M. (2010): Geomechanical Wellbore Imaging: Key to managing the asset life cycle. – in: *Dipmeter and Borehole Image Log Technology*. – ed. by M. Poppelreiter, Garcia - Carballido, C. & M. Kraaijveld. – vol. 92. – AAPG Memoir, pp. 81–112. – DOI: 10.1306/13181279M922689.

Barton, C. A. & Zoback, M. D. (1994): Stress perturbations associated with active faults penetrated by boreholes: Possible evidence for near-complete stress drop and a new technique for stress magnitude measurement. – in: *Journal of Geophysical Research: Solid Earth* 99 (B5), pp. 9373–9390. – DOI: 10.1029/93JB03359.

Barton, C. A., Zoback, M. D. & Burns, K. L. (1988): In-situ stress orientation and magnitude at the Fenton Geothermal Site, New Mexico, determined from wellbore breakouts. – in: *Geophysical Research Letters* 15 (5), pp. 467–470. – DOI: 10.1029/GL015i005p00467.

Bauer, J. F., Meier, S. & Philipp, S. L. (2015): Architecture, fracture system, mechanical properties and permeability structure of a fault zone in Lower Triassic sandstone, Upper Rhine Graben. – in: *Tectonophysics*. – DOI: 10.1016/j.tecto.2015.02.014.

Baumann, T., Bartels, J., Lafogler, M. & Wenderoth, F. (2017): Assessment of heat mining and hydrogeochemical reactions with data from a former geothermal injection well in the Malm Aquifer, Bavarian Molasse Basin, Germany. – in: *Geothermics* 66, pp. 50–60. – DOI: 10.1016/j.geothermics.2016.11.008.

Bell, J. S. (1996): Petro Geoscience 1. In situ stresses in sedimentary rocks (1) Measurement techniques. – in: *Geoscience Canada* 23 (2), pp. 85–100. – DOI: 10.12789/gs.v23i2.3902.

Bell, J. S. & Gough, D. I. (1979): Northeast-Southwest Compressive Stress in Alberta - Evidence from Oil-Wells. – in: *Earth and Planetary Science Letters* 45 (2), pp. 475–482. – DOI: 10.1016/0012-821x(79)90146-8.

Bell, J. S. & Lloyd, P. F. (1989): Modelling of stress refraction in sediments around the Peace River Arch western Canada. – in: *Geological Survey of Canada* (Paper 89-1D), pp. 49–54.

Betz, D. & Wendt, A. (1983): Neuere Ergebnisse der Aufschluss- und Gewinnungstätigkeiten auf Erdöl und Erdgas in Süddeutschland. – in: *Bulletin Verein Schweizer Petroleum-Geologen und -Ingenieure* 49 (117), pp. 9–36.

Billi, A., Salvini, F. & Storti, F. (2003): The damage zone-fault core transition in carbonate rocks: implications for fault growth, structure and permeability. – in: *Journal of Structural Geology* 25 (11), pp. 1779–1794. – DOI: 10.1016/S0191-8141(03)00037-3.

Biot, M. A. (1962): Mechanics of Deformation and Acoustic Propagation in Porous Media. – in: *Journal of Applied Physics* (Vol. 33, No. 4), pp. 1482–1498.

Birner, J., Fritzer, T., Jodocy, M., Savvatis, A., Schneider, M. & Stober, I. (2012): Hydraulische Eigenschaften des Malmaquifers im Süddeutschen Molassebecken und ihre Bedeutung für die geothermische Erschließung. – in: *Zeitschrift für Geologische Wissenschaften* 40 (2-3), pp. 133–156.

Boehm, F., Savvatis, A., Steiner, U., Schneider, M. & Koch, R. (2012): Lithofacies and characterization of the geothermal Malm reservoir in the greater area of Munich. – in: *Grundwasser* 18 (1), pp. 3–13. – DOI: 10.1007/s00767-012-0202-4.

Bradley, D. C. & Kidd, W. (1991): Flexural Extension of the Upper Continental-Crust in Collisional Foredeeps. – in: *Geological Society of America Bulletin* 103 (11), pp. 1416–1438. – DOI: 10.1130/0016-7606(1991)103<1416:Feotuc>2.3.Co;2.

Brady, B. H. G. & Brown, E. T. (2006): Rock mechanics for underground mining. – 3. ed., repr. with corr. – Dordrecht: Springer.

Brudy, M. & Zoback, M. D. (1993): Compressive and Tensile Failure of Boreholes Arbitrarily-Inclined to Principal Stress Axes - Application to the KTB Boreholes, Germany. – in: *International Journal of Rock Mechanics and Mining Sciences & Geomechanics* 30 (7), pp. 1035–1038. – DOI: 10.1016/0148-9062(93)90068-O.

Brudy, M. & Zoback, M. D. (1998): Drilling-induced tensile wall-fractures: implications for determination of in-situ stress orientation and magnitude. – in: *International Journal of Rock Mechanics and Mining Sciences* 36 (2), pp. 191–215. – DOI: 10.1016/S0148-9062(98)00182-X.

Brudy, M., Zoback, M. D., Fuchs, K., Rummel, F. & Baumgartner, J. (1997): Estimation of the complete stress tensor to 8 km depth in the KTB scientific drill holes: Implications for crustal strength. – in: *Journal of Geophysical Research-Solid Earth* 102 (B8), pp. 18453–18475. – DOI: 10.1029/96jb02942.

Budach, I., Moeck, I., Lüschen, E. & Wolfgramm, M. (2017): Temporal evolution of fault systems in the Upper Jurassic of the Central German Molasse Basin: Case study Unterhaching. – in: *International Journal of Earth Sciences* 85 (3), p. 519. – DOI: 10.1007/s00531-017-1518-1.

Byerlee, J. (1978): Friction of Rocks. – in: *Pure and Applied Geophysics* 116 (4-5), pp. 615–626. – DOI: 10.1007/Bf00876528.

Cacace, M. & Blöcher, G. (2015): MeshIt—a software for three dimensional volumetric meshing of complex faulted reservoirs. – in: *Environmental Earth Sciences* 74 (6), pp. 5191–5209. – DOI: 10.1007/s12665-015-4537-x.

Caine, J. S., Evans, J. P. & Forster, C. B. (1996): Fault zone architecture and permeability structure. – in: *Geology* 24 (11), pp. 1025–1028. – DOI: 10.1130/0091-7613(1996)024<1025:Fzaaps>2.3.Co;2.

Castillo, D. A., Bishop, D. J., Donaldson, I., Kuek, Ruig, M. de, Trupp, M. & Shuster, M. W. (2000): Trap integrity in the lam in aria high-nancar trough region, timor sea: prediction

of fault integrity failure using well-constrained stress tensors and fault SURFACES INTERPRETED FROM 3D SEISMIC. – in: *The APPEA Journal* 40 (1), p. 151. – DOI: 10.1071/AJ99009.

Childs, C., Nicol, A., Walsh, J. J. & Watterson, J. (1996): Growth of vertically segmented normal faults. – in: *Journal of Structural Geology* 18 (12), pp. 1389–1397. – DOI: 10.1016/S0191-8141(96)00060-0.

Colton-Bradley, V. A. C. (1987): Role of pressure in smectite dehydration - effects on geopressure and smectite-to-illite transition. – in: *AAPG Bulletin* (71), pp. 1414–1427.

Cornet, F. H. (2015): Elements of Crustal Geomechanics. – Cambridge: Cambridge University Press. – DOI: 10.1017/CBO9781139034050.

Couzens-Schultz, B. A. & Azbel, K. (2014): Predicting pore pressure in active fold–thrust systems: An empirical model for the deepwater Sabah foldbelt. – in: *Journal of Structural Geology* 69, pp. 465–480. – DOI: 10.1016/j.jsg.2014.07.013.

Davatzes, N. C. & Hickman, S. H. (2010): Stress, Fracture, and Fluid-flow Analysis Using Acoustic and Electrical Image Logs in Hot Fractured Granites of the Coso Geothermal Field, California, U.S.A. – in: *Dipmeter and Borehole Image Log Technology*. – ed. by M. Poppelreiter, Garcia - Carballido, C. & M. Kraaijveld. – vol. 92. – AAPG Memoir, pp. 259–293. – DOI: 10.1306/13181288M923134.

Dorsch, K. & Pletl, C. (2012): Bayerisches Molassebecken - Erfolgsregion der Tiefengeothermie in Mitteleuropa. – in: *Geothermische Energie* 73, pp. 14–18.

Drews, M. C., Seithel, R., Savvatis, A., Kohl, T. & Stollhofen, H. (2019a): A normal-faulting stress regime in the Bavarian Foreland Molasse Basin? New evidence from detailed analysis of leak-off and formation integrity tests in the greater Munich area, SE-Germany. – in: *Tectonophysics* 755, pp. 1–9. – DOI: 10.1016/j.tecto.2019.02.011.

Drews, M. C., Bauer, W., Caracciolo, L. & Stollhofen, H. (2018): Disequilibrium compaction overpressure in shales of the Bavarian Foreland Molasse Basin: Results and geographical distribution from velocity-based analyses. – in: *Marine and Petroleum Geology* 92, pp. 37–50. – DOI: 10.1016/j.marpetgeo.2018.02.017.

Drews, M. C., Hofstetter, P., Zosseder, K., Straubinger, R., Gahr, A. & Stollhofen, H. (2019b): Predictability and controlling factors of overpressure in the North Alpine Foreland Basin, SE Germany: An interdisciplinary post-drill analysis of the Geretsried GEN-1 deep geothermal well. – in: *Geothermal Energy* 7 (1), p. 1. – DOI: 10.1186/s40517-019-0121-z.

Eaton, B. A. (1969): Fracture gradient prediction and its application in oilfield operations. – in: *Journal of Petroleum Technology* 246, pp. 1353–1360.

Ellis, D. v. & Singer, J. M. (2008): Well logging for earth scientists. – 2nd ed, repr. with corrections. – Dordrecht: Springer.

Ellsworth, W. L. (2013): Injection-induced earthquakes. – in: *Science* 341 (6142), p. 1225942. – DOI: 10.1126/science.1225942.

Evans, K. F., Zappone, A., Kraft, T., Deichmann, N. & Moia, F. (2012): A survey of the induced seismic responses to fluid injection in geothermal and CO2 reservoirs in Europe. – in: *Geothermics* 41, pp. 30–54. – DOI: 10.1016/j.geothermics.2011.08.002.

Faulds, J. E., Hinz, N. H., Coolbaugh, M. F., Cashman, P. H., Kratt, C., Derling, G., Edwards, J., Mayhew, B. & McLachlan, H. (2011): Assessment of Favorable Structural Settings of Geothermal Systems in the Great Basin, Western USA. – in: . – vol. 35, pp. 777–783.

Faulkner, D. R., Jackson, C. A. L., Lunn, R. J., Schlische, R. W., Shipton, Z. K., Wibberley, C. A. J. & Withjack, M. O. (2010): A review of recent developments concerning the structure, mechanics and fluid flow properties of fault zones. – in: *Journal of Structural Geology* 32 (11), pp. 1557–1575. – DOI: 10.1016/j.jsg.2010.06.009.

Faulkner, D. R., Lewis, A. C. & Rutter, E. H. (2003): On the internal structure and mechanics of large strike-slip fault zones: field observations of the Carboneras fault in southeastem Spain. – in: *Tectonophysics* 367 (3-4), pp. 235–251. – DOI: 10.1016/S0040-1951(03)00134-3.

Fjaer, E., Holt, R. M., Horsrud, P., Raaen, A. M. & Risnes, R. (2008): Petroleum Related Rock Mechanics. – Amsterdam and Netherlands: Elsevier.

Frisch, W. (1979): Tectonic Progradation and Plate Tectonic Evolution of the Alps. – in: *Tectonophysics* 60 (3-4), pp. 121–139. – DOI: 10.1016/0040-1951(79)90155-0.

Frisch, W., Dunkl, I. & Kuhlemann, J. (2000): Post-collisional orogen-parallel large-scale extension in the Eastern Alps. – in: *Tectonophysics* 327 (3-4), pp. 239–265. – DOI: 10.1016/S0040-1951(00)00204-3.

Gaarenstroom, L., Tromp, R. A. J., Jong, M. C. d. & Brandenburg, A. M. (1993): Overpressures in the Central North Sea: implications for trap integrity and drilling safety. – in: *Petroleum Geology of Northwest Europe: Proceeding of the 4th Conference*, pp. 1305–1313. – DOI: 10.1144/0041305.

Gao, B., Flemings, P. B., Nikolinakou, M. A., Saffer, D. M. & Heidari, M. (2018): Mechanics of Fold-and-Thrust Belts Based on Geomechanical Modeling. – in: *Journal of Geophysical Research: Solid Earth* 123 (5), pp. 4454–4474. – DOI: 10.1029/2018JB015434.

Gaucher, E., Schoenball, M., Heidbach, O., Zang, A., Fokker, P. A., van Wees, J.-D. & Kohl, T. (2015): Induced seismicity in geothermal reservoirs: A review of forecasting approaches. – in: *Renewable and Sustainable Energy Reviews* 52, pp. 1473–1490. – DOI: 10.1016/j.rser.2015.08.026.

Geotis (2019): Geothermal Potentials. – https://www.geotis.de/geotis/templates/geotis.php.

Gier, S. (1998): Burial diagenetic processes and clay mineral formation in the Molasse zone of Upper Austria. – in: *Clays and Clay Minerals* (45), pp. 659–669.

Goertz-Allmann, B. P., Gibbons, S. J., Oye, V., Bauer, R. & Will, R. (2017): Characterization of induced seismicity patterns derived from internal structure in event clusters. – in: *Journal of Geophysical Research: Solid Earth* 122 (5), pp. 3875–3894. – DOI: 10.1002/2016JB013731.

Gölke, M. & Coblentz, D. (1996): Origins of the European regional stress field. – in: *Tectonophysics* 266 (1-4), pp. 11–24. – DOI: 10.1016/S0040-1951(96)00180-1.

Greiner, G. & Lohr, J. (1980): Tectonic Stresses in the Northern Foreland of the Alpine System Measurements and Interpretation. – in: *Tectonic Stresses in the Alpine-Mediterranean Region.* – ed. by A. E. Scheidegger. – Vienna: Spinger, pp. 5–55.

Grottenthaler, W. (2009): Geologische Karte von Bayern 1:25 000, erläuterungen zum Blatt Nr. 8131 Schongau. – München: Bayrisches Landesamt für Umwelt.

Grünthal, G. & Stromeyer, D. (1986): Stress pattern in Central Europe and adjacent areas. – in: *Gerlands Beitrage zur Geophysik* (Vol. 95/5), pp. 443–452.

Grünthal, G. & Stromeyer, D. (1992): The recent crustal stress field in central Europe: Trajectories and finite element modeling. – in: *Journal of Geophysical Research - Solid Earth* 97 (B8), p. 11805. – DOI: 10.1029/91JB01963.

Grünthal, G. & Wahlström, R. (2012): The European-Mediterranean Earthquake Catalogue (EMEC) for the last millennium. – in: *Journal of Seismology* 16 (3), pp. 535–570. – DOI: 10.1007/s10950-012-9302-y.

Grünthal, G. (2014): Induced seismicity related to geothermal projects versus natural tectonic earthquakes and other types of induced seismic events in Central Europe. – in: *Geothermics* 52, pp. 22–35. – DOI: 10.1016/j.geothermics.2013.09.009.

GTV (2014): Liste der tiefen Geothermieprojekte in Deutschland.

Gudmundsson, A., Simmenes, T. H., Larsen, B. & Philipp, S. L. (2010): Effects of internal structure and local stresses on fracture propagation, deflection, and arrest in fault zones. – in: *Journal of Structural Geology* 32 (11), pp. 1643–1655. – DOI: 10.1016/j.jsg.2009.08.013.

Gunzburger, Y. & Magnenet, V. (2014): Stress inversion and basement-cover stress transmission across weak layers in the Paris basin, France. – in: *Tectonophysics* 617, pp. 44–57. – DOI: 10.1016/j.tecto.2014.01.016.

Hagke, C. von, Oncken, O. & Evseev, S. (2014): Critical taper analysis reveals lithological control of variations in detachment strength: An analysis of the Alpine basal detachment (Swiss Alps). – in: *Geochemistry, Geophysics, Geosystems* 15 (1), pp. 176–191. – DOI: 10.1002/2013GC005018.

Haimson, B. C. & Fairhurst, C. (1970): In situ stress determination at great depth by means of hydraulic fracturing. – in: *11th Symposium on Rock Mechnaics.* – ed. by W. Somerton, pp. 559–584.

Hartmann, H. von, Tanner, D. C. & Schumacher, S. (2016): Initiation and development of normal faults within the German alpine foreland basin: The inconspicuous role of basement structures. – in: *Tectonics* 35 (6), pp. 1560–1574. – DOI: 10.1002/2016TC004176.

Heap, M. J. & Faulkner, D. R. (2008): Quantifying the evolution of static elastic properties as crystalline rock approaches failure. – in: *International Journal of Rock Mechanics and Mining Sciences* 45 (4), pp. 564–573. – DOI: 10.1016/j.ijrmms.2007.07.018.

Heidbach, O. & Reinecker, J. (2013): Analyse des rezenten Spannungsfeldes der Nordschweiz: Arbeitsbericht NAB 12-05. – Wettingen.

Heidbach, O., Reinecker, J., Tingay, M., Muller, B., Sperner, B., Fuchs, K. & Wenzel, F. (2007): Plate boundary forces are not enough: Second- and third-order stress patterns highlighted in the World Stress Map database. – in: *Tectonics* 26 (6). – DOI: 10.1029/2007tc002133.

Heidbach, O., Tingay, M., Barth, A., Reinecker, J., Kurfess, D. & Muller, B. (2010): Global crustal stress pattern based on the World Stress Map database release 2008. – in: *Tectonophysics* 482 (1-4), pp. 3–15. – DOI: 10.1016/j.tecto.2009.07.023.

Heidbach, O., Rajabi, M., Cui, X., Fuchs, K., Müller, B., Reinecker, J., Reiter, K., Tingay, M., Wenzel, F., Xie, F., Ziegler, M. O., Zoback, M.-L. & Zoback, M. (2018): The World Stress Map database release 2016: Crustal stress pattern across scales. – in: *Tectonophysics* 744, pp. 484–498. – DOI: 10.1016/j.tecto.2018.07.007.

Heidbach, O., Rajabi, M., Reiter, K. & Ziegler, M. (2016): World Stress Map 2016. – in: . – DOI: 10.5880/WSM.2016.001.

Heppard, P. D. & Cander, H.S., Eggertson, E.B. (1998): Abnormal pressure and the occurrence of hydrocarbons in offshore eastern Trinidad, West Indies. – in: *AAPG Memoir* (70), pp. 215–246.

Hergert, T., Heidbach, O., Reiter, K., Giger, S. B. & Marschall, P. (2015): Stress field sensitivity analysis in a sedimentary sequence of the Alpine foreland, northern Switzerland. – in: *Solid Earth* 6 (2), pp. 533–552. – DOI: 10.5194/se-6-533-2015.

Hickman, S. & Zoback, M. (1983): The interpretation of hydraulic fracturing pressure-time data for in-situ stress determination.. – in: *Hydraulic fracturing stress measurements*, pp. 44–54.

Hickman, S. H. & Zoback, M. D. (2004): Stress orientation and magnitudes in the SAFOD pilot hole. – in: *Geophysical Research Letters* 31. – DOI: 10.1029/2004GL020043.

Hiramatu, Y. & Oka, Y. (1968): Determination of Stress in Rock Unaffected by Boreholes or Drifts from Measured Strains or Deformations. – in: *International Journal of Rock Mechanics and Mining Sciences* 5 (4), pp. 337–353. – DOI: 10.1016/0148-9062(68)90005-3.

Homberg, C., Hu, J. C., Angelier, J., Bergerat, F. & Lacombe, O. (1997): Characterization of stress perturbations near major fault zones: Insights from 2-D distinct-element

numerical modelling and field studies (Jura mountains). – in: *Journal of Structural Geology* 19 (5), pp. 703–718. – DOI: 10.1016/S0191-8141(96)00104-6.

Hubbert, M. K. & Rubey, W. W. (1959): Role of fluid pressure in mechanics of overthrust faulting. – in: *Geological Society of America Bulletin* (70/2), pp. 115–166.

Hubbert, M. K. & Willis, D. G. (1972): Mechanics of Hydraulic Fracturing. – in: *Petroleum Transaction, AIME* 210.

Illies, J. H. & Greiner, G. (1978): Rhinegraben and the Alpine system. – in: *Geological Society of America Bulletin* 89 (5), pp. 770–782.

Illies, J. H., Baumann, H. & Hoffers, B. (1981): Stress pattern and strain release in the Alpine Foreland. – in: *Tectonophysics* 71 (1-4), pp. 157–172. – DOI: 10.1016/0040-1951(81)90059-7.

IPCC, ed. (2018): Global Warming of 1.5°C: An IPCC Special Report on the impacts of global warming of 1.5°C above pre-industrial levels and related global greenhouse gas emission pathways, in the context of strengthening the global response to the threat of climate change, sustainable development, and efforts to eradicate poverty.

Jaeger, J. C., Cook, Neville G. W & Zimmerman, R. W. (2007): Fundamentals of rock mechanics. – 4th ed.. – Malden, MA: Blackwell Pub.

Kang, J.-Q., Zhu, J.-B. & Zhao, J. (2019): A review of mechanisms of induced earthquakes: from a view of rock mechanics. – in: *Geomechanics and Geophysics for Geo-Energy and Geo-Resources* 34 (3), p. 3. – DOI: 10.1007/s40948-018-00102-z.

Kastrup, U., Zoback, M. L., Deichmann, N., Evans, K. F., Giardini, D. & Michael, A. J. (2004): Stress field variations in the Swiss Alps and the northern Alpine foreland derived from inversion of fault plane solutions. – in: *Journal of Geophysical Research - Solid Earth* 109 (B1), p. 104. – DOI: 10.1029/2003JB002550.

Kirsch, G. (1898): Die Theorie der Elastizität und die Bedürfnisse der Festigkeitslehre. – in: *Zeitschrift des Vereins deutscher Ingenieure* 42, pp. 797–807.

Kohli, A. H. & Zoback, M. D. (2013): Frictional properties of shale reservoir rocks. – in: *Journal of Geophysical Research: Solid Earth* 118 (9), pp. 5109–5125. – DOI: 10.1002/jgrb.50346.

Koschel, G. (1991): Geologischer Überblick: Hydrogeologische Rahmenbedingungen. – München, Freiburg.

Kraemer, C. (2009): Identifikation horizontaler Blattverschiebungen im Untergrund des Molassetrogs - neue Interpretationsergebnisse auf Grundlage von 2D-Seismik. – in: . – ed. by Geothermische Vereinigung.

Kuhlemann, J. & Kempf, O. (2002): Post-Eocene evolution of the North Alpine Foreland Basin and its response to Alpine tectonics. – in: *Sedimentary Geology* 152 (1-2), pp. 45–78. – DOI: 10.1016/S0037-0738(01)00285-8.

Laplaige, P., Lemale, J., Decottegnie, S., Desplan, A., Goyeneche, O. & Delobelle, G. (2005): Geothermal Resources in France - Current Situation and Prospects. – in: *World Geothermal Congress (WGC)*.

Lemcke, K. (1973): Zur nachpermischen Geschichte des nördlichen Alpenvorlandes. – in: *Geologica Bavarica* (63), pp. 5–48.

Lemcke, K. (1976): Übertiefe Grundwässer im süddeutschen Alpenvorland. – in: *Bulletin Verein Schweizer Petroleum-Geologen und -Ingenieure* (42), pp. 9–18.

Lemcke, K. (1988): Geologie von Bayern - Das bayerische Alpenvorland vor der Eiszeit. – Stuttgart: E. Schweizerbart' sche Verlagsbuchhandlung.

Lempp, C., Witthaus, M., Röckel, T., Hecht, C. & Herold, M. (2010): Geomechanisches Verhalten diagenetisch unterschiedlich stark verfestigter pelitischer Gesteine in tiefen Geothermiebohrungen. – in: *Zeitschrift der Deutschen Gesellschaft für Geowissenschaften* 161 (4), pp. 379–400. – DOI: 10.1127/1860-1804/2010/0161-0379.

Leydecker, G. (2009): Erdbebenkatalog für Deutschland mit Randgebieten für die Jahre 800 bis 2008: Catalog of earthquakes in Germany and adjacent areas between 800 AD and 2008. – vol. Reihe E, Band E 59. – Geologisches Jahrbuch.

LIAG (2017): Untersuchung der Seismizität am Standort des Geothermieprojekts Poing unter Einbeziehung von Strukturgeologie, Geohydraulik, Hydrochemie, Geomechanik und Dublettenbetrieb: Zusammenfassung. – Hannover.

Lin, W., Yeh, E.-C., Hung, J.-H., Haimson, B. & Hirono, T. (2010): Localized rotation of principal stress around faults and fractures determined from borehole breakouts in hole B of the Taiwan Chelungpu-fault Drilling Project (TCDP). – in: *Tectonophysics* 482 (1-4), pp. 82–91. – DOI: 10.1016/j.tecto.2009.06.020.

Ljunggren, C., Chang, Y., Janson, T. & Christiansson, R. (2003): An overview of rock stress measurement methods. – in: *International Journal of Rock Mechanics and Mining Sciences* 40 (7-8), pp. 975–989. – DOI: 10.1016/j.ijrmms.2003.07.003.

Lohr, J. (1969): Die seismischen Geschwindigkeiten der jüngeren Molasse im ostschweizerischen und deutschen Alpenvorland. – in: *Geophysical Prospecting* (17), pp. 111–125.

Lohr, J. (1978): Alpine stress documented by anomalous seismic velocities in the Molasse trough. – in: *Inter-Union Com. on Geodynamics. Sci. Rep.* (38), pp. 69–71.

Lüschen, E., Wolfgramm, M., Fritzer, T., Dussel, M., Thomas, R. & Schulz, R. (2014): 3D seismic survey explores geothermal targets for reservoir characterization at Unterhaching, Munich, Germany. – in: *Geothermics* 50 (167-179). – DOI: 10.1016/j.geothermics.2013.09.007.

Mardia, K. V. (1972): Statistics of directional data: probability and mathematical statistics. – London: London Academic Press.

Martin, C. D. & Chandler, N. A. (1993): Stress Heterogeneity and Geological Structures. – in: *International Journal of Rock Mechanics and Mining Sciences & Geomechanics Abstracts* 30 (7), pp. 993–999. – DOI: 10.1016/0148-9062(93)90059-M.

Martínez-Garzón, P., Kwiatek, G., Sone, H., Bohnhoff, M., Dresen, G. & Hartline, C. (2014): Spatiotemporal changes, faulting regimes, and source parameters of induced seismicity: A case study from The Geysers geothermal field. – in: *Journal of Geophysical Research: Solid Earth* 119 (11), pp. 8378–8396. – DOI: 10.1002/2014JB011385.

Mastin, L. (1988): Effect of Borehole Deviation on Breakout Orientation. – in: *Journal of Geophysical Research* 93 (B3), pp. 9187–9195. – DOI: 10.1029/JB093iB08p09187.

Megies, T., Ludwig-Maximilians-Universität München & Wassermann, J. (2017): Mikroseismische Aktivität geothermischer Systeme 2 - Vom Einzelsystem zur großräumigen Nutzung: Endbericht - MAGS2: Einzelprojekt 2 - Untersuchungen zur optimierten seismischen Überwachung hydrogeothermaler Systeme bei dichter räumlicher Lage der Bohrerlaubnisfelder am Beispiel der Situation im Süden Münchens. – München. – DOI: 10.2314/GBV:101142956X.

Megies, T. & Wassermann, J. (2013): Verbundprojekt MAGS – Konzepte zurBegrenzung der mikroseismischen Aktivitätbei der energetischen Nutzung geothermischer Systeme im tiefen Untergrund: EP 2: Untersuchung von Mikro-Beben in der bayerischen Molasse im Umfeld von geothermischen Reservoiren. – München.

Megies, T. & Wassermann, J. (2014): Microseismicity observed at a non-pressure-stimulated geothermal power plant. – in: *Geothermics* 52, pp. 36–49. – DOI: 10.1016/j.geothermics.2014.01.002.

Meyer, R. & Schmidt-Kaler, H. (1989): Paläogeographischer Atlas des süddeutschen Oberjura (Malm). – vol. 115. – Geologisches Jahrbuch. – Hannover.

Meyer, R. & Schmidt-Kaler, H. (1996): Jura.. – in: *Erläuterungen zur Geologischen Karte von Bayern 1:500.000.* – ed. by Bayerisches Geologisches Landesamt. – München, p. 329.

Michie, E., Haines, T. J., Healy, D., Neilson, J. E., Timms, N. E. & Wibberley, C. (2014): Influence of carbonate facies on fault zone architecture. – in: *Journal of Structural Geology* 65, pp. 82–99. – DOI: 10.1016/j.jsg.2014.04.007.

Mildren, S. D., Hillis, R. R. & Kaldi, J. (2002): Calibrating predictions of fault seal reactivation in the timor sea. – in: *The APPEA Journal* 42 (1), p. 187. – DOI: 10.1071/AJ01011.

Moeck, I., Kwiatek, G., Zimmermann, G., Backers, T. & Huenges, E. (2009): Assessment of Fault Reactivation Potential in a Deep Geothermal reservoir of the NE-German Basin (Germany). – in: *Geothermal Resources Council Transactions* (33), pp. 209–214.

Moos, D. & Zoback, M. D. (1990): Utilization of Observations of Well Bore Failure to Constrain the Orientation and Magnitude of Crustal Stresses - Application to Continental, Deep-Sea Drilling Project, and Ocean Drilling Program Boreholes. – in:

Journal of Geophysical Research - Solid Earth and Planets 95 (B6), pp. 9305–9325. – ᴅᴏɪ: 10.1029/Jb095ib06p09305.

Morley, C. K., Hagke, C. von, Hansberry, R., Collins, A., Kanitpanyacharoen, W. & King, R. (2018): Review of major shale-dominated detachment and thrust characteristics in the diagenetic zone: Part II, rock mechanics and microscopic scale. – in: *Earth-Science Reviews* 176, pp. 19–50. – ᴅᴏɪ: 10.1016/j.earscirev.2017.09.015.

Morris, A. P., Ferrill, D. A. & Henderson, D. B. (1996): Slip-tendency analysis and fault reactivation. – in: *Geology* 24 (3), pp. 275–278. – ᴅᴏɪ: 10.1130/0091-7613(1996)024<0275: STAAFR>2.3.CO;2.

Mraz, E. (2019): Reservoir Characterization to Improve Exploration Concepts of the Upper Jurassic in the Southern Bavarian Molasse Basin. – Dissertation. – München: Technische Universität München.

Müller, B., Wehrle, V., Zeyen, H. & Fuchs, K. (1997): Short-scale variations of tectonic regimes in the western European stress province north of the Alps and Pyrenees. – in: *Tectonophysics* 275 (1-3), pp. 199–219. – ᴅᴏɪ: 10.1016/S0040-1951(97)00021-8.

Müller, B., Zoback, M. L., Fuchs, K., Mastin, L., Gregersen, S., Pavoni, N., Stephansson, O. & Ljunggren, C. (1992): Regional patterns of tectonic stress in Europe. – in: *Journal of Geophysical Research - Solid Earth* 97 (B8), p. 11783. – ᴅᴏɪ: 10.1029/91JB01096.

Müller, M. & Nieberding, F. (1996): Principles of abnormal pressures related to tectonic developments and their implication for drilling activities (Bavarian Alps, Germany). – in: *EAGE Special Publications.* – ed. by G. Wessely & W. Liebl, pp. 119–126.

Müller, M., Nieberding, F. & Wanninger, A. (1988): Tectonic Style and Pressure Distribution at the Northern Margin of the Alps between Lake Constance and the River Inn. – in: *Geologische Rundschau* 77 (3), pp. 787–796. – ᴅᴏɪ: 10.1007/Bf01830185.

Nelson, E. J., Hillis, R. R., Meyer, J., Mildren, S. D., van Nispen, D. & Briner, A. (2005): The reservoir stress path and its implication for water-flooding, champion southeast field, Brunei. – in: *40th U.S. Symposium on Rock Mechanics.*

Nicolas, A., Fortin, J., Regnet, J. B., Dimanov, A. & Guéguen, Y. (2016): Brittle and semi-brittle behaviours of a carbonate rock: Influence of water and temperature. – in: *Geophysical Journal International* 206 (1), pp. 438–456. – ᴅᴏɪ: 10.1093/gji/ggw154.

Nitschke, F. (2017): Numerical and Experimental Characterization of Dissolution and Precipitation Processes in Deep Geothermal Reservoirs. – Dissertation. – Karlsruhe: Karlsruher Institut of Technology.

Nur, A. & Byerlee, J. d. (1971): An exact effective stress law for elastic deformation of rock with fluids. – in: *Journal of Geophysical Research* 76 (26), pp. 6414–6419. – ᴅᴏɪ: 10.1029/JB076i026p06414.

Obradors-Prats, J., Rouainia, M., Aplin, A. C. & Crook, A. J. L. (2017): Hydromechanical Modeling of Stress, Pore Pressure, and Porosity Evolution in Fold-and-Thrust Belt

Systems. – in: *Journal of Geophysical Research: Solid Earth* 122 (11), pp. 9383–9403. – DOI: 10.1002/2017JB014074.

Pannell, D. (1997): Sensitivity analysis of normative economic models: Theoretical framework and practical strategies. – in: *Agricultural Economics* 16 (2), pp. 139–152. – DOI: 10.1016/S0169-5150(96)01217-0.

Papazafeiropoulos, G., Muñiz-Calvente, M. & Martínez-Pañeda, E. (2017): Abaqus2Matlab: A suitable tool for finite element post-processing. – in: *Advances in Engineering Software* 105, pp. 9–16. – DOI: 10.1016/j.advengsoft.2017.01.006.

Peska, P. & Zoback, M. D. (1995): Compressive and Tensile Failure of Inclined Well Bores and Determination of in-Situ Stress and Rock Strength. – in: *Journal of Geophysical Research - Solid Earth* 100 (B7), pp. 12791–12811. – DOI: 10.1029/95jb00319.

Pfiffner, O. A. (1986): Evolution of the north Alpine foreland basin in the Central Alps. – in: *Foreland basins.* – vol. 8. – Spec. Publ. Int. Ass. Sediment, pp. 219–228.

Pletl, C., Stoyke, R. & Toll, H. (2010): Bohrerfahrungen bei Sueddeutschlands größtem Geothermieprojekt. – in: *bbr* 3, pp. 38–47.

Plumb, R. A. & Hickman, S. H. (1985): Stress-induced borehole elongation: A comparison between the four-arm dipmeter and the borehole televiewer in the Auburn Geothermal Well. – in: *Journal of Geophysical Research: Solid Earth* 90 (B7), pp. 5513–5521. – DOI: 10.1029/JB090iB07p05513.

Qian, W. & Pedersen, L. B. (1991): Inversion of borehole breakout orientation data. – in: *Journal of Geophysical Research* 96 (B12), p. 20093. – DOI: 10.1029/91JB01627.

Reinecker, J., Tingay, M. & Mueller, B. (2016): Borehole breakout analysis from four-arm caliper logs. – in: *WSM (World stress map): WSM quality ranking scheme, database description and anaylsis guidelines for stress indicator.*

Reinecker, J., Tingay, M., Mueller, B. & Heidbach, O. (2010): Present-day stress orientation in the Molasse Basin. – in: *Tectonophysics* 482 (1-4), pp. 129–138. – DOI: 10.1016/j.tecto.2009.07.021.

Reiter, K. & Heidbach, O. (2014): 3-D geomechanical–numerical model of the contemporary crustal stress state in the Alberta Basin (Canada). – in: *Solid Earth* 5 (2), pp. 1123–1149. – DOI: 10.5194/se-5-1123-2014.

Rühaak, W., Heldmann, C.-D., Pei, L. & Sass, I. (2017): Thermo-hydro-mechanical-chemical coupled modeling of a geothermally used fractured limestone. – in: *International Journal of Rock Mechanics and Mining Sciences* 100, pp. 40–47. – DOI: 10.1016/j.ijrmms.2017.10.019.

Sahara, D. P., Schoenball, M., Kohl, T. & Müller, B. (2014): Impact of fracture networks on borehole breakout heterogeneities in cristalline rock. – in: *International Journal of Rock Mechanics and Mining Sciences* 71, pp. 301–309. – DOI: 10.1016/j.ijrmms.2014.07.001.

Sassi, W. & Faure, J. L. (1997): Role of faults and layer interfaces on the spatial variation of stress regimes in basins: Inferences from numerical modelling. – in: *Tectonophysics* 266 (1-4), pp. 101–119. – DOI: 10.1016/S0040-1951(96)00185-0.

Savvatis, A. (2014): personal communication of well analyses.

Schmid, S. M., Fügenschuh, B., Kissling, E. & Schuster, R. (2004): Tectonic map and overall architecture of the Alpine orogen. – in: *Eclogae Geologicae Helvetiae* 97 (1), pp. 93–117. – DOI: 10.1007/s00015-004-1113-x.

Schmitt, D. R., Currie, C. A. & Zhang, L. (2012): Crustal stress determination from boreholes and rock cores: Fundamental principles. – in: *Tectonophysics* 580 (0), pp. 1–26. – DOI: 10.1016/j.tecto.2012.08.029.

Schneider, M. & Thomas, L. (2012): Wissenschaftliche und technische Grundlagen zur strukturgeologischen und hydrogeologischen Charakterisierung tiefer geothermisch genutzter Grundwasserleiter am Beispiel des süddeutschen Molassebeckens. – Berlin.

Schoenball, M., Glen, J. & Davatzes, N. C. (2016): Analysis and interpretation of stress indicators in deviated wells of the Coso Geothermal Field. – in: *41th Workshop on Geothermal Reservoir Engineering, Stanford, California.*

Schoenball, M., Sahara, D. P. & Kohl, T. (2014): Time-dependent brittle creep as a mechnaism for time-delayed wellbore failure. – in: *International Journal of Rock Mechanics and Mining Sciences* 70, pp. 400–406. – DOI: 10.1016/j.ijrmms.2014.05.012.

Schoenball, M. & Davatzes, N. C. (2017): Quantifying the heterogeneity of the tectonic stress field using borehole data. – in: *Journal of Geophysical Research: Solid Earth* 122 (8), pp. 6737–6756. – DOI: 10.1002/2017JB014370.

Schoenball, M., Walsh, F. R., Weingarten, M. & Ellsworth, W. L. (2017): How faults wake up: the Guthrie-Langston, Oklahoma earthquakes. – in: *The Leading Edge* 37 (2), pp. 810–816. – DOI: 10.1190/tle37020810.1.

Scholz, C. H. & Scholz, C. H. (2002): The Mechanics of Earthquakes and Faulting. – vol. 2. – Cambridge: Cambridge University Press. – DOI: 10.1017/9781316681473.

Schulz, R., Agemar, T., Alten, J.-A., Brunken, J., Heber, M., Kuder, J., Kuehne, K., Maul, A.-A., Pester, S., Schoenhofen, K., Fritzer, T., Birner, J., Schneider, M., Rauppach, K., Seibt, P., Wolfgramm, M., Brandes, J., Feldrappe, H., Obst, K., Jodocy, M. & Stober, I. (2009): Aufbau eines geothermischen Informationssystems für Deutschland - Endbericht. – Hannover.

Scott, D. R. & Thomas, L. A. (1993): A global algorithm for pore pressure prediction. – in: *8th SPE Middle East Oil Show and Conference.* – Manama, Bahrain, pp. 645–654.

Segall, P. & Fitzgerald, S. D. (1998): A note on induced stress changes in hydrocarbon and geothermal reservoirs. – in: *Tectonophysics* 289 (1-3), pp. 117–128. – DOI: 10.1016/S0040-1951(97)00311-9.

Seithel, R., Gaucher, E., Müller, B., Steiner, U. & Kohl, T. (2019a): Probability of fault reactivation in the Bavarian Molasse Basin. – in: *Geothermics* 82, pp. 81–90. – DOI: 10.1016/j.geothermics.2019.06.004.

Seithel, R., Niederhuber, T., Röckel, L., Müller, B. & Kohl, T. (2019b): Stress rotation in the Bavarian Molasse Basin inferred from borehole data and numerical simulation. – in: *preparation for submission.*

Seithel, R., Steiner, U., Müller, B., Hecht, C. & Kohl, T. (2015): Local stress anomaly in the Bavarian Molasse Basin. – in: *Geothermal Energy* 3 (1), p. 77. – DOI: 10.1186/s40517-014-0023-z.

Selg, M. & Wagenplast, P. (1990): Beckenarchitektur in südeutschen WeißenJura und die Bildung der Schwammriffe. – in: *Jahrbuch des Geologischen Landesamtes Baden-Württemberg* (32), pp. 171–206.

Seyberth, K. (2019): Impact of well orientation on borehole stability in deep geothermal wells, Bavarian Foreland Basin. – Masterarbeit. – Karlsruhe: KIT.

Shamir, G. & Zoback, M. D. (1992): Stress Orienation Profile to 3.5 km Depth Near the San Andreas Fault at Cajon Pass, California. – in: *Journal of Geophysical Research* 97 (B4), pp. 5059–5080. – DOI: 10.1029/91JB02959.

Sibson, R. H. (1977): Fault rocks and fault mechanisms. – in: *Journal of the Geological Society* 133 (3), pp. 191–213. – DOI: 10.1144/gsjgs.133.3.0191.

Sibson, R. H. (1974): Frictional constraints on thrust, wrench and normal faults. – in: *Nature* 249, pp. 542–544. – DOI: 10.1038/249542a0.

Sonder, L. J. (1990): Effects of density contrasts on the orientation of stresses in the lithosphere: Relation to principal stress directions in the Transverse Ranges, California. – in: *Tectonics* 9 (4), pp. 761–771. – DOI: 10.1029/TC009i004p00761.

Spann, H., Müller, B. & Fuchs, K. (1994): Interpretation of anomalies in observed stress data at the central graben (north sea) — numerical and analytical approach. – in: *Soil Dynamics and Earthquake Engineering* 13 (1), pp. 1–11. – DOI: 10.1016/0267-7261(94)90036-1.

Sperner, B., Mueller, B., Heidbach, O., Delvaux, D., Reinecker, J. & Fuchs, K. (2003): Tectonic stress in the earth's crust: advances in the World Stress Map project. – in: *New insights into structural interpretation and modelling*. – ed. by D. A. Nieuwland. – vol. 212. – Geological Society special publication, pp. 101–116.

Steiner, U. (2019): 4D Geomechanical Simulations (VISAGETN) to Evaluate Potential Stress Relocation in a Geothermal Targeted Fault System in Munich (South Germany). – in: *Proceeding of European Geothermal Congress (EGC).*

Steiner, U., Savvatis, A., Böhm, F. & Schubert, A. (2014): Explorationsstrategie tiefer geothermischer Ressourcen am Beispiel des süddeutschen Oberjuras (Malm). – in: *Handbuch Tiefe Geothermie*. – ed. by M. Bauer, W. Freeden, H. Jacobi & T. Neu. – Berlin, Hei-

delberg: Springer Berlin Heidelberg, pp. 429–461. – DOI: 10.1007/978-3-642-54511-5{\textunderscore}13.

Stier, P. & Prestel, R. (1991): Der Malmkarst im süddeutschen Molassebecken - Ein hydrogeologischer Überblick. – in: *Hydrogeologische Energiebilanz und Grundwasserhaushalt des Malmkarsts im süddeutschen Molassebeckens.* – ed. by B. LfW & LGRB. – vol. 03E-6240 A/B. – München: Schlussbericht zum Forschungsvorhaben, p. 12.

Stober, I., Jodocy, M. & Hintersberger, B. (2013): Gegenüberstellung von Durchlässigkeiten aus verschiedenen Verfahren im tief liegenden Oberjura des südwestdeutschen Molassebeckens. – in: *Zeitschrift der Deutschen Gesellschaft für Geowissenschaften*, pp. 663–679.

Streit, J. E. & Hillis, R. R. (2004): Estimating fault stability and sustainable fluid pressures for underground storage of CO2 in porous rock. – in: *Energy* 29 (9-10), pp. 1445–1456. – DOI: 10.1016/j.energy.2004.03.078.

Stump, B. B. & Flemings, P. B. (2002): Consolidation state, permeability, and stress ratio as determined from uniaxial strain experiments on mudstone samples from the Eugene Island 330 area, offshore Louisiana. – in: *Pressure Regimes in Sedimentary Basins and their Prediction.* – vol. 76. – AAPG Mem., pp. 131–144.

STWIVT (2010): Bayerischer Geothermieatlas - Hydrothermale Ernergiegewinnung. – München.

Su, S. & Stephansson, O. (1999): Effect of a fault on in situ stresses studied by the distinct element method. – in: *International Journal of Rock Mechanics and Mining Sciences* 36 (8), pp. 1051–1056. – DOI: 10.1016/S1365-1609(99)00119-7.

Sylvester, A. G. (1988): Strike-Slip Faults. – in: *Geological Society of America Bulletin* 100 (11), pp. 1666–1703. – DOI: 10.1130/0016-7606(1988)100<1666:Ssf>2.3.Co;2.

Taron, J. & Elsworth, D. (2009): Thermal–hydrologic–mechanical–chemical processes in the evolution of engineered geothermal reservoirs. – in: *International Journal of Rock Mechanics and Mining Sciences* 46 (5), pp. 855–864. – DOI: 10.1016/j.ijrmms.2009.01.007.

Terzaghi, K. (1962): Measurement of Stresses in Rock. – in: *Géotechnique* 12 (2), pp. 105–124. – DOI: 10.1680/geot.1962.12.2.105.

Terzaghi, R. D. (1965): Sources of Error in Joint Surveys. – in: *Geotechnique* 15 (3), pp. 287–304. – DOI: 10.1680/geot.1965.15.3.287.

Thorsen, K. (2011): In situ stress estimation using borehole failures — Even for inclined stress tensor. – in: *Journal of Petroleum Science and Engineering* 79 (3-4), pp. 86–100. – DOI: 10.1016/j.petrol.2011.07.014.

Tingay, M., Mueller, B., Reinecker, J. & Heidbach, O. (2006): State and Origin of the Present-Day Stress Field in Sedimentary Basins: New results from the World Stress Map Project. – in: *41st U.S. Symposium on Rock Mechanics.* – ed. by Golden Rocks. – ting2006.

Tingay, M., Reinecker, J. & Mueller, B. (2016): Borehole breakout and drilling-induced fracture analysis from image logs. – in: *WSM (World stress map): WSM quality ranking scheme, database description and anaylsis guidelines for stress indicator*, pp. 27–32.

Tondera, D., Klapperich, H., Blöcher, G., Moeck, I., Steiger, T., Bems, C. & Hild, S. (2013): Geothermie Forschungsprojekt "Allgäu 2.0" - Forschungsansätze, Laboruntersuchungen & Planungsschritte. – in: *Tagung für Ingenieurgeologie*.

Trice, R. (1999): A methodology for applying a non unique, morphological classification to sine wave events picked from borehole image log data. – in: *Borehole Imaging: applications and case histories.* – ed. by M. A. Lovell, G. Williamson & P. K. Harvey. – vol. Special Publications. – London: Geological Society, pp. 77–90. – DOI: 10.1144/GSL. SP.1999.159.01.04.

Ueckert, M. & Baumann, T. (2019): Hydrochemical aspects of high-temperature aquifer storage in carbonaceous aquifers: evaluation of a field study. – in: *Geothermal Energy* 7 (1), p. 50. – DOI: 10.1186/s40517-019-0120-0.

Unger, H. J. (1996): Tektonik des Molassebeckens. – in: *Erläuterungen zur Geologischen Karte von Bayern 1:500.000.* – ed. by Bayerisches Geologisches Landesamt. – München, pp. 265–266.

Unger, H. J. (2004): Schichtenverzeichnis und geologische Interpretation Unterhaching Gt1: unpublished technical report.

Unger, H. J. & Meyer, R. (1996): Kreide im Untergrund des Molassebeckens (Purbeck bis Campan). – in: *Erläuterungen zur Geologischen Karte von Bayern 1:500.000.* – ed. by Bayerisches Geologisches Landesamt. – München, pp. 125–128.

Unger, H. J. (1999a): Bayerische Molasse: Tektonik ; Nomenklaturen Ost-Westmolasse ; Pliozäne Stromsysteme. – vol. 125. – Documenta naturae. – München.

Unger, H. J. (1999b): Die tektonischen Strukturen der bayerischen Ostmolasse. – in: *Documenta naturae* (125), pp. 1–16.

Wagner, D., Mueller, B. & Tingay, M. (2004): Correction for tool decentralisation of oriented six-arm caliper logs for determination of contemporary tectonic stress orientation. – in: *Petrophysics* 42, pp. 1049–1076.

Walsh, F. R. & Zoback, M. D. (2016): Probabilistic assessment of potential fault slip related to injection-induced earthquakes: Application to north-central Oklahoma, USA. – in: *Geology* 44 (12), pp. 991–994. – DOI: 10.1130/G38275.1.

Wang, Y., Li, C., Hu, Y. & Mao, T. (2017): Brazilian Test for Tensile Failure of Anisotropic Shale under Different Strain Rates at Quasi-static Loading. – in: *Energies* 10 (9), p. 1324. – DOI: 10.3390/en10091324.

Wileveau, Y., Cornet, F. H., Desroches, J. & Blumling, P. (2007): Complete in situ stress determination in an argillite sedimentary formation. – in: *Physics and Chemistry of the Earth, Parts A/B/C* 32 (8-14), pp. 866–878. – DOI: 10.1016/j.pce.2006.03.018.

Wiprut, D. & Zoback, M. (2000a): Constraining the stress tensor in the Visund field: Norwegian North Sea: Application to wellbore stability and sand production. – in: *International Journal of Rock Mechanics and Mining Sciences* 37 (1-2), pp. 317–336. – DOI: 10.1016/S1365-1609(99)00109-4.

Wiprut, D. & Zoback, M. D. (2000b): Fault reactivation and fluid flow along a previously dormant normal fault in the northern North Sea. – in: *Geology* 28 (7), p. 595. – DOI: 10.1130/0091-7613(2000)28<595:FRAFFA>2.0.CO;2.

Wiprut, D., Zoback, M., Hanssen, T.-H. & Peska, P. (1997): Constraining the full stress tensor from observations of drilling-induced tensile fractures and leak-off tests: Application to borehole stability and sand production on the Norwegian margin. – in: *International Journal of Rock Mechanics and Mining Sciences* 34 (3-4), 365.e1–365.e12. – DOI: 10.1016/S1365-1609(97)00157-3.

Wolfgramm, M., Bartels, J., Hoffmann, F., Kittl, G., Lenz, G., Seibt, P., Schulz, R., Thomas, R. & Unger, H. J. (2007): Unterhaching geothermal well doublet: structural and hydrodynamic reservoir characteristic; Bavaria (Germany). – in: *Proceeding European Geothermal Congress*.

Wolfgramm, M., Birner, J., Diaz, S. & Lang, P. (2015): Ursachen der Injektivitätszunahme im Betrieb geothemischer Bohrungen im Malm des Molassebeckens. – in: *Der Geothermiekongress*.

Yale, D. P. (2003): Fault and Stress magnitude controls on variations in the orientation of in situ stress. – in: *Fracture and In-Situ Stress Characterization of Hydrocarbon Reservoirs*. – ed. by M. Ameen. – vol. 209. – London: Geological Society Special Publications, pp. 55–64. – DOI: 10.1144/GSL.SP.2003.209.01.06.

Zajac, B. J. (1997): The State of Stress as Inferred from Deviated Boreholes: Constrains on the Tectonics of Offshore Central California and Cook Inlet, Alaska. – Dissertation. – Pasadena, California: California Institute of Technology.

Zajac, B. J. & Stock, J. M. (1997): Using borehole breakouts to constrain the complete stress tensor: Results from the Sijan Deep Drilling Project and offshore Santa Maria Basin, California. – in: *Journal of Geophysical Research* 102 (B5), p. 10083. – DOI: 10.1029/96JB03914.

Zang, A. & Stephansson, O. (2010): Stress Field of the Earth's Crust. – Heidelberg: Springer.

Zang, A., Stephansson, O., Heidbach, O. & Janouschkowetz, S. (2012): World Stress Map Database as a Resource for Rock Mechanics and Rock Engineering. – in: *Geotechnical and Geological Engineering* 30 (3), pp. 625–646. – DOI: 10.1007/s10706-012-9505-6.

Zhang, Y. Z., Dusseault, M. B. & Yassir, N. A. (1994): Effects of Rock Anisotropy and Heterogeneity on Stress Distributions at Selected Sites in North-America. – in: *Engineering Geology* 37 (3-4), pp. 181–197.

Zhang, Y. & Zhang, J. (2017): Lithology-dependent minimum horizontal stress and in-situ stress estimate. – in: *Tectonophysics* 703-704, pp. 1–8. – DOI: 10.1016/j.tecto.2017.03.002.

Ziegler, M. O. (2017): The 3D in-situ stress field and its changes in geothermal reservoirs. – Dissertation. – Potsdam: Universität Potsdam.

Ziegler, M., Heidbach, O., Reinecker, J., Przybycin, A. M. & Scheck-Wenderoth, M. (2016): A multi-stage 3D stress field modelling approach exemplified in the Bavarian Molasse Basin. – in: *Solid Earth Discussions.* – DOI: 10.5194/se-2016-92,.

Ziegler, P. A. (1987): Compressional intra-plate deformation in the Alpine foreland- an introduction. – in: *Tectonophysics* 137, pp. 1–5. – DOI: 10.1016/0040-1951(87)90223-X.

Ziegler, P. A. (1995): Cenozoic rift system of Western and Central Europe; an overview. – in: *Geologie en Mijnbouw Netherlands Journal of Geosciences* 73 (2-4), pp. 99–127.

Zoback, M. D., Barton, C. A., Brudy, M., Castillo, D. A., Finkbeiner, T., Grollimund, B. R., Moos, D. B., Peska, P., Ward, C. D. & Wiprut, D. J. (2003): Determination of stress orientation and magnitude in deep wells. – in: *International Journal of Rock Mechanics and Mining Sciences* 40 (7-8), pp. 1049–1076. – DOI: 10.1016/j.ijrmms.2003.07.001.

Zoback, M. D., Moos, D., Mastin, L. & Anderson, R. N. (1985): Well Bore Breakouts and in Situ Stress. – in: *Journal of Geophysical Research-Solid Earth and Planets* 90 (Nb7), pp. 5523–5530. – DOI: 10.1029/Jb090ib07p05523.

Zoback, M. L. (1992): 1st-Order and 2nd-Order Patterns of Stress in the Lithosphere - the World Stress Map Project. – in: *Journal of Geophysical Research-Solid Earth* 97 (B8), pp. 11703–11728. – DOI: 10.1029/92jb00132.

Zoback, M. L., Zoback, M. D., Adams, J., Assumpcao, M., Bell, S., Bergman, E. A., Blumling, P., Brereton, N. R., Denham, D., Ding, J., Fuchs, K., Gay, N., Gregersen, S., Gupta, H. K., Gvishiani, A., Jacob, K., Klein, R., Knoll, P., Magee, M., Mercier, J. L., Muller, B. C., Paquin, C., Rajendran, K., Stephansson, O., Suarez, G., Suter, M., Udias, A., Xu, Z. H. & Zhizhin, M. (1989): Global Patterns of Tectonic Stress. – in: *Nature* 341 (6240), pp. 291–298. – DOI: 10.1038/341291a0.

Zoback, M. D. (2010): Reservoir geomechanics. – Cambridge: Cambridge University Press.

Zoback, M. L. & Richardson, R. M. (1996): Stress perturbation associated with the Amazonas and other ancient continental rifts. – in: *Journal of Geophysical Research* 101 (B3), pp. 5459–5475. – DOI: 10.1029/95JB03256.

Declaration of authorship

Lithology correlated S_h assessment based on formation-integrity and leak-off test data in the Bavarian Molasse Basin

This study is part of the joint research project of the Geothermal Alliance of Bavaria (GAB) and the Karlsruhe Institute of Technology (KIT) which is funded by the Bavarian State Ministry for Education and Culture Science and Art. For this study I developed the research concept, in cooperation with Erdwerk GmbH. I compiled the pressure data from drilling reports, developed the quality evaluation of the database for the interpretation of the stress field and finally wrote the manuscript. In an joint publication from the GAB I published as co-author the database for the shale-rich lithology (see Appendix B).

Stress rotation in basin structures inferred from borehole logging

Seithel, R., Niederhuber, T., Röckel, L., Müller, B. & Kohl, T. (2019b): Stress rotation in the Bavarian Molasse Basin inferred from borehole data and numerical simulation. – in: *preparation for submission.*

This study was conducted in collaboration with the GAB, which provided the Image log database and the financial support for the subcontract of "stress field analysis" in the topic "reservoir characterization". For this study I designed the research concept, performed the Image log interpretation, the calculations for the stress field analysis and the numerical sensitivity investigations. Subsequently, I interpreted the results and wrote the manuscript.

Potential of Fault Reactivation in the Bavarian Molasse Basin

Seithel, R., Gaucher, E., Müller, B., Steiner, U. & Kohl, T. (2019a): Probability of fault reactivation in the Bavarian Molasse Basin. – in: *Geothermics* 82, pp. 81–90. – DOI: 10.1016/j.geothermics.2019.06.004.

This study was performed in collaboration with the GAB, which provides financial support for the subcontract of "stress field analysis" in the topic "reservoir characterization". For this study I prepared the concept for the Monte-Carlo simulation of the reactivation potential study, analyzed the parameter sensitivity, interpreted the results and discussed the induced seismicity in the Bavarian Molasse Basin and finally wrote the manuscript.

Acknowledgment

Publications

Publications in peer-reviewed journals

Drews, M. C., Seithel, R., Savvatis, A., Kohl, T. & Stollhofen, H. (2019): A normal-faulting stress regime in the Bavarian Foreland Molasse Basin? New evidence from detailed analysis of leak-off and formation integrity tests in the greater Munich area, SE-Germany. – in: *Tectonophysics* 755, pp. 1–9. – DOI: 10.1016/j.tecto.2019.02.011.

Seithel, R., Gaucher, E., Müller, B., Steiner, U. & Kohl, T. (2019a): Probability of fault reactivation in the Bavarian Molasse Basin. – in: *Geothermics* 82, pp. 81–90. – DOI: 10.1016/j.geothermics.2019.06.004.

Seithel, R., Müller, B., Steiner, U., Kohl, T., Henk, A. & Stober, I. (2016): Slip Tendency Analysis & Frictional Strength of Reservoir Rocks in south Germany. – in: *Proceeding of European Geothermal Conference (EGC)*.

Seithel, R., Müller, B., Zosseder, K., Schilling, F. & Kohl, T. (2018): Betrachtung der Seismizität um Geothermie-Anlagen im Geomechanischen Kontext. – in: *Geothermische Energie* (89/2), pp. 24–27.

Seithel, R., Niederhuber, T., Röckel, L., Müller, B. & Kohl, T. (2019b): Stress rotation in the Bavarian Molasse Basin inferred from borehole data and numerical simulation. – in: *preparation for submission.*

Seithel, R., Schmidt, R. B., Kohl, T., Henk, A. & Stober, I. (2015a): Local Stress Anomaly, their Interplay to Deep Seated Fault Structures and Geomechanical Characterization of Geothermal Reservoirs in S-Germany. – in: *Proceeding of World Geothermal Congress (WGC)*.

Seithel, R., Steiner, U., Müller, B., Hecht, C. & Kohl, T. (2015c): Local stress anomaly in the Bavarian Molasse Basin. – in: *Geothermal Energy* 3 (1), p. 77. – DOI: 10.1186/s40517-014-0023-z.

Presentations with abstracts

Seithel, R. (2013a): Charakterisierung tektonischer Spannungen eines Geothermieprojektes im süddeutschen Molassebecken. – Oral presentation. – Joint Annual Meeting DMG & GV, Tübingen, 16-20.09.2013.

Seithel, R. (2013b): Charakterisierung tektonischer Spannungen eines Geothermieprojektes im süddeutschen Molassebecken. – Oral presentation. – 12. FKPE-Workshop Bohrlochgeophysik und Gesteinsphysik, Celle, 10-11.10.2013.

Seithel, R., Egert, R., Peters, M. & Kohl, T. (2017a): Studying overpressure and stress heterogeneity above a deep geothermal reservoir: a multi-physics rock mechanical approach. – Poster presentation. – 6th GeoProc Conference, Paris, France, 05-07.07.2017.

Seithel, R. & Kohl, T. (2013): Characterization of tectonic stress for a Geothermal Project in the southern Molasse Basin. – Oral presentation. – 2nd European Geothermal Workshop (EGW), Strasburg, 24.-25.10.2013.

Seithel, R. & Kohl, T. (2014): Application of Image Log Data for Geomechanical Reservoir Characterization of a Geothermal Project. – Oral presentation. – 10th International Geothermal Conference, Freiburg, 14.-12.05.2014.

Seithel, R. & Kohl, T. (2018a): Geomechanical considerations about induced seismicity in the Bavarian Molasse Basin. – Oral presentation. – Deutscher Geothermie Kongress (DGK), Essen, 27.-29.11.2018.

Seithel, R. & Kohl, T. (2018b): Geomechanical considerations about seismicity induced in the vicinity of geothermal plants. – Poster presentation. – 6th European Geothermal Workshop (EGW), Strasburg, 10.-11.10.2018.

Seithel, R. & Kohl, T. (2018c): Untersuchungen von Störungszonen im Umfeld von Geothermie-Anlagen in der Bayrischen Molasse. – Oral presentation. – Praxisforum Geothemie Bayern, München, 16.-17.10.2018.

Seithel, R., Peters, M. & Kohl, T. (2017b): Modelling stress heterogeneity within the Bavarian Molasse Basin. – Oral presentation. – 5th European Geothermal Workshop (EGW), Karlsruhe, 12.-13.10.2017.

Seithel, R., Peters, M. & Kohl, T. (2017c): Stress heterogeneities above and within a deep geothermal reservoir: From borehole observations to geomechanical modelling. – Oral presentation. – European Geosciences Union (EGU), Vienna, 23.-28.04.2017.

Seithel, R., Peters, M. & Kohl, T. (2017d): THM- Modellierung von Spannungsheterogenitäten oberhalb und innerhalb des Malm Reservoirs in München. – Oral presentation. – Der Geothermiekongress (DGK), München, 12.-14.09.2017.

Seithel, R., Schmidt, R. B., Kohl, T., Henk, A. & Stober, I. (2015b): Local Stress Anomaly, their Interplay to Deep Seated Fault Structures and Geomechanical Characterization of Geothermal Reservoirs in S-Germany. – Oral presentation. – World Geothermal Congress (WGC), Melbourne, Australia, 19-25.04.2015.